

Statics of Shallow Bistable Arches

A thesis submitted for the degree of

Doctor of Philosophy

in the Faculty of Engineering

by

Safvan Palathingal



Department of Mechanical Engineering

Indian Institute of Science

Bangalore 560012, India

March 2019

This thesis is dedicated to the memory of my grandmother, *Aysha*.

Acknowledgments

My PhD has been a wonderful learning experience and I am grateful to everyone who contributed to the work presented in this thesis. I thank my adviser, G. K. Ananthasuresh, wholeheartedly for his constant academic support as well as giving me opportunities to improve my writing, teaching, organisational, and management skills. I appreciate all the weekly and individual meetings with him, which made my time at IISc very productive.

I am thankful to the Department of Mechanical Engineering and its professors for providing a rigorous coursework. I thank Prof. C. S. Manohar, Prof. Ranjan Ganguly, Prof. C. S. Jog, and Prof. Ramsharan Rangarajan, for being my comprehensive examination panel and for their constructive suggestions.

I enjoyed working with Darshan, Anirudh, Niharika, Ramesh, Harishankar, Deepayan, Nitish, Varun, and Dhnanjay on various aspects of bistability over the last five years and I thank them for their contributions. I have learned a lot from all the fruitful discussions with them. I sincerely thank Late Prof. K. Lakshminarayana, Indian Institute of Technology - Madras, whose guidance to my adviser, Suresh, on roller-crank driven cam profiles inspired our work to consider analytical bilateral relationship between initial and toggled profiles. The 3D-printer in our Multidisciplinary and Multiscale Device and Design (M2D2) lab has been a great help in prototyping and validating our results; in this respect, the financial support from the Department of Science and Technology (DST) under the Technology Initiative for the Disabled and the Elderly (TIDE) programme is gratefully acknowledged. I also thank administrative staff in the department and in M2D2 for all their help.

I have immensely benefited from the calm and peace in the J N Tata library at IISc. Also, I hope that its magic spell to remain cool in hot summers without any air conditioning goes on unbroken forever. The indoor badminton court is one of my other favourite places in IISc and playing there was always fun.

I feel blessed to have met some amazing people outside lab and work. Thanks to Meera and Siddhartha for being there in tough times, for all the fun outings, and for

reminding me to live to the fullest. I also thank Ananya, Aditya, Emanuel, Koushik, Priyabrata, Namrata, Nirikshit, Ratan, Reena, Sreenath, Vageesh, and Vivek for their friendship.

I thank my family for their unconditional support and for putting my happiness ahead of theirs. All that I am and hope to be, I owe it to Immachi, Papa, and Rasha. Thank you.

Abstract

Bistable arches have two force-free stable equilibrium configurations. They also show multimodality by switching between their stable states in multiple deformation pathways. These two attributes and their nonlinear force-displacement characteristics are desirable in a range of engineering applications. The analytical and semi-analytical methods developed in this work enable a faster analysis than a finite element analysis and also facilitate closed-form relationships for the insightful design of bistable arches.

We show that arch profiles composed using the basis set of buckling mode shapes of the straight column with the corresponding boundary conditions exhibit bistability. We analyze such arches by expressing their deformed profiles also in the same basis set. We assume that the arches are slender and shallow to derive their potential energy comprising bending and compression strain energies as well as the work potential. We solve the equilibrium equations obtained by minimizing potential energy using a semi-analytical method for analytically intractable general boundary conditions. In this method, we obtain the critical points on the force-displacement curve corresponding to switching and switch back forces and travel of the mid-point of the arch. We use this method to analyze and optimize arches of varying as-fabricated stress-free shapes and boundary conditions.

We obtain an analytical relationship between the arch-profiles in the force-free states of the arch by equating the force to zero in the aforementioned equilibrium equations for both fixed-fixed and pinned-pinned boundary conditions. This relationship is bilateral, i.e., in one form it can be used for analysis and in another for design. We derive necessary and sufficient conditions as well as corollaries from the bilateral relationship pertaining to the shapes of bistable arches.

Deformation pathways in bistable arches can also be three-dimensional. These spatial deformation pathways can help reduce the switching and switch-back forces and might also, at times, adversely affect bistability. We model spatial pathways by incorporating additional energy terms due to out-of-plane bending and torsion into the analysis of planar arches. We use and extend a geometric relation by St. Venant and Michell to capture the coupling amongst the in-plane and out-of-plane deformations and rotation of

the cross-sections. Furthermore, we show that non-planar arches, i.e., spatial arches, can be bistable too. Our analysis is extended to spatial arches by modifying the geometric relation to consider the additional out-of-plane curvature.

We also present the design of two applications based on bistable arches: an RF-MEMS switch and a mechanical OR gate. The RF-MEMS switch utilizes bimodality and a novel initially-retracting electrothermal actuator to realize ON and OFF states with only two electrical terminals. The mechanical OR gate uses the bilateral relationship to design arch-profiles that achieve the OR gate logic.

Additionally, we present two studies on bistability in axisymmetric shallow thin shells. In the first study, we optimize the shell-profile for maximum travel by numerical and semi-analytical approaches and compare the results with the shell obtained by revolving the optimal arch for maximum travel. In the second study, we discuss the design of a passive universal gripper based on a bistable shell that can grasp objects of varying shapes.

List of publications

Journal

- Palathingal, S. and Ananthasuresh, G. K., Analytical modeling of spatial deformation pathways in planar and spatial shallow bistable arches, Proc. R. Soc. A 20190164 (2019).
<https://doi.org/10.1098/rspa.2019.0164>.
- Palathingal, S. and Ananthasuresh, G. K., Analysis and design of fixed-fixed bistable arch-profiles using a bilateral relationship, Journal of Mechanisms and Robotics (2019), pp.1-18.
<https://doi.org/10.1115/1.4043044>.
- Palathingal, S. and Ananthasuresh, G. K., A bilateral relationship between stable profiles of pinned-pinned bistable shallow arches, International Journal of Solids and Structures (2018).
<https://doi.org/10.1016/j.ijsolstr.2018.03.006>.
- Palathingal, S. and Ananthasuresh, G. K., Design of Bistable Arches by Determining Critical Points in the Force-displacement Characteristic, Mechanism and Machine Theory (2017), 117C, pp. 175-188.
<https://doi.org/10.1016/j.mechmachtheory.2017.07.009>.
- Yadav, D., Murthy, N. S., Palathingal, S., Shekhar, S., Giridhar, M. S. and Ananthasuresh, G. K., A Two-Terminal Bistable Electrothermally Actuated Microswitch. Journal of Microelectromechanical Systems (2019), 28(3), pp. 540-549.
<https://doi.org/10.1109/JMEMS.2019.2904997>.

Book-chapter

- Palathingal, S. and Ananthasuresh, G. K., Design of Bistable Pinned-Pinned Arches with Torsion Springs by Determining Critical Points, Chapter 56 in Mechanism and Machine Science, Ed., Springer Nature, Singapore, 2016, pages 12.
https://doi.org/10.1007/978-981-10-2875-5_56

Conference

- Varun, M., Palathingal, S., and Ananthasuresh, G. K., A passive universal grasping mechanism based on an everting shell, in: Fifth IFToMM Asian Mechanism and Machine Science (Asian MMS 2018), December 17th-20th, Bengaluru, India, 2018. (Recognised with the Best paper award)

- Banik, D., Palathingal, S., Ananthasuresh, G. K., and Ghosh, A., A mechanical OR gate using pinned-pinned bistable arches, in: Fifth IFToMM Asian Mechanism and Machine Science (Asian MMS 2018), December 17th-20th, Bengaluru, India, 2018.
- Palathingal, S., and Ananthasuresh, G. K., Bistability in arches and shells: designing for failure, in: Solvay workshop on Mechanics of slender structure in physics, biology and engineering: from failure to functionality, Solvay Institute, August 27th-29th, Brussels, Belgium, 2018.
- Gupta, N., Palathingal, S., and Ananthasuresh, G. K., Optimization of depth-profile of bistable arches for microsystems applications, in: Eighth ISSS International Conference on Smart Materials, Structures and Systems, July 5th-7th, Bengaluru, India, 2017.
- Palathingal, S. and Ananthasuresh, G. K., Optimization of Bistable Shallow- thin Shells without Pre-stress, in: 12th World Congress of Structural and Multidisciplinary Optimisation (WCSMO12), June 5th-9th, Braunschweig, Germany, 2017.
- Gupta, N., Palathingal, S., and Ananthasuresh, G. K., Optimization of Width- Profiles of Bistable Arches, in: 12th World Congress of Structural and Multidisciplinary Optimisation (WCSMO12), June 5th-9th, Braunschweig, Germany, 2017.
- Palathingal, S., Sarojini, D., Katti, A. N., and Ananthasuresh, G. K. , A generalized method to investigate the bistability of curved beams using buckling analysis, in: 2nd International and 17th National Conference on Machines and Mechanisms, December 16th-19th, Kanpur, India, iNaCoMM, 2015, p. 73. (Recognised with the Best Application Paper award)
<http://www.inacomm2015.ammindia.org/img/73.pdf>

Contents

1	Introduction	1
1.1	Bistability in elastic systems	1
1.2	Motivation	4
1.3	Scope of the thesis	8
1.4	Organization of the thesis	13
1.5	Closure	14
2	Literature review	15
2.1	Snapping in planar arches	15
2.1.1	Statics	15
2.1.2	Dynamics	17
2.2	Bistable arches	17
2.2.1	Planar arches	17
2.2.2	Spatial arches	19
2.3	Analysis on bistable buckled beams	20
2.4	Bistable shells	20
2.5	Applications	21
2.5.1	Switches	23
2.5.2	Universal passive grippers	24
2.6	Closure	25
3	Design and analysis of bistable arches by determining critical points in the force-displacement curve	27
3.1	Introduction	27
3.2	Analysis	28
3.2.1	As-fabricated and deformed profiles	30
3.2.2	Equilibrium equations	30
3.3	Critical-point method	35

3.3.1	Switching point	36
3.3.2	Switch-back point	38
3.3.3	Second stable point	39
3.4	Design and optimization using the critical-point method	39
3.4.1	Bistable arches with revolute flexures at the ends	39
3.4.2	Pinned-pinned bistable arches	44
3.4.3	Asymmetric bistable arches	44
3.4.4	Fixed-fixed double cosine bistable arches with restricted asymmetric mode	46
3.5	Closure	49
4	A bilateral relationship between stable profiles of bistable shallow arches	51
4.1	Introduction	51
4.2	Necessary and sufficient conditions for force-free equilibrium states in bistable arches with pinned-pinned boundary conditions	54
4.3	Analytical relation between initial and toggled profiles of pinned-pinned bistable arches	58
4.3.1	Results	58
4.3.1.1	Conditions on fundamental mode-weights	58
4.3.1.2	Relation between A_i and a_i	58
4.3.1.3	An equation in A_1 (for analysis)	59
4.3.1.4	A formula for a_1 (for design)	59
4.3.1.5	Corollaries	59
4.3.2	Proofs and derivations	60
4.3.2.1	Conditions on fundamental mode-weights	60
4.3.2.2	Relation between A_i and a_i	61
4.3.2.3	Proofs of corollaries	64
4.4	Illustrative examples of analysis and design	67
4.4.1	Analysis of bistable arches with specified initial profiles	67
4.4.2	Design of specified toggled profiles	69
4.4.3	Adding higher buckling modes to bistable arches	71
4.5	Necessary and sufficient conditions for force-free equilibrium states in fixed-fixed bistable arches	76
4.6	Analytical relation between the initial and toggled profiles of fixed-fixed bistable arches	78
4.6.1	Conditions on fundamental mode-weights of fixed-fixed force-free shallow bistable arch	78

4.6.2	An upper limit on $3Q^2C$ for fixed-fixed boundary conditions . . .	79
4.6.3	Bilateral relationship for fixed-fixed boundary conditions	80
4.6.4	Corollaries	82
4.7	Illustrative Examples	84
4.7.1	Analysis	84
4.7.2	Design	85
4.8	Closure	90
5	Analytical modeling of spatial deformation pathways in planar and spatial shallow bistable arches	91
5.1	Introduction	91
5.2	Analytical model for arches that deform spatially	93
5.2.1	Extension of St. Venant and Michell's relationship	95
5.2.2	Total potential energy	96
5.3	Spatial arches	98
5.3.1	Hinged and fixed support	98
5.3.2	Fixed fixed support	106
5.4	Extensions using the spatial arch model	108
5.4.1	As-fabricated profiles other than the fundamental shapes	109
5.4.2	Lateral torsional buckling in planar arches	111
5.4.3	Eccentric load	111
5.5	Comparison with finite element analysis	113
5.6	A note	114
5.7	Closure	115
6	Applications	117
6.1	Application 1 - A two-terminal bistable electrothermally actuated microswitch ¹	117
6.1.1	Design	118
6.1.2	Analytical Model	122
6.1.2.1	Modeling the bistable arch	122
6.1.2.2	Optimization of the initially-retracting actuator	127
6.1.2.3	Optimization of the V-beam actuator	128
6.1.3	Testing and Discussion	130
6.2	Application 2 - A mechanical OR gate using pinned-pinned bistable arches ²	132

¹Work done with Dhananjay Yadav

²Work done with Deepayan Banik

6.2.1	The OR logic	133
6.2.2	The design for the mechanical OR gate	133
6.2.2.1	Switching of the arch from binary 0 to binary 1	134
6.2.2.2	Switching of the arch from Binary 1 to Binary 0	136
6.3	Closure	138
7	Bistable shells	139
7.1	Introduction	139
7.2	Shape optimization for shell travel	141
7.2.1	Numerical approach	142
7.2.2	Semi-analytical approach	143
7.3	A passive universal gripper using a bistable shell ³	146
7.3.1	Working principle	146
7.3.2	Bistable shell	148
7.3.3	Switching mechanism and grasping arms	150
7.3.4	Results and performance	150
7.4	Closure	151
8	Closure and future work	153
8.1	Summary	153
8.2	Contributions of the thesis	154
8.3	Future work	158
A	An analytical model of electrothermal actuator	161
B	Design of bistable arches using a non-dimensional kinetoelastostatic map	165
	Bibliography	168

³Work done with Mytra V. S. Balakuntala

List of Figures

1.1	Examples of bistable systems in our daily life: (a) hair-clip, (b) spectacle-frame, (c) sippy-cup, (d) tin-lid, (e) shampoo-bottle-cap, (f) hibiscus leaf, (g) MCB, (h) windmill-blades, and (i) aircraft-wings (https://www.flxsys.com/).	2
1.2	Typical force-displacement characteristics of a bistable arch	4
1.3	How to design arch-profiles that are bistable for given boundary conditions?	5
1.4	A chair for the elderly designed using multimodal bistability.	5
1.5	(a) Planar and spatial deformation pathways of a planar arch; dashed lines aid visualization of the curvature of the arch during deformation (b) Switching forces of a spatially-deforming bistable arch are found to be smaller than those of an arch deforming in the plane.	6
1.6	How to design an arch-profile such that we get a desired shape in State 2 of the arch?	7
1.7	3D-printed bistable arches with various boundary conditions and as-fabricated profiles in their two stable states. (a) pinned-pinned sine arch (b) travel-optimized pinned-pinned arch (c) asymmetric pinned-pinned arch (d) asymmetric pinned-fixed arch (e) split-tube flexure-based arch, and (f) constrained double-cosine arch	9
1.8	Initial and toggled profiles of 3D-printed prototypes designed using the bilateral relationship.	10
1.9	3D-printed gripper in its open (a) and closed (b) configurations.	10
1.10	A pinned-pinned spatial arch in its as-fabricated stress-free, in-between stressed, and second stressed stable states.	11
1.11	(a) A two-terminal bistable micro-switch and (b) a passive universal gripper.	12
3.1	Typical force-displacement characteristics of a bistable arch	28

3.2	3D-printed bistable arches with various boundary conditions and as-fabricated profiles in their two stable states. (a) pinned-pinned sine arch (b) travel-optimized pinned-pinned arch (c) asymmetric pinned-pinned arch (d) asymmetric pinned-fixed arch (e) split-tube flexure-based arch, and (f) constrained double-cosine arch (Same as Fig. 1.7)	29
3.3	Buckling of a straight beam with rotary springs at the ends	30
3.4	Model of a bistable arch with flexures at the ends	31
3.5	Asymmetric mode of switching lowers the switching force	36
3.6	Effect of torsion stiffness on bistable characteristics	41
3.7	Critical-point method compared to FEA in Comsol using continuum elements	42
3.8	Dependence of F_s, F_{sb} , and U_{tr} on the as-fabricated shape	43
3.9	Optimal profiles of a bistable arch with split-tube flexure at the ends	44
3.10	Critical-point method compared to FEA in Comsol using continuum elements for pinned-pinned boundary conditions	44
3.11	Critical-point method compared to FEA in Comsol using continuum elements for asymmetric bistable arches with (a) asymmetric initial shape and (b) asymmetric boundary conditions	45
3.12	Critical-point method compared to FEA in Comsol using continuum elements for fixed-fixed boundary conditions with (a) $K_H = \infty$ (b) $K_H = 3 \times 10^5 N/m$	48
3.13	Limiting horizontal stiffness of fixed-fixed double-cosine arch	48
4.1	Strain energy profile of a bistable arch. Initial-profile and toggled profile are the arch-profiles corresponding to State 1 and State 2, respectively.	52
4.2	Schematic of two bistable arches gripping a circular object.	52
4.3	Strain energy profile of a buckled beam. Here, strain energies in the stable states are identical.	53
4.4	Schematic of a bistable gripper in the closed configuration.	54
4.5	A bistable arch with pinned-pinned boundary conditions. The solid curve is the as-fabricated shape, $h(x)$ and the dashed curve is the deformed profile, $w(x)$. L is the span of the arch, t , in-plane depth and b , the out-of-plane width.	55
4.6	An asymmetric initial profile and its toggled profile with $a_{10} = a_{20} = 0.1$ and $Q = 10$	66
4.7	Angulated arch-profile	67
4.8	Toggled profiles of the arches obtained using the relation for analysis.	68

4.9	Convergence of $h(x)$ to the specified-profile with higher values of n . . .	68
4.10	Two stable arch-profiles and an unstable arch-profile for $c = \frac{L}{2}$	69
4.11	Force-displacement curve showing snap-through but not bistability when $c = 25$ mm, $L = 10$ mm, $E = 1.2$ GPa, $b = 5$ mm, and $t = 0.5$ mm . . .	69
4.12	Elliptical arch-profile	69
4.13	Angulated profile in the second stable shape	70
4.14	Initial profiles of arches obtained using the relation for design	71
4.15	Schematic of a bistable cup-valve	71
4.16	Design of a bistable clamp	72
4.17	Design of bistable arch-profiles with higher mode weights	73
4.18	Comparison of a toggled profile with FEA	74
4.19	Initial and toggled profiles of 3D-printed prototypes. (a1)-(f1) are stress- free as-fabricated profiles; (a2)-(f2) are the corresponding toggled profiles.	75
4.20	Fixed-fixed bistable arches with an arbitrary initial profile	76
4.21	Double bistable arch with constrained asymmetric deformation.	78
4.22	Specified and approximated initial profiles	84
4.23	Toggled profile corresponding to the initial profile in Fig. 4.22.	85
4.24	As-fabricated profile of the arch.	85
4.25	Toggled profile corresponding to the initial profile in Fig. 4.24.	86
4.26	Specified arch-profile in the second stable state	86
4.27	Initial profile designed using Eq. (4.63).	86
4.28	Schematic of a bistable valve mechanism.	87
4.29	Specified arch-profile in the second stable state	87
4.30	Initial profile designed using Eq. (4.63).	87
4.31	Bistable arch with a change of angle of 45° at $x = 0.25$ mm for $h_{mid} =$ 13.46 mm $t = 0.5$ mm, and $L = 100$ mm.	88
4.32	3D-printed gripper in its open (a) and closed (b) configurations.	88
4.33	3D-printed bistable arches with fixed boundary conditions	89
4.34	Verification of the analytical profiles using FEA and 3D-printed proto- types.	89
5.1	(a) Planar and spatial deformation pathways of a planar arch; dashed lines aid visualisation of the curvature of the arch during deformation (b) Switching forces of a spatially-deforming bistable arch are found to be smaller than those of an arch deforming in the plane.	92
5.2	A pinned-pinned spatial arch in its as-fabricated stress-free, in-between stressed, and second stressed stable states.	92

5.3	A spatial arch with breadth, b , depth, t , span, L , and mid-span height in the xy plane, h_{mid}	94
5.4	(a) Force-displacement characteristics, (b) asymmetric deformation pathway, (c) potential energy landscape for the OACEGIT pathway, (d) deformation pathway from ABAQUS, and (e) time-lapse using high-speed photography (the hook that pushed the arch can be seen in the figures) for a spatial bistable arch with pinned-pinned boundary conditions.	103
5.5	(a) Force-displacement characteristics, (b) potential energy landscape, (c) time-lapses of switching and (d) switch-back for symmetric deformation pathways of a pinned-pinned spatial bistable arch.	105
5.6	(a) Force-displacement characteristics and (b and c) deformations pathways of a fixed-fixed spatial arch with parameters: $a_1 = 0.5$, $b_1 = 0.5$, $h_{mid} = 5$ mm, $b = 2$ mm, $t = 0.2$ mm, and $L = 100$ mm. (d) The two stable states of the arch in a 3D-printed prototype.	109
5.7	Force-displacement characteristics and deformation time-lapses of a spatial arch with as-fabricated starting shapes with (a and b) $a_3 = 0.2$ and (c and d) $a_7 = 0.1$	110
5.8	(a) Force-displacement characteristics and time-lapse of deformation of a planar arch with $a_1 = 1$, $b_1 = 0$, $h_{mid} = 5$ mm, $b = 0.9$ mm, $t = 0.5$ mm, and $L = 100$ mm, which shows bistability in the presence of a spatial deformation pathway. (b) Force-displacement characteristics and time-lapse of deformation of a planar arch with $a_1 = 1$, $b_1 = 0$, $h_{mid} = 5$ mm, $b = 0.6$ mm, $t = 0.5$ mm, and $L = 100$ mm, which is not bistable due to the presence of a spatial deformation pathway.	112
5.9	Comparison of force-displacement characteristics with (dashed curve) and without (solid curve) eccentric loading for spatial and planar pinned arches.	113
5.10	Comparison of force-displacement characteristics obtained from analytical modelling with FEA in ABAQUS for (a) pinned-pinned spatial (b) fixed-fixed spatial arch (c) fixed-fixed planar arch with spatial deformation, and (d) pinned-pinned arch with an eccentric load.	114
5.11	Comparison of force-displacement characteristics obtained from analytical modelling with FEA in Abaqus for a varying number of mode shapes.	115
5.12	(a) Spatial and planar arches with the same volume and pinned-pinned boundary conditions, and (b) comparison of their force-displacement characteristics.	116

6.1	Schematic of the proposed device and its working.	119
6.2	Initially-retracting actuator: (a) schematic, (b) transient behavior, and (c) plot depicting desired transient profile vs. possible with V-beam actuator.	121
6.3	Lumped model of a spring restrained arch.	122
6.4	Analytically obtained axial force (P) vs. axial displacement (U) of the bistable arch.	126
6.5	Axial force vs. axial displacement of displacement-amplifier for switch ON.	129
6.6	SEM images of the fabricated switch showing critical dimensions: (a) full view, (b)-(c) two stable states of the switch, (d) initially-retracting actuator, and (e) bistable arch.	130
6.7	Image of fabricated switch in (a) stable state 1 (OFF), and (b) stable state 2 (ON). In stable state 1, connection between ports P_1 and P_2 is closed while P_3 and P_4 are open and in stable state 2, vice versa.	131
6.8	Thermal imaging of (a) V-beam actuator and, (b) initially-retracting actuator. (Temperature scale in °C)	131
6.9	Comparison of analytical, FEM and experimentally measured transient displacement of (a) V-beam actuator, and (b) initially-retracting actuator.	132
6.10	The as-fabricated (middle) and toggled (bottom-most) shapes with travel (top-most). The arrows represent the direction of actuation.	134
6.11	Schematic arrangement of the input and output arches	134
6.12	Force-displacement curve for eccentric actuation (location 1 or 2).	135
6.13	Force-displacement curve for symmetric eccentric actuation (location 1 and 2).	135
6.14	Force-displacement curve for actuation at the mid-point of the input arches 1 and 2	136
6.15	Schematic arrangement of the input and output arches for reverse actuation.	136
6.16	3D-printed prototype of the OR gate design	137
7.1	A typical force-displacement curve of a bistable shell with time lapse showing as-fabricated, unstable, and everted configurations.	140
7.2	A section of a bistable shell	140
7.3	Travel of the mid-point of the shell between two stable states of a bistable shell	141

7.4	Optimal bistable shells that maximize travel at the mid-point between the two stable states.	143
7.5	Optimal bistable shells that maximize travel at the mid-point between the two stable states obtained using a semi-analytical approach.	145
7.6	Design space of arches with contours indicating the travel of shells . . .	145
7.7	Optimal shell obtained from revolving an arch with optimal travel . . .	146
7.8	A compliant monolithic grasping mechanism based on a bistable shell. The mechanism consists of three parts, (1) switching mechanism, (2) bistable shell, and (3) grasping arms.	147
7.9	Bistable shell with contracting mechanism and grasping arms attached. .	147
7.10	Working of the grasping mechanism simulated in Abaqus.	148
7.11	Bistable shell with contracting mechanism and grasping arms attached. .	149
7.12	Grasping arms can capture objects of varying sizes, shapes, and weights: (a) ring (b) paper clip (c) aluminum cylinder (d) mini motor (e) plastic spoon. 3D-printed prototype made in Object Connex 260. The grasping mechanism (f) grasps a screwdriver, (g) holds, and (h) releases it using the switching mechanism.	151
8.1	Model of a bistable arch with flexures at the ends	154
8.2	Critical points on the force-displacement curve.	155
8.3	Optimal profiles of a bistable arch with split-tube flexure at the ends . .	155
8.4	Asymmetric bistable arches with (a) asymmetric initial shape and (b) asymmetric boundary conditions designed using the critical-point method. 155	
8.5	A pinned-pinned spatial arch in its as-fabricated stress-free, in-between stressed, and second stressed stable states.	157
8.6	A spatial arch with breadth, b , depth, t , span, L , and mid-span height in the xy plane, h_{mid}	157
8.7	Symmetric deformation pathways of a pinned-pinned spatial bistable arch. 158	
A.1	Geometric parameters of an actuator beam.	163
B.1	Kinetoelastostatic map for fixed-fixed bistable arches.	166
B.2	Force-displacement curve for a bistable arch designed using a KES map simulated in Comsol Multiphysics 5.0	167

List of Tables

2.1	A summary of analysis on bistable arches	22
2.2	Comparative summary of bistable MEMS switches	24
3.1	Normalized parameters used in the spring-restrained pinned-pinned arch	34
3.2	Geometric and material parameters	40
6.1	Arch Parameters	123
6.2	Optimized values of an initially-retracting actuator	128
6.3	Optimized values of V-beam actuator	130
A.1	Parameters Involved In Actuator Modeling	162

Chapter 1

Introduction

Synopsis

This thesis describes the analysis, design, optimization, and applications of planar and spatial arches that have two force-free stable equilibrium states, namely *bistable arches*. Interestingly, to switch between two stable states, these arches can take multiple deformation pathways. Two force-free stable states and multiple deformation pathways enable bistable arches to have a wide range of applications. Analytical models that describe nonlinear force-displacement characteristics in the post-buckling regime of such structures are key to understanding bistability.

1.1 Bistability in elastic systems

Bistable elastic systems have two force-free stable equilibrium states. Hair-clips, spectacle-frames, sippy-cups, tin-lids, shampoo-bottle-caps, and hibiscus leaves (Fig. 1.1a-f) are examples of such systems with which we interact in our daily life. Bistability ensures that power is required only for switching between the two stable states but not for maintaining them. Thus, they are power-efficient. They are widely used in switch-based applications, for example, a miniature circuit breaker (MCB) shown in Fig. 1.1g. Using elastic bistable elements can reduce the number of parts in an MCB to just one or two. They can also be used in large-scale applications to orient windmill-blades based on the wind direction (Fig. 1.1h) and to orient aircraft-wings (Fig. 1.1i) based on the flight mode.

In each of the applications given in Fig. 1.1, there is a key elastic structural element that makes the system bistable. For instance the hair-clip in Fig. 1.1a has two prestressed

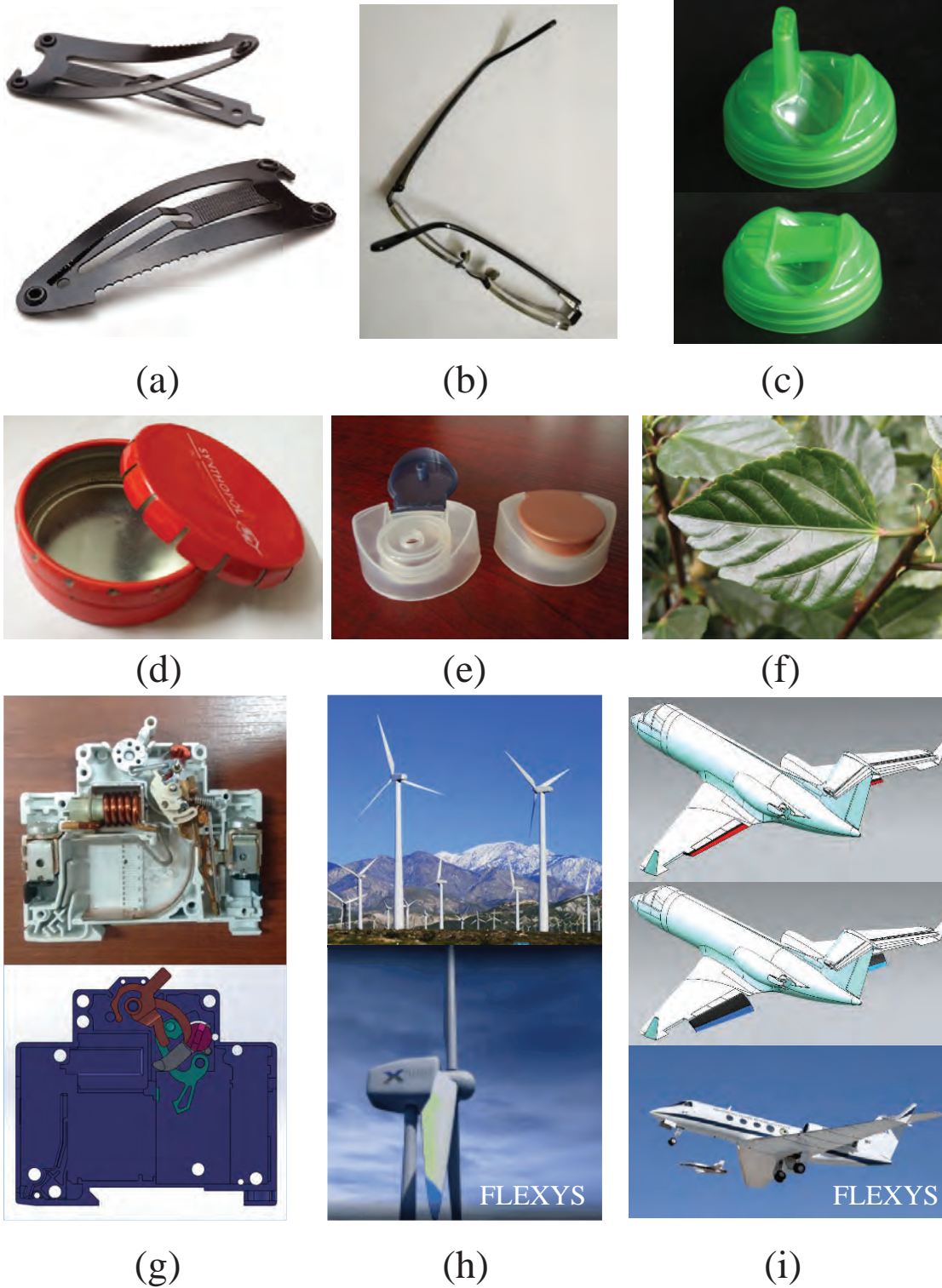


Figure 1.1: Examples of bistable systems in our daily life: (a) hair-clip, (b) spectacle-frame, (c) sippy-cup, (d) tin-lid, (e) shampoo-bottle-cap, (f) hibiscus leaf, (g) MCB, (h) windmill-blades, and (i) aircraft-wings (<https://www.flxsys.com/>).

bistable beams, the tin-lid in Fig. 1.1d is a bistable shell, and the MCB in Fig. 1.1g has two bistable arches. Buckled beams, arches, and shells are the three monolithic compliant bistable structures. Buckled beams are bistable only due to the prestress in them. On the other hand, arches and shells can be bistable solely due to their as-fabricated stress-free shape. In this thesis, we study stress-free bistable arches. Additionally, there is a chapter on bistable shells.

The bistable structures considered in this study are slender. This assumption comes from the fact that slender structures are prone to buckling, which is necessary for them to be bistable. Moreover, structures being slender helps simplify otherwise intractable analytical equilibrium equations. Another underlying assumption in all the analysis presented in the thesis is that the structures are shallow, i.e., the height of the arch is much less than its span. This is because only shallow arches exhibit snap-through buckling leading to bistability.

Figure 1.2a shows a typical force-displacement characteristic of a shallow slender bistable arch. There are three force-free points on the curve. The first and the last points correspond to the stable State 1 and State 2 of the arch, and the point in between corresponds to an unstable equilibrium. As shown in Fig. 1.2b, State 1 is the as-fabricated force-free equilibrium state and State 2 is the stressed force-free equilibrium state. Switching force, F_s , is the minimum force required to switch the arch from State 1 to State 2; switch-back force, F_{sb} , is the minimum force required to switch back to State 1 from State 2; and travel, u_{tr} , is the distance the midpoint of the arch moves between the two stable states. Generally, points on the force-displacement curve corresponding to F_s , F_{sb} and u_{tr} are useful metrics for analyzing and designing a bistable arch. Hence, we identify and refer to these three points as the *critical points* on the force-displacement curve in the rest of the thesis.

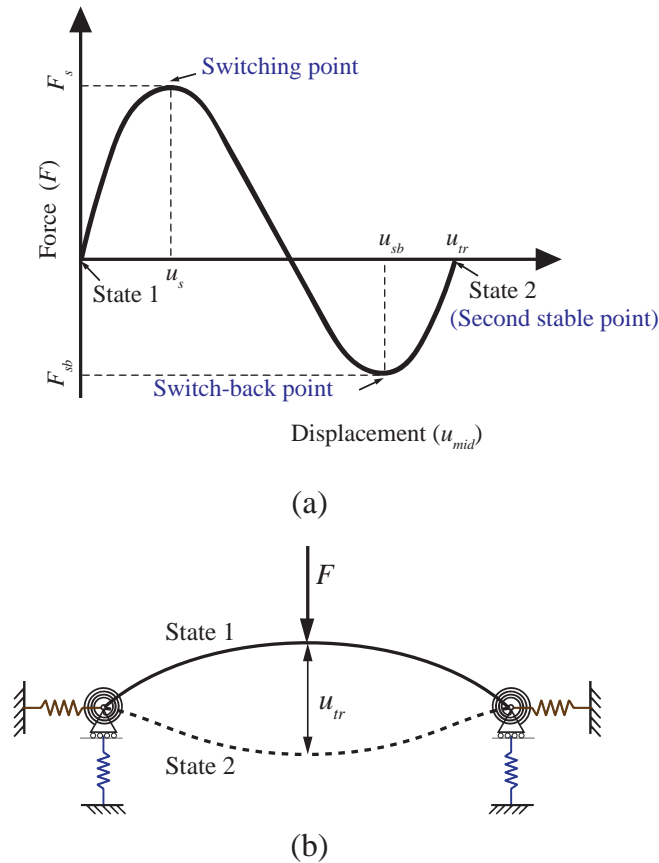


Figure 1.2: Typical force-displacement characteristics of a bistable arch

1.2 Motivation

This thesis is motivated by the absence of analytical techniques in the literature to design bistable arches. The theory of structural stability, starting from Leonhard Euler's seminal work on buckling columns (Euler, 1744), is well established. The effect of nonlinearity arising from large deflections, dynamic stability, and snap-through in arches has also been studied. However, these studies do not aid in the design of bistable arches. For example, to design an arch-profile for given boundary conditions, as shown in Fig. 1.3, ensuring bistable behaviour, the stability theory is not directly useful. This is mainly due to the change in perspective to design for buckling rather than to prevent it. Note that in the aforementioned question, we are looking for an arch that buckles between two configurations. In other words, the studies in structural stability were primarily intended in finding the critical load of failure of the arch. Our focus is in studying the post-buckling behavior of the arch to ensure that it buckles and has the desired metrics (F_s , F_{sb} , u_{tr}) and arch-profile.

For given boundary conditions, to find an arch-profile that is bistable, we need to en-

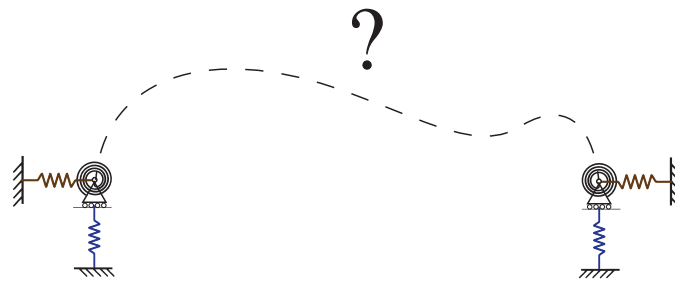


Figure 1.3: How to design arch-profiles that are bistable for given boundary conditions?

sure that the force-displacement characteristics of the arch have three force-free points. Furthermore, we are also interested in analyzing the critical points corresponding to the switching and switch-back forces, and travel. This seems to be a problem that finite element analysis (FEA) can solve. However, obtaining FEA-based numerical solutions in the post-buckling regime is computationally challenging due to a high degree of geometric nonlinearity and the presence of multiple buckling solutions that splits from a single point.

Note that each buckling solution corresponds to a certain *deformation pathway* of the arch. In other words, these solutions indicate that bistable arches can be switched from one state to another by multiple deformation pathways, i.e., bistable arches are *multimodal*. Let us understand a simple case of multimodality with the help of a chair for the elderly (Sarojini et al., 2016) conceptualized using bistable arches. As shown in Fig. 1.4, the weight of the person switches the seat attached to a bistable arch from

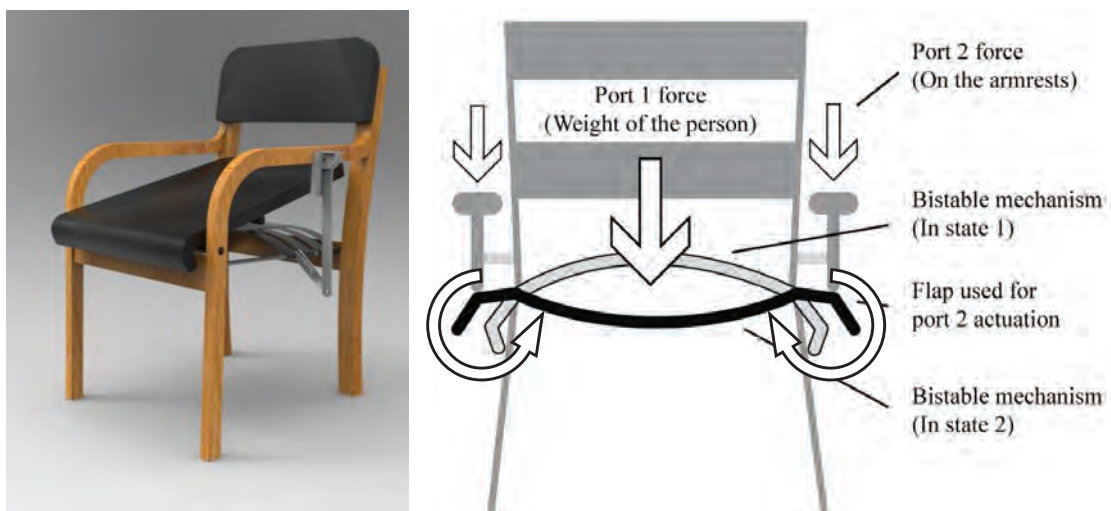


Figure 1.4: A chair for the elderly designed using multimodal bistability.

its first to second stable configuration, which is labeled actuation port 1. The moment applied at the pivot when the person tries to get up by pressing down the chair handle

switches the seat back and assists the person to rise, which is labeled actuation port 2. In this example, *bimodality* arises from two different modes of actuation; however, that is not the case always. Multiple deformation pathways exist for the same mode of actuation. For e.g., a bistable arch when actuated at a point at the mid-span can deform taking either symmetric or asymmetric pathways. How do we capture all these deformation pathways? Moreover, out of all the deformation pathways, how do we predict the pathway the arch will follow? How do we design arches to follow or not follow certain pathways? These are the questions that arise in designing arches.

In addition to planar deformation pathways, arches can be actuated to follow a spatial deformation pathway as shown in Fig. 1.5a. A comparison between force-displacement

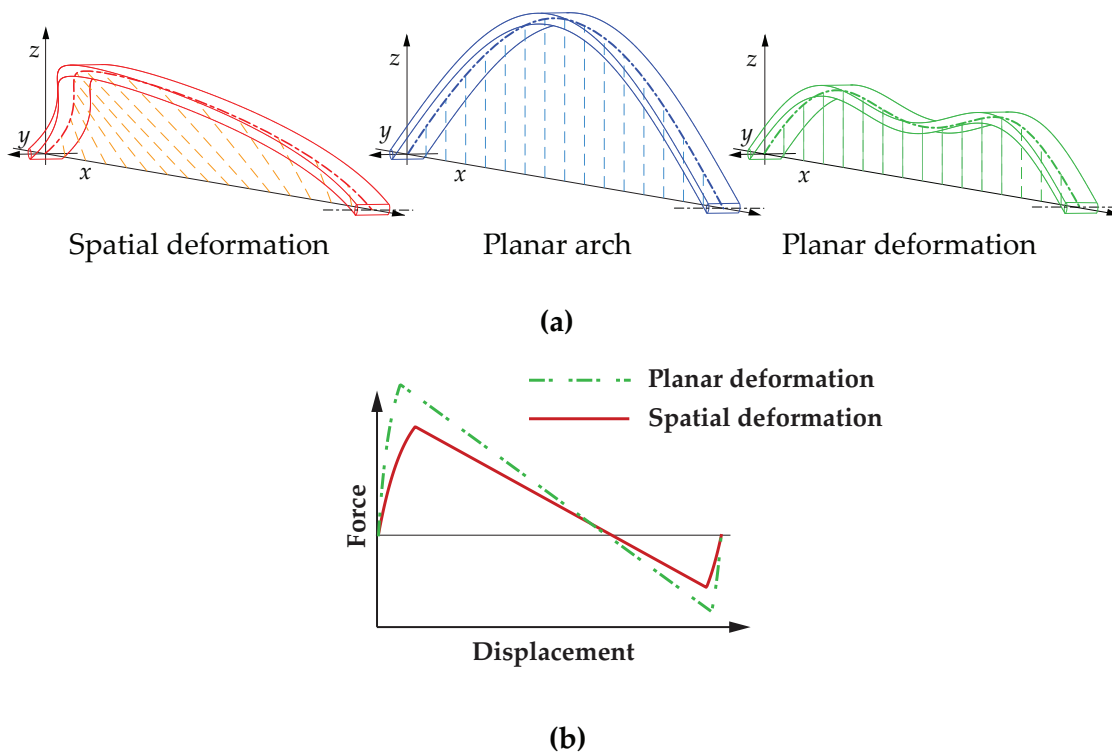


Figure 1.5: (a) Planar and spatial deformation pathways of a planar arch; dashed lines aid visualization of the curvature of the arch during deformation (b) Switching forces of a spatially-deforming bistable arch are found to be smaller than those of an arch deforming in the plane.

characteristics corresponding to spatial and planar deformation pathways is given in Fig. 1.5b. It can be noted that spatial deformation pathways in planar bistable arches reduce the switching and switch-back forces. In the context of bistability, this is sometimes desirable as it reduces the force required for switching between the equilibrium configurations of the bistable arch. Nonetheless, this also implies that these pathways reduce the stiffness and stability of the arch. Thus, the geometric and material parame-

ters that excessively favor spatial deformations can adversely affect bistability. How do we ensure that planar bistable arches do not lose bistability due to the presence of spatial deformation pathways? Answering this question requires insights into the spatial buckling of arches. Such insights are hard to come by through FEA as spatial deformation of unstable structures is computationally expensive even with today's computer hardware and software. The aforementioned analysis and design problems underline the need for analytical models to capture bistability.

Let us consider one more design problem to illustrate the utility of analytical solutions. How do we design an arch-profile such that we get a desired shape in State 2 of the arch, as for instance shown in Fig. 1.6? This question is not straightforward to solve

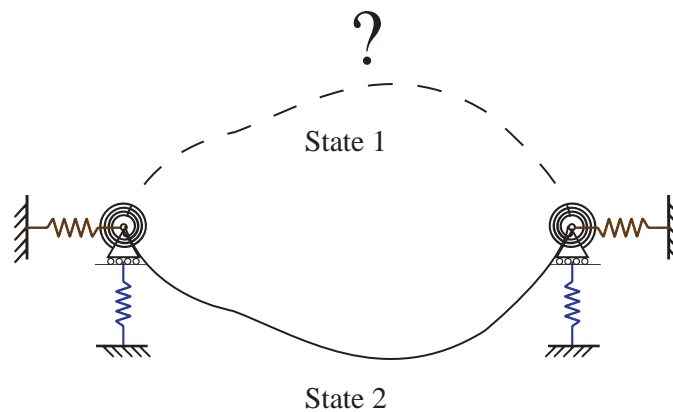


Figure 1.6: How to design an arch-profile such that we get a desired shape in State 2 of the arch?

with FEA, where an approach involving numerous iterations is the only way. Even if this approach works, it is cumbersome and not practical. In contrast, an analytical solution, which can either design for any given arch-profile or indicate that a solution for the specified arch-profile does not exist, would be ideal. Thus, analytical models for the analysis and design of bistable arches are imperative. To summarize, we address the following five questions using analytical models in this thesis:

- What are the key geometric and material parameters that affect curvature-induced bistability in shallow slender arches and how do we design and analyze such arches for any given boundary conditions?
- How does one obtain optimal bistable arches that have minimal switching force, maximum travel at the mid-span between two stable states, and maximum switch-back force?

- How to design for an arch-profile when the arch-profile in the other stable state is specified?
- How does spatial deformation affect planar bistable arches?
- Can arches with spatial curvatures be bistable and how do they compare to planar bistable arches?

By answering these questions, we capture the statics of bistable arches, which forms the subject matter of this thesis.

1.3 Scope of the thesis

Our interest in bistable-buckling is in line with the emerging trend in mechanics to use instabilities in structures for functionality. Other instabilities like wrinkling, crumpling, folding, etc., are also being used for a range of interesting applications (Reis, 2015). This “design for failure” approach is reviving some seminal works in structural instabilities. For example, the analysis presented by Fung and Kaplan in 1952 (Fung and Kaplan, 1952) is the backbone of the analytical models developed in this thesis. Another example is the geometric relation given by St. Venant and Michell (Love, 2013) to describe lateral-torsional buckling in arches, which inspired our analytical modeling of spatial deformation pathways in arches.

As described in the previous section, analytical models that describe nonlinear force-displacement characteristics in the post-buckling regime of such structures are key to understanding bistability. This thesis includes the analysis, design, optimization, and applications of shallow bistable planar and spatial arches.

We model planar arches with rotary and translational springs at pin joints anchored to the ground. The arches are modeled with springs at the joints to capture general boundary conditions with finite stiffness values as well as the extreme cases of pinned-pinned and fixed-fixed conditions. The equilibrium equations for a post-buckling analysis are derived by writing the deflected profile as a linear combination of the buckling mode shapes of the corresponding straight beam with torsion and translational springs at the pinned ends, a technique introduced by Fung and Kaplan (1952). These equations are solved to obtain the force-displacement characteristics and deformation pathways. We propose a computational approach based on critical points on the force-displacement curve. An algorithm to obtain the critical-points for arches with general boundary con-

ditions is presented. The critical-point method enables the design of bistable arches with a wide range of boundary conditions and initial shapes as shown in Fig. 1.7.

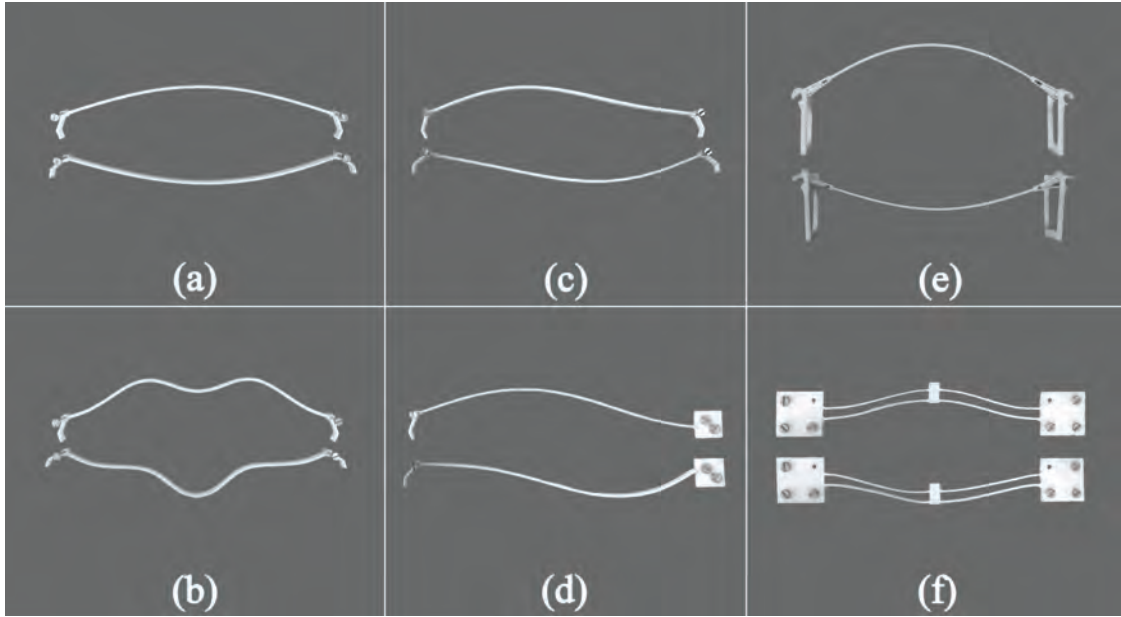


Figure 1.7: 3D-printed bistable arches with various boundary conditions and as-fabricated profiles in their two stable states. (a) pinned-pinned sine arch (b) travel-optimized pinned-pinned arch (c) asymmetric pinned-pinned arch (d) asymmetric pinned-fixed arch (e) split-tube flexure-based arch, and (f) constrained double-cosine arch

Our model relies on capturing various energy components in the arches. In planar arches, irrespective of the boundary conditions, bistability arises from the interplay of transverse bending and axial compression strain energies. Quantitatively, bending and compression energies are proportional to the squares of change in the curvature and arc-length of the arch, respectively. Since there is always a change in curvature associated with a deforming arch, bending energy attains a minimum only in the as-fabricated stress-free state of the arch. On the contrary, a change in arch-length can assume minimal values at multiple deformed states of the arch. The existence of two such minimum points in the axial energy landscape is essential to have two minima in the total strain energy curve and therefore it is essential for bistability in arches with no prestress.

To analyze and design bistable arches of arbitrary profiles efficiently, we derive a two-way, i.e., bilateral, relationship between the stress-free initial profile and the stressed toggled profile. This relationship is presented for pinned-pinned and fixed-fixed boundary conditions. We prove that the fundamental mode weights should be non-zero for an arch to be bistable. The following corollaries arise from the aforementioned relation: (1)

the symmetry in initial and toggled profiles remains unchanged; (2) all the mode weights other than the fundamental mode weight have the same sign in both stable states; (3) the magnitudes of corrugations in stable force-free arch-profiles are approximately equal. Figures 1.8 and 1.9 show 3D-printed prototypes of arch-profiles conceived using the bilateral relationship. The arch-profiles in Figure 1.8 have pinned-pinned boundary con-

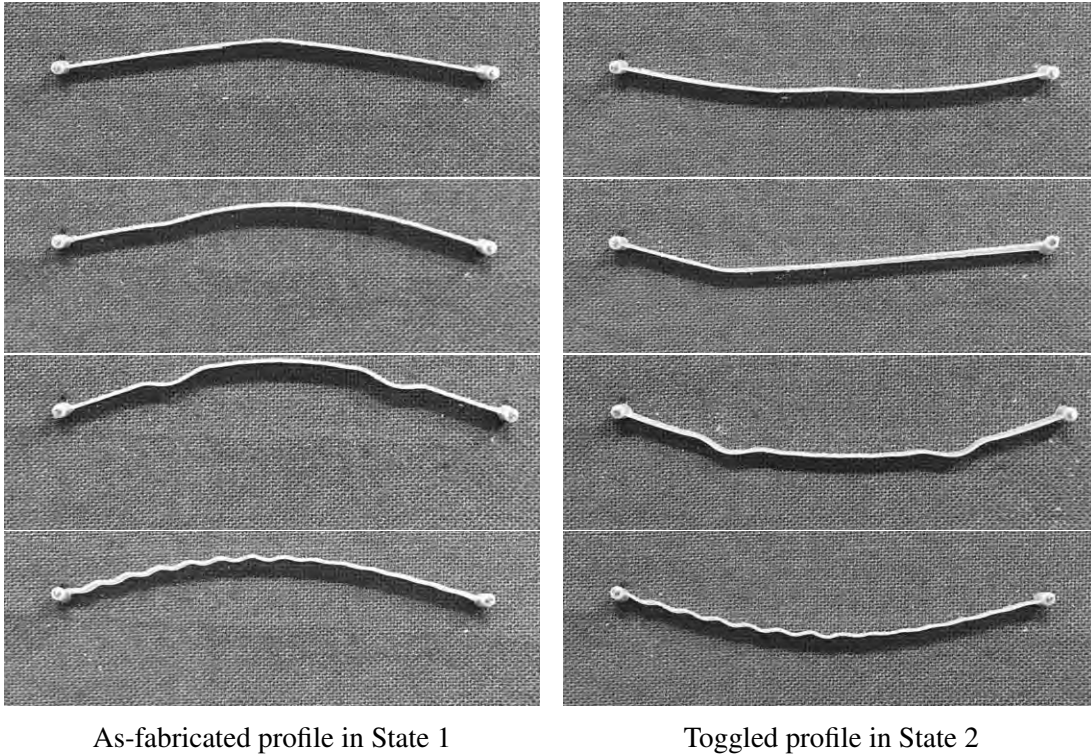


Figure 1.8: Initial and toggled profiles of 3D-printed prototypes designed using the bilateral relationship.

ditions and the bistable gripper-profile designed to grasp a circular disk in Fig. 1.9 have fixed end conditions.

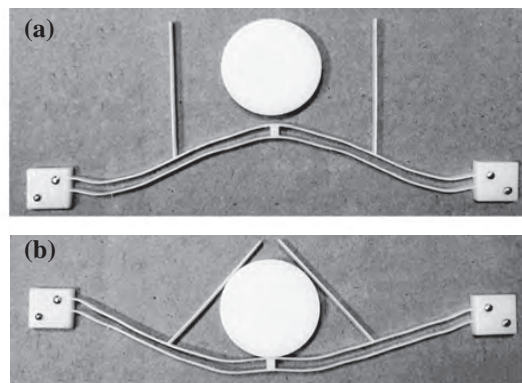


Figure 1.9: 3D-printed gripper in its open (a) and closed (b) configurations.

Our model captures multiple deformation pathways, including spatial deformation pathways, in bistable arches. With the aid of potential energy landscapes, we predict the preferred pathway of any given arch. Note that when arches deform in spatial deformation pathways, in addition to axial and transverse bending energies, there are torsional and out-of-plane bending energies as well. We show that the key to modeling these interrelated energy terms is a geometric relation, which we obtain by modifying the St. Venant and Michell relationship discussed in 1969 [Love \(2013\)](#); [Ojalvo et al. \(1969\)](#). We use the understanding of spatial deformation pathways to design planar arches with a reduced switching force and to eliminate the loss of bistability due to spatial deformation pathways in planar bistable arches.

Our studies on spatial deformation pathways in planar bistable arches led us to a new and general class of structures, namely *spatial bistable arches*. As shown in [Fig. 1.10](#), the curvature of the spatial arch is not restricted to a single plane. Two varying orthog-

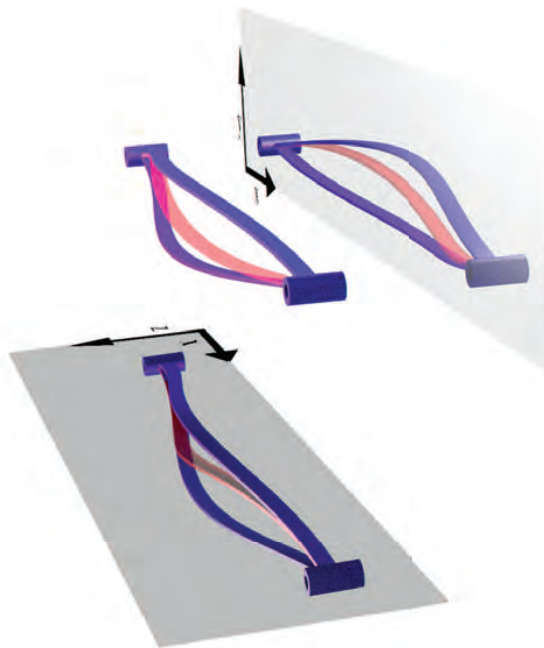


Figure 1.10: A pinned-pinned spatial arch in its as-fabricated stress-free, in-between stressed, and second stressed stable states.

onal curvatures of the arch can be seen in the reflections of the arch in the xy and xz planes. Spatial arches only exhibit spatial deformation pathways. Spatial arch-profiles of in-between, and second stable states of the arch are also given in [Fig. 1.10](#). We show the analysis of spatial bistable arches with varying as-fabricated shapes and eccentric loading for pinned-pinned as well as fixed-fixed end conditions.

In this thesis, we also consider shallow-thin shells that can be bistable without pre-

stress. We show that there is scope for the optimization of shallow-thin shells in view of switching and switch-back forces as well as the distance travelled by points of interest between the two states. We vary the shape of the shell for a chosen thickness-profile and support conditions. Three approaches are followed to pose and solve the optimization problem for maximizing the travel with constraints on the switching and switch-back forces.

Numerous examples are presented throughout the thesis to illustrate the utility of the analytical models developed for design and analysis. Furthermore, we present the design of three applications of bistability. The first two applications are based on bistable arches. The first application is a two-terminal bistable electrothermally actuated micro-switch shown in Fig. 1.11a. The proposed design has bimodal bistability which is ob-

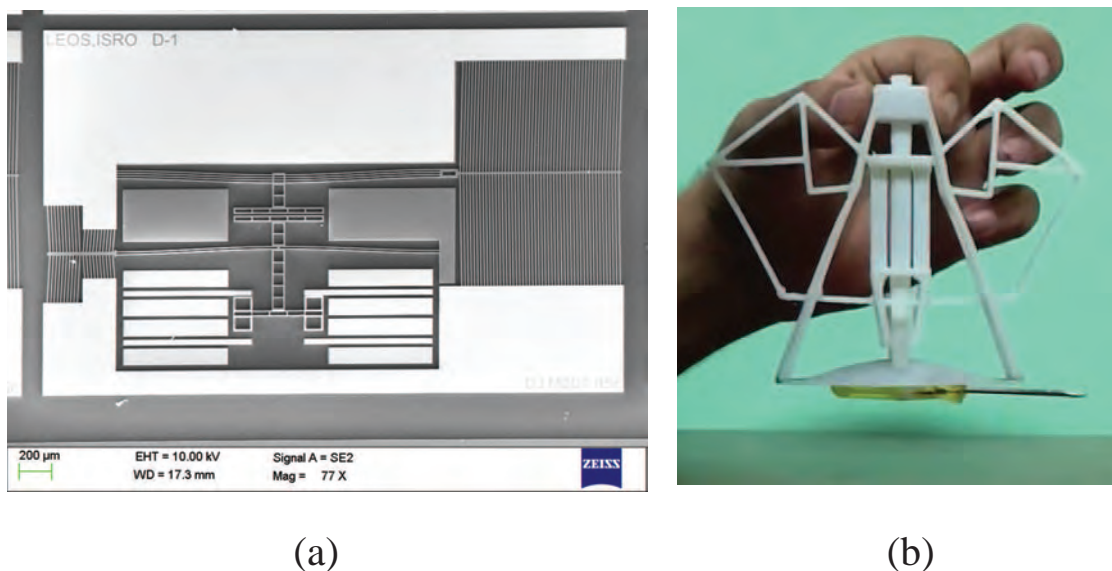


Figure 1.11: (a) A two-terminal bistable micro-switch and (b) a passive universal gripper.

tained by using a pair of bistable arches. A V-beam electrothermal actuator, and a novel initially-retracting actuator are the two other crucial design elements of the microswitch. The salient feature of the design is the use of only a single pair of electrodes to switch between on and off states, even though there are two actuators. The switch design is experimentally verified by realizing on a silicon-on-insulator (SOI) wafer using a single-layer micro-fabrication technique.

In the second application, an OR gate is designed using pinned-pinned bistable arches. The compliant OR gate consists of five bistable arches arranged in such a way that a central arch acts as the output with 0 and 1 stable states while two pairs of arches, with their own 0 and 1 states, act as inputs. The arch-profiles of all the arches are de-

signed so that the forces of switching and switching back between the two stable states and the travel between the two stable configurations are as desired. A macro-scale prototype is made using 3D-printing to validate the OR logic behaviour of the device.

The third application is a passive universal gripper based on a bistable shell. The gripper is a monolithic design that combines a switching mechanism, an everting shell, and grasping arms as shown in Fig. 1.11b. The switching mechanism releases the grasped objects by transmitting the input force to the everting shell. The bistable shell everts upon contact with the object to enable the grasping arms to envelop the object.

1.4 Organization of the thesis

In Chapter 2 of this thesis, we present the literature of bistable structures. We discuss the seminal papers on structural stability that were key to the subsequent development of the analysis of bistable arches and shells. Important work on the optimization of bistable structures is reviewed. We also present the recent literature that focuses on bistability and its applications.

Chapter 3 presents a semi-analytical method for the analysis and shape-synthesis of bistable arches with general boundary conditions. This is done by numerically determining critical points in the force-displacement curve of a bistable arch. The critical-point method is used for shape optimization for improving the travel and the switch-back force of the arch using the critical-point method.

In Chapter 4, we derive a bilateral relationship between the stress-free initial profile and the stressed toggled profile of pinned-pinned and fixed-fixed bistable arches. This bilateral relationship is derived in two forms: a nonlinear single-variable equation for analysis and a closed-form analytical expression for design. Some symmetrical features of shape as well as necessary and sufficient conditions are presented as corollaries.

In Chapter 5, we analyze spatial deformation pathways in bistable arches and present an analytical model incorporating axial, two transverse bending, and torsion energy components. In this model, we extend the St. Venant and Michell relationship used in the flexural-torsional buckling of planar arches and use it in modeling spatial arches. We show that not considering spatial deformation leads to incorrect inferences concerning the bistability of planar arches too. Thus, this model serves as a generalised framework for the existing analysis on planar arches since they belong to a subset of spatial arches.

In Chapter 6, we present two applications using bistable arches. One is the design of an electrothermally-actuated two-terminal bistable microswitch. The salient feature

of the design is the use of only a single pair of electrodes to switch between the on and off states, even though there are two actuators. We demonstrate the use of the analytical model described in Chapter 3 in deciding the parameters of the bistable arch used in this design. In the second application, we design a mechanical OR gate using bistable arches.

Chapter 7 comprises optimization and an application using shallow-thin bistable shells. We follow three approaches to pose and solve optimization problems for maximizing the travel with constraints on the switching and switch-back forces. In the application part, a passive monolithic compliant grasping mechanism is conceptualized. The grasper is capable of picking up stiff objects of any shape up to a maximum size and weight.

The contributions of this thesis and the scope of future work are discussed in Chapter 8. A design technique using kinetoelastostatic maps is presented in Appendix A. This design method is useful to scale the designs created using the analytical tools discussed in chapters 3, 4, and 5. An analytical model of the electrothermal actuator used in the design of a two-terminal bistable microswitch is given in Appendix B.

1.5 Closure

Bistability in structures finds numerous applications in our daily lives. We discussed the importance of analytical modeling in designing bistable arches. In this context, we highlighted the analysis and design problems of bistable arches, which forms the subject matter of this thesis. We noted the scope and contributions of this thesis. In the next chapter, we give a detailed review of the literature on the analysis of bistable structures and show where the contributions from this thesis fit in.

Chapter 2

Literature review

Synopsis

The analysis of bistable arches has benefited from the existing literature on the snapping of arches. An overview of the important results from the static and dynamic studies of buckling in arches is presented followed by the development in analytical techniques of bistable arches. The literature on analyses of bistability in buckled beams, elastica, spatial arches and shells is discussed. Along with the literature, the work on which this thesis is based is also described. Additionally, a review of mechanism designs and applications involving bistable structures is presented.

2.1 Snapping in planar arches

Before bistability in arches found extensive use in engineering applications, the characteristic buckling in shallow arches was widely referred to as snapping (also known as snap-buckling or oil-canning) in arches. Studies on snapping helped in designing arches that resisted buckling. In this section, we discuss studies on static and dynamic analyses of buckling in arches.

2.1.1 Statics

Arches can be classified into two types based on their height to span ratio. Arches with this ratio closer to or greater than one, i.e., the height is comparable to the span, are called high arches. In low or shallow arches, this ratio is small and so the height is much smaller compared to their span. Buckling in both high and low arches has been studied since the beginning of the 20th century.

In finding the critical load in high arches, capturing the axial compression energy is not crucial since their dominant mode of buckling is bending. In other words, while finding the critical buckling load, high arches are considered inextensional. [Hurlbrink \(1907\)](#), [Chwalla \(1927\)](#), [Timoshenko \(1936\)](#), R. Mayer, E. Gaber, and L. Nicolai (the last three works are referred to in [Timoshenko \(1936\)](#)) studied buckling in high circular arches under uniformly distributed loading with various types of boundary conditions.

To predict buckling in shallow arches, capturing axial compression energy is as important as bending energy. According to [Timoshenko \(1936\)](#), this problem was first discussed by [Navier \(1864\)](#). As in the case of high arches, initial stability studies on shallow arches by [Biezeno \(1938\)](#); [Friedrichs \(1945\)](#); [Marguerre \(1938\)](#) considered circular arch-profiles. [Timoshenko \(1936\)](#) analyzed a low arch with a sine-curved initial shape. These studies observed that buckling in shallow arches led to sudden reversal in their curvature, which was referred to as snapping or snapthrough buckling or oil-canning. These studies assumed symmetric buckling solutions which resulted in a significant error in the predicted buckling loads.

The foremost comprehensive analysis considering asymmetric buckling modes and varying arch shapes was by [Fung and Kaplan \(1952\)](#). The key step in the analysis was to approximate the deflection of the arch with a Fourier series. The axial compression energy was modeled by using the change in the arch length as the axial strain. They investigated pinned-pinned shallow arches of various as-fabricated shapes and load conditions and showed that the height of the shallow arch determines whether the arch snaps through symmetrically or asymmetrically. They verified their analytical results with experimental data.

Thereafter, several extensions to [Fung and Kaplan \(1952\)](#)'s model have appeared in the literature in the context of stability. [Gjelsvik and Bodner \(1962\)](#) attempted the problem of buckling in a fixed-fixed shallow circular arch with a concentrated load at the midpoint and obtained an approximate solution. An exact solution for this was later given by [Schreyer and Masur \(1966\)](#). [Masur and Lo \(1972\)](#) presented a general discussion on the behavior of shallow circular arches concerning buckling, post-buckling and imperfection sensitivity by using [Koiter \(1970\)](#)'s theory of elastic stability that showed the importance of imperfection sensitivity using an asymptotic analysis.

The snapping of shallow pinned arches resting on an elastic foundation under distributed loads was studied by [Simitse \(1973\)](#). The influence of the load position of the snap-through instability was investigated by [Plaut \(1979\)](#). [Chen et al. \(2009\)](#) derived the exact static critical loads for a pinned sine arch under a quasi-static concentrated force

at the midpoint and couples at the endpoints (Chen and Lin, 2005b). In both of these studies, they start their analysis from the governing differential equation of the arches. Then they guess the deformed profile to be a sum of buckling mode shapes similar to the aforementioned energy-based methods.

2.1.2 Dynamics

Hoff and Bruce (1953) first analyzed dynamic snapping in arches. This work was published alongside Fung and Kaplan (1952)'s work and a part in both the papers was identical. Several works that discussed the dynamics of the snapping of shallow arches followed later. Humphreys (1966) extended Hoff and Bruce (1953)'s analytical method for different boundary conditions and Lock (1966) considered dynamic snapping under a step pressure load. Hsu showed the effect of various parameters and initial conditions on the dynamic stability for arches of arbitrary shapes (Hsu, 1966, 1967, 1968a,c). Some of the other notable contributions are due to Fulton and Barton (1971); Gregory and Plaut (1982); Huang and Nachbar (1968); Johnson (1980); Johnson and McIvor (1978); Lo and Masur (1976); Patrcio et al. (1998); Sundararajan and Kumani (1972).

Recently, Chen analyzed dynamic snap-through in laterally loaded arches under prescribed end motion with constant speed (Chen Jen-San and Lin Jian-San, 2004; Lin and Chen, 2003). He derived exact dynamic critical loads for a pinned sine arch under a concentrated force at the midpoint (Chen et al., 2009).

2.2 Bistable arches

In the early 2000s, the force-free stable equilibrium configurations arising from snapping in arches started to find use in switch-based applications at the micro scale. In this context, snapping arches gained popularity as bistable arches. This revoked interest in designing for buckling in arches for specific switching forces and travel of a point between two stable states.

2.2.1 Planar arches

Lee et al. (1999) analyzed the buckling of planar microactuators with bistable shallow arch-shaped leaf springs for use in micro-optical switches and microrelays. Qiu et al. (2004) showed analytically that the analysis by Lee does not reveal the key design requirement involved in designing bistable arches with fixed-fixed boundary conditions.

They showed that an arch can be made bistable by taking an as-fabricated shape as a double-cosine curve joined at the mid-span. This is to physically restrict the asymmetric mode of deformation, which, if not prevented, affects bistability.

A bistable arch with pinned-pinned boundary conditions has advantages over fixed-fixed arches. First, a pinned-pinned arch does not need a connected double cosine curve to restrict the asymmetric mode of switching. Second, it has an enhanced range of travel between its two stable states and reduced switching force. Third, it has provision for secondary lateral actuation, which was used by [Sarojini et al. \(2016\)](#) in a bimodal actuation of an assistive chair. However, pin joints lead to difficulties in manufacturing at the micro scale and problems in operation due to friction and wear. Therefore, we ([Palathingal et al., 2015](#)) proposed bistable arches with rotational flexures at the ends with a monolithic design retaining the aforementioned three advantages while easing manufacturing. Furthermore, we observed that the choices of sine curves for the initial profile for pinned-pinned ([Fung and Kaplan, 1952](#)) and the cosine profile for fixed-fixed ([Qiu et al., 2004](#)) boundary conditions were not arbitrary. They are the fundamental buckling mode shape of a straight column with respective boundary conditions. Therefore, we ([Palathingal et al., 2015](#)) took the initial profile of a bistable arch as a weighted combination of all the buckling mode shapes of the column with the corresponding boundary conditions of the arch.

We presented a computational approach to design bistable arches with general boundary conditions ([Palathingal and Ananthasuresh, 2017a,b](#)) by determining critical points on the force-displacement curve. In this critical-point method, a bistable arch is modelled with one rotational and two translational springs at its endpoint. It enables the design of bistable arches with a wide range of boundary conditions. Boundary conditions other than extreme cases of pinned-pinned and fixed-fixed are realized using compliant revolute flexures. The analysis assumes that the translational spring stiffness is much higher than the torsional stiffness, which is justifiable in the case of compliant revolute flexures and, in particular, the split-tube flexure ([Goldfarb and Speich, 1999](#)) used in the work. By taking the as-fabricated shape as a linear combination of mode shapes, the method is shown to be applicable on arches with varying initial shapes. Moreover, they obtained arch profiles that optimize each of the critical bistable characteristics for given boundary conditions.

Bistability in arches can also be studied by considering force-free stable equilibrium states without the deformation pathways that switch the arch between these states. [Hsu \(1968b\)](#) analyzed the effect of various parameters on the stable states in arches. We

derived a closed-form analytical relationship between the stable arch-profiles of bistable arches (Palathingal and Ananthasuresh, 2018) for design. This relationship is bilateral, i.e., it can also be written in a form amenable to analysis. We also derived an upper bound on compression energy and conditions on the shapes of the arch for it to be bistable. The design aspect of the bistable arch-profiles with pinned-pinned boundary conditions was studied and a wide range of design applications were illustrated. However, pinned-pinned boundary conditions pose a practical difficulty in the fabrication of micromachined mechanisms. Hence, we extended the analytical tools developed for pinned-pinned to fixed-fixed boundary conditions (Palathingal and Ananthasuresh, 2019a). We showed that the analytical bilateral relationship and insights derived from it for the pinned-pinned bistable arches are valid for fixed-fixed bistable arches as well.

2.2.2 Spatial arches

Flexural-torsional buckling causes spatial deformation in planar arches. This mode of buckling in arches has been well studied. Those studies dealt with determining the critical load of buckling, especially in circular arches (Mohri et al., 2002; Papangelis and Trahair, 1987; Pi et al., 2010; Timoshenko, 1936; Vlasov, 1959). Snapping of buckled beam with twist-induced deformation was studied by Sano and Wada (2019). In contrast, Palathingal and Ananthasuresh (2019b) studied spatial deformation in arches in the context of bistability. This study is relevant in planar arches since the switching and switch-back forces resulting from spatial pathways are smaller than those in planar deformation pathways. Therefore, in such arches, a planar analysis would over-predict switching forces resulting in a poor design.

Furthermore, Palathingal and Ananthasuresh (2019b) analyzed spatial bistable arches. These arches, being three dimensional in their fabricated state itself, only exhibit spatial deformation pathways. When an arch deforms spatially, its cross-sections undergo displacement in a plane perpendicular to its central axis. Along with the displacement, the cross-sections rotate about the central axis. The displacement and rotation are related to each other. The geometric relationship described by St. Venant and Michell (Love, 2013; Ojalvo et al., 1969) for lateral-torsional buckling analysis in planar arches is used by Palathingal and Ananthasuresh (2019b) for analyzing planar arches with spatial deformation pathways. Furthermore, for the analysis pertaining to spatial arches, they generalised the St. Venant and Michell relation considering the additional curvature of the arch. That is to say, when one of curvatures of the arch in the modified relationship by Palathingal and Ananthasuresh (2019b) is taken to be zero, the relationship reduces

to its original form given in [Love \(2013\)](#); [Ojalvo et al. \(1969\)](#).

2.3 Analysis on bistable buckled beams

Bistability in arches can be due to either the prestress in them or their as-fabricated shape. The most commonly used bistable structures with prestress are buckled beams. The downside in using buckled beams is that precise prestress is hard to realize during bulk-manufacturing and in microfabrication. However, from the analysis point of view, bistability arising from prestress is not different from that which arises solely due to the initial shape except that the initial stress should be accounted for.

[Huddleston \(1970\)](#) studied buckling and the snap-through behavior of a steep prestressed arch obtained by first buckling a thin elastic strut into a deformed shape and then attaching it to its supports. An experimental study on the effect of an angle at the boundary on a buckled beam reported by [Pippard \(1990\)](#) and [Patricio et al. \(1998\)](#) explained it using the elastica approach. [Vangbo \(1998\)](#) showed the importance of compression energy in the analysis of bistable buckled beams. He followed an approach similar to that followed by [Fung and Kaplan \(1952\)](#) for fixed-fixed boundary conditions. [Cazottes et al. \(2009\)](#) extended the analysis by [Vangbo \(1998\)](#) to consider non-central actuation. In recent studies, dynamics of snapping of buckled inextensible elastica subjected to rotations at their ends was considered by [Gomez et al. \(2017\)](#); [Plaut and Virgin \(2009\)](#) and the exact snapping loads of a buckled beam actuated at the mid-span was obtained by [Chen and Hung \(2012\)](#).

A summary of our discussion on the contributions to the analysis of snapping and bistability in arches is given in [Table 2.1](#). Now, we briefly describe the work on bistable shells.

2.4 Bistable shells

The classical mechanics problem of bistability in shallow shells was initiated by von Karman and Tsien ([Karman, 1939](#)). [Kaplan and Fung \(1954\)](#) analyzed spherical thin elastic shells. [Huang \(1964\)](#) showed that unsymmetrical snapping is possible when the rise parameter of the axisymmetrical shallow shell is above a certain limit. [Budiansky and Roth \(1962\)](#) treated the case of a clamped shell of parabolic revolution under a uniform pressure applied suddenly for a finite time. Buckling and post-buckling behavior of clamped spherical caps loaded by an concentrated force at the apex was studied by

Fitch (1968) and showed the importance of considering asymmetric mode of buckling in determining critical load. The eversion of bistable shells when subjected to in-plane edge tension was first studied by Akkas and Odeh (2001) using a numerical method. Shallow spherical shells with uniform in-plane tension on their outer rims were considered assuming axisymmetric deformation. Bistability in cylindrical shells has been studied in detail by Guest and Pellegrino (2006); Iqbal and Pellegrino (2000); Iqbal et al. (2000); Kebabze et al. (2004); Seffen and Guest (2011).

Chen and Lin (2005a) described snap-through behaviour in spinning shells. They analytically investigated the deformation of a spinning annular non-flat disk using Von-Karman's plate equations. In this problem, the in-plane loading that switches the bistable shell is due to centrifugal force. One of the important findings of the paper is *reverse-snapping*, i.e. the snapping that can occur only in one direction, from the strained state back to the initial state on the opposite side of the base plane when a certain critical rotation speed is reached. This result was later generalized for all in-plane loading conditions (Chen and Huang, 2006) and asymmetrical deformations (Chen and Chang, 2007).

In a recent study, Medina et al. (2016) analyzed the axisymmetric snap-through of an initially curved circular micro plate, subjected to a distributed electrostatic force. Based on a reduced degree of freedom Galerkin approximation, they predicted the equilibrium path of the shell under snap-through buckling. In another study on axisymmetric shells, Sobota and Seffen (2017) explored the effect of boundary conditions on bistability. Their analysis was done using polynomial displacement fields and the Foppl-von Karman model that assume in-plane displacements to be small. Recently, Taffetani et al. (2018) studied bistability in spherical caps while considering symmetric as well as asymmetric modes of deformations.

2.5 Applications

Bistable arches, owing to their ability to maintain two force-free equilibrium states, find applications in mechanisms that need two distinct stable configurations. Their nonlinear force-displacement relations find application in energy harvesters. Bistable arches and shells, due to their ability to take two distinct configurations, find application in shape-changing and morphing applications. Comprehensive reviews on their applications in smart systems, energy harvesters, morphing, and shape-changing applications were published recently by Hu and Burgueño (2015); Pellegrini et al. (2013); Pontecorvo et al. (2013) and Holmes (2019), respectively. Brief accounts of the history of two

applications—RF-MEMS switches and universal passive grippers, designs of which are part of this thesis—are given next.

Author(s)	Significance
Navier (1864)	First considered snap-through buckling in shallow arches
Chwalla (1927); Hurlbrink (1907); Timoshenko (1936)	Foremost analysis on buckling in high circular arches
Biezeno (1938); Friedrichs (1945); Marguerre (1938)	Foremost analysis on buckling in shallow circular arches
Timoshenko (1936)	Study on snapping in sine-curved arch
Fung and Kaplan (1952)	Comprehensive analysis on pinned-pinned shallow arches considering asymmetric buckling modes, varying arch shapes, and multiple loading conditions
Hoff and Bruce (1953)	Studied the dynamic problem of snapping of shallow-arches .
Hsu (1968b)	Analyzed the relationship between the stable equilibrium states in arches.
Simitses (1973)	Studied snapping of shallow pinned arches resting on an elastic foundation under distributed loads
Vangbo (1998)	Analytically modeled bistable buckled beams and showed the importance of the compression energy term.
Lee et al. (1999)	First use of bistable arches in an application: planar microactuators for use in micro optical switches and microrelays
Qiu et al. (2004)	Analytically showed the need for physically restricting the asymmetric mode of deformation in fixed-fixed double cosine arches.
Chen and Lin (2005b); Chen et al. (2009)	Derived the exact static critical loads for a pinned sine arch under a quasi-static concentrated force at the midpoint and couples at the endpoints.
Palathingal and Ananthasuresh (2017a,b)	Presented a computational approach to design bistable arches with general boundary conditions by determining critical points on the force-displacement curve.
Palathingal and Ananthasuresh (2018, 2019a)	Derived a bilateral relationship between arch-profiles that could be used for both analysis and design for fixed-fixed and pinned-pinned boundary conditions
Palathingal and Ananthasuresh (2019b)	Studied spatial deformation pathways in bistable arches and introduced spatial bistable arches

Table 2.1: A summary of analysis on bistable arches

2.5.1 Switches

Table 2.2 lists various bistable switches reported in the literature. Baker and Howell (2002) presented an in-plane compliant bistable micromechanism in a four-bar linkage configuration actuated by V-beam thermal actuators. Qiu et al. (2004) proposed a double curved beam to be used as a bistable device with a detailed analysis of a heatuator provided by Qiu et al. (2005). Sterner et al. (2007) developed a latching-based DC-to-RF bistable switch with electrostatic actuation. A cantilever-based bistable RF switch was presented by Zhang et al. (2007) employing electromagnetic actuation. Permanent magnets were used to keep the switch in the ON state without using external power. Many switch designs use two actuators acting one at a time, for switching between the two states, and require three terminals for their operation including the common ground.

Recently, Huang and Yang (2013) reported a novel device that consists of a single electrothermal V-beam actuator (VBA) to achieve both states (ON and OFF) of the switch. They used a double cosine arch as the bistable element and a hinge-lever mechanism (Huang et al., 2016). The actuating voltage signal is applied in the form of pulses of different durations, across a single pair of terminals to switch between both states. Generally, switch selection and latching are done by a drive-electronics module involving power electronics and logic components. The two-terminal design simplifies the drive-electronic requirements, as the generation of command pulses is much easier to achieve than operating three terminals. While there is the advantage of using a single actuator, it increases the size and limits the performance of the device due to the use of a hinge and lever arrangement. Also, the hinge, realized as a narrow flexural connection, is the weakest link in the design due to stress concentration.

To overcome these shortcomings of (Huang et al., 2016)'s design, we proposed a dual actuator system while retaining the two-terminal design (Yadav et al., 2019). The two-terminal bistable switch has a distributed compliant design (Yin and Ananthasuresh, 2003) that limits the maximum stress, thus increasing the potential for high reliability. A double cosine arch is used as the bistable element. In contrast to Huang et al. (2016)'s design, a secondary actuator is used to axially pull the arch, which shares a single pair of terminals with the primary electrothermal actuator. Thus, the desirable two-terminal actuation is still retained through the mechanically-decoupled but electrically coupled actuator arrangement. Mechanical decoupling facilitates the distribution of compliance using a secondary actuator instead of lumping it in a highly stressed flexural pivot. For push-on and push-off capability, a novel initially-retracting microactuator (Yadav and Ananthasuresh, 2018) is used.

Number of terminals (including ground)	Number of electrothermal actuators	Bistable mechanisms	Type of electrothermal actuator used	References
Three	Double actuator	Bistable arches	V-beam	Lee and Wu (2004), Steiner et al. (2014), Yang et al. (2007)
			Heatuator	Qiu et al. (2005)
		Latching	V-beam	Hu et al. (2016), Dellaert and Doutreloigne (2014), Weight et al. (2002)
			Heatuator	Pirmoradi et al. (2015)
		Straight beam segments	V-beam	Que et al. (2004)
Compliant four-bar linkage	V-beam	Baker and Howell (2002), Masters and Howell (2003)		
Two	Single actuator	Bistable arches	V-beam	Huang and Yang (2013)
	Double actuator	Bistable arches	V-beam and initially-retracting actuator	Yadav et al. (2019)

Table 2.2: Comparative summary of bistable MEMS switches

2.5.2 Universal passive grippers

Universal passive grippers can grasp objects of varying sizes and shapes. In comparison with active multi-fingered grippers, they do not need sophisticated grasping algorithms

and thus are easier to implement (Bicchi and Kumar, 2000; Murray, 2017). Passive grippers can be broadly classified as follows: grippers with soft contacts (Choi and Koc, 2006; Maruyama et al., 2013), granular grippers (Amend et al., 2012; Brown et al., 2010; Manti et al., 2016), and underactuated grippers (Laliberté et al., 2002; Stavenuiter et al., 2017). A planar passive gripper using bistable arches was considered before by Nguyen and Wang (2016). We explored an alternative way to passively grip objects of arbitrarily shaped objects using a monolithic compliant grasping mechanism based on bistable shells, also known as everting shells (Balakuntala et al., 2018). The bistable shell considered is stress-free in its as-fabricated state and stressed in its everted state. The ability to maintain two structural orientations without consuming power makes bistable shells ideal to be used in a passive gripper. By using an everting shell as the critical element and attaching grasping arms to it, (Balakuntala et al., 2018) conceived a gripper that is passive as well as capable of picking up objects of a variety of shapes.

2.6 Closure

Arches, one of the most commonly used structural elements, have been studied extensively in the literature. When subjected to a transverse load, they can undergo buckling resulting in two force-free equilibrium states. Most of the initial studies on the stability of arches were focused on finding the critical buckling load. Its dependence on geometrical parameters and geometrical imperfections was investigated as well. However, in the past two decades, snap-through in arches has been studied in the context of bistability, and analytical models have been developed for its design and use in innovative applications. In the next chapter, we discuss such a semi-analytical strategy to analyze and design bistable arches for generalized boundary conditions.

Chapter 3

Design and analysis of bistable arches by determining critical points in the force-displacement curve

Synopsis

The points on the force-displacement curve corresponding to the switching and switch-back forces, and the travel of a point between the stable states are critical to characterizing bistability. We present a semi-analytical technique, namely the *critical-point method*, to compute these points for arches with general boundary conditions. The ease of implementation of this method enables analysis and shape-optimization of bistable arches. Furthermore, with the aid of the analytical model, we gain some insights into the effect of boundary conditions on bistability.

3.1 Introduction

We consider bistable arches with a transverse force at their midspan. We intend to find the switching force, F_s , switch-back force, F_{sb} , and travel, u_{tr} , given in Fig. 3.1 for bistable arches with general boundary conditions. That arches are assumed to be stress-free in their as-fabricated state. These critical points on the force-displacement curve corresponding to F_s , F_{sb} and u_{tr} are useful for analyzing and designing bistable arches.

In this chapter, we explain our approach of approximating the initial stress-free shape and the deformed shape of an arch as a linear combination of the buckling mode shapes of their corresponding straight column with the rotary springs at the ends. The equilib-

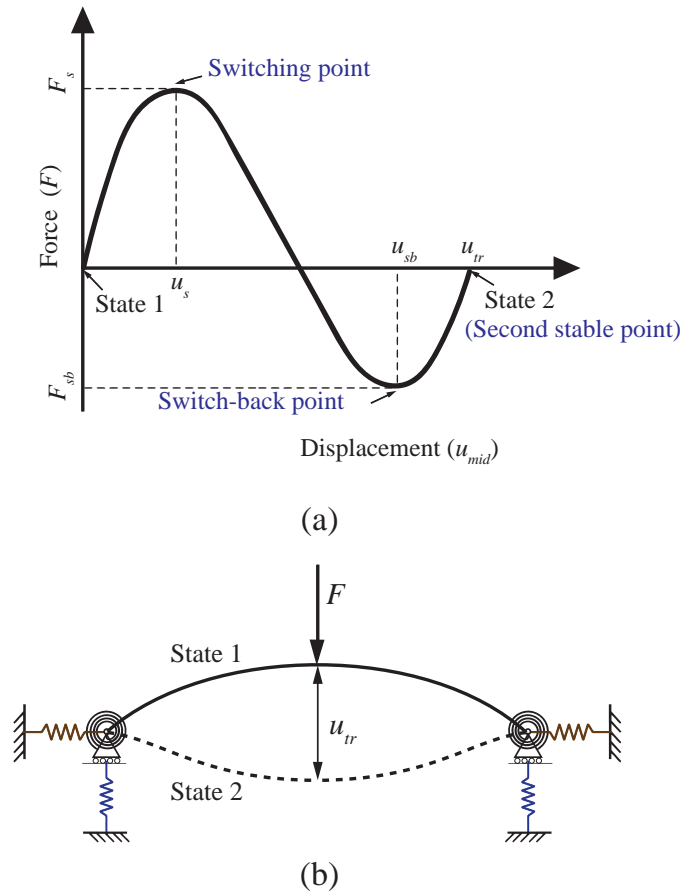


Figure 3.1: Typical force-displacement characteristics of a bistable arch

rium equations are found by minimizing the potential energy of the system with respect to the mode weights of the deformed shape and the displacements in the translational springs. We discuss a numerical strategy, which we call the critical-point method, to find the critical points from the equilibrium equations. We use the critical-point method as a tool to design the bistable arches shown in Fig. 3.2. The design and shape optimization of arches with split-tube flexures and the effect of the rotary stiffness and initial shape on them is presented. We show that the critical-point method is equally effective in the design of pinned-pinned and fixed-fixed bistable arches. We also present the design of asymmetric bistable arches—a new class of bistable structures—using the same method.

3.2 Analysis

The critical-point method is semi-analytical, meaning we obtain the equilibrium equations analytically and solve them numerically. In this method, we solve only for the critical points without obtaining the entire force-displacement curve, thus making the

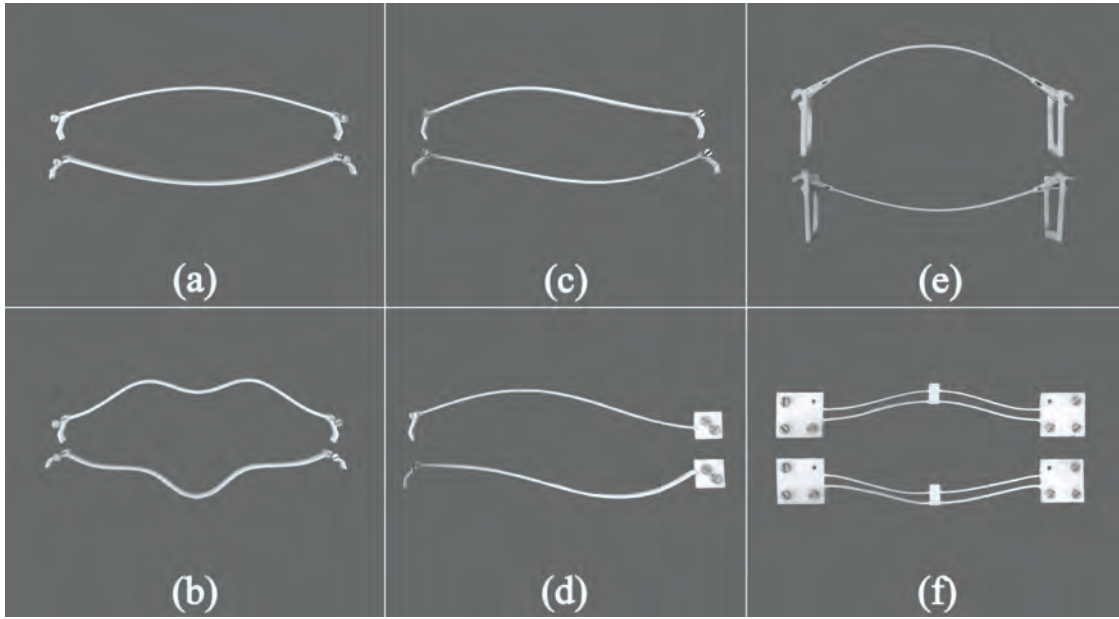


Figure 3.2: 3D-printed bistable arches with various boundary conditions and as-fabricated profiles in their two stable states. (a) pinned-pinned sine arch (b) travel-optimized pinned-pinned arch (c) asymmetric pinned-pinned arch (d) asymmetric pinned-fixed arch (e) split-tube flexure-based arch, and (f) constrained double-cosine arch (Same as Fig. 1.7)

solutions tractable. The equilibrium equations derived in this section are used to find the critical points in Section 3.3. As mentioned before, a column that is buckled into its first fundamental buckling mode can act like a bistable arch if there is prestress. Moreover, arches with the fundamental buckling mode shape as their as-fabricated shape are found to be bistable for pinned-pinned boundary conditions. For fixed-fixed boundary conditions too, their corresponding fundamental buckling mode shape is bistable although restricting their asymmetric mode is necessary, as shown in Fig. 3.2f. This prompts us to explore arches with as-fabricated shape, $h(x)$, as a weighted combination of the buckling mode shapes of their corresponding straight column. For the case of a bistable arch with revolute flexures, the buckling mode shapes of a column with rotary springs with equivalent stiffness of the flexure at the ends will be considered as shown in Fig. 3.3. It may be noted that we are not taking the translational stiffnesses of the revolute flexures into account for computing the buckling mode shapes as we only study arch profiles with ends at the same level (i.e., we consider only the loads that are perpendicular to the line joining the ends). Buckling mode shapes, w_i , for a column with rotary springs at the ends can be obtained from a linear buckling analysis (Simites and Hodges, 2006).

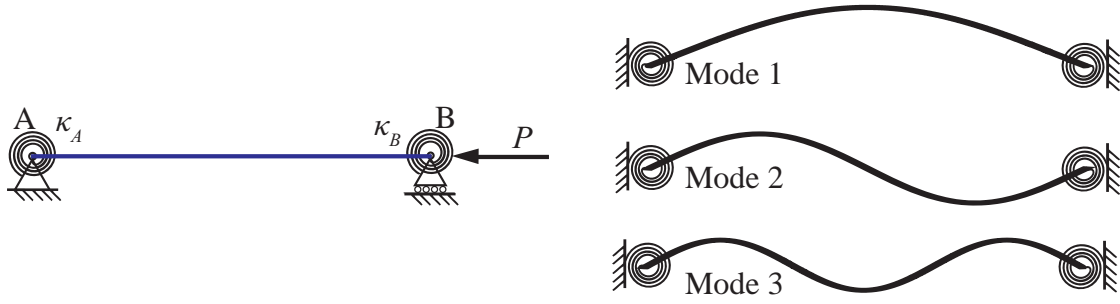


Figure 3.3: Buckling of a straight beam with rotary springs at the ends

3.2.1 As-fabricated and deformed profiles

Let $h(x)$ denote the arch-profile and w_i denote the i^{th} buckling mode shape of the straight beam of the same boundary conditions. Since it is likely to obtain bistable behaviour from a linear combination of w_i s, we write:

$$h(x) = \sum_{i=1}^n a_i w_i(x) \quad (3.1)$$

where a_i is the mode weight for $w_i(x)$ and n is the number of buckling modes considered. Suppose that a point transverse load applied at the mid-point of the arch deforms it to a shape given by $w(x)$. Since, buckling mode shapes form a basis set, we approximate $w(x)$ as follows by accounting for end-displacements:

$$w(x) = \sum_{i=1}^m A_i w_i(x) + \frac{(w_B - w_A)x}{L} + w_A \quad (3.2)$$

where A_i is the weight for each buckling mode shape in the deformed shape, w_A and w_B are the deformations in transverse springs at A and B respectively, L is the span of the arch and m is the number of mode shapes used for approximating the deformed profile. It may be noted that m should not be smaller than n because to capture the as-fabricated shape itself m should be equal to n .

3.2.2 Equilibrium equations

We continue our analysis of the generalized bistable arch shown in Fig. 3.4 in a normalized framework to identify the decisive geometric parameters that define bistability. It may be noted that all normalized quantities are denoted by uppercase symbols.

The potential energy of the system (PE) includes strain energy due to bending in the beam (SE_b), strain energy due to compression along the length of the arch (SE_c), strain

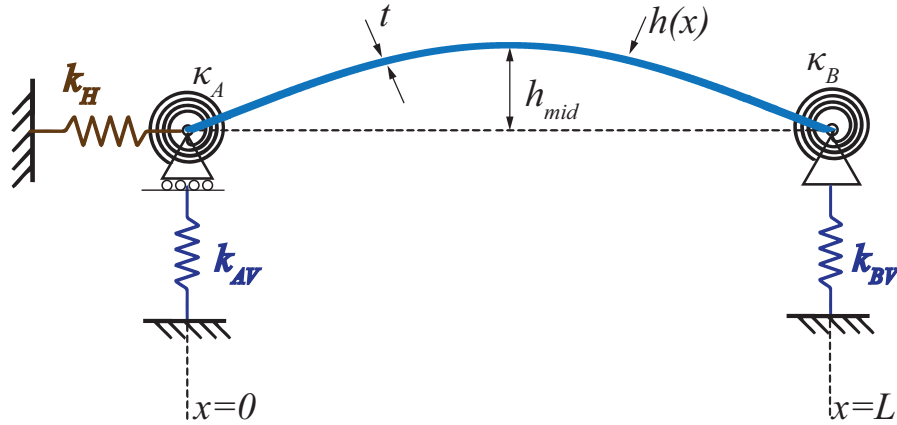


Figure 3.4: Model of a bistable arch with flexures at the ends

energy in the elastic flexures accounted for by the rotary and translational springs (SE_s), and the work potential (WP) due to the external transverse force F applied at the midpoint. As shown in Fig. 3.4, revolute flexures at the ends of the bistable arch have been modeled by two equivalent rotary springs, κ_A and κ_B , two transverse springs, k_{AV} and k_{BV} , and an axial spring, k_H . Modeling with a single axial spring instead of two, one for each revolute flexure, does not result in a loss of generality as two springs in series can always be replaced with a single spring of equivalent stiffness. This analysis assumes that the translational spring stiffness is much higher than the rotary stiffness, which is justifiable in the case of compliant revolute flexures and, in particular, the split-tube flexure (Goldfarb and Speich, 1999) used in this work.

The normalized as-fabricated profile, $H(X)$, the normalized deformed shape, $W(X)$, and the normalized transverse deformations in the spring, W_A and W_B are given below. Note that uppercase letters will be used for representing normalized expressions.

$$H(X) = \sum_{i=1}^n a_i W_i(X) \quad (3.3)$$

$$W_j(X) = \sum_{i=1}^n A_i W_i(X) + (W_B - W_A)X + W_A \quad (3.4)$$

where

$$X = \frac{x}{L} \quad h_{mid} = \sum_{i=1}^n a_i W_i\left(\frac{L}{2}\right) \quad W(X) = \frac{w(X)}{h_{mid}} \quad H(X) = \frac{h(X)}{h_{mid}}$$

$$W_A = \frac{w_A}{h_{mid}} \quad W_B = \frac{w_B}{h_{mid}}$$

Note that h_{mid} is assumed to be nonzero while writing Eqs. (3.3) and (3.4). For arches with $h_{mid} = 0$, a non-zero height of the arch should be used as the normalizing parameter. The strain energy due to bending is given by

$$se_b = \frac{EI}{2} \int_0^L \left(\frac{d^2h}{dx^2} - \frac{d^2w}{dx^2} \right)^2 dx$$

By normalizing, we get

$$SE_b = \frac{se_b L^3}{EI h_{mid}^2} = \frac{1}{2} \int_0^1 \left(\frac{d^2H}{dX^2} - \frac{d^2W}{dX^2} \right)^2 dX \quad (3.5)$$

where I is the second moment of the area of cross-section and E is Young's modulus. The compression energy due to the axial force p is given by

$$se_c = p(s_{initial} - s + u)$$

where u is the deformation of the spring k_H , s the length of the beam as it deforms and $s_{initial}$ the as-fabricated length of the beam. They are given by

$$\begin{aligned} s &= \int_0^L \sqrt{1 + \left(\frac{dw}{dx} \right)^2} dx \approx \int_0^L \left[1 + \frac{1}{2} \left(\frac{dw}{dx} \right)^2 \right] dx \\ s_{initial} &= \int_0^L \left[1 + \frac{1}{2} \left(\frac{dh}{dx} \right)^2 \right] dx \\ p &= Ebt \left(1 - \frac{s + u}{s_{initial}} \right) \end{aligned} \quad (3.6)$$

By normalizing, we get

$$\begin{aligned} S &= \frac{sL}{h^2} = \int_0^1 \left[\frac{L^2}{h^2} + \frac{1}{2} \left(\frac{dW}{dX} \right)^2 \right] dX \\ S_{initial} &= \frac{s_{initial}L}{h^2} = \int_0^1 \left[\frac{L^2}{h^2} + \frac{1}{2} \left(\frac{dH}{dX} \right)^2 \right] dX \\ SE_c &= \frac{se_p L^3}{EI h_{mid}^2} = \frac{1}{2} P (S_{initial} - S + U) \\ P &= \frac{pL^2}{EI} = \frac{12L^2}{t^2} \left(1 - \frac{S + U}{S_{initial}} \right) \end{aligned} \quad (3.7)$$

where $U = \frac{uL}{h_{mid}^2}$. The strain energy in the springs is given by

$$se_s = \frac{1}{2}\kappa_A \left(\frac{dw}{dx} - \frac{dh}{dx} \right)^2 \Big|_{x=0} + \frac{1}{2}\kappa_B \left(\frac{dw}{dx} - \frac{dh}{dx} \right)^2 \Big|_{x=L} + \frac{1}{2}k_H u^2 + \frac{1}{2}k_{AV} w_A^2 + \frac{1}{2}k_{BV} w_B^2$$

By normalizing, we get

$$SE_s = \frac{1}{2}K_A \left(\frac{dW}{dX} - \frac{dH}{dX} \right)^2 \Big|_{x=0} + \frac{1}{2}K_B \left(\frac{dW}{dX} - \frac{dH}{dX} \right)^2 \Big|_{x=1} + \frac{1}{2}K_H U^2 + \frac{1}{2}K_{AV} W_A^2 + \frac{1}{2}K_{BV} W_B^2 \quad (3.8)$$

where

$$\begin{aligned} K_A &= \frac{\kappa_a L}{EI} & K_B &= \frac{\kappa_b L}{EI} \\ K_H &= \frac{k_h L h_{mid}^2}{EI} & U &= \frac{uL}{h_{mid}^2} \\ K_{AV} &= \frac{k_{AV} L^3}{EI} & K_{BV} &= \frac{k_{BV} L^3}{EI} \end{aligned}$$

The work potential due to the transverse force f is given by

$$wp = -f u_{mid}$$

where u_{mid} is the deflection under the application of force f acting vertically downwards at the mid-span of the beam. It is given by

$$u_{mid} = h_{mid} - w \left(\frac{L}{2} \right) \quad (3.9)$$

Normalization yields

$$\begin{aligned} WP &= -FU_{mid} \\ F &= \frac{fL^3}{EIh_{mid}} \end{aligned} \quad (3.10)$$

$$U_{mid} = \frac{u_{mid}}{h_{mid}} \quad (3.11)$$

The normalized potential energy, PE , is given by

$$\begin{aligned}
PE &= SE_b + SE_c + SE_s + WP \\
&= \frac{1}{2} \int_0^1 \left(\frac{d^2 H}{dX^2} - \frac{d^2 W}{dX^2} \right)^2 dX + \frac{1}{2} P (S_{initial} - S + \Delta_H) + \\
&\quad \frac{1}{2} K_A \left(\frac{dW}{dX} - \frac{dH}{dX} \right)^2 \Big|_{x=0} + \frac{1}{2} K_B \left(\frac{dW}{dX} - \frac{dH}{dX} \right)^2 \Big|_{x=1} + \\
&\quad \frac{1}{2} K_{AH} \Delta_H^2 + \frac{1}{2} K_{AV} \Delta_{AV}^2 + \frac{1}{2} K_{BV} \Delta_{BV}^2 - F U_{mid}
\end{aligned} \tag{3.12}$$

By substituting for P , S , $S_{initial}$ from Eqn. 3.7,

$$\begin{aligned}
PE &= SE_b + SE_c + SE_s + WP \\
&= \frac{1}{2} \int_0^1 \left(\frac{d^2 H}{dX^2} - \frac{d^2 W}{dX^2} \right)^2 dX + \\
&\quad 6Q^2 \left\{ \int_0^1 \left[\frac{1}{2} \left(\frac{dH}{dX} \right)^2 - \frac{1}{2} \left(\frac{dW}{dX} \right)^2 \right] dX + U \right\}^2 \\
&\quad \frac{1}{2} K_A \left(\frac{dW}{dX} - \frac{dH}{dX} \right)^2 \Big|_{X=0} + \frac{1}{2} K_B \left(\frac{dW}{dX} - \frac{dH}{dX} \right)^2 \Big|_{X=1} + \\
&\quad \frac{1}{2} K_H U^2 + \frac{1}{2} K_{AV} W_A^2 + \frac{1}{2} K_{BV} W_B^2 - F (H_{mid} - W_{mid})
\end{aligned} \tag{3.13}$$

where $Q = \frac{h_{mid}}{t}$ is a geometry parameter. Table 3.1 summarizes the normalizing factors for these parameters. To obtain Eq. (3.13), the arch is assumed to be shallow (i.e., $(\frac{dh}{dx})^2 \ll 1$) while approximating the change in curvature of the beam.

Parameter	Normalized quantity	Normalizing factor
x	X	$\frac{1}{L}$
$h(x), w(x), w_A, w_B$	$H(X), W(X), W_A, W_B$	$\frac{1}{h_{mid}}$
κ_A, κ_B	K_A, K_B	$\frac{L}{EI}$
k_{AV}, k_{BV}	K_{AV}, K_{BV}	$\frac{L^3}{EI}$
k_H	K_H	$\frac{L h_{mid}^2}{EI}$
u	U	$\frac{L}{h_{mid}^2}$
f	F	$\frac{L^3}{E I h_{mid}}$
-	Q	$\frac{h_{mid}}{t}$

Table 3.1: Normalized parameters used in the spring-restrained pinned-pinned arch

The potential energy expression in Eq. 3.13 shows the dependence of bistability on

the geometry and the boundary conditions of the arch. Strain energy in the springs, SE_s , is dependent on the boundary conditions. The terms involving the normalized as-fabricated shape, $H(X)$, and the geometric quantity, Q , indicate the dependence of geometry on bistability. The role of parameter Q is significant as Q times change in the length of the arch gives the compression energy term, which is crucial to any bistable behaviour. The initial shape, Q , and the boundary conditions determine bistability, whereas geometric parameters h_{mid} , L , t and b decide the magnitude of the bistable characteristics.

The equilibrium equations obtained from the principle of minimum potential energy are:

$$\frac{\partial PE}{\partial A_i} = 0 \quad \text{where } i = 1, 2, 3, \dots m \quad (3.14)$$

$$\frac{\partial PE}{\partial U} = 0 \quad \frac{\partial PE}{\partial W_A} = 0 \quad \frac{\partial PE}{\partial W_B} = 0 \quad (3.15)$$

By taking only the fundamental mode shape as the as-fabricated shape, the preceding equations can be solved analytically for the cases of pinned-pinned and fixed-fixed boundary conditions. On the other hand, getting analytical solutions for bistable arches with flexures at their ends is computationally demanding. In the next section, we explain the critical-point method that can be used to design flexure-based bistable arches as well as pinned-pinned and fixed-fixed arches, which are the limiting cases of the flexure stiffnesses.

3.3 Critical-point method

If we take mode shapes to approximate the deformed shape, i.e. for larger values of m , the accuracy of the solution improves at the expense of solving a larger system of equations. It will be shown later that if we take only the first three mode shapes, i.e. $m = 3$, the results will be closer to those obtained using the nonlinear finite element analysis using continuum elements. This assumption leaves us with a system of six equations (Eq. 3.14 with $m = 3$ and Eq. 3.15) and seven unknowns: $A_1, A_2, A_3, U, W_A, W_B$, and F . Using these, the parameters corresponding to the critical points mentioned earlier (see Fig. 3.1) are determined, as discussed next.

3.3.1 Switching point

The force at the switching point (F_s) is the minimum force required to switch the bistable arch to the second stable state. It is a critical factor in design. Switching from the first stable state to the second can happen either with a symmetry-dominant deformation (symmetric switching) or with an asymmetry-dominant deformation (asymmetric switching). A_2 will have a larger magnitude in asymmetric switching than in symmetric switching. The solid curve in Fig. 3.5 shows a typical force-displacement curve for symmetric switching and the dashed curve shows asymmetric switching. F_s is dependent on the mode of switching of the bistable arch. Asymmetric switching lowers the switching force significantly by taking a path with reduced compressive strain energy during the deformation. Equations (3.14) and (3.15) satisfy both symmetric switching and asymmetric switching conditions. An arch would prefer one mode of switching over the other depending on its as-fabricated shape, Q , and boundary conditions. So, it is important to identify the mode of switching between the two for a given arch. As noted earlier in Chapters 1 and 2, for the cases of pinned-pinned and fixed-fixed boundary conditions these two modes of switching can be described analytically. An analytical solution has not been possible so far when springs are included. Therefore, it is done numerically by solving for two different switching forces: one assuming symmetric switching (F_{ss} at u_{ss}) and the other assuming asymmetric switching (F_{as} at u_{as}).

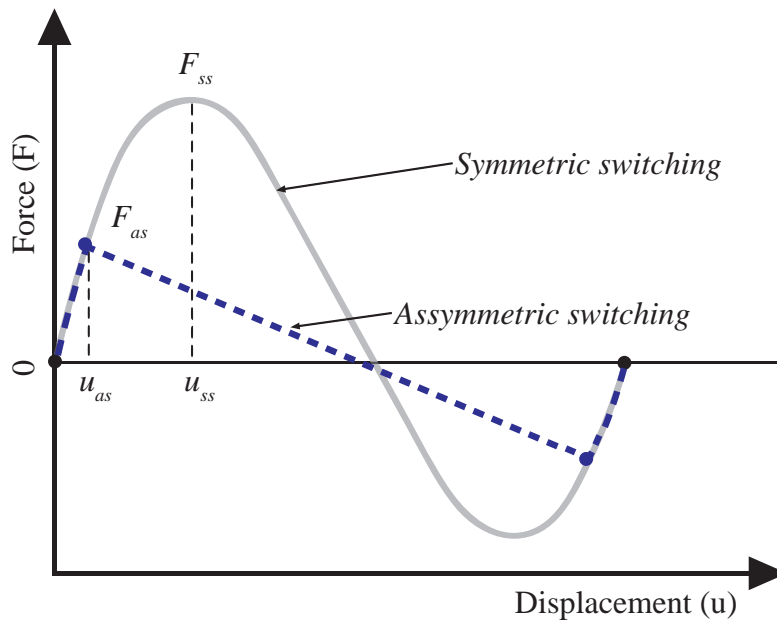


Figure 3.5: Asymmetric mode of switching lowers the switching force

F_s will be equal to F_{as} if u_{as} is less than u_{ss} as shown in Fig. 3.5. In this case the arch

prefers asymmetric switching over symmetric switching. It can happen that $F_s = F_{ss}$ if $u_{ss} < u_{as}$. In some other cases, when only one mode of switching is present, F_s would be the switching force corresponding to the only existing switching-mode. The asymmetric arches in Fig. 3.2c and Fig. 3.2d have only asymmetric modes of switching, and hence F_s is equal to F_{as} . The double-cosine arch with a restraint in the middle, as in Fig. 3.2f, switches only symmetrically as the asymmetric mode of switching is physically constrained. In this arch, F_s is equal to F_{ss} .

F_{ss} is the point where the force is maximum with respect to the displacement on the force-displacement curve such that the equilibrium equations are satisfied. This maximum will always be a symmetric switching force since F_{as} cannot be greater than F_{ss} . The finite variable optimization problem to obtain F_{ss} can be written as:

$$\begin{aligned}
 & \underset{A_1, A_2, A_3, U, W_A, W_B}{\text{Maximize}} && F \\
 & \text{Subject to} && \\
 & \Lambda_i : && \frac{\partial PE}{\partial A_i} = 0 \quad \text{where } i = 1, 2, 3 \\
 & \Lambda_4 : && \frac{\partial PE}{\partial U} = 0 \\
 & \Lambda_5 : && \frac{\partial PE}{\partial W_A} = 0 \\
 & \Lambda_6 : && \frac{\partial PE}{\partial W_B} = 0 \\
 & \text{Data : } && a_1, a_2, a_3, Q, K_A, K_B, K_H, K_{AV}, K_{BV}
 \end{aligned} \tag{3.16}$$

with the necessary conditions:

$$\begin{aligned}
 & \frac{\partial L}{\partial A_i} = 0 \quad \text{where } i = 1, 2, 3 \\
 & \frac{\partial L}{\partial U} = 0 \quad \frac{\partial L}{\partial W_A} = 0 \quad \frac{\partial L}{\partial W_B} = 0 \\
 & \frac{\partial L}{\partial \Lambda_i} = 0 \quad \text{where } i = 1, 2, 3, 4, 5, 6
 \end{aligned} \tag{3.17}$$

where L is the lagrangian of the optimization problem Eq. (3.16). These equations can be solved numerically using the Newton-Raphson method as

$$x_{n+1} = x_n - [Hf(x_n)]^{-1} \nabla f(x_n) \tag{3.18}$$

where

$$x_n = [A_1, A_2, A_3, U, W_A, W_B, \Lambda_1, \Lambda_2, \Lambda_3, \Lambda_4, \Lambda_5, \Lambda_6]^T$$

$$f = \left[\frac{dL}{dA_1}, \frac{dL}{dA_2}, \frac{dL}{dA_3}, \frac{dL}{dU}, \frac{dL}{dW_A}, \frac{dL}{dW_B}, \frac{\partial L}{\partial \Lambda_1}, \frac{\partial L}{\partial \Lambda_2}, \frac{\partial L}{\partial \Lambda_3}, \frac{\partial L}{\partial \Lambda_4}, \frac{\partial L}{\partial \Lambda_5}, \frac{\partial L}{\partial \Lambda_6} \right]^T$$

$Hf(x_n)$ the Hessian of $f(x_n)$, and $\nabla f(x_n)$ the gradient of $f(x_n)$.

An asymmetric switching force is the minimum amount of force required for the arch to switch from State 1 to State 2 with an asymmetric switching path. In the case of symmetric arches, this is also the point at which the arch begins to deflect asymmetrically. Starting from this point, two solutions can exist for the equilibrium equations; a symmetric solution, where the change, $|A_2 - a_2|$ remains negligible and an asymmetric solution with a higher A_2 along the deformation. This is one of the points where the equilibrium equations have repeated roots with respect to A_2 , i.e., at this point, we have

$$\frac{d^2 PE}{d^2 A_2} = 0 \quad (3.19)$$

F_{as} for symmetric arches is found by solving Eqs. (3.14), (3.15) and (3.19) numerically using the Newton-Raphson method as

$$x_{n+1} = x_n - [\nabla f(x_n)]^{-1} f(x_n) \quad (3.20)$$

where

$$x_n = [A_1, A_2, A_3, U, W_A, W_B, F]^T$$

$$f = \left[\frac{dPE}{dA_1}, \frac{dPE}{dA_2}, \frac{dPE}{dA_3}, \frac{d^2 PE}{d^2 A_2}, \frac{dPE}{dU}, \frac{dPE}{dW_A}, \frac{dPE}{dW_B} \right]^T$$

The initial values of the unknowns are taken to be their corresponding values in State 1 of the arch. In the case of asymmetric arches, where only asymmetric-switching is present, F_{as} is found by solving Eq. (3.17).

3.3.2 Switch-back point

The switch-back force, F_{sb} , is the minimum force required to switch a bistable arch from State 2 to State 1. F_{sb} can also be thought of as a measure of bistability. The larger the switch-back force, the higher the stability of the arch in the second stable state. Similar to F_s , F_{sb} also depends on the nature of switching. The existence of asymmetric switching from State 2 to State 1 reduces the stability. As in the case of

the switching point, we proceed by solving for two different F_{sb} s, corresponding to symmetric and asymmetric switching. The symmetric and the asymmetric switch-back points are found as described in the previous section using Eqs. (3.18) and (3.20). To get the switch-back point, the initial guess corresponding to State 2 is taken. While implementing the critical-point method, the second stable point (State 2) is determined before the switch-back point so that it can be used as the initial guess in the numerical procedure.

3.3.3 Second stable point

The second stable point corresponds to the second force-free equilibrium state of the arch. Since $F = 0$ at this point, we have six equations and six unknowns, which can be solved numerically as

$$x_{n+1} = x_n - [\nabla f(x_n)]^{-1} f(x_n) \quad (3.21)$$

where

$$x_n = [A_1, A_2, A_3, U, W_A, W_B]^T$$

$$f = \left[\frac{dPE}{dA_1}, \frac{dPE}{dA_2}, \frac{dPE}{dA_3}, \frac{dPE}{dU}, \frac{dPE}{dW_A}, \frac{dPE}{dW_B} \right]_{F=0}^T$$

By taking $x_0 = [-a_1, a_2, a_3, 0, 0, 0]$, it was observed that the numerical method does not converge to a point corresponding to the unstable force-free equilibrium state, which also satisfies the same equations. This is because of the broad basin of attraction at the second stable point.

3.4 Design and optimization using the critical-point method

In this section, we first discuss the design and profile-optimization of flexure-based bistable arches. Then, we illustrate the generality of the method by applying it to four special cases of flexure-based bistable arches: (1) bistable arches with pinned-pinned boundary conditions, (2) design of asymmetric bistable arches, (3) bistable arches with fixed-fixed boundary conditions, and (4) limiting axial spring stiffness design for a bistable arch.

3.4.1 Bistable arches with revolute flexures at the ends

An ideal revolute flexure has minimal rotary stiffness, with high axial and transverse stiffnesses. It is important to understand how the torsion stiffness affects bistability. In

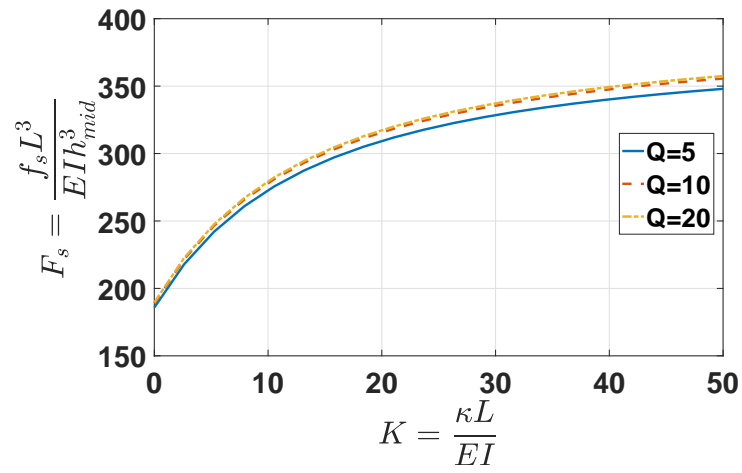
Fig. 3.6, the bistable characteristics are plotted against a non-dimensional rotary stiffness for a range of values of Q by taking the first buckling mode shape to be the as-fabricated shape with equal torsion stiffnesses at the ends. A higher rotary stiffness implies that the arch has to overcome more resistance at the boundaries. This would cause an increase in the switching force and a reduction of the switch-back force and travel. We see a decrease in desirable bistable characteristics as K increases, i.e., as we move from pinned-pinned to fixed-fixed boundary conditions. When we design revolute flexure-based bistable arches, it is advisable to restrict the normalized torsion stiffness K to less than 5 to take advantage of the rotational compliance at the joints. As shown in Figs. 3.6a and 3.6b, as Q increases, the switching force increases but the switch-back force decreases. The travel is reduced as K increases only if Q is small as in Fig. 3.6c. The increase in the rotary stiffness at the ends will restrict the travel. If the arch is compliant enough to deform by overcoming the stiffness experienced at the ends, the travel would be independent of K . We observe this independence of the travel on torsion stiffness when Q is 20 or larger.

We now discuss the design of a bistable arch with split-tube flexures at the ends for the data given in Table 3.2 for maximum stability for a given h_{mid} of 10 mm. Taking $t = 1$ mm, $b = 10$ mm, and $L = 200$ mm, the non-dimensional rotational stiffness is $K = \frac{\kappa L}{EI} = 0.6$; this retains characteristics comparable to that of a pinned-pinned bistable arch. One may note that the linear and axial stiffness values are large enough to justify the assumptions made in our analysis. By taking the first mode shape as the as-fabricated shape, we find the critical points: $F_s = 197.30$, $F_{sb} = -83.23$, $U_{tr} = 2.00$. In Fig. 3.7, the critical points obtained from the critical-point method are plotted on the force-displacement curve obtained from the finite element analysis (FEA) using continuum elements in COMSOL software.

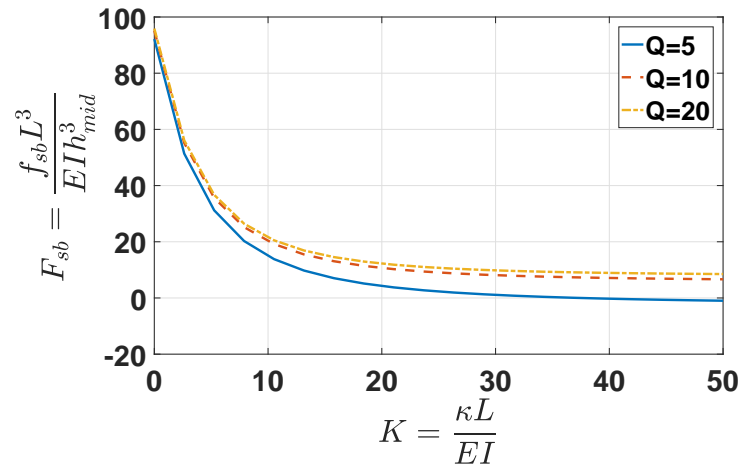
Table 3.2: Geometric and material parameters

E	κ_A	κ_B
$2.1 \times 10^9 N/m^2$	$0.00525 Nm/rad$	$0.00525 Nm/rad$
k_H	$k_A V$	$k_B V$
$7.3 \times 10^5 N/m$	$1.45 \times 10^6 N/m$	$1.45 \times 10^6 N/m$

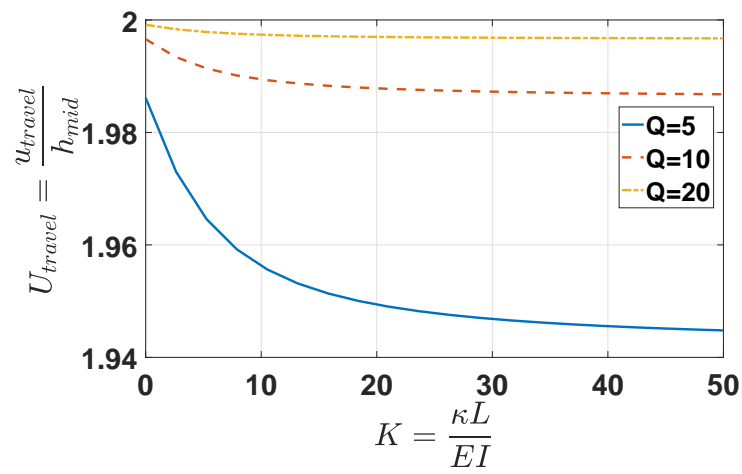
For low K values, since the switch-back force is independent of Q , we can optimize the shape of the profile to achieve maximum stability. The bistable characteristics can be optimized with respect to a_1 , a_2 and a_3 , the unknown weights of the first three buckling modes in the as-fabricated shape, using a numerical approach. By utilizing the fact that the critical-point method is computationally fast, contour plots are constructed for a



(a) Switching force



(b) Switch-back force



(c) Travel

Figure 3.6: Effect of torsion stiffness on bistable characteristics

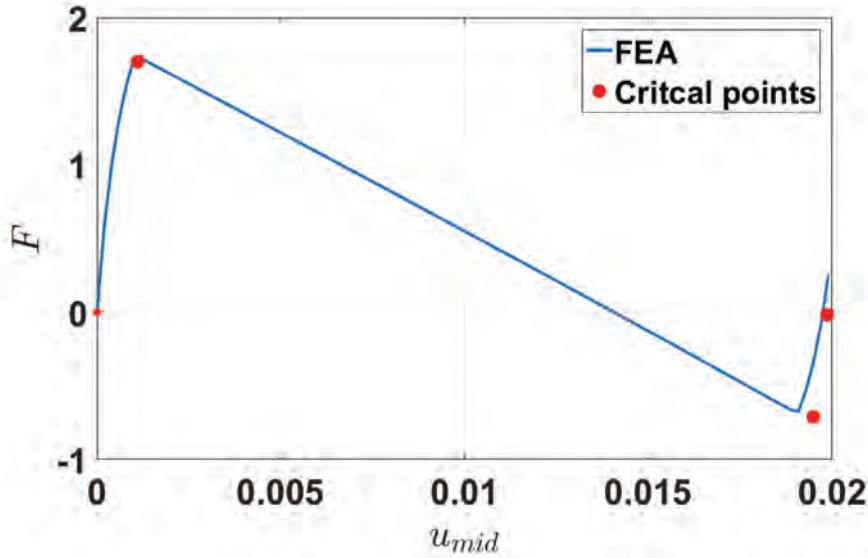
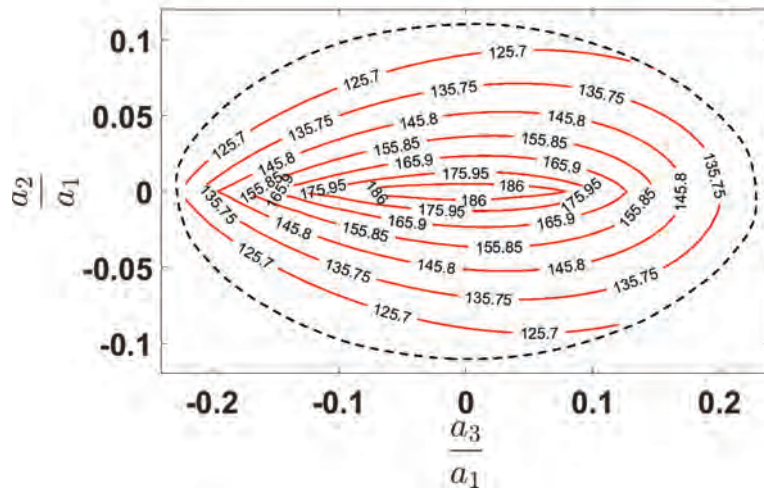


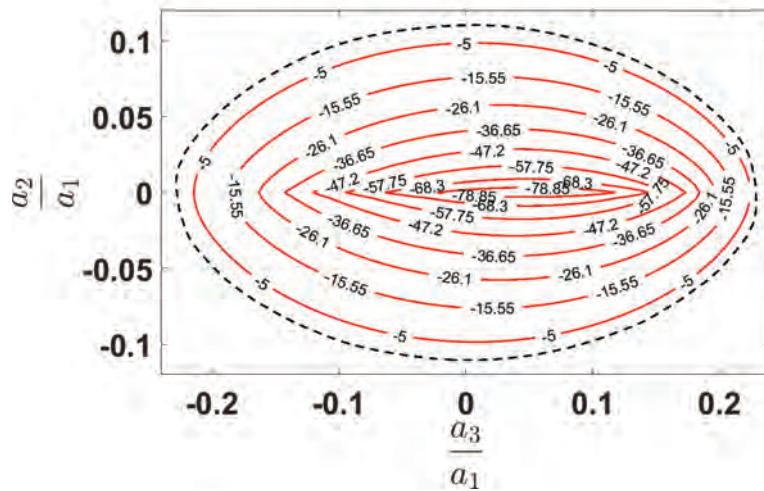
Figure 3.7: Critical-point method compared to FEA in Comsol using continuum elements

range of $\frac{a_2}{a_1}$ and $\frac{a_3}{a_1}$ ratios taking $a_1 = 1$. An arch is not bistable for any combination of a_1 , a_2 and a_3 . Each point inside the dashed contour in Fig. 3.8 gives combinations of a_1 , a_2 and a_3 that are bistable. Arches are bistable for a broader range of $\frac{a_3}{a_1}$ ratios as compared to $\frac{a_2}{a_1}$. The loss of bistability beyond certain combinations of $\frac{a_2}{a_1}$ and $\frac{a_3}{a_1}$ can be understood from Fig. 3.8b. The switch-back force is a measure of the stability of the bistable arch in the second stable state. As we approach the dashed contour, the F_{sb} decreases to zero indicating an unstable State 2. Physically, this implies that even a slight disturbance can bring the arch back from the second to the first equilibrium state. We also observe that the ratios $\frac{a_3}{a_1} = 0.049$ and $\frac{a_2}{a_1} = 0$ (Profile A in Fig. 3.9) maximize the switch-back force, the arch profile with the highest stability for the selected revolute flexure. Arch (e) in Fig. 3.2 shows the optimized 3D printed bistable arch with compound split-tube flexures and its two stable force-free equilibrium states.

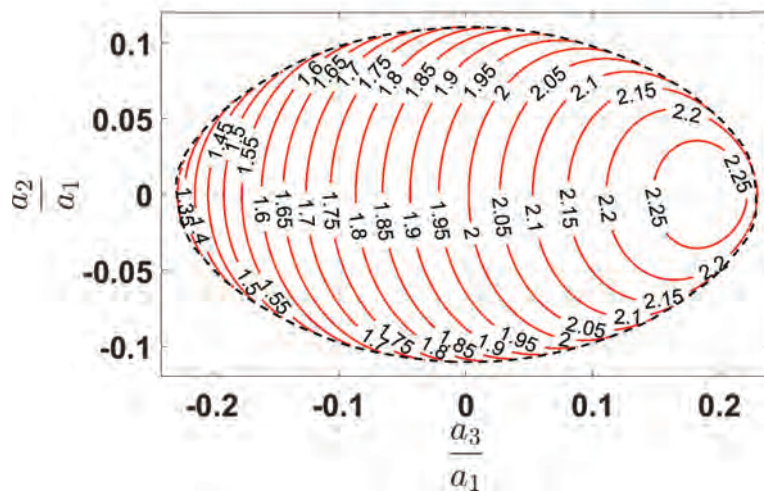
We see in Fig. 3.8a that the switching force decreases as the $\frac{a_3}{a_1}$ and $\frac{a_2}{a_1}$ ratios increase. But it does not have a minimum in the feasible space. The ratios $\frac{a_3}{a_1} = 0.192$ and $\frac{a_2}{a_1} = 0$ (Profile B in Fig. 3.9) maximize the travel as seen in Fig. 3.8c. But this increased travel comes at the expense of a reduced switch-back force. So, it is advisable to keep a lower limit on the switch-back force while maximizing the travel in bistable arches.



(a) Contour plot of the switching force in the feasible space



(b) Contour plot of the switch-back force in the feasible space



(c) Contour plot of the travel in the feasible space

Figure 3.8: Dependence of F_s, F_{sb} , and U_{tr} on the as-fabricated shape

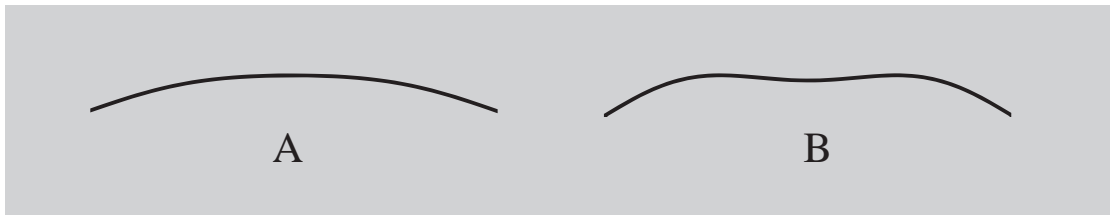


Figure 3.9: Optimal profiles of a bistable arch with split-tube flexure at the ends

3.4.2 Pinned-pinned bistable arches

The analysis for pinned-pinned arches is a special case of flexure-based arches with $\kappa_A = \kappa_B = 0$ and very high translational and axial stiffness. The reduced number of unknown displacements, as $W_A = W_B = U = 0$, makes the analysis for pinned-pinned arches even faster than is the case with a flexure joint. Following a procedure similar to the previous problem, geometric parameters can be designed from the non-dimensional critical points obtained. Figure 3.10 shows a good agreement between the critical-point method and FEA for $t = 1 \text{ mm}$, $b = 5 \text{ mm}$, $E = 2.1 \text{ GPa}$ and $L = 100 \text{ mm}$. Furthermore, a geometric profile optimization can also be carried out to obtain the optimal bistable arches with pinned-pinned boundary conditions. For example, arch (b) in Fig. 3.2 maximizes the travel between the two states for a given initial height.

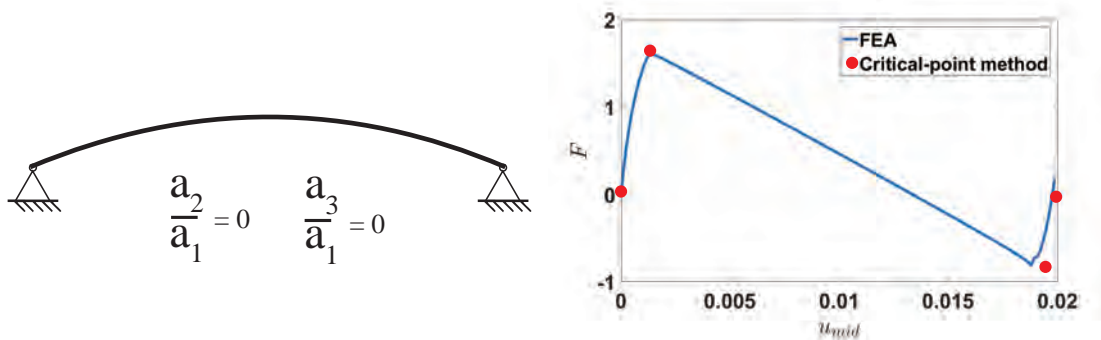


Figure 3.10: Critical-point method compared to FEA in Comsol using continuum elements for pinned-pinned boundary conditions

3.4.3 Asymmetric bistable arches

Asymmetric arch profiles of bistable arches (Fig. 3.2c and Fig. 3.2d) have not been explored in the literature. One can observe that the point at the maximum height shifts along the span as an asymmetric arch switches between the states. This shift can be utilized in switch embodiments requiring offset contact points. They can be good candidates to utilize the bimodality in the bistable arches for two-port actuation as well.

Asymmetric bistable arches can be designed in two ways: (1) by having a non-zero a_2 in the as-fabricated profile of a bistable arch, and (2) by having two different rotary stiffnesses at the ends of the arch. We have already considered asymmetric arches with non-zero $\frac{a_2}{a_1}$ as we optimized the as-fabricated profile for the case of split-tube flexure-based bistable arches using the critical-point method. In Fig. 3.8, we observe that the asymmetry in the initial profile decreases the switching and switch-back forces. Asymmetry in the as-fabricated shape makes the choice between symmetric and asymmetric switching easy for the arch, making it go directly into asymmetric deformation causing a decrease in the switching force. As the arch is already asymmetric, a symmetric solution is absent, i.e. $F_s = F_{as}$. Figure 3.11(a) compares the critical-point method to FEA for an asymmetric bistable arch of $t = 1 \text{ mm}$, $b = 5 \text{ mm}$, $E = 2.1 \text{ GPa}$ and $L = 100 \text{ mm}$ with pinned-pinned boundary conditions. The smooth FEA curve that is unlike the curves for symmetric designs with two sharp points indicates the absence of multiple switching solutions.

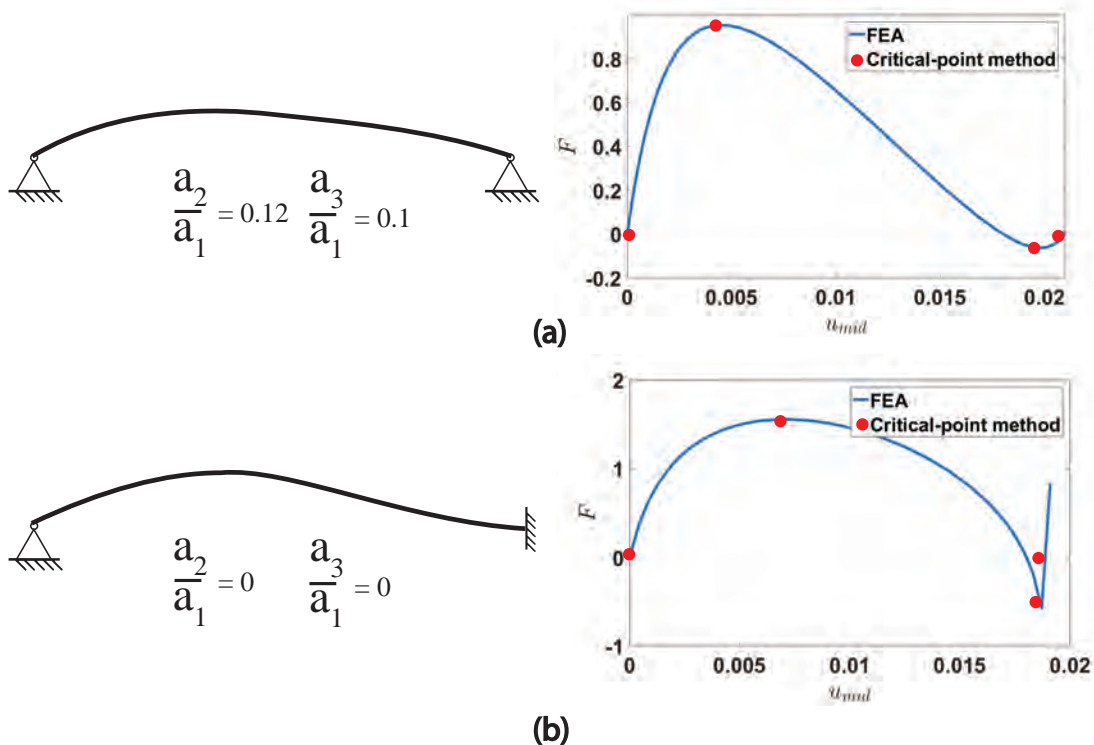


Figure 3.11: Critical-point method compared to FEA in Comsol using continuum elements for asymmetric bistable arches with (a) asymmetric initial shape and (b) asymmetric boundary conditions

The second way to design asymmetric bistable arches is to take unequal rotary stiffnesses at the two ends. Buckling mode shapes including the fundamental mode shape

will be asymmetric for the straight column with unequal torsion stiffness at the ends. For example, taking pinned-fixed boundary conditions with the fundamental buckling mode as the as-fabricated shape yields the asymmetric bistable arch shown in Fig. 3.2d. The critical-point method for this case with $t = 1 \text{ mm}$, $b = 5 \text{ mm}$, $E = 2.1 \text{ GPa}$ and $L = 100 \text{ mm}$ also agrees quite well with FEA as shown in Fig. 3.11b. The sharp region at the switch-back force is due to an instantaneous deformation of the arch into a symmetric profile. The stability of the asymmetric bistable arches that belong to the second design method is found to be better than that of the first.

3.4.4 Fixed-fixed double cosine bistable arches with restricted asymmetric mode

For fixed-fixed boundary conditions, it can be shown that the first fundamental buckling mode shape is not bistable unless its asymmetric mode of switching is restricted (Qiu et al., 2004). This can be physically realized by taking two cosine-shaped arches parallel to each other and joining them at the center. The analysis described in the last two sections needs to be modified by taking into consideration two arches instead of one with the second mode of deformation restricted. The bending energy and compression energy components in Eq. (3.13) will become double and the strain energy in the springs will be zero as the displacements at the boundary will be zero for fixed-fixed boundary conditions. The total potential energy can be written as

$$PE = 2SE_b + 2SE_c + WP \quad (3.22)$$

The equilibrium equations of the double cosine bistable arch with fixed-fixed boundary conditions and a restricted asymmetric mode have multiple solutions w.r.t. A_3 . As the asymmetric deformation is restricted, A_2 will always be zero. Moreover, at the point where multiple solutions exist, one of the solutions corresponds to the case when $A_3 = 0$. So, instead of Eq. (3.19), we have

$$\begin{aligned} A_2 &= 0 \\ A_3 &= 0 \\ \frac{d^2 PE}{d^2 A_3} &= 0 \end{aligned} \quad (3.23)$$

Let us consider a design example of a bistable arch with a minimum travel, u_{tr} of 18 mm , a maximum switching force, f_s of 15 N , a span not exceeding 100 mm and

a depth not less than 1 *mm*. Let us assume the height, h_{mid} to be equal to 10 *mm* to achieve a travel greater than 18 *mm*. By taking the depth to be minimum we have

$$Q = \frac{h_{mid}}{t} = 10$$

By substituting this into the equilibrium equations and taking the as-fabricated to be the first buckling mode shape, we obtain from the critical-point method:

$$F_s = \frac{f_s l^3}{EI h_{mid}} = 1486.57$$

$$U_{tr} = \frac{u_{tr}}{h_{mid}} = 1.98$$

which implies that the travel, $u_{tr} = 19.8$ *mm*, which is greater than 18 *mm*. Solving for width, we get $b = \frac{100Et^3 h_{mid}}{12f_s l^3} = 11.67$ *mm*. By taking $b = 10$ *mm* the switching force can be reduced below 15 *N*. The FEA results juxtaposed with the critical points are shown in Fig. 3.12(a) for the final fixed-fixed design. Note that in the case of fixed-fixed bistable arches, the first five mode shapes were used for approximation, i.e., $m = 5$, for improved accuracy.

Next, let us design for an axial spring attached to one of the ends of the designed bistable arch. As we reduce the axial stiffness, the compression energy at the intermediate unstable equilibrium that helps the arch to have two stable states reduces, eventually resulting only in snap-through but not bistability. The results from the critical-point method for an axial stiffness $K_H = 3 \times 10^5$ *N/m* attached to the fixed-fixed double-cosine designed previously are shown in Fig. 3.12(b). The deviation of the critical points from FEA is mainly because of the displacement in the axial spring. The reduction of the bending energy of the arch due to this displacement is not accounted for in Eq. (3.13) to simplify the model. As a result, the critical-point method over-estimates the switching and switch-back forces when the axial displacement is significant. The limiting stiffness, i.e., the minimum stiffness of the lumped axial spring required so that the arch is bistable is found to be 1.19×10^4 *N/m* (K_H) as shown in Fig. 3.13. We can observe how the switch-back force decreases and eventually becomes zero as the limiting stiffness decreases. Note that the critical points are joined with lines only for ease in visualization. They are neither considered to be approximate force-displacement curves nor are they used for obtaining the limiting stiffness.

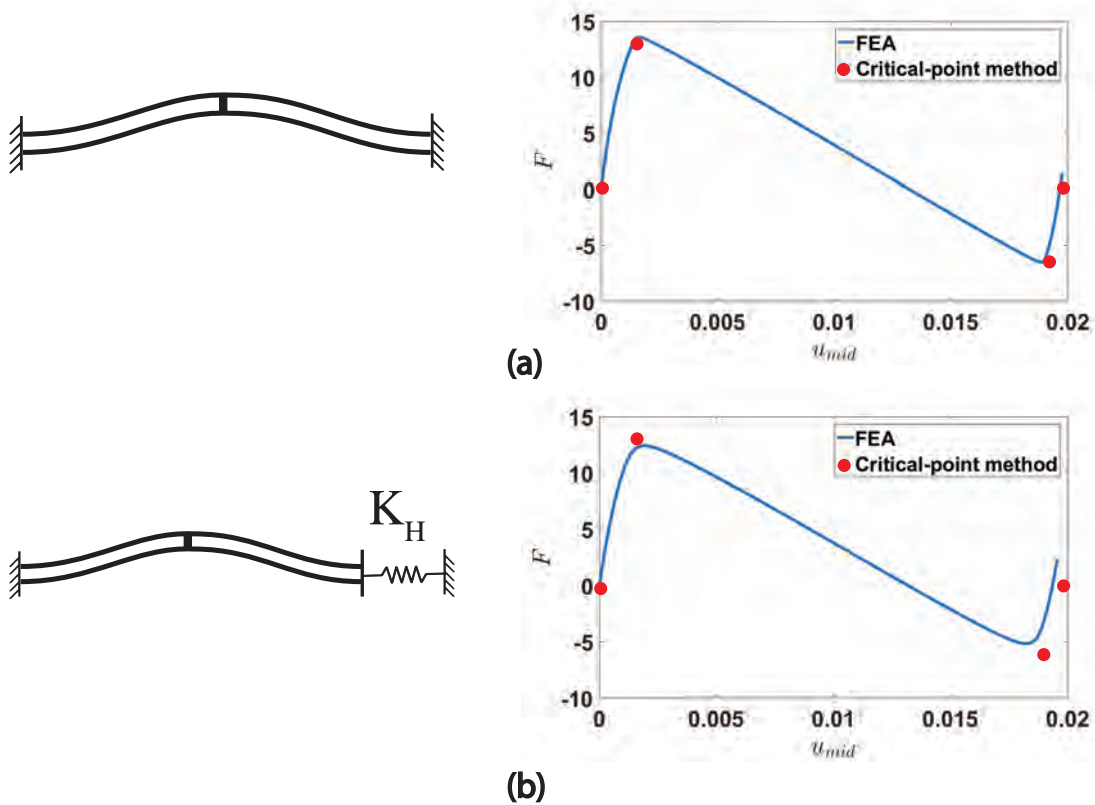


Figure 3.12: Critical-point method compared to FEA in Comsol using continuum elements for fixed-fixed boundary conditions with (a) $K_H = \infty$ (b) $K_H = 3 \times 10^5 \text{ N/m}$

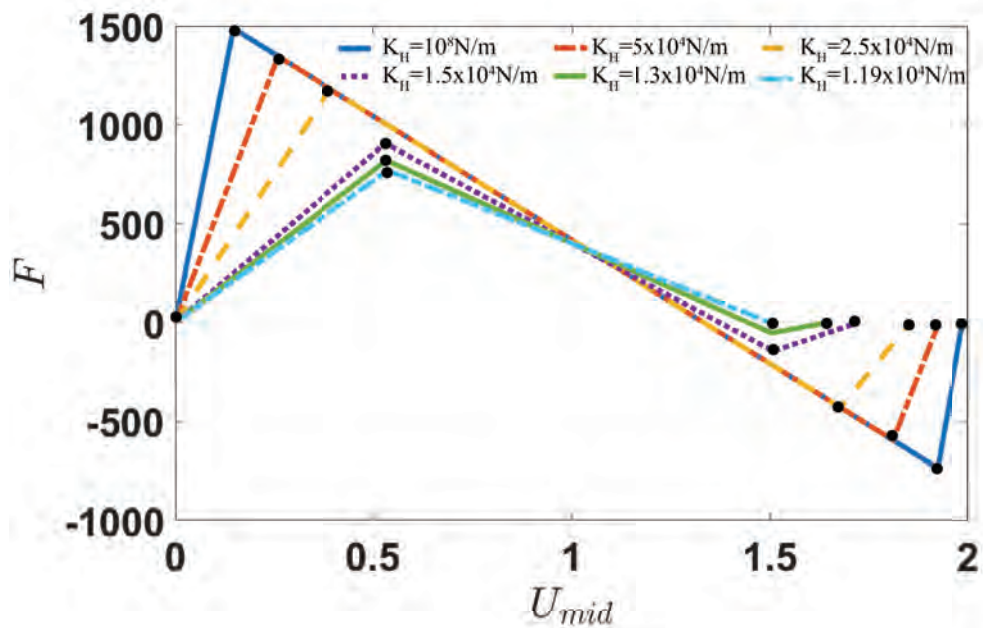


Figure 3.13: Limiting horizontal stiffness of fixed-fixed double-cosine arch

3.5 Closure

The motivation for developing bistable arches with revolute flexures was to make them amenable to assembly-free fabrication. Such a bistable arch with compound split-tube flexures at the pinned-pinned ends has been fabricated as shown in Fig. 3.2e. A semi-analytical yet powerful critical-point design method has been presented to design bistable arches with revolute flexures. The effectiveness of the method was illustrated for solving various bistable arch design problems. If needed, the accuracy of the results can be improved by adding more terms in the number of mode shapes used in approximating the deformed profile.

With the aid of the critical-point method, we studied the effect of the rotary stiffness and the as-fabricated shape on the bistable characteristics. It was found that including higher mode shapes in the as-fabricated geometric profile can lead to improved designs with reduced a switching force and a larger switch-back force and travel. One of the important observations from the contours of feasible space is the possibility of asymmetric bistable arches, i.e., arches with non-zero $\frac{a_2}{a_1}$, which are rarely seen and utilized in the literature.

Even though the critical-method point enables analysis, it does not help us design bistable arches for any given shape. In the next chapter, we follow a completely analytical approach to derive a relationship between the stable arch-profiles and use such a relationship for their design.

Chapter 4

A bilateral relationship between stable profiles of bistable shallow arches

Synopsis

In the previous chapter, we presented an analysis and design technique to find the critical bistable characteristics such as: switching and switch-back forces, switching and switch-back displacements, and travel for a limited range of arch-profiles. In this chapter, we examine bistability without considering the force-displacement characteristics. The necessary and sufficient conditions derived here are at the force-free stable equilibrium states of the arch. The importance is given to design arch-profiles of any shape at the force-free stable states using a closed-form analytical solution instead of obtaining the force-displacement characteristics of the arch. We derive the necessary conditions of the arch-profiles for ensuring bistability. We discuss the analysis using a bilateral relationship, where given an initial profile, we obtain the toggled profile. We present the design where as-fabricated initial shapes corresponding to a prescribed stressed toggled profile are obtained analytically.

4.1 Introduction

Bistable arches have two distinct arch-profiles corresponding to the two stable states: *initial profile* and *toggled (inverted) profile* (Fig. 4.1). The initial profile is the as-fabricated shape of the arch, wherein the arch is stress-free and the toggled profile is the profile of the bistable arch when it is in the stressed second stable state, i.e., in its state of self-stress. These two profiles must be related to each other, i.e., an arch with an

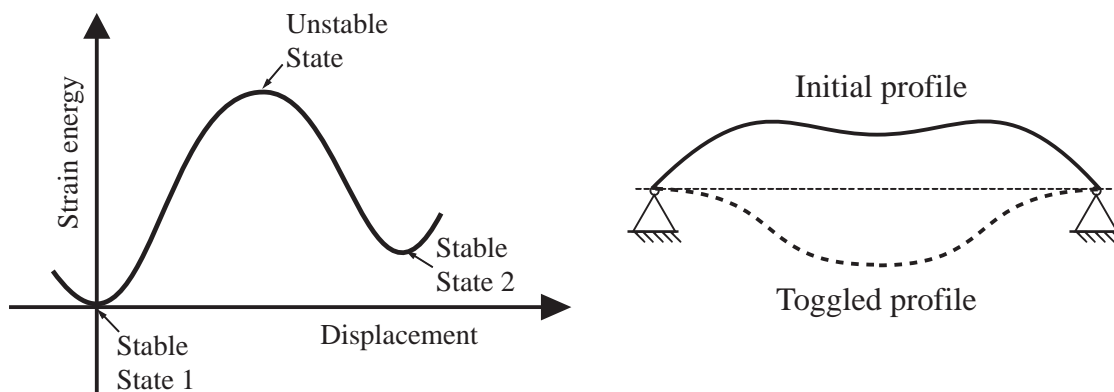


Figure 4.1: Strain energy profile of a bistable arch. Initial-profile and toggled profile are the arch-profiles corresponding to State 1 and State 2, respectively.

as-fabricated shape has a corresponding toggled profile. An analytical relation between the two profiles not only provides insights into the behavior of bistable arches but also helps in design. Incidentally, the design problem of obtaining a stress-free initial profile from a given toggled profile (sans stress distribution) is a closed form analytical solution. A relevant design problem is that of a compliant gripper or clamp, as shown in Fig. 4.2, where a pair of bistable arches grasps a circular object. Here, the gripper requires a

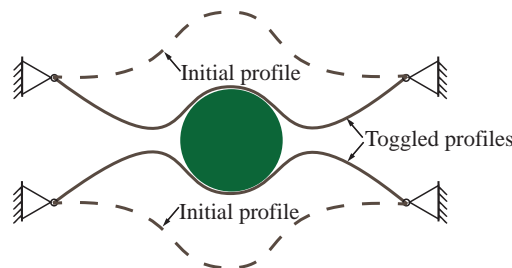


Figure 4.2: Schematic of two bistable arches gripping a circular object.

toggled profile that matches the cylindrical profile at the mid-span for a substantive area of contact. Numerical optimization approaches may be able to solve such problems, albeit with considerable difficulty. An analytical relation between the arch-profiles, on the other hand, can easily solve this and similar design problems as illustrated in this chapter.

Bistability is due to the interaction of bending and compression energies in the arch as it deforms. A typical strain energy profile of a bistable arch is shown in Fig. 4.1. Strain energy, which comprises bending and compression energies, increases from zero to reach a maximum and then decreases to attain a minimum in the second stable state. We note that bistable arches show asymmetric-bistability when one of the stable equilibrium states is stress-free: their two equilibrium states do not have equal strain energy.

The arch when in State 1—its as-fabricated shape—has no strain energy. The second stable state, State 2, has positive strain energy. Thus, it is not surprising that the initial and toggled profiles differ in shape. Equivalently, for a bistable mechanism with symmetric-bistability, both the stable configurations are expected to be identical. For example, a pre-loaded buckled beam with pinned-pinned boundary conditions shown in Fig. 4.3 has two stable states with positive and equal strain energy. Therefore, the initial and the toggled profiles are mirror images of each other; effectively, they are one and the same. Thus, the difference between strain energies in the two equilibrium states gives us a hint to decipher the relation between the two profiles.

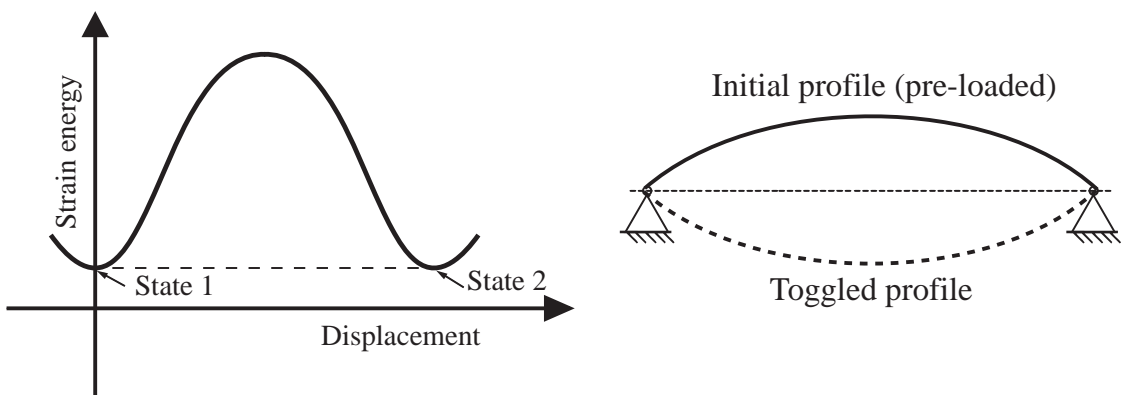


Figure 4.3: Strain energy profile of a buckled beam. Here, strain energies in the stable states are identical.

We assume the initial profile to be a weighted combination of all the buckling mode shapes of the column to analytically derive the relation between the arch-profiles of two force-free stable states. By using this relation, we describe the analysis and design of the two stable arch-profiles of shallow pinned-pinned bistable arches, and thereafter we show that these results are valid for fixed-fixed arches as well. It may be noted that not every initial profile has a corresponding toggled profile, i.e., certain as-fabricated shapes might not be bistable. Similarly, not every toggled-shape has a stress-free initial profile. Hence, the existence of initial and toggled profiles is also addressed. We prove that the components of fundamental buckling mode shapes should not be absent in the initial profile of the arch for it to be bistable. Furthermore, insights gained from this relation, which set basic guidelines for designing arch-profiles, are presented as the corollaries from the relation. Since the relation is derived for force-free equilibrium states, the solutions obtained from it are independent of the force-displacement characteristics of the arch. In other words, once a pair of stable arch-profiles is obtained, bistability can be achieved using an appropriate mode of actuation.

First, the necessary and sufficient conditions for the force-free equilibrium states are derived in terms of two sets of mode shape weights corresponding to the initial and toggled profiles, a_i s and A_i s respectively for pinned-pinned boundary conditions. The necessary conditions for bistability and the analytical relation between the mode weights are derived. The relation is presented in two forms: a closed-form equation for design, and a simplified nonlinear expression in one variable for analysis. Furthermore, three key results are deduced from the relation. They are concerned with symmetry in the arch-profiles and special cases of changes in the signs and magnitudes of mode weights. Analysis and design examples are illustrated, which are verified with 3D-printed prototypes and finite element analysis (FEA). Additionally, the bilateral relationship, necessary conditions, and corollaries are shown to hold good for fixed-fixed end conditions as well. The design capabilities of analytical results for fixed-fixed arches are illustrated through three design examples. One such example is that of a bistable gripper to grasp a circular object shown in Fig. 4.4.

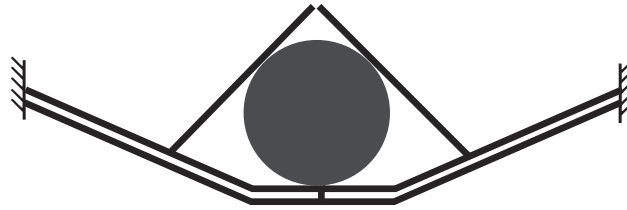


Figure 4.4: Schematic of a bistable gripper in the closed configuration.

4.2 Necessary and sufficient conditions for force-free equilibrium states in bistable arches with pinned-pinned boundary conditions

The initial profile, $h(x)$, and the deformed profile, $w(x)$, are taken as weighted combinations of all the buckling mode shapes of a straight pinned-pinned column. The normalized as-fabricated profile, $H(X)$, and the normalized deformed shape, $W(X)$, can be written as

$$H(X) = \frac{h(XL)}{h_{mid}} = \sum_{i=1}^{\infty} a_i \sin(M_i X) \quad (4.1)$$

$$W(X) = \frac{w(XL)}{h_{mid}} = \sum_{i=1}^{\infty} A_i \sin(M_i X) \quad (4.2)$$

where $M_i = i\pi$, $X = \frac{x}{L}$, L the span of the arch, and h_{mid} , the mid-span height, as shown in Fig. 4.5. A_i and a_i are the unknown weights corresponding to the i th buckling mode

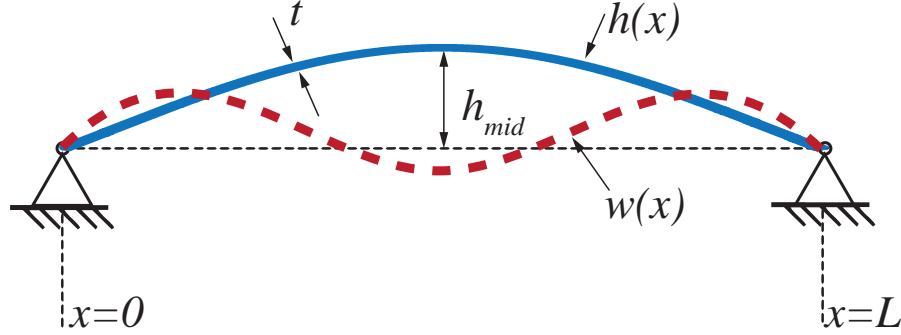


Figure 4.5: A bistable arch with pinned-pinned boundary conditions. The solid curve is the as-fabricated shape, $h(x)$ and the dashed curve is the deformed profile, $w(x)$. L is the span of the arch, t , in-plane depth and b , the out-of-plane width.

shape; they approximate the deformed profile and as-fabricated shape, respectively, to the desired level of accuracy. The total strain energy comprises bending and compression energies.

For an arch with Young's modulus, E , breadth, b , depth, t and second moment of area for rectangular cross-section, $I = \frac{bt^3}{12}$, the strain energy due to bending is given by

$$se_b = \frac{EI}{2} \int_0^L \left(\frac{d^2h}{dx^2} - \frac{d^2w}{dx^2} \right)^2 dx$$

By normalizing, we get

$$\begin{aligned} SE_b &= \frac{se_b L^3}{EI h_{mid}^2} = \frac{1}{2} \int_0^1 \left(\frac{d^2H}{dX^2} - \frac{d^2W}{dX^2} \right)^2 dX \\ &= \frac{1}{4} \left(\sum_{i=1}^{\infty} a_i^2 M_i^4 + \sum_{i=1}^{\infty} A_i^2 M_i^4 - 2 \sum_{i=1}^{\infty} a_i A_i M_i^4 \right) \end{aligned} \quad (4.3)$$

As the shallow arch deforms, the axial force, p , leads to compression energy, se_c , which is given by

$$se_c = \frac{1}{2} p (s_{initial} - s) \quad (4.4)$$

where s is the length of the arch as it deforms and $s_{initial}$, the as-fabricated arc-length of

the arch. For a linear elastic material, we write

$$p = Ebt \left(\frac{s_{initial} - s}{L} \right) \quad (4.5)$$

Assuming the arch to be shallow, i.e., $\left(\frac{dh}{dx}\right)^2 \ll 1$, arc-lengths can be approximated as

$$s = \int_0^L \sqrt{1 + \left(\frac{dw}{dx}\right)^2} dx \approx \int_0^L \left[1 + \frac{1}{2} \left(\frac{dw}{dx}\right)^2 \right] dx \quad (4.6)$$

$$s_{initial} = \int_0^L \left[1 + \frac{1}{2} \left(\frac{dh}{dx}\right)^2 \right] dx \quad (4.7)$$

Using Eqs. (4.1), (4.2) and (4.4) to (4.7), the normalized compression strain energy, SE_c , can be written as

$$SE_c = \frac{se_c L^3}{EI h_{mid}^2} = \frac{1}{2} P (S_{initial} - S) = \frac{3h_{mid}^2}{8t^2} \left(\sum_{i=1}^{\infty} a_i^2 M_i^2 - \sum_{i=1}^{\infty} A_i^2 M_i^2 \right)^2 \quad (4.8)$$

where the normalized arc-lengths, S and $S_{initial}$, and the normalized axial force, P , are

$$\begin{aligned} S &= \frac{sL}{h_{mid}^2} = \int_0^1 \left[\frac{L^2}{h_{mid}^2} + \frac{1}{2} \left(\frac{dW}{dX}\right)^2 \right] dX \\ &= \frac{L^2}{h_{mid}^2} + \frac{1}{4} \sum_{i=1}^{\infty} A_i^2 M_i^2 \end{aligned} \quad (4.9)$$

$$S_{initial} = \frac{s_{initial} L}{h_{mid}^2} = \frac{L^2}{h_{mid}^2} + \frac{1}{4} \sum_{i=1}^{\infty} a_i^2 M_i^2 \quad (4.10)$$

$$\begin{aligned} P &= \frac{pL^2}{EI} = \frac{12h_{mid}^2 L^2}{Lt^2} \left(\frac{S_{initial} - S}{L} \right) \\ &= \frac{3h_{mid}^2}{t^2} \left(\sum_{i=1}^{\infty} a_i^2 M_i^2 - \sum_{i=1}^{\infty} A_i^2 M_i^2 \right) \end{aligned} \quad (4.11)$$

The normalized strain energy, SE , includes normalized bending energy and compression energy. By substituting for SE_b and SE_c from Eqs. (4.3) and (4.8), the strain energy can be expressed as

$$SE = \frac{1}{4} \left(\sum_{i=1}^{\infty} a_i^2 M_i^4 + \sum_{i=1}^{\infty} A_i^2 M_i^4 - 2 \sum_{i=1}^{\infty} a_i A_i M_i^4 \right) + \frac{3h_{mid}^2}{8t^2} \left(\sum_{i=1}^{\infty} a_i^2 M_i^2 - \sum_{i=1}^{\infty} A_i^2 M_i^2 \right)^2 \quad (4.12)$$

The necessary conditions for the force-free equilibrium states are obtained as

$$\frac{\partial SE}{\partial A_i} = 0 \quad \text{for } i = 1, 2, 3, \dots \infty \quad (4.13)$$

which leads to

$$\begin{aligned} & \frac{1}{4} (2A_i M_i^4 - 2a_i M_i^4) - \frac{3h_{mid}^2}{8t^2} 2 \left(\sum_{k=1}^{\infty} a_k^2 M_k^2 - \sum_{k=1}^{\infty} A_k^2 M_k^2 \right) 2A_i M_i^2 = 0 \\ \implies & (A_i M_i^2) - \frac{3h_{mid}^2}{t^2} \left(\sum_{k=1}^{\infty} a_k^2 M_k^2 - \sum_{k=1}^{\infty} A_k^2 M_k^2 \right) A_i = a_i M_i^2 \quad \text{for } i = 1, 2, 3, \dots \infty \\ \implies & A_i (M_i^2 - 3Q^2 C) = a_i M_i^2 \quad \text{for } i = 1, 2, 3, \dots \infty \end{aligned} \quad (4.14)$$

where $Q = \frac{h_{mid}}{t}$, t , the in-plane depth and $C = \sum_{k=1}^{\infty} a_k^2 M_k^2 - \sum_{k=1}^{\infty} A_k^2 M_k^2$, which is the normalized change of arc-length. The necessary conditions are satisfied by all the force-free equilibrium states of a bistable arch. This includes two stable states and the in-between unstable state shown in Fig. 4.1. However, our interest is in the two arch-profiles corresponding to the two stable equilibrium states. Hence, we need to distinguish solutions corresponding to the stable arch-profiles from that of the unstable arch-profile. The second partial derivative test can be used to check if the solution obtained from Eq. (4.14) is indeed a minimum. The Hessian matrix, \mathbf{H} , is computed by differentiating strain energy twice. The diagonal elements in the matrix, H_{ii} , are obtained as

$$\begin{aligned} H_{ii} &= \frac{\partial^2 SE}{\partial A_i^2} = \frac{M_i^4}{2} - \frac{3Q^2 M_i^2}{2} \left(\sum_{k=1}^{\infty} a_k^2 M_k^2 - \sum_{k=1}^{\infty} A_k^2 M_k^2 \right) + 3Q^2 A_i^2 M_i^4 \\ &= \frac{M_i^4}{2} - \frac{3Q^2 M_i^2 C}{2} + 3Q^2 A_i^2 M_i^4 \end{aligned} \quad (4.15)$$

and the non-diagonal elements as

$$H_{ij} = \frac{\partial^2 SE}{\partial A_i \partial A_j} = 3Q^2 A_i A_j M_i^2 M_j^2 \quad (4.16)$$

The positive definiteness of \mathbf{H} at the third equilibrium point ensures its stability, i.e., for the arch to be bistable

$$v^T \mathbf{H} v > 0 \quad (4.17)$$

for all nonzero vectors v .

4.3 Analytical relation between initial and toggled profiles of pinned-pinned bistable arches

We state and prove a few results in this section. We begin with conditions of bistability on the fundamental mode-weights, a_1 and A_1 . The analytical relation between the two stable arch-profiles, deduced from Eq. (4.14) and the necessary conditions, is presented in two forms: one for analysis and the other for design. The corollaries described subsequently improve our understanding of bistability and set certain guidelines for designing bistable arches.

4.3.1 Results

4.3.1.1 Conditions on fundamental mode-weights

A pinned-pinned force-free shallow bistable arch should satisfy the following necessary conditions.

1. The fundamental mode weight a_1 is not zero in the initial profile of the arch.
2. The fundamental mode weight A_1 is not zero in the toggled profile of an arch.

4.3.1.2 Relation between A_i and a_i

The weight corresponding to the i th mode shape in the toggled profile, A_i , is only dependent on the i th mode shape in the initial profile, a_i , i , and ratio of weights of the fundamental mode shape, $\frac{a_1}{A_1}$. This relation can be expressed as

$$A_i = \frac{a_i}{1 - \frac{1}{i^2} \left(1 - \frac{a_1}{A_1}\right)} \quad (4.18)$$

This relation between the weights of the mode shapes in the initial and toggled profiles determines all the mode weights a_i s and A_i s once a_1 and A_1 become known from the equation presented next.

4.3.1.3 An equation in A_1 (for analysis)

The analytical relation for analysis can be expressed as

$$3Q^2 \sum_{i=1}^{\infty} \left\{ \frac{\frac{1}{i^2} \left(1 - \frac{a_1}{A_1}\right) - 2}{\left[1 - \frac{1}{i^2} \left(1 - \frac{a_1}{A_1}\right)\right]^2} \right\} a_i^2 = 1 \quad (4.19)$$

Once Q and the as-fabricated profile (i.e., a_i s) are specified, Eq. (4.19) is a nonlinear equation in only one variable, A_1 . Thus, A_1 can be determined numerically and then the rest of the coefficients can be found using Eq. (4.18), thereby giving the toggled profile. If all the eigenvalues of the Hessian matrix (see Eqs. (4.15) and (4.16)) are positive, one can conclude that the arch under consideration is bistable.

4.3.1.4 A formula for a_1 (for design)

Designing the initial profile for a specified toggled profile entails determining a_i s for a given set of A_i s and Q . Unlike the equation for A_1 in analysis, a_1 for design of an as-fabricated shape can be expressed in closed-form as

$$a_1 = A_1 \frac{\sum_{i=1}^{\infty} \frac{A_i^2}{i^2} - 2 \sum_{i=1}^{\infty} A_i^2 - \frac{1}{3Q^2}}{\sum_{i=1}^{\infty} \frac{A_i^2}{i^2}} \quad (4.20)$$

After a_1 is obtained from Eq. (4.20), the rest of the a_i s can be determined from Eq. (4.18). This formula simplifies the design of the toggled profile considerably. It only involves evaluating Eqs. (4.18) and (4.20) and checking the Hessian matrix (Eq. (4.17)) for positive definiteness.

Next, we state three corollaries deduced from Eqs. (4.19) and (4.20).

4.3.1.5 Corollaries

- *1a. For $i > 1$, $A_i = 0$ implies $a_i = 0$ and vice versa.*

1b. The toggled-profile of a bistable arch with a symmetric initial profile will also be symmetric and vice versa.

1c. For $i > 1$, $A_i \neq 0$ implies $a_i \neq 0$ and vice versa.

1d. The toggled-profile of a bistable arch with an asymmetric initial profile will also be asymmetric and vice versa.

- 2a. $(a_1 A_1) < 0$

- 2b. $(a_{i>1} A_{i>1}) > 0$

- 3a (inexact). A_i is approximately equal to a_i for higher values of i .

3b (inexact). For arch-profiles composed of only a_i s with higher values of i ($i \geq m$) along with a_1 , $a_1^2 - 8 \sum_{i=m}^{\infty} a_i^2 - \frac{4}{3Q^2} > 0$ is necessary and sufficient for bistability.

4.3.2 Proofs and derivations

4.3.2.1 Conditions on fundamental mode-weights

1. If the fundamental mode weight a_1 is zero in the initial profile of an arch, it cannot be bistable.

This result can be shown from the necessary and sufficient conditions, Eqs. (4.14) to (4.16). Consider a bistable arch with $a_1 = 0$. Then, we have from Eq. (4.14)

$$A_1(M_1^2 - 3Q^2C) = 0 \quad (4.21)$$

For this equation to hold good, either A_1 has to be zero or $3Q^2C$ should be equal to $M_1^2 = \pi^2$. In the latter case, Eq. (4.14) simplifies to

$$A_i = \frac{a_i^2 M_i^2}{M_i^2 - 3Q^2C} = \frac{a_i i^2 \pi^2}{i^2 \pi^2 - \pi^2} = \frac{a_i i^2}{i^2 - 1} \quad \text{for } i = 2, 3, \dots, \infty \quad (4.22)$$

This implies that $|A_i|$ is greater than $|a_i|$. By using $C = \sum_{i=1}^{\infty} a_i^2 M_i^2 - \sum_{i=1}^{\infty} A_i^2 M_i^2$, when a_1 is zero, $A_1 M_1^2$ can be written as

$$\begin{aligned} A_1^2 M_1^2 &= \frac{-M_1^2}{3Q^2} + \sum_{i=2}^{\infty} a_i^2 M_i^2 - \sum_{i=2}^{\infty} A_i^2 M_i^2 \\ \implies A_1^2 &= \frac{-1}{3Q^2} + \sum_{i=2}^{\infty} a_i^2 i^2 - \sum_{i=2}^{\infty} A_i^2 i^2 \end{aligned} \quad (4.23)$$

Since $|A_i|$ is greater than $|a_i|$, the right hand side of Eq. (4.23) is negative resulting in imaginary solutions for A_1 . Thus, Eq. (4.21) has a real solution only when

$A_1 = 0$. From Eq. (4.16), we see that all the elements in the first row and column except H_{11} are zero when $A_1 = 0$. Hence, at the stable equilibrium points, H_{11} should be positive. Using Eq. (4.15),

$$\begin{aligned} H_{11} &= \frac{M_1^2}{2} (M_1^2 - 3Q^2C) > 0 \\ \implies 3Q^2C &< M_1^2 \end{aligned} \quad (4.24)$$

Let us now consider two cases, one where $3Q^2C$ is positive and other in which it is negative. In both the cases, using Eq. (4.14) all the mode weights other than the fundamental mode weights can be written as

$$A_i = \frac{a_i^2 M_i^2}{M_i^2 - 3Q^2C} \quad (4.25)$$

In the first case, C is positive since the sign of $3Q^2C$ is determined by C . Then, Eq. (4.25) implies that $|A_i|$ is greater than $|a_i|$. However, this contradicts our starting assumption that C is positive, since $C = \sum_{i=1}^{\infty} a_i^2 M_i^2 - \sum_{i=1}^{\infty} A_i^2 M_i^2$. Similarly, in the second case of $3Q^2C < 0$, $|A_i|$ should be less than $|a_i|$ and C should be negative at the same time, which is not possible. Therefore, $3Q^2C$ must be zero to satisfy Eq. (4.24), which corresponds to $a_i = A_i$, the as-fabricated shape. Thus, the arch cannot have two stable arch-profiles with $a_1 = 0$.

2. *The fundamental mode weight A_1 cannot be zero in the toggled profile of an arch.* When $A_1 = 0$, Eq. (4.14) implies that $a_1 = 0$. Hence, following the preceding arguments, the arch has only one stable state when $A_1 = 0$.

4.3.2.2 Relation between A_i and a_i

For deriving this relation, it is important to note that in the stable force-free equilibrium state of the arch, $3Q^2C$ should be less than $4\pi^2$. To show this, let us assume that $3Q^2C = M_j^2 = j^2\pi^2$ at the force-free equilibrium state. For the arch to be bistable, H_{11} should be greater than zero, i.e.,

$$H_{11} = \frac{M_1^4}{2} - \frac{3Q^2 M_1^2 C}{2} + 3Q^2 A_1^2 M_1^4 = \frac{\pi^4}{2} (1 - j^2 + 6Q^2 A_1^2) > 0 \quad (4.26)$$

$$\implies j^2 < 1 + 6Q^2 A_1^2 \quad (4.27)$$

Hence, from Eq. (4.27) we can say that the arch cannot be bistable when $j^2 > 1 + 6Q^2 A_1^2$. According to Sylvester's criterion, the determinant of the upper left 2×2 corner of H should also be positive for the positive definiteness of \mathbf{H} . This determinant can be written as

$$H_{11}H_{22} - H_{12}^2 = \pi^8 [A_1^2 Q^2 (24 - 6j^2) + 24A_2^2 Q^2 (1 - j^2) + j^4 - 5j^2 + 4] \quad (4.28)$$

Since Eq. (4.28) is quadratic in j^2 , its sign can change only twice as we increase j from 0 to ∞ . $H_{11}H_{22} - H_{12}^2$ equals to $18\pi^8 A_1^2 Q^2$, $-72\pi^8 A_2^2 Q^2$, and $-144\pi^8 A_1^2 A_2^2 Q^4$ when j^2 is 1, 4, and $1 + 6Q^2 A_1^2$, respectively. This means that $H_{11}H_{22} - H_{12}^2$ is negative when j is greater than 2 but less than $\sqrt{1 + 6Q^2 A_1^2}$. Combining the result from Eq. (4.27), we can say that j should be less than 2 when the arch is in a force-free stable equilibrium state. Also, in the preceding section it was proved that $3Q^2 C \neq \pi^2$ in the second stable state. Thus, for a bistable arch in its force-free equilibrium state, $3Q^2 C \neq k^2 \pi^2$, where k is an integer.

As proved earlier, the necessary conditions for bistability imply that the component of the fundamental buckling mode in the initial and toggled profiles is not zero for an arch to be bistable, i.e., $a_1 \neq 0$ and $A_1 \neq 0$. Thus, from Eq. (4.14), we have

$$3Q^2 C = \left(M_1^2 - \frac{a_1}{A_1} M_1^2 \right) \quad (4.29)$$

Equations (4.14) and (4.29) help us write A_i in terms of a_i , i , a_1 , and A_1 as

$$\begin{aligned} A_i &= \frac{a_i M_i^2}{M_i^2 - M_1^2 \left(1 - \frac{a_1}{A_1} \right)} \\ &= \frac{a_i}{1 - \frac{1}{i^2} \left(1 - \frac{a_1}{A_1} \right)} \quad \because M_i = i\pi \end{aligned}$$

Hence, Eq. (4.18) is proved. Note that $M_i^2 - M_1^2 \left(1 - \frac{a_1}{A_1} \right)$ cannot be zero as $3Q^2 C$ cannot be equal to $i^2 \pi^2$ in the force-free equilibrium states.

To derive the results in Eqs. (4.19) and (4.20), C is written in terms of A_i s using

Eq. (4.18) as follows:

$$\begin{aligned}
 C &= \sum_{i=1}^{\infty} a_i^2 M_i^2 - \sum_{i=1}^{\infty} A_i^2 M_i^2 \\
 &= \sum_{i=1}^{\infty} a_i^2 M_i^2 - \sum_{i=1}^{\infty} \left[\frac{a_i}{1 - \frac{1}{i^2} \left(1 - \frac{a_1}{A_1}\right)} \right]^2 M_i^2 \\
 &= \sum_{i=1}^{\infty} \left\{ 1 - \frac{1}{\left[1 - \frac{1}{i^2} \left(1 - \frac{a_1}{A_1}\right)\right]^2} \right\} a_i^2 i^2 \pi^2 \\
 &= \sum_{i=1}^{\infty} \left\{ \frac{\frac{1}{i^4} \left(1 - \frac{a_1}{A_1}\right)^2 - \frac{2}{i^2} \left(1 - \frac{a_1}{A_1}\right)}{\left[1 - \frac{1}{i^2} \left(1 - \frac{a_1}{A_1}\right)\right]^2} \right\} a_i^2 i^2 \pi^2 \\
 &= \left(1 - \frac{a_1}{A_1}\right) \pi^2 \sum_{i=1}^{\infty} \left\{ \frac{\frac{1}{i^2} \left(1 - \frac{a_1}{A_1}\right) - 2}{\left[1 - \frac{1}{i^2} \left(1 - \frac{a_1}{A_1}\right)\right]^2} \right\} a_i^2
 \end{aligned} \tag{4.30}$$

By inserting this expression in Eq. (4.14), we get

$$\begin{aligned}
 A_i &= \frac{a_i}{1 - \frac{3Q^2 C}{i^2 \pi^2}} \\
 &= \frac{a_i}{1 - \frac{3Q^2}{i^2} \left(1 - \frac{a_1}{A_1}\right) \sum_{i=1}^{\infty} \left\{ \frac{\frac{1}{i^2} \left(1 - \frac{a_1}{A_1}\right) - 2}{\left[1 - \frac{1}{i^2} \left(1 - \frac{a_1}{A_1}\right)\right]^2} \right\} a_i^2}
 \end{aligned} \tag{4.31}$$

Comparing Eq. (4.31) with Eq. (4.18) and ignoring the trivial solution ($A_i = a_i$), we get Eq. (4.19), which is the relation that can be used for analysis of bistable arches. This is a nonlinear equation in only A_1 , when a_i s are known. Equation (4.18) can be written as

$$a_i = A_i \left[1 - \frac{1}{i^2} \left(1 - \frac{a_1}{A_1}\right) \right] \tag{4.32}$$

To obtain the relation used for designing arches, we substitute Eq. (4.32) in Eq. (4.19)

$$1 = 3Q^2 \left[\left(1 - \frac{a_1}{A_1}\right) \sum_{i=1}^{\infty} \frac{A_i^2}{i^2} - 2 \sum_{i=1}^{\infty} A_i^2 \right] \tag{4.33}$$

By rearranging the terms, we obtain a_1 as in Eq. (4.20).

4.3.2.3 Proofs of corollaries

1a. For $i > 1$, $A_i = 0$ implies $a_i = 0$ and vice versa.

When a_i is zero, Eq. (4.14) becomes

$$A_i(M_i^2 - 3Q^2C) = 0 \quad (4.34)$$

Equation (4.34) implies that either $A_i = 0$ or $3Q^2C = M_i^2$. However, we showed in the preceding section that the latter cannot be true. So, the only possible solution to Eq. (4.34) is $A_i = 0$. To prove the inverse, from Eq. (4.14) we see that $a_i = 0$ when $A_i = 0$.

To illustrate the utility of Result 1a, let us consider a sine-arch with $h = 5$ mm and $t = 0.5$ mm. Since it is a pure sine-arch, $a_1 = 1$ and the remaining a_i s are zero. By numerically solving the nonlinear equation, Eq. (4.19), we obtain $A_1 = 0.9967$. From Eq. (4.18), since all the remaining a_i s are zero, A_i s ($i \neq 1$) are also zero. The eigenvalues of \mathbf{H} , with the first five buckling mode shapes used for approximation are, 0.04×10^4 , 0.30×10^4 , 1.09×10^4 , 2.80×10^4 , 2.89×10^4 , which are all positive indicating that the obtained shapes form a bistable arch-profile pair. Thus, we observe that a pure sine-arch has the same shape in both the states, but the height of the inverted toggled profile is smaller than that of the initial profile.

1b. The toggled profile of a bistable arch with a symmetric initial profile will also be symmetric and vice versa.

In a symmetric bistable arch, all the even mode weights are zero, i.e., $a_m = 0$ for $m = 2, 4, 6, \dots \infty$. From Result 1a, we know that the corresponding A_i s are also zero, i.e., the toggled profile is also symmetric. Similarly, from Result 1a, a_m s are zero when A_m s corresponding to even mode shapes are zero.

1c. For $i > 1$, $A_i \neq 0$ implies $a_i \neq 0$ and vice versa.

As mentioned before in Result 1a, $3Q^2C$ cannot be equal to M_i^2 such that the resulting toggled profile is stable. Thus, from Eq. (4.14), if a mode weight is non-zero in one of the stable states, its corresponding mode weight in the other stable state is also non-zero.

1d. The toggled-profile of a bistable arch with an asymmetric initial profile will also be asymmetric and vice versa.

Bistable arches with asymmetric buckling modes in their as-fabricated shape are called asymmetric bistable arches. When an even mode shape is present in one of the stable arch-profiles, according to Result 1c, it would be present in the other stable state as well. Hence, if one of the stable arch-profiles is asymmetric the other profile is also asymmetric.

2a. $(a_1 A_1) < 0$.

The fundamental buckling mode is always present in the stable arch-profiles (see Section 4.3.1.1). Intuitively, $a_1 A_1$ being negative means that the arch flips with respect to this fundamental buckling mode. This can be seen from Eq. (4.20). Since $\sum_{i=1}^{\infty} \frac{A_i^2}{i^2}$ is always positive, the sign of a_1 is determined by the sign of A_1 and $\sum_{i=1}^{\infty} \frac{A_i^2}{i^2} - 2 \sum_{i=1}^{\infty} A_i^2 - \frac{1}{3Q^2}$. The latter will be negative as $\frac{A_i^2}{i^2}$ is less than $2A_i^2$. Thus, we have that $(a_1 A_1) < 0$.

2b. $(a_{i>1} A_{i>1}) > 0$. The signs of all the mode weights except the fundamental mode weight remain unchanged as the arch toggles from one stable state to the other. In Section 4.3.2.2, we observed that $3Q^2 C$ should be less than $4\pi^2$. Using Eq. (4.29), the maximum value of $1 - \frac{a_1}{A_1}$ is less than 4. Hence, $\frac{1}{i^2} \left(1 - \frac{a_1}{A_1}\right)$ cannot be greater than one, even when $i = 2$. Thus, from Eq. (4.18) we see that the sign of A_i is the same as the sign of a_i and vice versa, for $i > 1$.

3a. (inexact) A_i is approximately equal to a_i for higher values of i .

Result 3a is an approximate result on the magnitude of higher mode weights (a_i/A_i with larger values of i). For higher values of i , the term $\frac{1}{i^2} \left(1 - \frac{a_1}{A_1}\right)$ can be neglected in Eq. (4.18). Hence, Eq. (4.18) becomes

$$A_i \approx a_i \tag{4.35}$$

In other words, the weights of higher buckling mode shapes in the toggled profile and initial profile would be approximately equal. In Section 4.3.2.3, where we proved that $a_{i>1} A_{i>1} > 0$, it was observed that $1 - \frac{a_i}{A_i}$ is less than 4. Hence, the approximation $a_i \approx A_i$ will have a maximum error of 4% if i is greater than 10. The maximum error will come down to 1% for $i > 20$.

3b. (inexact) For arch-profiles composed of only a_i s with higher values of i ($i \geq m$, where m is the least value of i such that Result 3a is valid) along with $a_1, a_1^2 - 8 \sum_{i=m}^{\infty} a_i^2 - \frac{4}{3Q^2} > 0$ is necessary and sufficient for bistability.

For arch-profiles with only corrugations on the sine-curved profile (all a_i s with values of i other than $i = 1$ and $i \geq m$ are absent), Result 3a is valid for $i \geq m$. Using Eq. (4.35) in Eq. (4.19), the relation for analysis can then be approximated as

$$A_1^2 + a_1 A_1 + 2 \sum_{i=m}^{\infty} a_i^2 + \frac{1}{3Q^2} = 0 \quad (4.36)$$

When this quadratic equation in A_1 , Eq. (4.36), has two real roots the arch is bistable. These two roots correspond to the unstable equilibrium and the stressed second stable equilibrium. This can be expressed mathematically using the discriminant of Eq. (4.36) as

$$a_1^2 - 8 \sum_{i=m}^n a_i^2 - \frac{4}{3Q^2} > 0 \quad (4.37)$$

Consider a bistable arch with two higher buckling modes in the initial profile with $Q = 10$ given in Fig. 4.6. The solid curve is the initial profile and the dashed curve is the toggled profile. The nonzero mode weights in the as-fabricated shape are

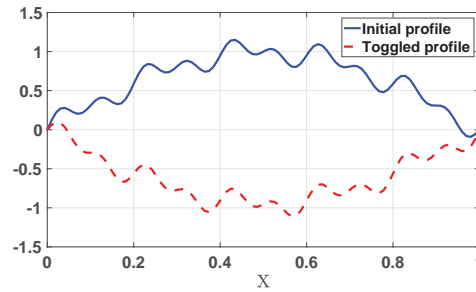


Figure 4.6: An asymmetric initial profile and its toggled profile with $a_{10} = a_{20} = 0.1$ and $Q = 10$.

$a_1 = 1$, $a_{10} = 0.1$, and $a_{20} = 0.1$, which satisfies Eq. (4.37). The toggled profile has $A_1 = -0.9537$, $A_{10} = 0.1021$, and $A_{20} = 0.1005$ as its mode weights. As the value of i increases, from 10 to 20, we notice that the difference between A_i and a_i decreases. This result is useful when slight local modifications are needed in an arch profile.

4.4 Illustrative examples of analysis and design

In this section, we use the results presented in the preceding sections to analyze and design bistable arches. The examples illustrated here are organized into three subsections: (1) Analysis of specified initial profiles, (2) design of toggled profiles, and (3) adding higher buckling modes to bistable arches. The comparison of the obtained toggled profiles with finite element analysis (FEA) and 3D-printed prototypes concerned with the examples are given at the end of this section.

4.4.1 Analysis of bistable arches with specified initial profiles

All a_i s are known when the initial profile is specified. In the first step of the analysis, it should be ensured that a_1 is non-zero (see the condition on fundamental mode-weights). For example, a straight beam, i.e., an arch with all a_i s equal to zero, cannot be bistable. A_1 can be obtained by numerically solving Eq. (4.19). Note that Eq. (4.19) is a nonlinear equation and may have multiple solutions. A numerical approach with an initial guess as $-a_1$ usually gives A_1 corresponding to the toggled profile. Other solutions correspond to in-between unstable arch-profiles. The remaining A_i s are determined from Eq. (4.18). In the last step, by substituting a_i s and A_i s in Eqs. (4.15) and (4.16), \mathbf{H} is obtained. The positive definiteness of the Hessian ensures that the A_i s correspond to a stable toggled profile.

Example 1

An angulated profile is shown in Fig. 4.7. When $c = \frac{L}{2}$, a symmetric V-beam profile is

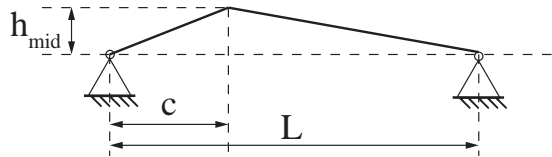


Figure 4.7: Angulated arch-profile

obtained. Taking the first 30 buckling mode shapes, i.e., $n = 30$, the specified profile can be written in terms of a_i s as shown in Fig. 4.8a. The value of n is decided based on a convergence study. As given in Fig. 4.9, with higher values of n , $h(x)$ fits tightly to the specified profile. For $n = 30$, the specified arch-profile is approximated with sufficient accuracy. For $h_{mid} = 5$ mm, $L = 100$ mm, and $t = 0.5$ mm, the arch is bistable with $A_1 = -0.77$ as determined using Eq. (4.19).

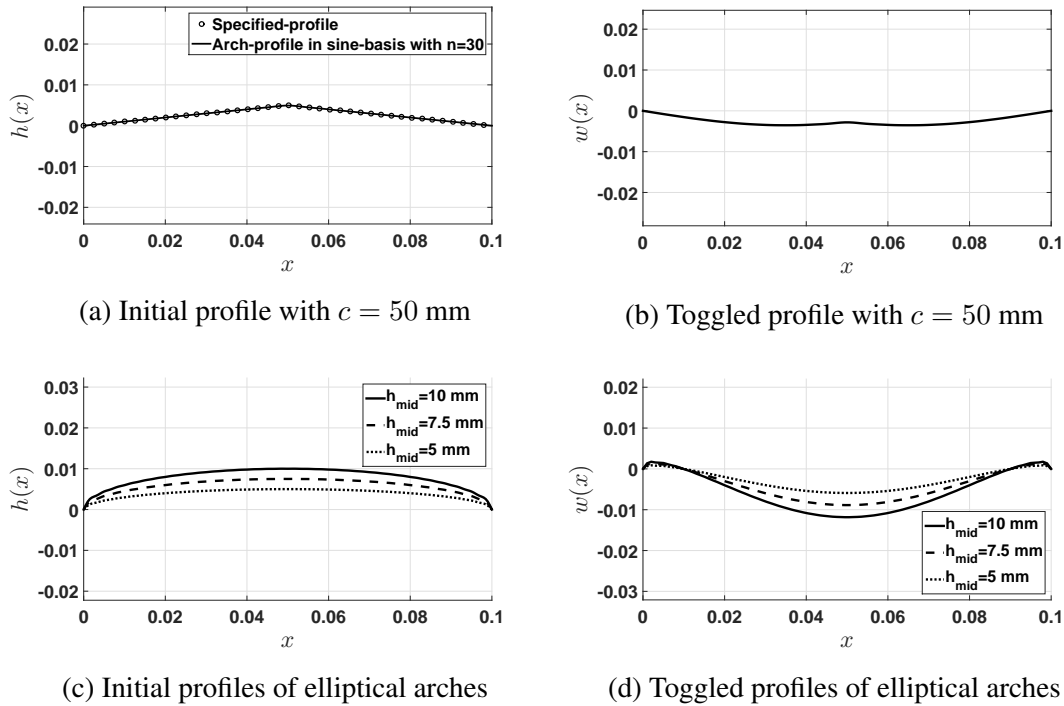


Figure 4.8: Toggled profiles of the arches obtained using the relation for analysis.

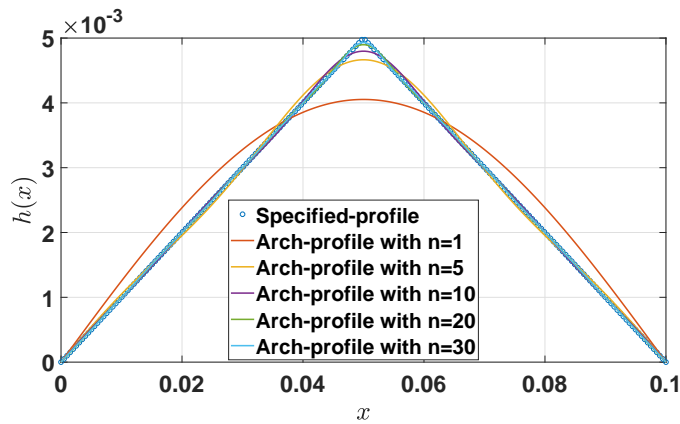


Figure 4.9: Convergence of $h(x)$ to the specified-profile with higher values of n

As mentioned before, the in-between unstable solutions also satisfy Eq. (4.19). Figure 4.10 shows the unstable arch-profile along with its two stable arch-profiles when $c = \frac{L}{2}$. However, bistability is not observed for all the values of c . For example, when $c = \frac{L}{4}$ and $Q = 10$, Eq. (4.19) does not have a root that gives a stable toggled profile. The force-displacement characteristic at the mid-span when $c = 25$ mm is shown in Fig. 4.11.

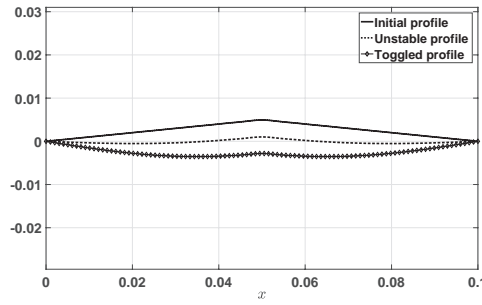


Figure 4.10: Two stable arch-profiles and an unstable arch-profile for $c = \frac{L}{2}$

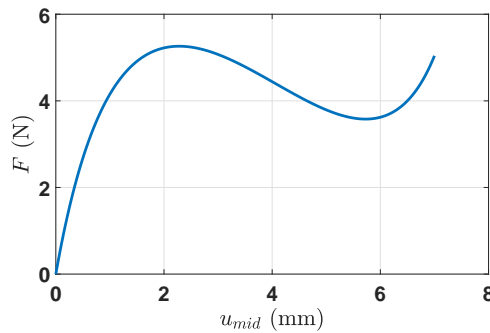


Figure 4.11: Force-displacement curve showing snap-through but not bistability when $c = 25$ mm, $L = 10$ mm, $E = 1.2$ GPa, $b = 5$ mm, and $t = 0.5$ mm

Example 2

Elliptical arches (see Fig. 4.12) can be bistable. The minor axis of the ellipse is varied

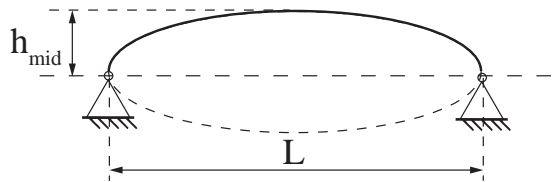


Figure 4.12: Elliptical arch-profile

to change h_{mid} with $L = 100$ mm for $t = 0.5$ mm. The initial and toggled arch-profiles are shown in Figs. 4.8c and 4.8d, respectively. A_1 when h_{mid} is 10 mm, 7.5 mm, and 5 mm, is -0.9973 , -0.9965 , and -0.9943 respectively. It may be noted that the toggled profile is above the axis near the end-supports.

4.4.2 Design of specified toggled profiles

The next five examples illustrate the utility of Eq. (4.20). As the number of mode shapes (n) used to represent the arch-profile was not truncated, Eq. (4.20) can be used for designing arches of arbitrary profiles.

Example 3

We seek an initial profile such that the toggled profile is an angulated beam shown in Fig. 4.13. Unlike the example where angulated shapes were used as initial pro-

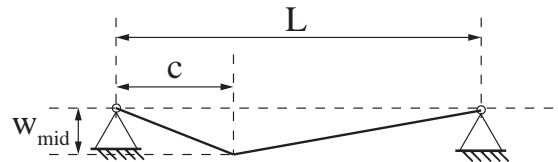


Figure 4.13: Angulated profile in the second stable shape

files, bistable arches with toggled profiles as angulated shapes are possible for both $c = 25$ mm and $c = 50$ mm. Figure 4.14b shows the designed initial profiles.

Example 4

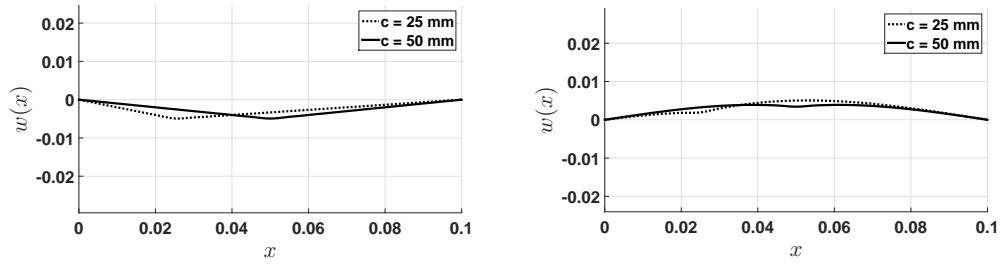
A normally-closed valve based on a bistable arch is considered in this example. As shown in Fig. 4.15, the toggled profile is desired to take a cup-shape. The initial profile that gives the cup-shape for $L = 100$ mm and $Q = 10$ is given in Fig. 4.14d. Similarly, a circular-valve can also be obtained instead of the cup-shape valve.

Example 5

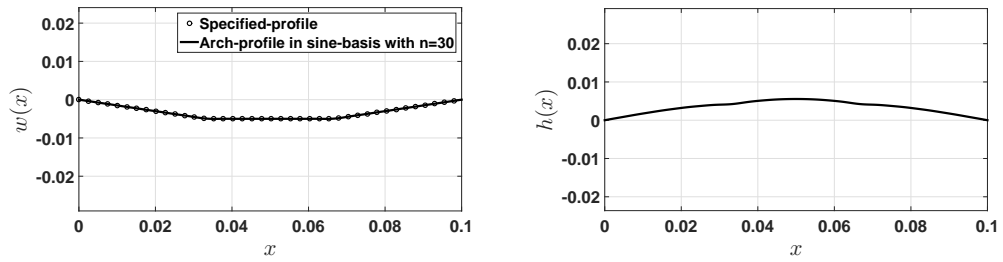
A bistable arch design with a polynomial curve as its toggled profile is shown in Fig. 4.14f. This example shows that the toggled profile need not be completely below the axis of switching.

Example 6

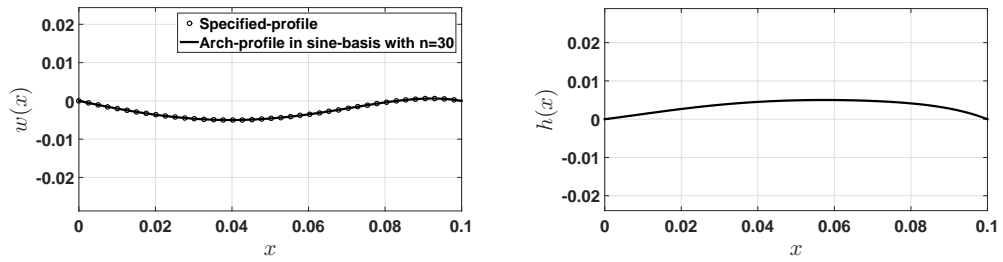
This example considers a partially specified toggle-profile. When the toggled profile is only partially specified, the rest of the profile can be selected arbitrarily. A design example for a clamp application (see Fig. 4.2) illustrates this. It is desired that the initial profile of the arch should be such that its toggled profile should wrap around a circular object as in Fig. 4.2. The desired and approximated toggled profiles using $n = 100$ for a circular object with a 10 mm diameter are shown in Fig. 4.16b and Fig. 4.16a, respectively. The arch is designed with $L = 100$ mm, $w_{mid} = 10$ mm, and $t = 0.5$ mm. The initial profile corresponding to the toggled profile given in Fig. 4.16b satisfies the second partial derivative test.



(a) Toggled profiles of angulated bistable arches (b) Initial profiles of angulated toggled profiles



(c) Toggled profile of cup-valve (d) Initial profile of cup-valve



(e) Polynomial curve as toggled profile with $W = X - 0.6X^2 - X^3 - X^4 + 1.6X^5$ (f) Initial profile of polynomial toggled profile

Figure 4.14: Initial profiles of arches obtained using the relation for design

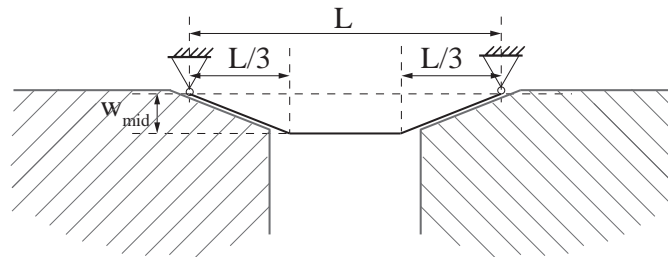


Figure 4.15: Schematic of a bistable cup-valve

4.4.3 Adding higher buckling modes to bistable arches

In this section, examples with higher-order buckling mode shapes are presented.

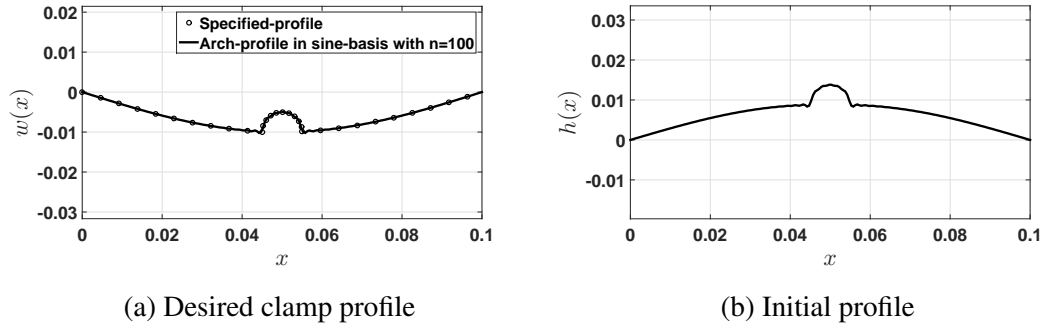


Figure 4.16: Design of a bistable clamp

Example 7

Bistable circular valves can benefit from two protrusions when they come into contact with the valve-seat, providing a tight fit to prevent leakage. The toggled profile shown in Fig. 4.17a shows such a design; its initial profile is given in Fig. 4.17b.

Example 8

Corollary 3 discusses the case when higher buckling mode shapes are added to the sine-curve profile. In this example, the initial profile is obtained by adding the 49th mode to the fundamental buckling mode, i.e.,

$$H(X) = a_1 \sin(\pi X) + a_{49} \sin(49\pi X) \quad (4.38)$$

For the arch to remain bistable, from Eq. (4.37), we have

$$a_1^2 - 8a_{49}^2 - \frac{4}{3Q^2} > 0 \quad (4.39)$$

The geometric parameters of the arch are taken as $L = 100$ mm, $t = 0.5$ mm, $h_{mid} = 5$ mm, and $a_1 = 1$. Thus, Eq. (4.39) is simplified to

$$\begin{aligned} 1 - 8a_{49}^2 - \frac{4}{300} &> 0 \\ \implies a_{49} &< 0.351 \end{aligned}$$

Figures 4.17c and 4.17d show the initial and toggled profiles with $a_{49} = 0.34$.

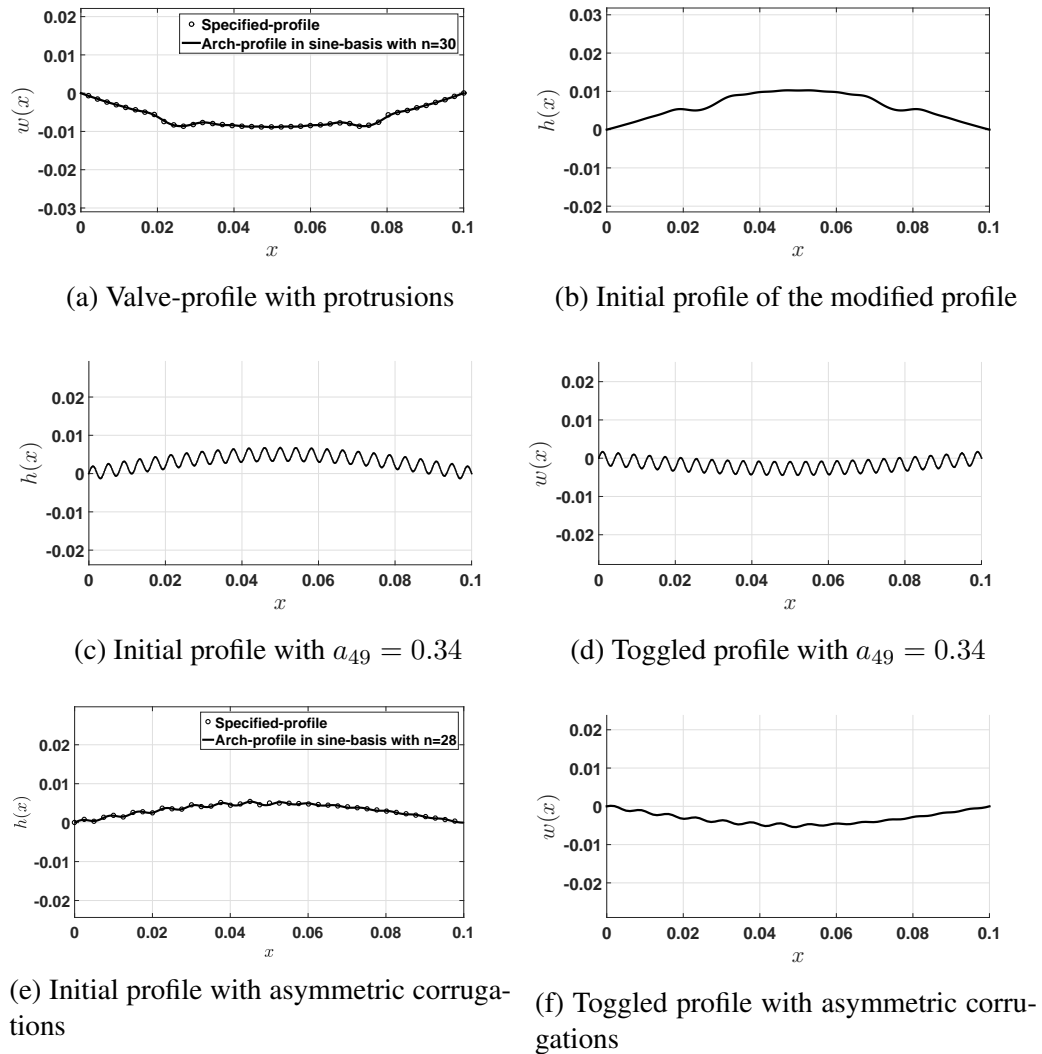
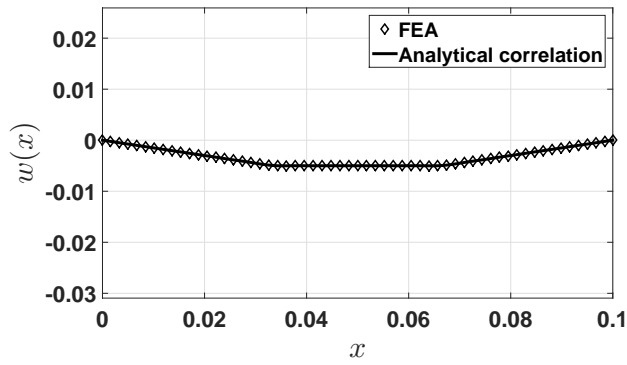


Figure 4.17: Design of bistable arch-profiles with higher mode weights

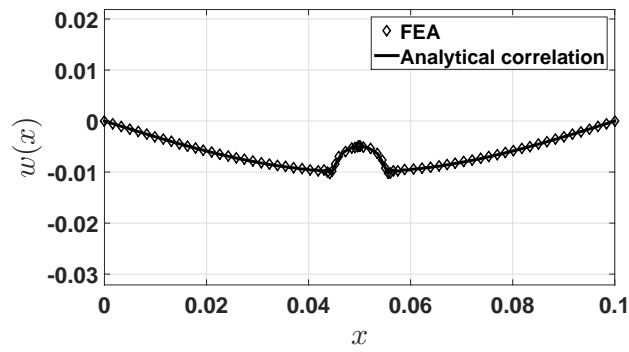
Example 9

The corrugations can also be added asymmetrically to the arch-profile. Figures 4.17e and 4.17f show two force-free arch-profiles of a bistable arch with corrugations only on the left half of the span.

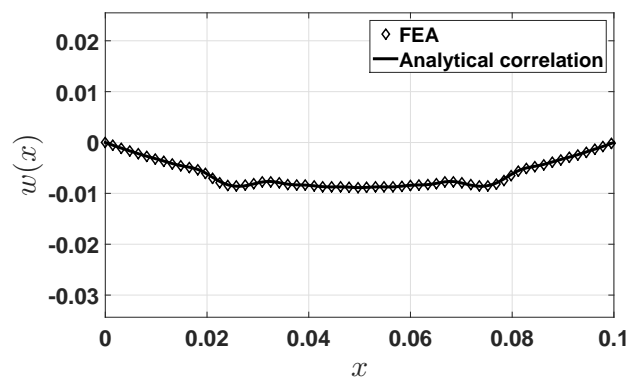
All the examples considered here are verified using FEA with continuum elements in Comsol (www.comsol.com). The toggled profiles obtained from FEA are compared with Examples 4, 6, and 7 in Fig. 4.18. 3D-printed prototypes of the arches illustrated in analysis and design with and without higher buckling modes are shown in Fig. 4.19.



(a) Example 4



(b) Example 6



(c) Example 7

Figure 4.18: Comparison of a toggled profile with FEA

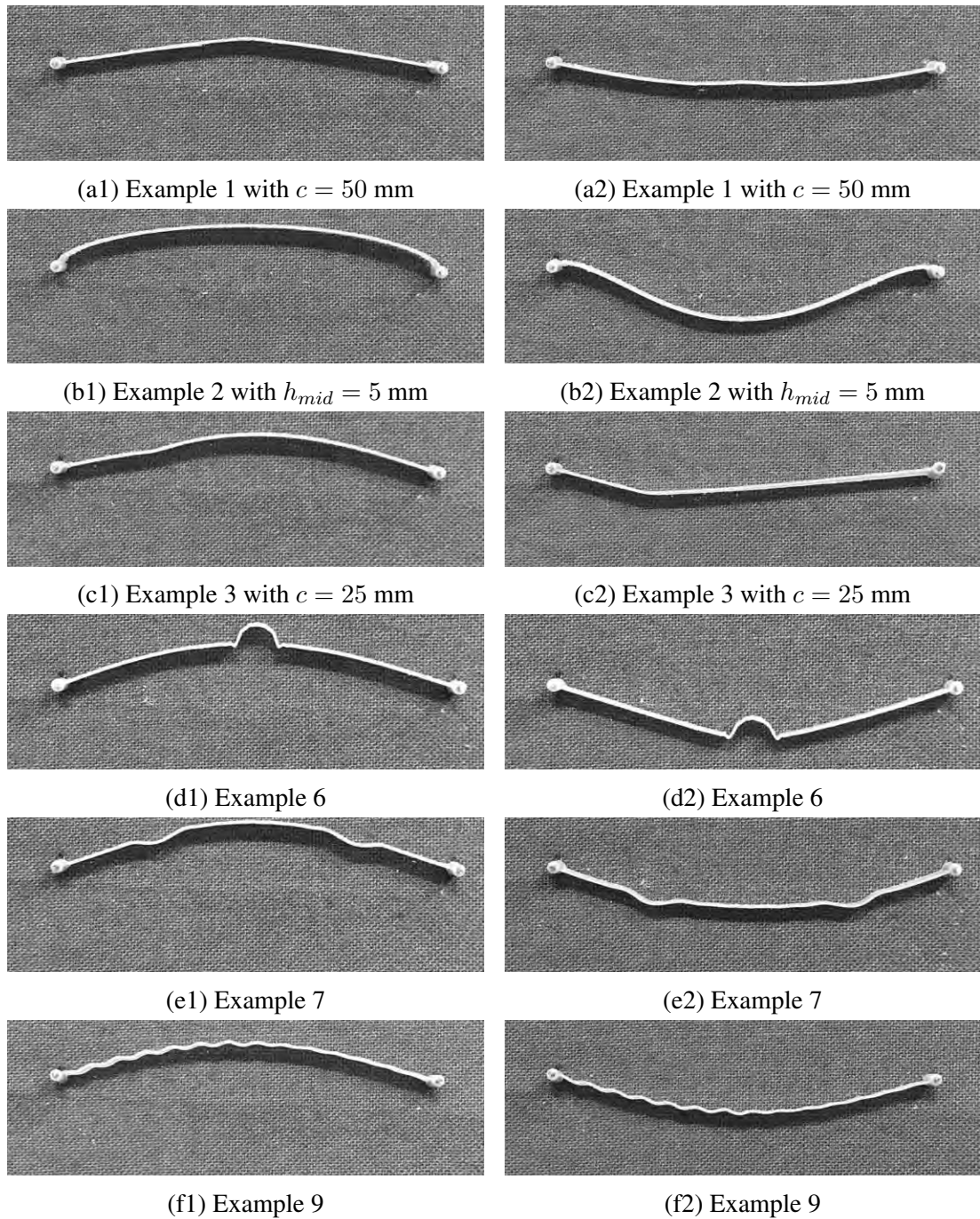


Figure 4.19: Initial and toggled profiles of 3D-printed prototypes. (a1)-(f1) are stress-free as-fabricated profiles; (a2)-(f2) are the corresponding toggled profiles.

4.5 Necessary and sufficient conditions for force-free equilibrium states in fixed-fixed bistable arches

Now we show that the bilateral relationship and the results derived from it are valid for fixed-fixed end conditions as well. The proofs for fixed-fixed boundary conditions are similar, the key difference being M_1 is 2π instead of π . Hence, the derivations are presented succinctly. For arbitrarily curved arches with fixed-fixed boundary conditions (see Fig. 4.20), the initial profile, $h(x)$, and the deformed profile, $w(x)$, are taken as the weighted combinations of the buckling mode shapes of a straight fixed-fixed column. The arch-profiles obtained from such a choice of basis set are kinematically admissible and tend to show bistability.

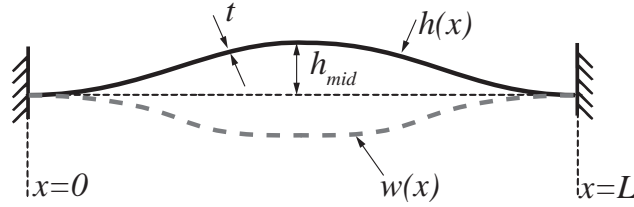


Figure 4.20: Fixed-fixed bistable arches with an arbitrary initial profile

Similar to the case of pinned-pinned end conditions, by taking A_i and a_i as the unknown weights corresponding to the i th buckling mode shape, the normalized as-fabricated profile, $H(X)$, and the normalized deformed shape, $W(X)$, are written as

$$H(X) = \frac{h(XL)}{h_{mid}} = \sum_{i=1}^{\infty} a_i W_i \quad (4.40)$$

$$W(X) = \frac{w(XL)}{h_{mid}} = \sum_{i=1}^{\infty} A_i W_i \quad (4.41)$$

where

$$W_i(X) = \begin{cases} 1 - \cos(M_i X) & i = 1, 3, 5 \dots \\ 1 - 2X - \cos(M_i X) + 2 \frac{\sin(M_i X)}{M_i} & i = 2, 4, 6 \dots \end{cases} \quad (4.42)$$

$$M_i = \begin{cases} (i+1)\pi & i = 1, 3, 5 \dots \\ 2.86\pi, 4.92\pi, 6.94\pi \dots & i = 2, 4, 6 \dots \end{cases} \quad (4.43)$$

$X = \frac{x}{L}$, L , the span of the arch, and h_{mid} , the mid-span height. Note that M_i for $i = 2, 4, 6, \dots$ satisfies the equation $\tan(\frac{M_i}{2}) = \frac{M_i}{2}$. The total strain energy, which

consists of bending and compression energies, is written in terms of the mode weights as

$$SE = \frac{1}{4} \left(\sum_{i=1}^{\infty} a_i^2 M_i^4 + \sum_{i=1}^{\infty} A_i^2 M_i^4 - 2 \sum_{i=1}^{\infty} a_i A_i M_i^4 \right) + \frac{3h_{mid}^2}{8t^2} \left(\sum_{i=1}^{\infty} a_i^2 M_i^2 - \sum_{i=1}^{\infty} A_i^2 M_i^2 \right)^2 \quad (4.44)$$

We note that the change in the basis set for fixed end-conditions has not changed the total strain energy expression. By minimizing the strain energy with respect to the unknown weights corresponding to the deformed profile, the necessary conditions for the force-free equilibrium states are obtained as

$$\frac{\partial SE}{\partial A_i} = 0 \quad \text{for } i = 1, 2, 3, \dots \infty \quad (4.45)$$

which simplify to

$$A_i(M_i^2 - 3Q^2C) = a_i M_i^2 \quad \text{for } i = 1, 2, 3, \dots \infty \quad (4.46)$$

$$C = \sum_{k=1}^{\infty} a_k^2 M_k^2 - \sum_{k=1}^{\infty} A_k^2 M_k^2 \quad (4.47)$$

where $Q = \frac{h_{mid}}{t}$, and t , is the in-plane depth. The Hessian matrix \mathbf{H} , obtained by differentiating Eq. (4.44) twice should be positive definite if the arch-profile pair obtained from the necessary conditions is stable. The diagonal elements in the matrix, H_{ii} , and the non-diagonal elements, H_{ij} , are obtained as

$$H_{ii} = \frac{\partial^2 SE}{\partial A_i^2} = \frac{M_i^4}{2} - \frac{3Q^2 M_i^2 C}{2} + 3Q^2 A_i^2 M_i^4 \quad (4.48)$$

$$H_{ij} = \frac{\partial^2 SE}{\partial A_i \partial A_j} = 3Q^2 A_i A_j M_i^2 M_j^2 \quad (4.49)$$

The positive definiteness of \mathbf{H} is checked by

$$v^T \mathbf{H} v > 0 \quad (4.50)$$

for all nonzero vectors v

For cosine-curved bistable arches, the second asymmetric mode of deformation needs to be constrained to ensure bistable operation. This restraint is physically realized by

connecting two cosine-curved arches at the center. Such double-cosine arches, when they switch between the stable equilibrium states, do not undergo asymmetric switching. Nonetheless, the aforementioned analysis remains valid as the constraint does not affect the arch-profiles in their stable states, but influences only the in-between deformation between them. However, the profiles obtained from the design equations presented in this work need to be made double-curved while fabricating them as shown in Fig. 4.21.



Figure 4.21: Double bistable arch with constrained asymmetric deformation.

4.6 Analytical relation between the initial and toggled profiles of fixed-fixed bistable arches

By using the necessary conditions for equilibrium, i.e., Eq. (4.46), a bilateral relationship between force-free arch-profiles can be obtained analytically. The key observation that leads to this derivation is that the constant C is common in Eq. (4.46) for all the values of i . By solving for C from Eq. (4.46) when $i = 1$, $\frac{A_i}{a_i}$ is written in terms of $\frac{A_1}{a_1}$ and M_i . This step in turn simplifies the expansion for C to arrive at the bilateral relationship.

We begin this section by stating and proving two conditions on fundamental mode weights. Then, an upper limit on the term $3Q^2C$ that corresponds to the compression energy in the arch is obtained. Both these conditions are essential in deriving the bilateral relationship. Further, the relationship is derived in forms amenable to analysis and design. Subsequently, insights gained from the bilateral relationship are presented as corollaries.

4.6.1 Conditions on fundamental mode-weights of fixed-fixed force-free shallow bistable arch

1. The fundamental mode weight a_1 is not zero in the initial profile of a bistable arch.
2. The fundamental mode weight A_1 is not zero in the toggled profile of a bistable arch.

To prove the first condition, consider Eq. (4.46) with $a_1 = 0$. We have

$$A_1(M_1^2 - 3Q^2C) = 0 \quad (4.51)$$

Here, $3Q^2C$ cannot be equal to $M_1^2 = 4\pi^2$ as it results in imaginary solutions for A_1 . When $3Q^2C = 4\pi^2$, from Eq. (4.46) we have

$$A_i = \frac{a_i M_i^2}{M_i^2 - 3Q^2C} \quad (4.52)$$

$$= \frac{a_i M_i^2}{M_i^2 - 4\pi^2} \quad i = 2, 3, \dots, \infty \quad (4.53)$$

Thus, $|A_i|$ is greater than $|a_i|$, since M_i is greater than 2π for i greater than 1. Therefore, we see from Eq. (4.47) that C is negative which contradicts our starting assumption that $C = \frac{4\pi^2}{3Q^2}$. Further, by substituting $a_1 = 0$ and $3Q^2C = 4\pi^2$ in Eq. (4.47), we get that A_1^2 is negative. So, the only real solution for Eq. (4.51) is when $A_1 = 0$. However, we see next that these real solutions do not lead to stable arch-profiles. We construct this argument on the stability of the arch-profiles based on the Hessian \mathbf{H} . By substituting $A_1 = 0$ in Eqs. (4.48) and (4.49), we see that the only element that remains non zero in the first row and column of \mathbf{H} is H_{11} . Hence, for the arch-profile to be stable, $H_{11} = \frac{M_1^2}{2} (M_1^2 - 3Q^2C) > 0$. This implies that

$$3Q^2C < M_1^2 \quad (4.54)$$

$3Q^2C$, and thereby C , can be positive, negative, or zero while satisfying this inequality. When C is positive, Eq. (4.52) implies that $|A_i|$ is greater than $|a_i|$. This further implies that C is negative, which is a contradiction to the starting assumption that C is positive. A similar situation arises when C is assumed to be negative. Hence, C should be zero while satisfying Eq. (4.54). This solution, $a_i = A_i$, corresponds to the starting as-fabricated shape of the arch. Hence, the fundamental mode weight a_1 is not zero in the initial profile of a bistable arch.

To prove that the fundamental mode weight A_1 is not zero in the toggled profile of a bistable arch, we note that $a_1 = 0$ when $A_1 = 0$. We already showed that when a_1 and A_1 are zero, the arch has only one stable state.

4.6.2 An upper limit on $3Q^2C$ for fixed-fixed boundary conditions

The term $3Q^2C$ is the measure of the change of length of the arch. We obtain an upper limit on $3Q^2C$ to aid in the derivation of the bilateral relationship and the corollaries presented thereafter. Let us assume that $3Q^2C = j^2\pi^2$ at the force-free equilibrium state. For the arch to be bistable, H_{11} and the determinant of the upper left 2×2 corner

of H , $H_{11}H_{22} - H_{12}^2$, should be positive, i.e.,

$$\begin{aligned} H_{11} &= \frac{M_1^4}{2} - \frac{3Q^2 M_1^2 C}{2} + 3Q^2 A_1^2 M_1^4 \\ &= \pi^4 (8 - 2j^2 + 48Q^2 A_1^2) > 0 \end{aligned}$$

$$\implies j^2 < 4 + 24Q^2 A_1^2 \quad (4.55)$$

$$H_{11}H_{22} - H_{12}^2 = C_1 j^4 + C_2 j^2 + C_3 > 0 \quad (4.56)$$

where C_1 , C_2 , and C_3 can be expressed in terms of A_1 , A_2 , and Q . We observe that Eq. (4.56) is a quadratic expression in j^2 . This expression takes the values $821.51\pi^8 A_1^2 Q^2$, $-1680.59\pi^8 A_2^2 Q^2$, and $-9642.44\pi^8 A_1^2 A_2^2 Q^4$ when j is 2, 2.86, and $\sqrt{4 + 24Q^2 A_1^2}$, respectively. This suggests that $H_{11}H_{22} - H_{12}^2$ is negative when j is greater than 2.86 but less than $\sqrt{4 + 24Q^2 A_1^2}$. This condition along with Eq. (4.55) implies that j should be less than 2.86 when the arch is in a force-free stable equilibrium state. Also, in the preceding section, while proving the conditions on the fundamental mode weights, it was shown that $3Q^2 C \neq 4\pi^2$ in the second stable state. Thus, for a bistable arch in its force-free equilibrium state, $3Q^2 C \neq M_i^2$.

4.6.3 Bilateral relationship for fixed-fixed boundary conditions

We first derive a relation between A_i and a_i by expressing $3Q^2 C$ in terms of a_1 , A_1 , and M_1 . In Section 4.6.1, we showed that A_1 and a_1 are non zero in the stable equilibrium states of the bistable arch. By using Eq. (4.46), this helps us write $3Q^2 C$ as

$$3Q^2 C = \left(M_1^2 - \frac{a_1}{A_1} M_1^2 \right) \quad (4.57)$$

By substituting Eq. (4.57) back into Eq. (4.46), A_i s for $i > 1$ can be written as

$$A_i = \frac{a_i}{1 - \frac{M_1^2}{M_i^2} \left(1 - \frac{a_1}{A_1} \right)} \quad (4.58)$$

By using this relation, Eq. (4.47) is simplified as follows:

$$\begin{aligned}
 C &= \sum_{i=1}^{\infty} a_i^2 M_i^2 - \sum_{i=1}^{\infty} A_i^2 M_i^2 \\
 &= \sum_{i=1}^{\infty} a_i^2 M_i^2 - \sum_{i=1}^{\infty} \left[\frac{a_i}{1 - \frac{M_1^2}{M_i^2} \left(1 - \frac{a_1}{A_1}\right)} \right]^2 M_i^2 \\
 &= \sum_{i=1}^{\infty} \left\{ 1 - \frac{1}{\left[1 - \frac{M_1^2}{M_i^2} \left(1 - \frac{a_1}{A_1}\right)\right]^2} \right\} a_i^2 M_i^2 \\
 &= \left(1 - \frac{a_1}{A_1}\right) M_1^2 \sum_{i=1}^{\infty} \left\{ \frac{\frac{M_1^2}{M_i^2} \left(1 - \frac{a_1}{A_1}\right) - 2}{\left[1 - \frac{M_1^2}{M_i^2} \left(1 - \frac{a_1}{A_1}\right)\right]^2} \right\} a_i^2
 \end{aligned} \tag{4.59}$$

By substituting for C in Eq. (4.46), we get

$$\begin{aligned}
 A_i &= \frac{a_i}{1 - \frac{3Q^2 C}{M_i^2}} \\
 &= \frac{a_i}{1 - \frac{3Q^2 M_1^2}{M_i^2} \left(1 - \frac{a_1}{A_1}\right) \sum_{i=1}^{\infty} \left\{ \frac{\frac{M_1^2}{M_i^2} \left(1 - \frac{a_1}{A_1}\right) - 2}{\left[1 - \frac{M_1^2}{M_i^2} \left(1 - \frac{a_1}{A_1}\right)\right]^2} \right\} a_i^2}
 \end{aligned} \tag{4.60}$$

By comparing the denominators in Eqs. (4.58) and (4.60), we get

$$3Q^2 \sum_{i=1}^{\infty} \left\{ \frac{\frac{M_1^2}{M_i^2} \left(1 - \frac{a_1}{A_1}\right) - 2}{\left[1 - \frac{M_1^2}{M_i^2} \left(1 - \frac{a_1}{A_1}\right)\right]^2} \right\} a_i^2 = 1 \tag{4.61}$$

Note that we have ignored the trivial solution corresponding to the initial profile ($A_i = a_i$) in writing Eq. (4.61). This equation can be written in terms of A_i s by substituting for a_i from Eq. (4.58) as

$$3Q^2 \left[\left(1 - \frac{a_1}{A_1}\right) \sum_{i=1}^{\infty} \frac{A_i^2 M_1^2}{M_i^2} - 2 \sum_{i=1}^{\infty} A_i^2 \right] = 1 \tag{4.62}$$

Upon rearranging the terms, we get a closed-form expression for a_1 :

$$a_1 = A_1 \frac{\sum_{i=1}^{\infty} \frac{M_1^2 A_i^2}{M_i^2} - 2 \sum_{i=1}^{\infty} A_i^2 - \frac{1}{3Q^2}}{\sum_{i=1}^{\infty} \frac{M_1^2 A_i^2}{M_i^2}} \quad (4.63)$$

Equations (4.58), (4.61) and (4.63) capture the bilateral relationship between the force-free profiles of a fixed-fixed bistable arch. Equation (4.61) is used for analysis, i.e., to obtain the stressed toggled profile for a given stress-free as-fabricated profile. This equation reduces to a nonlinear equation in a single variable A_1 once the as-fabricated shape (a_i s) is specified. By using Eq. (4.58), the remaining A_i s can be obtained. To design bistable arches for a desired toggled profile, i.e., to obtain the values of a_i s given A_i s, the closed form analytical relation Eq. (4.63) is used. The bistability of the arch-profile pairs obtained from analysis and design problems is checked for sufficiency conditions using Eq. (4.50). Section 4.7 comprises examples using the bilateral relationship for the design and analysis of fixed-fixed arch-profiles. We discuss a few useful insights of the bilateral relationship before that.

4.6.4 Corollaries

In this section, we summarize the results and insights pertaining to the magnitude and sign of the mode weights deduced from the bilateral relationship.

- 1a. *For $i > 1$, $A_i = 0$ implies $a_i = 0$ and vice versa.*

When a_i is zero, Eq. (4.46) becomes

$$A_i(M_i^2 - 3Q^2C) = 0 \quad (4.64)$$

In Section 4.6.2, we showed that $3Q^2C$ cannot be equal to M_i^2 when the arch is in a stable equilibrium state. Thus, Equation (4.64) implies that $A_i = 0$. To prove the converse, we see from Eq. (4.46) that $a_i = 0$ when $A_i = 0$.

- 1b. *The toggled profile of a bistable arch with a symmetric initial profile will also be symmetric and vice versa.*

From Corollary 1a, we know that when $a_m = 0$, the corresponding A_m is also zero for $m = 2, 4, 6, \dots \infty$, i.e., the toggled profile is symmetric when the initial profile is symmetric. Similarly, the converse is also true.

1c. For $i > 1$, $A_i \neq 0$ implies $a_i \neq 0$ and vice versa.

As mentioned before in Result 1a, $3Q^2C$ cannot be equal to M_i^2 such that the resulting toggled profile is stable. Thus, from Eq. (4.46), if a mode weight is non zero in one of the stable states, its corresponding mode weight in the other stable state is also non zero.

1d. Toggled-profile of a bistable arch with asymmetric initial profile will also be asymmetric and vice versa.

If a bistable arch is asymmetric, at least one mode weight corresponding to an asymmetric mode is not zero in its as-fabricated shape. From Corollary 1c, we have that the same mode will be non zero in the other stable state as well.

2a. $(a_1 A_1) < 0$.

This can be deduced from the bilateral relationship for design. The term $\sum_{i=1}^{\infty} \frac{M_1^2 A_i^2}{M_i^2} - 2 \sum_{i=1}^{\infty} A_i^2 - \frac{1}{3Q^2}$ in Eq. (4.63) is negative because $\frac{M_1^2}{M_i^2}$ is always less than 2. Thus, the signs of a_1 and A_1 are different.

2b. $(a_{i>1} A_{i>1}) > 0$. We proved in Section 4.6.2 that $3Q^2C$ should be less than $2.86^2 \pi^2$. This implies that the maximum value of $1 - \frac{a_1}{A_1}$ is less than 1.045 (from Eq. (4.57)). Hence, $\frac{1}{i^2} \left(1 - \frac{a_1}{A_1}\right)$ cannot exceed unity for any value of i . Thus, from Eq. (4.58) we see that the sign of A_i is determined by the sign of a_i and vice versa, for $i > 1$.

3a. (inexact) A_i is approximately equal to a_i for higher values of i .

Corollary 3a is an approximate result that becomes accurate for larger values of i . This result is obtained by neglecting the term $\frac{M_1^2}{M_i^2} \left(1 - \frac{a_1}{A_1}\right)$ in Eq. (4.58). Hence, Eq. (4.58) becomes

$$A_i \approx a_i \tag{4.65}$$

In Section 4.6.4, we observed that $1 - \frac{a_i}{A_i}$ is less than 1.045. Hence, the approximation $a_i \approx A_i$ will have a maximum error of 3.5% if i is greater than 10.

3b. (inexact) For arch-profiles composed of only a_i s with higher values of i ($i \geq m$, where m is the least value of i such that Corollary 3a is valid) along with a_1 , $a_1^2 - 8 \sum_{i=m}^{\infty} a_i^2 - \frac{4}{3Q^2} > 0$ is necessary and sufficient for bistability.

For arch-profiles with only higher mode shapes ($i \geq m$) along with the fundamental mode shape, Corollary 3a is valid for $i \geq m$. By substituting Eq. (4.65) in Eq. (4.61), we get

$$A_1^2 + a_1 A_1 + 2 \sum_{i=m}^{\infty} a_i^2 + \frac{1}{3Q^2} = 0 \quad (4.66)$$

For the arch to be bistable, Eq. (4.66) should have two real roots, i.e., the discriminant needs to be positive. Thus, we have

$$a_1^2 - 8 \sum_{i=m}^n a_i^2 - \frac{4}{3Q^2} > 0 \quad (4.67)$$

4.7 Illustrative Examples

4.7.1 Analysis

The nonlinear form of the bilateral relationship, i.e., Eq. (4.61), is used to obtain the toggled second stable profile of the bistable arch for a given as-fabricated profile. Consider the initial profile specified in Fig. 4.22. As mentioned before, the initial profile consid-

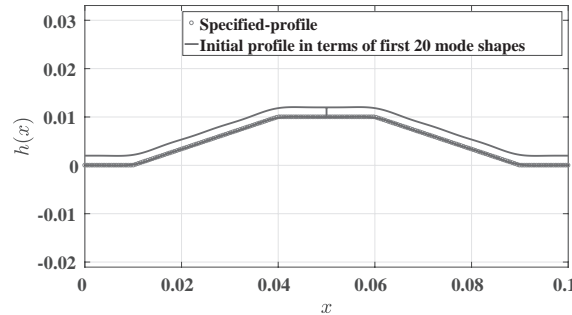


Figure 4.22: Specified and approximated initial profiles

ered here is a double curve to restrict the asymmetric switching mode in the arch. The first step in the analysis is to represent this profile on the basis of buckling mode shapes as in Eq. (4.40); here, the first 20 buckling mode shapes are used for the approximation. Thus, we have the a_i s ($i = 1, 2, \dots, 20$) corresponding to this profile. Note that the number of mode shapes is taken to be 20 on the basis of a convergence analysis. Depending on the arch-profile this number can vary, nonetheless, in this case we observe in Fig. 4.22 that by taking $n = 20$ specified-profile is well approximated. For $h_{mid} = 10$ mm and $t = 0.5$ mm, Q is 20. By numerically solving Eq. (4.61), A_1 is obtained to be -0.5388 .

The remaining A_i s are found using Eq. (4.58). The toggled profile is given in Fig. 4.23. The matrix \mathbf{H} is found to be positive definite. We know that every as-fabricated profile might not exhibit bistability. Such cases would result in \mathbf{H} with negative eigenvalues. When compared to the bistable arch profiles with pinned-pinned boundary conditions, one would come across more fixed-fixed profiles that are not bistable. This can be attributed to the compliance at the ends for a pinned arch compared to a fixed arch. The pinned arch by rotating at the ends reduces the compression energy stored in the second stable state, thus, allowing a broader range of arch-profiles that are bistable.

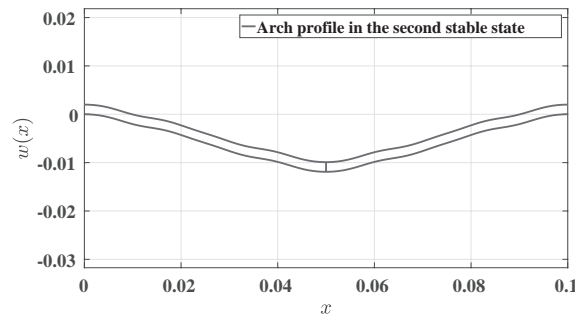


Figure 4.23: Toggled profile corresponding to the initial profile in Fig. 4.22.

In the next example, a quartic polynomial is taken as the initial profile of the arch. The height, $H(X)$ can be expressed as $8X^2(X-1)^2$ as shown in Fig. 4.24. The toggled profile of the arch for $Q = 20$ is given in Fig. 4.25.

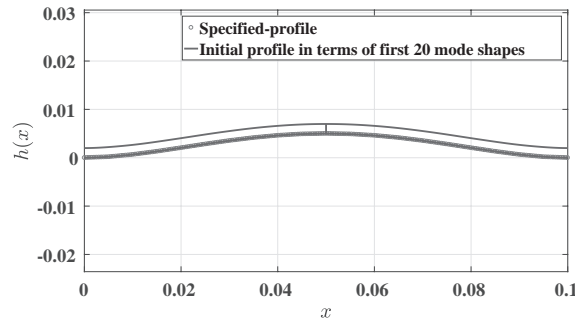


Figure 4.24: As-fabricated profile of the arch.

4.7.2 Design

The bilateral relationship in the form given in Eq. (4.63) is a powerful design tool. Similar to the example in Section 4.7.1, the first step involves representing the desired toggled profile in the form of Eq. (4.41). By taking $Q = 20$, a_i s are obtained from Eqs. (4.58)

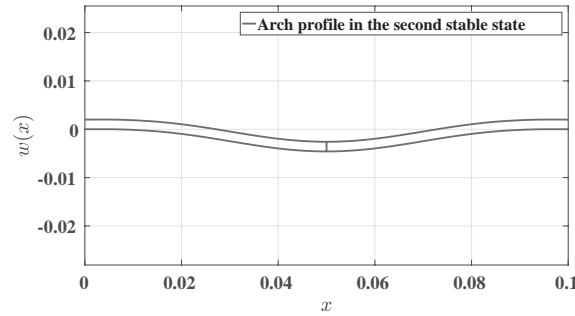


Figure 4.25: Toggled profile corresponding to the initial profile in Fig. 4.24.

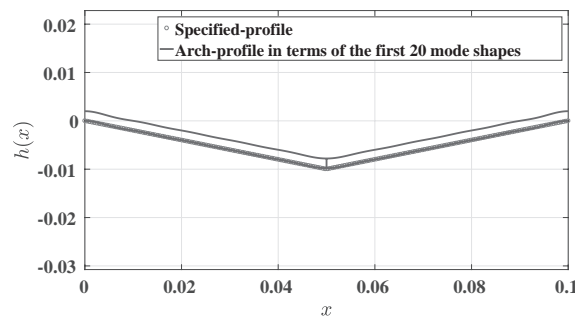


Figure 4.26: Specified arch-profile in the second stable state

and (4.63); the corresponding arch-profile to the toggled profile taken in Fig. 4.26 is given in Fig. 4.27. The positive definitiveness of \mathbf{H} is ensured for bistability.

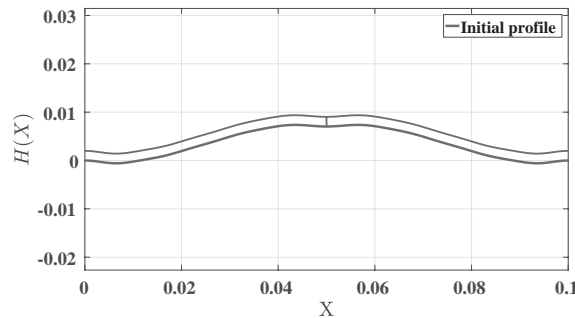


Figure 4.27: Initial profile designed using Eq. (4.63).

Can we design an arch such that the inverted form of the arch-profile considered in Fig. 4.22 is the toggled profile? Such an arch can be used as an initially-curved valve mechanism as shown in Fig. 4.28. By taking the a_i s of the profile in Fig. 4.22 as the A_i s in the design equation Eq. (4.63), the initial profile obtained is shown in Fig. 4.30. Note that the arch-profile in Fig. 4.22 and Fig. 4.29 are stress-free and stressed, respectively.

With the aid of the analytical equations for the stable profiles, arches with specific

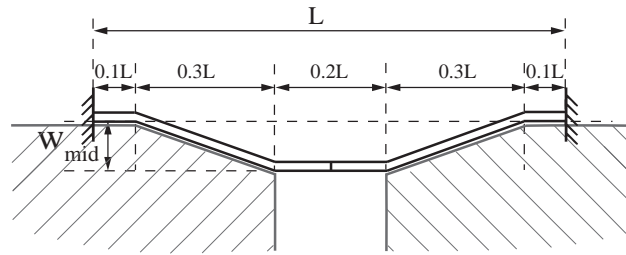


Figure 4.28: Schematic of a bistable valve mechanism.

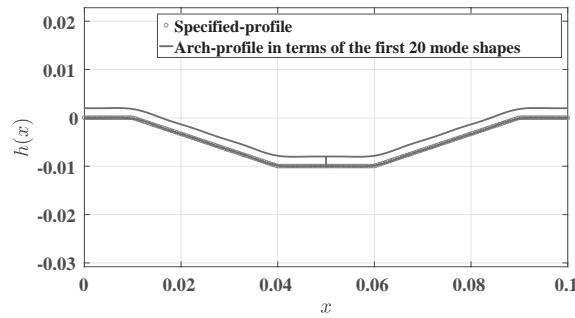


Figure 4.29: Specified arch-profile in the second stable state

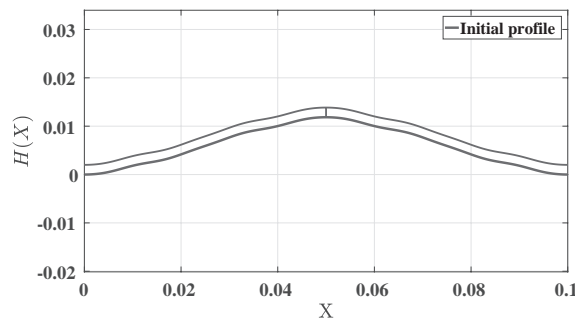


Figure 4.30: Initial profile designed using Eq. (4.63).

changes in slope at any point on the arch can be designed. The points of interest are taken at $X = 0.25$ and $X = 0.75$. For the geometric parameters $h_{mid} = 13.46$ mm $t = 0.5$ mm, and $L = 100$ mm, an enclosing mechanism design using a bistable arch is given in Fig. 4.31. When the arch is in the second stable state, the mechanism forms an enclosure due to a 45° rotation of the vertical arms attached to the initial arch profile. A 3D-printed model of the design is given in Fig. 4.32. Note that all the arch-profiles designed using the analytical equations presented here have zero slopes at the end.

The 3D-printed prototypes of the design examples in their two stable states are given in Fig. 4.33. The shape of the arch-profiles match the analytical prediction. The design cases of the bistable valve and gripper considered are verified using finite element analysis (FEA) and the arch-profiles in the second stable state are compared in Fig. 4.34.

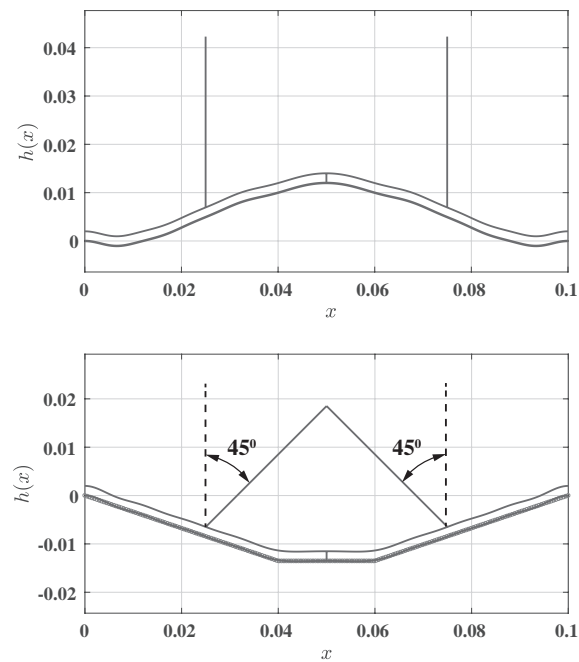


Figure 4.31: Bistable arch with a change of angle of 45° at $x = 0.25$ mm for $h_{mid} = 13.46$ mm $t = 0.5$ mm, and $L = 100$ mm.

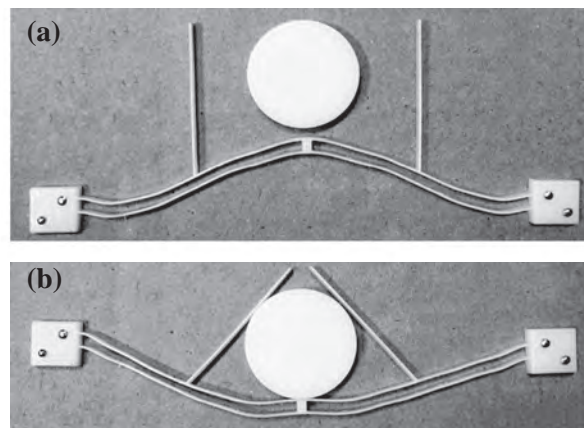
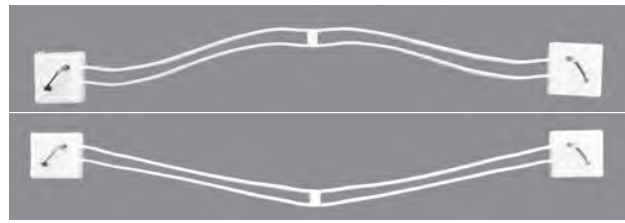
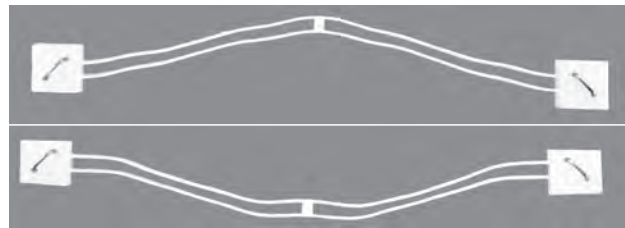


Figure 4.32: 3D-printed gripper in its open (a) and closed (b) configurations.

The solid curve is obtained from the bilateral relationship and the dotted curve is obtained from nonlinear FEA using continuum elements. The analytical prediction and FEA show good agreement, whereas the the 3D-printed profile shows slight deviations from the predicted profile. This is mainly due to the stiffening that happens at the center of the arch due to the interconnection between the arches.



(a)



(b)

Figure 4.33: 3D-printed bistable arches with fixed boundary conditions

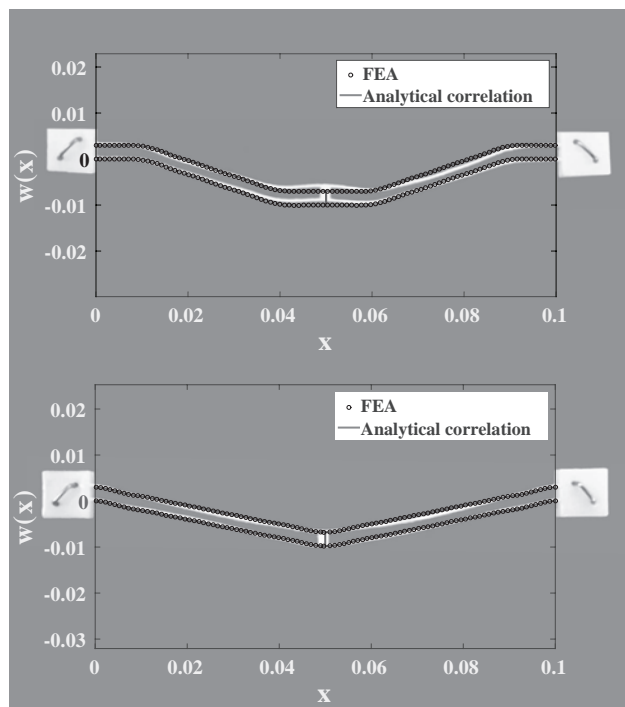


Figure 4.34: Verification of the analytical profiles using FEA and 3D-printed prototypes.

4.8 Closure

Bistable arches find a wide range of applications. Currently, only a limited variety of arch-profiles are used and analyzed. The bilateral relationship of initial and toggled profiles in the two force-free equilibrium states of shallow bistable arches with the pinned-pinned and fixed-fixed boundary conditions derived in this work fills this gap. Here, the initial and toggled profile were considered to be weighted combinations of buckling mode shapes without truncating any terms. Consequently, intricate arch-profiles can be analyzed and designed. The corollaries presented further improve the understanding of the changes in magnitudes and signs of the mode weights of the arch-profile as they switch from one stable state to another. Design examples of bistable arches and mechanisms using bistable arches are presented to illustrate the ease of design using the bilateral relationship. We note that the analytical solutions are insightful in design because they allow visualization of the other shape rather easily. They also indicate whether a given stress-free arch-profile is bistable or not without having to perform finite element analysis.

In the next chapter, we approach bistability in a generalized framework where the arches are spatial. This way of modeling also captures spatial deformations in planar arches. We show a few non-intuitive results for bistable arches that planar analysis fail to capture.

Chapter 5

Analytical modeling of spatial deformation pathways in planar and spatial shallow bistable arches

Synopsis

We analyse spatial bistable arches and present an analytical model incorporating axial, two transverse bending, and torsion energy components. We extend the St. Venant and Michell relationship used in the flexural-torsional buckling of planar arches and use it in modelling spatial arches. We study deformation pathways in spatial arches and their effect on the critical characteristics of bistability and show that not considering spatial deformation leads to incorrect inferences concerning the bistability of planar arches. Thus, this model serves as a generalised framework for the existing analysis on planar arches since they belong to a subset of spatial arches.

5.1 Introduction

Spatial deformation pathways in planar bistable arches reduce switching and switch-back forces. A planar bistable arch can be actuated with an in-plane force so that it remains in its plane throughout as it reaches its other planar stable state. In addition to this planar deformation pathway, the same arch can be actuated to follow a spatial deformation pathway as shown in Fig. 5.1a. A comparison between the force-displacement characteristics corresponding to spatial and planar deformation pathways is given in Fig. 5.1b. Our attempt to understand and analytically model spatial deformation path-

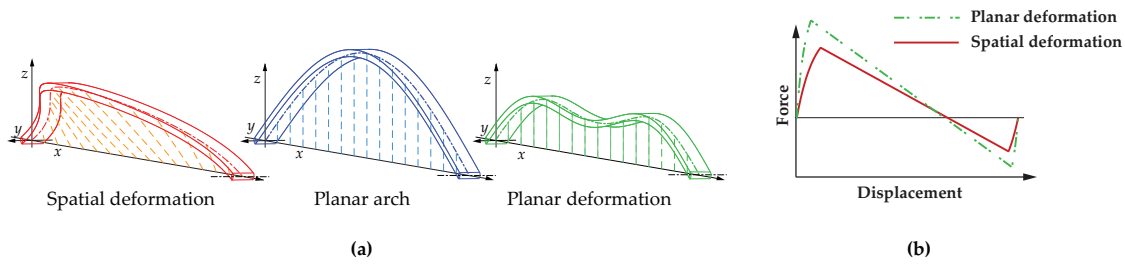


Figure 5.1: (a) Planar and spatial deformation pathways of a planar arch; dashed lines aid visualisation of the curvature of the arch during deformation (b) Switching forces of a spatially-deforming bistable arch are found to be smaller than those of an arch deforming in the plane.

ways in planar bistable arches lead us to a new and general class of structures, namely spatial bistable arches. As shown in Fig. 5.2, the curvature of the spatial arch is not restricted to a single plane. Two varying orthogonal curvatures of the arch can be seen in the reflections of the arch in the xy and xz planes. Spatial arches exhibit only spatial deformation pathways. Spatial arch-profiles of in-between and second stable states of the arch are also given in Fig. 5.2. Since planar arches with spatial deformations belong to a subclass of spatial arches, the analytical work presented in this chapter captures three dimensional deformations in both spatial and planar bistable arches.

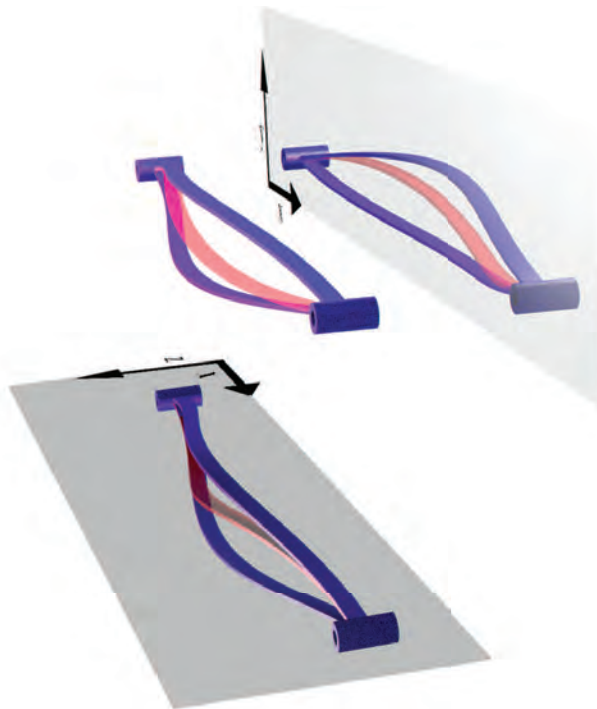


Figure 5.2: A pinned-pinned spatial arch in its as-fabricated stress-free, in-between stressed, and second stressed stable states.

First, using the modified St. Venant and Michell relationship we describe an analytical model that captures spatial deformation in shallow spatial arches that are not stressed in their as-fabricated shape. The model is applicable to arches with varying as-fabricated shapes with fixed-fixed as well as pinned-pinned boundary conditions. Second, we focus on the implications of spatial deformation pathways. We show that these pathways reduce the force required for buckling and post-buckling deformations as compared to planar pathways. In the context of bistability, this is sometimes desirable as it reduces the force required for switching between the equilibrium configurations of the bistable arch. Nonetheless, this also implies that these pathways reduce the stiffness and stability of the arch. Thus, the geometric and material parameters that excessively favor spatial deformations can adversely affect bistability; we illustrate this with examples. Furthermore, we study the effect of eccentric loading on the force-displacement characteristics of spatially deforming arches.

For arches with arbitrary as-fabricated shapes and general boundary conditions, our analytical model improves the understanding of bistability in four ways: (1) analysing spatial bistable arches with reduced switching force; (2) designing planar arches with reduced switching force owing to spatial bistability; (3) eliminating the loss of bistability due to spatial deformation pathways in planar bistable arches; (4) understanding the effect of eccentric loading on switching forces.

5.2 Analytical model for arches that deform spatially

We present an analytical model for spatial deformations in non-planar arches in the post-buckling regime. Such a model also explains the out-of-plane deformations in planar arches. Let us consider a spatial arch with breadth b , depth t , span L , and mid-span height h_{mid} as shown in Fig. 5.3. The projections of the central axis of the as-fabricated stress-free shape of the spatial arch in the xy and xz planes are denoted as $w_0(x)$ and $u_0(x)$, respectively. The projections of the deformed central line of the spatial arch in the xy and xz planes are $w(x)$ and $u(x)$. The initial twist in the cross-section is taken to be zero and the rotational displacement of the cross section is denoted by $\phi(x)$. We

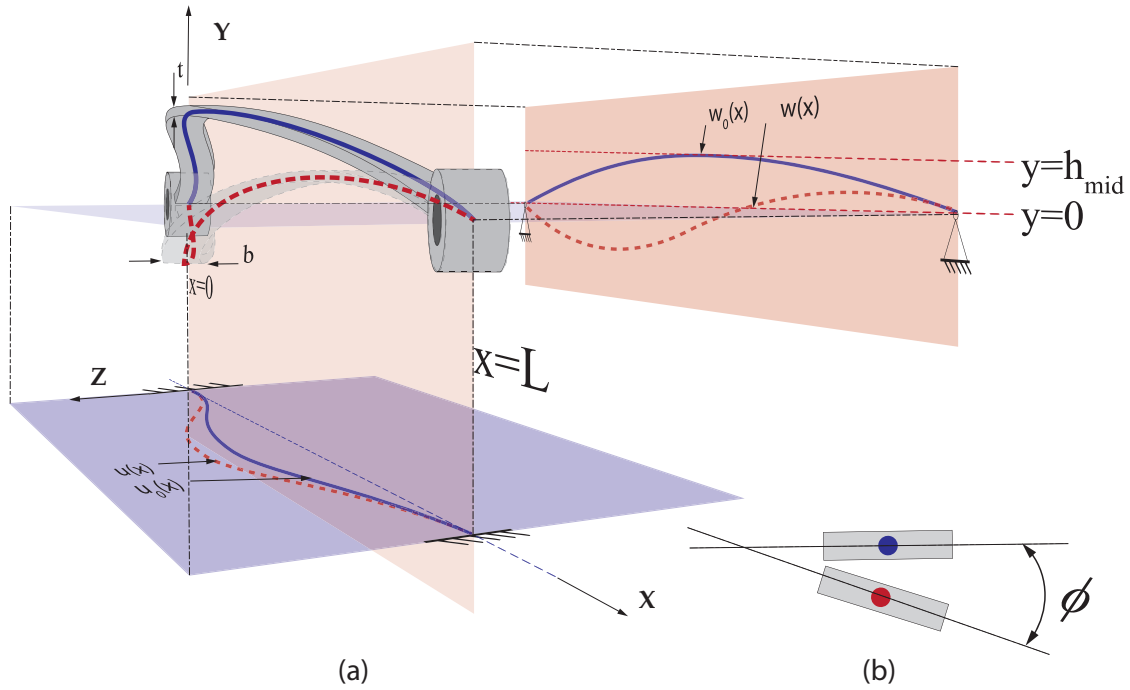


Figure 5.3: A spatial arch with breadth, b , depth, t , span, L , and mid-span height in the xy plane, h_{mid} .

express these displacements as follows:

$$w_0(x) = h_{mid} \sum_{i=1}^{\infty} a_i w_i(x) \quad (5.1)$$

$$u_0(x) = h_{mid} \sum_{i=1}^{\infty} b_i u_i(x) \quad (5.2)$$

$$w(x) = h_{mid} \sum_{i=1}^{\infty} A_i w_i(x) \quad (5.3)$$

$$u(x) = h_{mid} \sum_{i=1}^{\infty} B_i u_i(x) \quad (5.4)$$

$$\phi(x) = \sum_{i=1}^{\infty} C_i \phi_i(x) \quad (5.5)$$

where w_i , u_i , and ϕ_i comprise a basis set that satisfies the boundary conditions of w , u , and ϕ , respectively; in fact, they are the buckling mode shapes of a straight column with corresponding boundary conditions. For the given a_i s and b_i s, we determine the mode weights A_i s, B_i s, and C_i s of the deformed profile by minimizing the potential energy.

5.2.1 Extension of St. Venant and Michell's relationship

Axial compression, transverse bending, out-of-plane bending, and torsional energies are interrelated. We capture this interrelation by extending the St. Venant and Michell's relationship to spatial arches. It is helpful to first understand the relation as presented by St. Venant and Michell for lateral torsional buckling, [Ojalvo et al. \(1969\)](#), in planar arches. This relation, for an arch in the xy plane with curvature κ_{pxy0} deforming out-of-plane with displacement u_p , and rotation of cross-section ϕ_p , the effective change in curvature in the xz plane $\Delta\kappa_{pxz}$ is given as follows:

$$\Delta\kappa_{pxz} = \frac{d^2 u_p}{dx^2} - \phi_p \kappa_{pxy0} \quad (5.6)$$

Note that the subscript p indicates that these equations are only valid for the planar case. Equation (5.6) implies that the effective change in the curvature of projection of the deformed arch-profile, in the xz plane, is a combined effect of the rotation of the cross-section and deformation of the central axis. The first term is the curvature due to the deformation of the arch in the xz plane. Since the coordinates of the deformed central axis of the arch are u_p , the final curvature of the arch is $\frac{d^2 u_p}{dx^2}$. However, the term $\frac{d^2 u_p}{dx^2}$ also includes the contribution from the projection of the curvature of the central axis due to the rotation of the cross-section. For a positive rotation, ϕ_p , this projection has a positive and upward curvature with a magnitude of $\phi_p \kappa_{pxy0}$, the second term in Eq. (5.6). Thus, the effective change in curvature is the difference between these two terms. Intuitively, this is equivalent to the change in the curvature of an arch with an initial curvature $\phi_p \kappa_{pxy0}$ with a deformed profile u_p .

By denoting the curvatures of $w_0(x)$, and $u_0(x)$ as κ_{xy0} , and κ_{xz0} , respectively, the extended St. Venant and Michell's relationship is given by

$$\Delta\kappa_{xz} = \frac{d^2 u}{dx^2} - (\kappa_{xz0} + \phi \kappa_{xy0}) \quad (5.7)$$

$$\Delta\kappa_{xy} = \frac{d^2 w}{dx^2} - (\kappa_{xy0} - \phi \kappa_{xz0}) \quad (5.8)$$

Equation (5.7) is the equivalent of Eq. (5.6) for spatial arches. The extra term κ_{xz0} is due to the out-of-plane curvature of the spatial arch. Similarly, Eq. (5.8) is the change of curvature in the xy plane. However, here the sign of the term $\phi \kappa_{xz0}$ is negative. This is because a positive rotation of the cross-section results in a projection of downward curvature in the xy plane. Note that ϕ is assumed to be small (i.e., $\sin(\phi) \approx \phi$) in Eqs. (5.7) and (5.8). Furthermore, by taking $\kappa_{xz0} = \frac{d^2 u_0}{dx^2}$, $\kappa_{xy0} = \frac{d^2 w_0}{dx^2}$, and ignoring

higher order terms, Eqs. (5.7) and (5.8) are simplified as:

$$\Delta\kappa_{xz} = \frac{d^2u}{dx^2} - (\kappa_{xz0} + \phi\kappa_{xy0}) = \frac{d^2u}{dx^2} - \frac{d^2u_0}{dx^2} - \phi\frac{d^2w_0}{dx^2} \quad (5.9)$$

$$\Delta\kappa_{xy} = \frac{d^2w}{dx^2} - (\kappa_{xy0} - \phi\kappa_{xz0}) = \frac{d^2w}{dx^2} - \frac{d^2w_0}{dx^2} + \phi\frac{d^2u_0}{dx^2} \quad (5.10)$$

5.2.2 Total potential energy

For an arch with Young's modulus E , and a second moment of area for a rectangular cross-section about the z -axis and y -axis, I_z and I_y , the strain energy due to bending is given by

$$SE_b = \frac{EI_z}{2} \int_0^L (\Delta\kappa_{xy})^2 dx + \frac{EI_y}{2} \int_0^L (\Delta\kappa_{xz})^2 dx \quad (5.11)$$

By substituting Eqs. (5.9) and (5.10) into Eq. (5.11), the bending strain energy becomes

$$SE_b = \frac{EI_z}{2} \int_0^L \left(\frac{d^2w}{dx^2} - \frac{d^2w_0}{dx^2} + \phi\frac{d^2u_0}{dx^2} \right)^2 dx \quad (5.12)$$

$$+ \frac{EI_y}{2} \int_0^L \left(\frac{d^2u}{dx^2} - \frac{d^2u_0}{dx^2} - \phi\frac{d^2w_0}{dx^2} \right)^2 dx \quad (5.13)$$

We note in Eq. (5.12) that the u , w , and ϕ contribute to bending strain energy in the preceding equation. As the shallow arch deforms, the axial force, f , leads to compression energy, SE_c , which is given by

$$SE_c = \frac{1}{2}f(s_{initial} - s) \quad (5.14)$$

where s is the length of the arch as it deforms and $s_{initial}$, the as-fabricated arc-length of the arch. Here, we assume that the axial displacement of the arch is uniform along the length of the arch. This assumption gives accurate results in planar arches and in spatial arches as we show in subsequent sections. Thus, for a linear elastic material, we write

$$f = Ebt \left(\frac{s_{initial} - s}{L} \right) \quad (5.15)$$

By assuming the arch to be shallow, i.e., $\left(\frac{dw_0}{dx}\right)^2 \ll 1$ and $\left(\frac{du_0}{dx}\right)^2 \ll 1$, arc-lengths can be approximated as

$$s = \int_0^L \sqrt{1 + \left(\frac{dw}{dx}\right)^2 + \left(\frac{du}{dx}\right)^2} dx$$

$$\approx \int_0^L \left[1 + \frac{1}{2} \left(\frac{dw}{dx}\right)^2 + \frac{1}{2} \left(\frac{du}{dx}\right)^2 \right] dx \quad (5.16)$$

$$s_{initial} \approx \int_0^L \left[1 + \frac{1}{2} \left(\frac{dw_0}{dx}\right)^2 + \frac{1}{2} \left(\frac{du_0}{dx}\right)^2 \right] dx \quad (5.17)$$

The rotation of the cross-sections, ϕ , results in torsional strain energy given by

$$SE_t = \frac{GJ}{2} \int_0^L \left(\frac{d\phi}{dx}\right)^2 dx \quad (5.18)$$

where g is the shear modulus and J is the polar moment of inertia. A point force, F , is applied at the center of the arch at a point eccentric to the xy plane by e . The displacements of the midpoint along the y -axis and z -axis, and the work potential due to these displacements are given by

$$\delta_y = w_0 \left(\frac{L}{2}\right) - w \left(\frac{L}{2}\right) + e\phi \left(\frac{L}{2}\right) \quad (5.19)$$

$$WP = -F\delta_y \quad (5.20)$$

The potential energy, PE , includes bending, compression, and torsional energies, and the work potential. Thus the total potential energy can be expressed as

$$PE = SE_b + SE_c + SE_t + WP \quad (5.21)$$

The equilibrium equations are obtained by minimizing the potential energy with respect to the unknown mode weights, A_i s, B_i s, and C_i s as follows:

$$\frac{dPE}{dA_i} = 0 \quad (5.22)$$

$$\frac{dPE}{dB_i} = 0 \quad (5.23)$$

$$\frac{dPE}{dC_i} = 0 \quad (5.24)$$

The analytical solutions for Eqs. (5.22) to (5.24) are obtained, as discussed later, for five unknown mode weights. In the subsequent sections, we consider these analytical solutions for varying boundary and loading conditions as well as for as-fabricated profiles.

5.3 Spatial arches

In this section, we analyse spatial arches with pinned-pinned and fixed-fixed boundary conditions and understand the deformation pathways. An example problem is presented for discussing the post-buckling analysis for each of the boundary conditions.

5.3.1 Hinged and fixed support

Consider an arch with pinned-pinned and fixed-fixed boundary conditions in the xy and xz planes, respectively. As mentioned before, the buckling mode shapes of a column with similar boundary conditions are taken as the basis functions to represent the arch-profile as follows:

$$w_i(x) = \sin(i\pi \frac{x}{L}) \quad i = 1, 2, 3, \dots \quad (5.25)$$

$$u_j(x) = \begin{cases} 1 - \cos(M_j \frac{x}{L}) & j = 1, 3, 5 \dots \\ 1 - 2\frac{x}{L} - \cos(M_j \frac{x}{L}) + 2\frac{\sin(M_j \frac{x}{L})}{M_j} & j = 2, 4, 6 \dots \end{cases} \quad (5.26)$$

$$M_j = \begin{cases} (j + 1)\pi & j = 1, 3, 5 \dots \\ 2.86\pi, 4.92\pi, 6.94\pi \dots & j = 2, 4, 6 \dots \end{cases} \quad (5.27)$$

$$\phi_k(x) = \begin{cases} 1 - \cos(M_k \frac{x}{L}) & k = 1, 3, 5 \dots \\ 1 - 2\frac{x}{L} - \cos(M_k \frac{x}{L}) + 2\frac{\sin(M_k \frac{x}{L})}{M_k} & k = 2, 4, 6 \dots \end{cases} \quad (5.28)$$

$$M_k = \begin{cases} (k + 1)\pi & k = 1, 3, 5 \dots \\ 2.86\pi, 4.92\pi, 6.94\pi \dots & k = 2, 4, 6 \dots \end{cases} \quad (5.29)$$

Note that M_j and M_k for $j = k = 2, 4, 6, \dots$ satisfy $\tan(\frac{M_j}{2}) = \frac{M_j}{2}$.

We consider a class of spatial arches with as-fabricated shapes given by

$$w_0(x) = h_{mid} (a_1 w_1(x) + a_2 w_2(x) + a_3 w_3(x)) \quad (5.30)$$

$$u_0(x) = h_{mid} b_1 u_1(x) \quad (5.31)$$

The mode shapes used for describing the as-fabricated shapes would also be present in the basis set of the deformed profile. Thus, for the initial profiles given by Eqs. (5.30) and (5.31), the first three mode shapes are used to approximate the deformations in the xy plane and one mode shape is used to approximate the deformed profile in the xz plane as follows:

$$w(x) = h_{mid} (A_1 w_1(x) + A_2 w_2(x) + A_3 w_3(x)) \quad (5.32)$$

$$u(x) = h_{mid} B_1 u_1(x) \quad (5.33)$$

$$\phi(x) = C_1 \phi_1(x) \quad (5.34)$$

Note that with this choice of basis functions we have six unknowns, for which analytical solutions are obtained. The applied load is resisted by the stiffness of the arch, which results in the arch having an undulating curvature in the loading plane. Hence, we assume a larger number of mode shapes to express the deformed arch-profile in the loading plane compared to the plane perpendicular to it, where undulations are absent. Therefore, in this case, we use three mode shapes to capture the in-plane deformation and one mode shape each for both out-of-plane deformation as well as rotation.

The bending strain energy, axial compression energy, torsional energy, and work potential are obtained by substituting Eqs. (5.30) to (5.34) in Eq. (5.12), Eq. (5.14), Eq. (5.18), and Eq. (5.20), respectively.

$$\begin{aligned}
SE_b &= \frac{EI_z}{2} \int_0^L \left(\frac{d^2 w_0}{dx^2} - \frac{d^2 w}{dx^2} + \phi \frac{d^2 u_0}{dx^2} \right)^2 dx + \frac{EI_y}{2} \int_0^L \left(\frac{d^2 u_0}{dx^2} - \frac{d^2 u}{dx^2} - \phi \frac{d^2 w_0}{dx^2} \right)^2 dx \\
&= \frac{Ebh_{mid}^2 t^3}{24L^3} \pi^3 \left(\frac{\pi A_1^2}{2} - \frac{64A_1 C_1 b_1}{5} - 1\pi A_1 a_1 + 8\pi A_2^2 - 16\pi A_2 a_2 + \frac{81\pi A_3^2}{2} \right) + \\
&\quad \frac{Ebh_{mid}^2 t^3}{24L^3} \left(\frac{3264A_3 C_1 b_1}{35} - 81\pi A_3 a_3 + 14\pi C_1^2 b_1^2 + \frac{64C_1 a_1 b_1}{5} - \frac{3264C_1 a_3 b_1}{35} \right) + \\
&\quad \frac{Ebh_{mid}^2 t^3}{24L^3} \left(\frac{\pi a_1^2}{2} + 8\pi a_2^2 + \frac{81\pi a_3^2}{2} \right) - \frac{Eb^3 h_{mid}^2 t \pi^3}{24L^3} \left(\frac{45\pi C_1^2 a_1 a_3}{4} + 10\pi C_1^2 a_2^2 \right) \\
&\quad \frac{Eb^3 h_{mid}^2 t \pi^3}{24L^3} \left(8\pi B_1^2 + \frac{64B_1 C_1 a_1}{5} - \frac{3264B_1 C_1 a_3}{35} - 16\pi B_1 b_1 + \frac{5\pi C_1^2 a_1^2}{4} \right) + \\
&\quad \frac{Eb^3 h_{mid}^2 t \pi^3}{24L^3} \left(\frac{243\pi C_1^2 a_3^2}{4} - \frac{64C_1 a_1 b_1}{5} + \frac{3264C_1 a_3 b_1}{35} + 8\pi b_1^2 \right) \quad (5.35)
\end{aligned}$$

$$\begin{aligned}
s &= \int_0^L \left[1 + \frac{1}{2} \left(\frac{dw}{dx} \right)^2 + \frac{1}{2} \left(\frac{du}{dx} \right)^2 \right] dx \\
&= L + \frac{B_1^2 h_{mid}^2 \pi^2}{L} + \frac{h_{mid}^2 \pi^2 (A_1^2 + 4A_2^2 + 9A_3^2)}{4L} \quad (5.36)
\end{aligned}$$

$$\begin{aligned}
s_{initial} &= \int_0^L \left[1 + \frac{1}{2} \left(\frac{dw_0}{dx} \right)^2 + \frac{1}{2} \left(\frac{du_0}{dx} \right)^2 \right] dx \\
&= L + \frac{b_1^2 h_{mid}^2 \pi^2}{L} + \frac{h_{mid}^2 \pi^2 (a_1^2 + 4a_2^2 + 9a_3^2)}{4L} \quad (5.37)
\end{aligned}$$

$$\begin{aligned}
SE_c &= \frac{1}{2} p (s_{initial} - s) \\
&= \frac{Ebh_{mid}^4 t \pi^4 (A_1^2 + 4A_2^2 + 9A_3^2 + 4B_1^2 - a_1^2 - 4a_2^2 - 9a_3^2 - 4b_1^2)^2}{32L^3} \quad (5.38)
\end{aligned}$$

$$\begin{aligned}
SE_t &= \frac{GJ}{2} \int_0^L \left(\frac{d\phi}{dx} \right)^2 dx \\
&= \frac{C_1^2 GJ \pi^2}{L} \quad (5.39)
\end{aligned}$$

$$\begin{aligned}\delta_y &= w_0 \left(\frac{1}{2} \right) - w \left(\frac{1}{2} \right) - e\phi \left(\frac{L}{2} \right) \\ &= -2C_1e - h_{mid}(A_1 - A_3) + h_{mid}(a_1 - a_3)\end{aligned}\quad (5.40)$$

$$\begin{aligned}WP &= -F\delta_y \\ &= -F(-2C_1e - h_{mid}(A_1 - A_3) + h_{mid}(a_1 - a_3))\end{aligned}\quad (5.41)$$

And the total potential energy is

$$PE = SE_b + SE_c + SE_t + WP \quad (5.42)$$

To obtain the F - δ_y characteristics we solve for six unknowns namely, A_1 , A_2 , A_3 , B_1 , C_1 , and F using five equilibrium equations obtained by minimizing the total potential energy with respect to each of the unknown mode weights (i.e., Eqs. (5.22) to (5.24)) and Eq. (5.19). By substituting, Eqs. (5.30) to (5.34) in Eq. (5.21), the equilibrium equations can be expressed as:

$$\begin{aligned}\frac{dPE}{dA_1} &= Fh_{mid} - \frac{Ebh_{mid}^2t^3\pi^3 \left(\frac{64C_1b_1}{5} + \pi a_1 - \pi A_1 \right)}{24L^3} + \\ &\frac{A_1Ebh_{mid}^4t\pi^4 (A_1^2 + 4A_2^2 + 9A_3^2 + 4B_1^2 - a_1^2 - 4a_2^2 - 9a_3^2 - 4b_1^2)}{8L^3} = 0\end{aligned}\quad (5.43)$$

$$\begin{aligned}\frac{dPE}{dA_2} &= \frac{2Ebh_{mid}^2t^3\pi^4 (A_2 - a_2)}{3L^3} + \\ &\frac{A_2Ebh_{mid}^4t\pi^4 (A_1^2 + 4A_2^2 + 9A_3^2 + 4B_1^2 - a_1^2 - 4a_2^2 - 9a_3^2 - 4b_1^2)}{2L^3} = 0\end{aligned}\quad (5.44)$$

$$\begin{aligned}\frac{dPE}{dA_3} &= \frac{Ebh_{mid}^2t^3\pi^3 \left(\frac{3264C_1b_1}{35} - 81\pi a_3 + 81\pi A_3 \right)}{24L^3} - Fh_{mid} + \\ &\frac{9A_3Ebh_{mid}^4t\pi^4 (A_1^2 + 4A_2^2 + 9A_3^2 + 4B_1^2 - a_1^2 - 4a_2^2 - 9a_3^2 - 4b_1^2)}{8L^3} = 0\end{aligned}\quad (5.45)$$

$$\frac{dPE}{dB_1} = \frac{Eb^3h_{mid}^2t\pi^3 \left(\frac{64C_1a_1}{5} - \frac{3264C_1a_3}{35} - 16\pi b_1 + 16\pi B_1 \right)}{24L^3} + \frac{B_1Ebh_{mid}^4t\pi^4 \left(A_1^2 + 4A_2^2 + 9A_3^2 + 4B_1^2 - a_1^2 - 4a_2^2 - 9a_3^2 - 4b_1^2 \right)}{2L^3} = 0 \quad (5.46)$$

$$\begin{aligned} \frac{dPE}{dC_1} &= \frac{2C_1GJ\pi^2}{L} + 2Fe \\ &+ \frac{Ebb_1h_{mid}^2t^3\pi^3 (816A_3 - 112A_1 + 112a_1 - 816a_3 + 245\pi C_1b_1)}{210L^3} \\ &+ \frac{Eb^3h_{mid}^2t\pi^3}{24L^3} \left(\frac{64B_1a_1}{5} - \frac{3264B_1a_3}{35} - \frac{64a_1b_1}{5} + \frac{3264a_3b_1}{35} + \frac{5\pi C_1a_1^2}{2} \right) \\ &+ \frac{Eb^3h_{mid}^2t\pi^3}{24L^3} (20\pi C_1a_2^2) + \frac{Eb^3h_{mid}^2t\pi^3}{24L^3} \left(\frac{243\pi C_1a_3^2}{2} - \frac{45\pi C_1a_1a_3}{2} \right) = 0 \end{aligned} \quad (5.47)$$

To understand the nature of deformations, let us take the as-fabricated shape to constitute only the fundamental buckling mode shape, i.e., only the first mode shape, in both the planes of the arch. So, we substitute $a_1 = 1$, $b_1 = 0.5$, $h_{mid} = 5$ mm, $b = 2$ mm, $t = 0.5$ mm, $L = 100$ mm, and the remaining a_i s and e are taken to be zero in Eqs. (5.19) and (5.43) to (5.47). The E and ν of the material are taken as 2.1 GPa and 0.3, respectively. We solve for F using Eqs. (5.43) to (5.47), for δ_y ranging from 0 mm to twice the height of the arch, i.e., 10 mm. The force-displacement characteristics obtained after ignoring complex solutions are shown in Fig. 5.4a.

In Fig. 5.4a, the points O and T refer to the first and second stable states of the arch, respectively. Corresponding to each combination of paths between O and T, there are multiple deformation pathways that the arch can take to switch between these stable states. Note that on pathways OABCFHIT, OABDEFHIT, and OABDGHIT the arch switches symmetrically, i.e., with $A_2 = 0$. And it switches asymmetrically along OACEGIT.

It is not straightforward to predict the preferred deformation pathway from the F - δ_y curves in Fig. 5.4a. We infer this by visualizing the potential energy landscape of the arch given in Fig. 5.4c. Each curve in the landscape corresponds to the potential energy curve along δ_y for a constant force. The extremum of the curve is the equilibrium position of the arch for the assumed force value. Hence, when there are multiple pathways having the same force value for a given displacement, there will be as many extrema for that displacement. Thus, by generating potential energy curves for the force values in

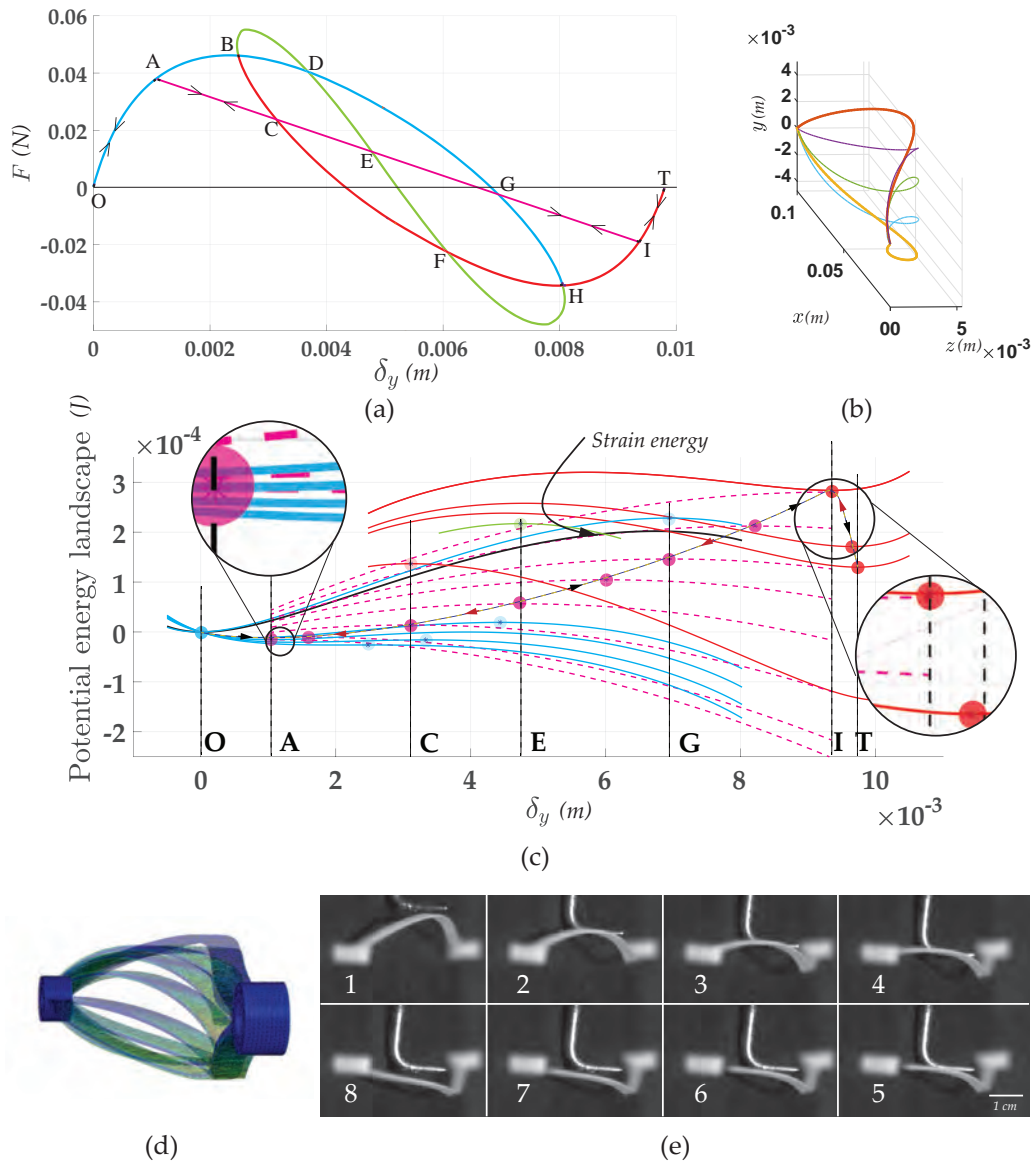


Figure 5.4: (a) Force-displacement characteristics, (b) asymmetric deformation pathway, (c) potential energy landscape for the OACEGIT pathway, (d) deformation pathway from ABAQUS, and (e) time-lapse using high-speed photography (the hook that pushed the arch can be seen in the figures) for a spatial bistable arch with pinned-pinned boundary conditions.

the F - δ_y curve, each deformation pathway can be compared by observing the locations of the extrema across these curves. The solid curves (cyan) passing through point O in Fig. 5.4c correspond to the force-displacement curve OABDGH. And the solid curves (red) passing through the displacement at point T follow the force pathway TIHFCB. The dashed curves (magenta) are for the force values along ACEGI and the short green curve passing through E corresponds to the BDEFH pathway.

The points of extrema on the curves in Fig. 5.4c are annotated with a circular marker. It is helpful to visualise the marker to be a ball on the hill or valley formed by the potential energy curve. When the arch is in the stable equilibrium state at O, the force is zero; so, the ball is resting on the black solid curve (labeled the strain energy) at O. The ball rolls along the minima on cyan curves from point O to point A. Since there are two pathways for the force value at point A, the ball has the option to either continue rolling on the extrema of solid curves or jump to the maxima on the dashed curve. In Fig. 5.4c, we observe that the dashed potential energy curve at A (an enlarged view is shown in the inset) is positioned below the solid curve. Thus, the ball rolls from the minimum on the solid curve to the maxima on the dashed curve. It continues on the dashed curve until I, where the asymmetric solution ceases to exist. Note that the solution pathway does not change at the points C, E, and G since the potential energy of the respective intersecting pathways is larger than the potential energy of asymmetric deformation pathway ACEGI at these points. Hence, the pathway that the arch takes is OACEGIT. That is to say the arch deforms symmetrically (OA and IT) near its stable states and asymmetrically (ACEGI) in between, as shown in Fig. 5.4b. The predicted deformation pathway from the model is reproduced using finite element analysis (FEA) software ABAQUS (ABAQUS (2015)), in Fig. 5.4d. See Section 5.5 for a quantitative validation using FEA. Furthermore, a 3D-printed prototype switching asymmetrically along OACEGIT is depicted in Fig. 5.4e using high-speed photography. The prototype is made using Verowhite, a material used in the Objet260 Connex 3D-printer. The deformed configurations were captured using a high-speed camera, Photron SA5, at the speed of 2000 frames per second.

Now, if we consider the switch-back deformation of the arch, similar arguments are valid as the arch retraces the path while switching back and follows TIGECAO. However, this is not always the case; bistable arches can switch and switch-back along two different pathways. Let us consider a case where the asymmetric mode of switching is constrained, i.e., the arch cannot deform along the pathway ACEGI anymore. Hence, the arch can only take the deformation pathways shown in Fig. 5.5a. Let us observe the implications of this restriction in the potential energy landscape given in Fig. 5.5b. The ball starts from point O on the solid cyan curve and continues to deform along the curve OABDGH since the extrema on the BCFHIT pathway are at a higher potential energy at B. The pathway does not change at point D too since the potential energy corresponding to BDEFH is at a larger value. At point H, it switches to the pathway BCFHIT and achieves the second stable state along the curve HIT. While switching back, the arch

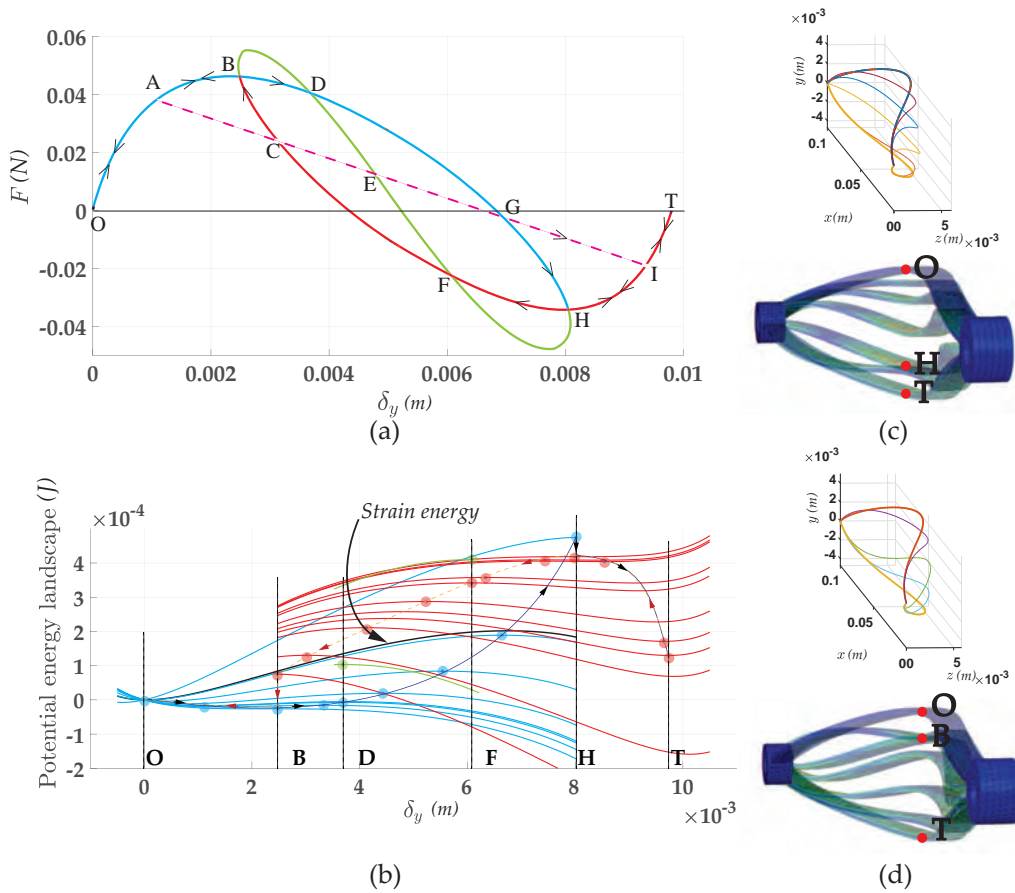


Figure 5.5: (a) Force-displacement characteristics, (b) potential energy landscape, (c) time-lapses of switching and (d) switch-back for symmetric deformation pathways of a pinned-pinned spatial bistable arch.

retraces the switching curve till point H since there is no other pathway the arch can assume until this point. At point H, since the pathway HGDBAO is at a higher potential energy, the ball continues to roll along TIHFCB. At point B, it returns to BAO and reaches the initial stress-free at point O. Again, note that the pathway does not change due to HFEDB at point F. Thus, the pathways for switching and switch-back are OAB-DGHIT and TIHFCBAO, respectively. The time lapses of arch switching and switching-back from the model and ABAQUS are given in Fig. 5.4c and Fig. 5.4d, respectively. The FEA simulation in ABAQUS is carried out with a symmetric constraint with respect to a plane parallel to the yz plane passing through the mid-span of the arch. A physical intuition for the lack of smoothness in the force-displacement characteristics at point H while switching, and at point B while switching back, is evident in these time lapses. At these points, the curvature of the arch snaps symmetrically and flips its curvature—a sudden movement—resulting in sharp points on the F - δ_y curve. In the next subsection, we consider spatial bistable arches with fixed-fixed boundary conditions. For the sake of

brevity, we restrict our discussion to the force-displacement characteristics and resulting deformation pathways without examining into their potential energy landscape.

5.3.2 Fixed fixed support

For a spatial arch with fixed supports, deformations in both the xy and xz planes have fixed-fixed boundary conditions. Hence, similar to the case of the pinned-pinned arch, u_j and ϕ_k are taken as Eqs. (5.26) and (5.28), respectively, and w_i as:

$$w_i(x) = \begin{cases} 1 - \cos(M_i \frac{x}{L}) & i = 1, 3, 5 \dots \\ 1 - 2\frac{x}{L} - \cos(M_i \frac{x}{L}) + 2\frac{\sin(M_i \frac{x}{L})}{M_i} & i = 2, 4, 6 \dots \end{cases} \quad (5.48)$$

$$M_i = \begin{cases} (i + 1)\pi & i = 1, 3, 5 \dots \\ 2.86\pi, 4.92\pi, 6.94\pi \dots & i = 2, 4, 6 \dots \end{cases} \quad (5.49)$$

We consider fixed arches with first harmonics in their as-fabricated shapes given by:

$$w_0(x) = h_{mid} (a_1 w_1(x) + a_2 w_2(x) + a_3 w_3(x)) \quad (5.50)$$

$$u_0(x) = h_{mid} b_1 u_1(x) \quad (5.51)$$

$$w(x) = h_{mid} (A_1 w_1(x) + A_2 w_2(x) + A_3 w_3(x)) \quad (5.52)$$

$$u(x) = h_{mid} B_1 u_1(x) \quad (5.53)$$

$$\phi(x) = C_1 \phi_1(x) \quad (5.54)$$

The equilibrium equations obtained by minimizing the potential energy Eq. (5.21) and simplifying using Eqs. (5.50) to (5.54) can be written as follows:

$$\begin{aligned} \frac{dPE}{dA_1} = & 2Fh_{mid} - \frac{2Ebh_{mid}^2 t^3 \pi^4 (a_1 - A_1 + C_1 b_1)}{3L^3} + \frac{2A_1 Ebh_{mid}^4 t \pi^2 (B_1^2 - b_1^2) \pi^2}{L^2 L} + \\ & \frac{A_1 Ebh_{mid}^4 t \pi^2}{L^2} \left(\frac{2\pi^2 A_1^2 - 4A_2^2 + 8\pi^2 A_3^2}{L} - \frac{A_2^2 M_2^2 (\cos(M_2) + 3)}{2L (\cos(M_2) - 1)} \right) - \\ & \frac{A_1 Ebh_{mid}^4 t \pi^2}{L^2} \left(\frac{2\pi^2 a_1^2 - 4a_2^2 + 8\pi^2 a_3^2}{L} - \frac{M_2^2 a_2^2 (\cos(M_2) + 3)}{2L (\cos(M_2) - 1)} \right) = 0 \end{aligned} \quad (5.55)$$

$$\begin{aligned}
 \frac{dPE}{dA_2} = & \frac{EM_2^4bh_{mid}^2t^3(A_2 - a_2)}{24L^3} - \\
 & \frac{A_2Ebh_{mid}^4t(8\cos(M_2) + 3M_2^2 + M_2^2\cos(M_2) - 8)}{4L^2(\cos(M_2) - 1)} \left(\frac{2\pi^2a_1^2 - 4a_2^2 + 8\pi^2a_3^2}{L} \right) + \\
 & \frac{A_2Ebh_{mid}^4t(8\cos(M_2) + 3M_2^2 + M_2^2\cos(M_2) - 8)}{4L^2(\cos(M_2) - 1)} \left(\frac{M_2^2a_2^2(\cos(M_2) + 3)}{2L(\cos(M_2) - 1)} \right) - \\
 & \frac{A_2Ebh_{mid}^4t(8\cos(M_2) + 3M_2^2 + M_2^2\cos(M_2) - 8)}{4L^2(\cos(M_2) - 1)} \left(\frac{2\pi^2A_1^2 - 4A_2^2 + 8\pi^2A_3^2}{L} \right) + \\
 & \frac{A_2Ebh_{mid}^4t(8\cos(M_2) + 3M_2^2 + M_2^2\cos(M_2) - 8)}{4L^2(\cos(M_2) - 1)} \left(\frac{A_2^2M_2^2(\cos(M_2) + 3)}{2L(\cos(M_2) - 1)} \right) - \\
 & \frac{A_2Ebh_{mid}^4t(8\cos(M_2) + 3M_2^2 + M_2^2\cos(M_2) - 8)}{4L^2(\cos(M_2) - 1)} \left(\frac{2B_1^2\pi^2}{L} - \frac{2b_1^2\pi^2}{L} \right) = 0
 \end{aligned} \tag{5.56}$$

$$\begin{aligned}
 \frac{dPE}{dA_3} = & \frac{4Ebh_{mid}^2t^3\pi^4(8A_3 - 8a_3 + C_1b_1)}{3L^3} + \\
 & \frac{4A_3Ebh_{mid}^4t\pi^2}{L^2} \left(\frac{2\pi^2A_1^2 - 4A_2^2 + 8\pi^2A_3^2}{L} - \frac{A_2^2M_2^2(\cos(M_2) + 3)}{2L(\cos(M_2) - 1)} \right) - \\
 & \frac{4A_3Ebh_{mid}^4t\pi^2}{L^2} \left(\frac{2\pi^2a_1^2 - 4a_2^2 + 8\pi^2a_3^2}{L} - \frac{M_2^2a_2^2(\cos(M_2) + 3)}{2L(\cos(M_2) - 1)} \right) + \\
 & \frac{4A_3Ebh_{mid}^4t\pi^2}{L^2} \left(\frac{2B_1^2\pi^2}{L} - \frac{2b_1^2\pi^2}{L} \right) = 0
 \end{aligned} \tag{5.57}$$

$$\begin{aligned}
 \frac{dPE}{dB_1} = & \frac{2Eb^3h_{mid}^2t\pi^4(B_1 - b_1 + C_1a_1 - 2C_1a_3)}{3L^3} + \frac{B_1Ebh_{mid}^4t\pi^2}{L^2} \left(\frac{2B_1^2\pi^2}{L} - \frac{2b_1^2\pi^2}{L} \right) \\
 & \frac{B_1Ebh_{mid}^4t\pi^2}{L^2} \left(\frac{2\pi^2A_1^2 - 4A_2^2 + 8\pi^2A_3^2}{L} - \frac{A_2^2M_2^2(\cos(M_2) + 3)}{2L(\cos(M_2) - 1)} \right) - \\
 & \frac{B_1Ebh_{mid}^4t\pi^2}{L^2} \left(\frac{2\pi^2a_1^2 - 4a_2^2 + 8\pi^2a_3^2}{L} - \frac{M_2^2a_2^2(\cos(M_2) + 3)}{2L(\cos(M_2) - 1)} \right) = 0
 \end{aligned} \tag{5.58}$$

$$\begin{aligned}
 \frac{dPE}{dC_1} = & 2Fe + \frac{2C_1 G J \pi^2}{L} + \frac{E b b_1 h_{mid}^2 t^3 \pi^4 (8A_3 - 4A_1 + 4a_1 - 8a_3 + 7C_1 b_1)}{6L^3} + \\
 & \frac{E b^3 h_{mid}^2 t}{96L^3 \sin\left(\frac{M_2}{2}\right)^2 (M_2^4 - 5\pi^2 M_2^2 + 4\pi^4)} (6C_1 M_2^8 a_2^2 - 30C_1 M_2^6 a_2^2 \pi^2) + \\
 & \alpha (256B_1 a_1 \pi^8 - 512B_1 a_3 \pi^8 - 256a_1 b_1 \pi^8 + 512a_3 b_1 \pi^8 + 448C_1 a_1^2 \pi^8) - \\
 & \alpha (560C_1 M_2^2 a_1^2 \pi^6 + 112C_1 M_2^4 a_1^2 \pi^4 + 24C_1 M_2^4 a_2^2 \pi^4 - 7680C_1 M_2^2 a_3^2 \pi^6) + \\
 & \alpha (1536C_1 M_2^4 a_3^2 \pi^4 - 2048C_1 a_1 a_3 \pi^8 - 320B_1 M_2^2 a_1 \pi^6 + 64B_1 M_2^4 a_1 \pi^4) + \\
 & \alpha (640B_1 M_2^2 a_3 \pi^6 - 128B_1 M_2^4 a_3 \pi^4 + 320M_2^2 a_1 b_1 \pi^6 - 64M_2^4 a_1 b_1 \pi^4) - \\
 & \alpha (640M_2^2 a_3 b_1 \pi^6 + 128M_2^4 a_3 b_1 \pi^4 + 2560C_1 M_2^2 a_1 a_3 \pi^6) \\
 & \alpha (6144C_1 a_3^2 \pi^8 - 512C_1 M_2^4 a_1 a_3 \pi^4) \tag{5.59}
 \end{aligned}$$

where $\alpha = \frac{E b^3 h_{mid}^2 t}{96L^3 \sin\left(\frac{M_2}{2}\right)^2 (M_2^4 - 5\pi^2 M_2^2 + 4\pi^4)} \sin\left(\frac{M_2}{2}\right)^2$. The force-displacement curve for the numerical values of $E = 2.1$ GPa, $\nu = 0.3$, $a_1 = 0.5$, $b_1 = 0.5$, $h_{mid} = 5$ mm, $b = 2$ mm, $t = 0.2$ mm, and $L = 100$ mm is shown in Fig. 5.6a.

The arch, when unconstrained, takes the deformation pathway OAT. This pathway corresponds to an asymmetric solution given in Fig. 5.6b. However, it can be observed in Fig. 5.6a that OAT cuts the axis $F = 0$ only twice, indicating snap through but bistability. Incidentally, this case is similar to that of a planar fixed-fixed arch, where the asymmetric mode needs to be restricted for the arch to be bistable. Thus, by constraining the asymmetric mode of deformation in the arch, we facilitate the arch to take the path OABCT. In this deformation pathway, the arch switches symmetrically as shown in Fig. 5.6c and retraces the same curve during switching back. The constraining of the asymmetric mode is physically achieved by connecting two arches at the mid-span as shown in the 3D-printed prototype in Fig. 5.6d.

5.4 Extensions using the spatial arch model

In this section, we illustrate that the spatial arch model described in the preceding section can be easily extended to: (1) spatial arches with as-fabricated shapes other than the fundamental profile, (2) lateral-torsional buckling in planar arches, and (3) arches with eccentric loading.

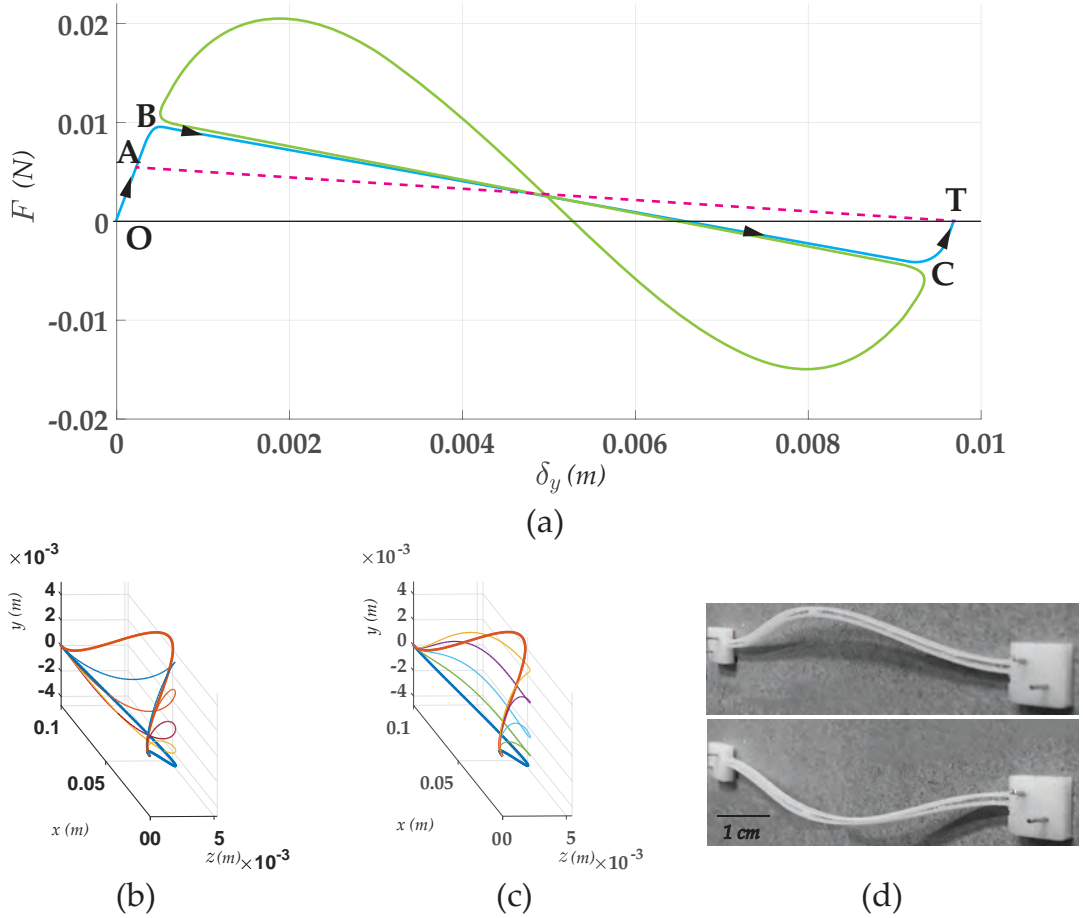


Figure 5.6: (a) Force-displacement characteristics and (b and c) deformations pathways of a fixed-fixed spatial arch with parameters: $a_1 = 0.5$, $b_1 = 0.5$, $h_{mid} = 5$ mm, $b = 2$ mm, $t = 0.2$ mm, and $L = 100$ mm. (d) The two stable states of the arch in a 3D-printed prototype.

5.4.1 As-fabricated profiles other than the fundamental shapes

The equilibrium equations derived for spatial arches in Section 3(a) consider the first three modes in the as-fabricated shape. Let us consider a spatial arch with $a_1 = 0.5$, $a_3 = 0.2$, $b_1 = 0.5$, $h_{mid} = 5$ mm, $b = 2$ mm, $t = 0.5$ mm, and $L = 100$ mm. Here, an additional third mode (a_3) is added to the starting shape of the hinged spatial arch considered previously. The force-displacement curve of the arch is shown in Fig. 5.7a. In comparison with Fig. 5.4a, we see that this arch can only switch symmetrically. The straight line shown in Fig. 5.7 corresponds to the asymmetric mode of switching. However, the arch cannot deform in this mode of switching as the line cuts the curve corresponding to symmetric deformation only once. Thus, reaching any of the stable states becomes impossible once the arch starts deforming along this pathway. Furthermore,

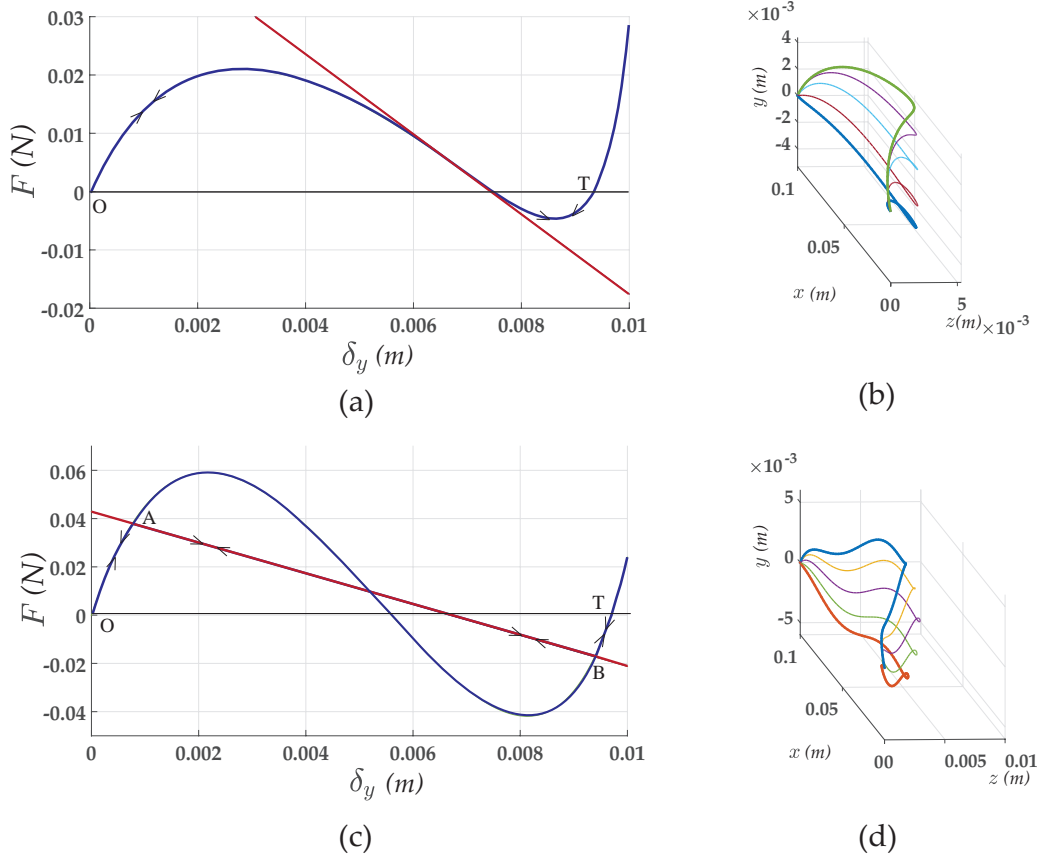


Figure 5.7: Force-displacement characteristics and deformation time-lapses of a spatial arch with as-fabricated starting shapes with (a and b) $a_3 = 0.2$ and (c and d) $a_7 = 0.1$.

unlike in the previous examples, in this case, the asymmetric pathway is not reducing the force required for deforming. The arch-profiles in various stages of deformation between the stable states in the symmetric switching are depicted in Fig. 5.7b.

Arch-profiles with mode shapes other than the first three mode shapes can also be analysed using the model. However, we need to ensure that all the mode shapes used for constructing the as-fabricated shape should be used in approximating the deformed profile as well. We noticed in the three examples presented earlier that the arch can either switch symmetrically or asymmetrically. To capture these two pathways of switching, A_1 and A_2 are essential in approximating the deformed profile. We have to use the mode weights B_1 and C_1 for approximating $u(x)$ and $\phi(x)$. Since we can solve for five unknown mode weights, an additional mode weight can be added to $w(x)$, e.g., A_i . This enables us to use an additional a_i in the as-fabricated shape along with a_1 and a_2 , and represent it as $w_0(x) = h_{mid}(a_1w_1(x) + a_2w_2(x) + a_iw_i(x))$. For example, the F - δ_y relations of a spatial arch with $a_1 = 0.5$, $a_7 = 0.1$, $b_1 = 0.5$, $h_{mid} = 5$ mm, $b = 2$ mm, $t = 0.5$ mm, and $L = 100$ mm is given in Fig. 5.7c. The deformation pathway taken by

the arch is OABT and the arch deforms as given in Fig. 5.7d.

5.4.2 Lateral torsional buckling in planar arches

A planar arch is a special case of a spatial arch with its curvature limited to a single plane. For instance, by taking all the b_i s to be zero, the as-fabricated shape reduces to the xy plane. When the out-of-plane bending stiffness of the planar arch is comparable to the in-plane bending stiffness of the arch, the arch may deform out-of-plane and undergo lateral-torsional buckling. The compression energy formed in a planar arch when it deforms out of the plane is smaller than its in-plane deformation. This causes a reduction of the minimum force required to switch the bistable arch. We consider such an example next.

The force-displacement characteristics for a planar arch with $a_1 = 1$, $h_{mid} = 5$ mm, $b = 0.9$ mm, $t = 0.5$ mm, $L = 100$ mm, and with fixed-fixed boundary conditions are given in Fig. 5.8a. The path OAT represents the in-plane asymmetric switching that needs to be restricted so that the arch can attain the other stable state. When an arch is constrained to not take the asymmetric deformation pathway, it is expected to follow in-plane switching shown in Fig. 5.8a and indicated by the pathway OCDT. However, due to the presence of the lateral-torsional deformation, i.e., spatial deformation pathway, the arch prefers the force-displacement profile given by OBET. Thus, the arch switches with reduced switching force as indicated in Fig. 5.8a. The in-plane deformation corresponding to OBET is shown in Fig. 5.8b. Note that ignoring the spatial deformation in this problem leads to about a 30% error in the prediction of the actual critical force.

A contrasting case arises when the switching force reduces in such a way that it affects the bistability of the arch. Figure 5.8d shows a force-displacement curve where the out-of-plane deformation (Fig. 5.8c) path, AE, makes the arch not bistable. Note that if this arch with $a_1 = 0.5$, $b_1 = 0$, $h_{mid} = 5$ mm, $b = 0.6$ mm, $t = 0.5$ mm, and $L = 100$ mm were to be analysed as a planar arch, it would have shown bistability with force-displacement pathway OCDT. These observations are applicable to planar arches with pinned-pinned boundary conditions as well.

5.4.3 Eccentric load

When an arch is loaded eccentric to the xy plane at a distance e , it experiences a force as well as a moment. The moment causes the cross sections to rotate more compared to the case of an arch with only a point load. In the case of a planar arch, the moment

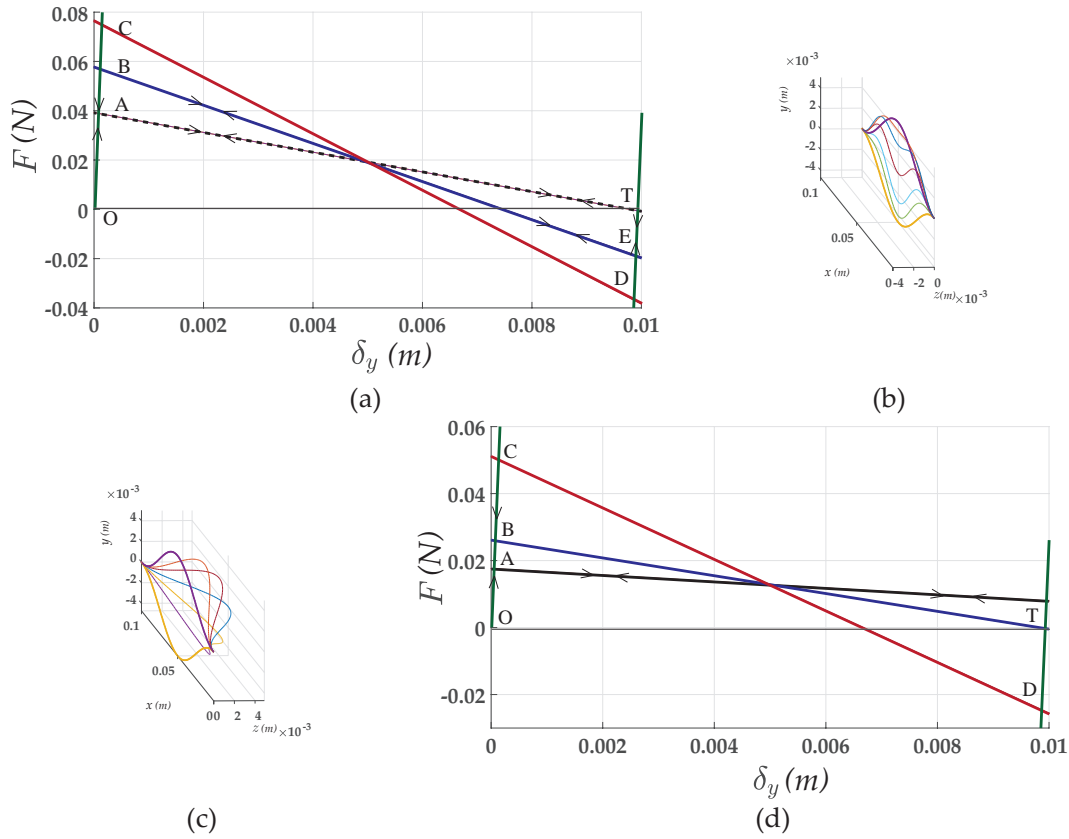
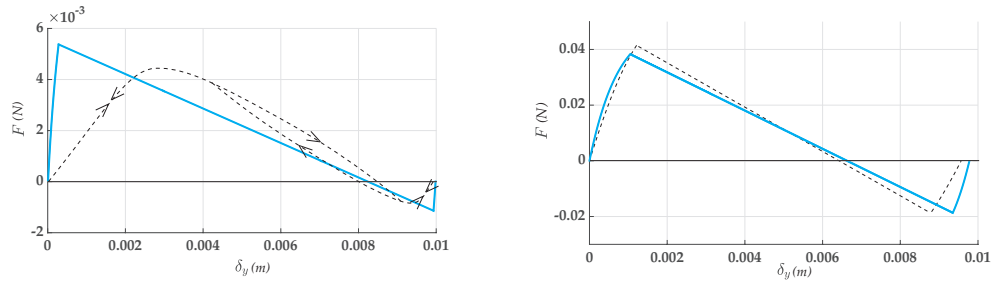


Figure 5.8: (a) Force-displacement characteristics and time-lapse of deformation of a planar arch with $a_1 = 1$, $b_1 = 0$, $h_{mid} = 5$ mm, $b = 0.9$ mm, $t = 0.5$ mm, and $L = 100$ mm, which shows bistability in the presence of a spatial deformation pathway. (b) Force-displacement characteristics and time-lapse of deformation of a planar arch with $a_1 = 1$, $b_1 = 0$, $h_{mid} = 5$ mm, $b = 0.6$ mm, $t = 0.5$ mm, and $L = 100$ mm, which is not bistable due to the presence of a spatial deformation pathway.

favors the lateral-torsional mode of deformation. Figure 5.9a shows a comparison of a planar pinned sine-curved arch with and without eccentric loading. The dashed curve corresponds to the case with eccentric loading with $e = 10$ mm for an arch with $h_{mid} = 5$ mm, $b = 0.4$ mm, $t = 0.5$ mm, $L = 100$ mm, $E = 2.1$ GPa, and $\nu = 0.3$. We observe that eccentric loading reduces the switching and switch-back forces. The F - δ_y characteristic plot shown in Fig. 5.9b is of a spatial arch with $a_1 = 1$, $b_1 = 0.5$, $h_{mid} = 5$ mm, $b = 2$ mm, $t = 0.5$ mm, $L = 100$ mm, $E = 2.1$ GPa, $\nu = 0.3$, and $e = 10$ mm. Here, the switching force increases due to the additional torsional energy in the cross-sections due to the moment arising from eccentricity. This effect is not seen in Fig. 5.9a because of the smaller width considered there. It can be observed that the third point, where the force is zero, is not the same for both the loading cases in Fig. 5.9b. This is because of the rotation of the cross sections of the arch. Due to the rotation, the



(a) The planar arch parameters are $h_{mid} = 5$ mm, $b = 0.4$ mm, $t = 0.5$ mm, $L = 100$ mm, $E = 2.1$ GPa, $\nu = 0.3$, and $e = 10$ mm .

(b) The spatial arch parameters are $a_1 = 1$, $b_1 = 0.5$, $h_{mid} = 5$ mm, $b = 2$ mm, $t = 0.5$ mm, $L = 100$ mm, $E = 2.1$ GPa, $\nu = 0.3$, and $e = 10$ mm .

Figure 5.9: Comparison of force-displacement characteristics with (dashed curve) and without (solid curve) eccentric loading for spatial and planar pinned arches.

points attached eccentric to the arch move vertically. In this case, the spatial arch in its second stable state has a positive rotation causing the point of application of load to go up. Hence, the dashed force-displacement curve shows a smaller travel of the midpoint of the arch between the two stable states.

5.5 Comparison with finite element analysis

The force-displacement characteristics obtained from the analytical modelling show good agreement with the finite element analysis (FEA). A comparison of illustrative examples discussed in this work with FEA is given in Fig. 5.10. The solid curves represent results from the analytical model and the dashed curves are obtained from FEA done in ABAQUS. In ABAQUS, continuum tetrahedral elements are used with quasi-static dynamic-implicit analysis for all the four cases. In Fig. 5.10a, asymmetric and symmetric deformation pathways of a spatial arch with hinged and fixed support discussed in Section 3a (Fig. 5.4) are compared. In obtaining the analytical solution, five mode shapes are used. The symmetric and asymmetric deformations, wherein the magnitude of force ranges from 0.04 N to -0.03 N, have mean errors of 0.0012 N and 0.0015 N, respectively. The analytical approach solves this problem within a CPU time of 187 seconds compared to 14151 seconds of FEA and thus, it is 70 times faster than FEA. However, this speed varies from problem to problem. Nonetheless, the analytical method always solves the problem much faster than FEA.

Note that the error from the numerical solution is larger at the points where the arch switches from one deformation pathway to the other. By using a larger number of mode

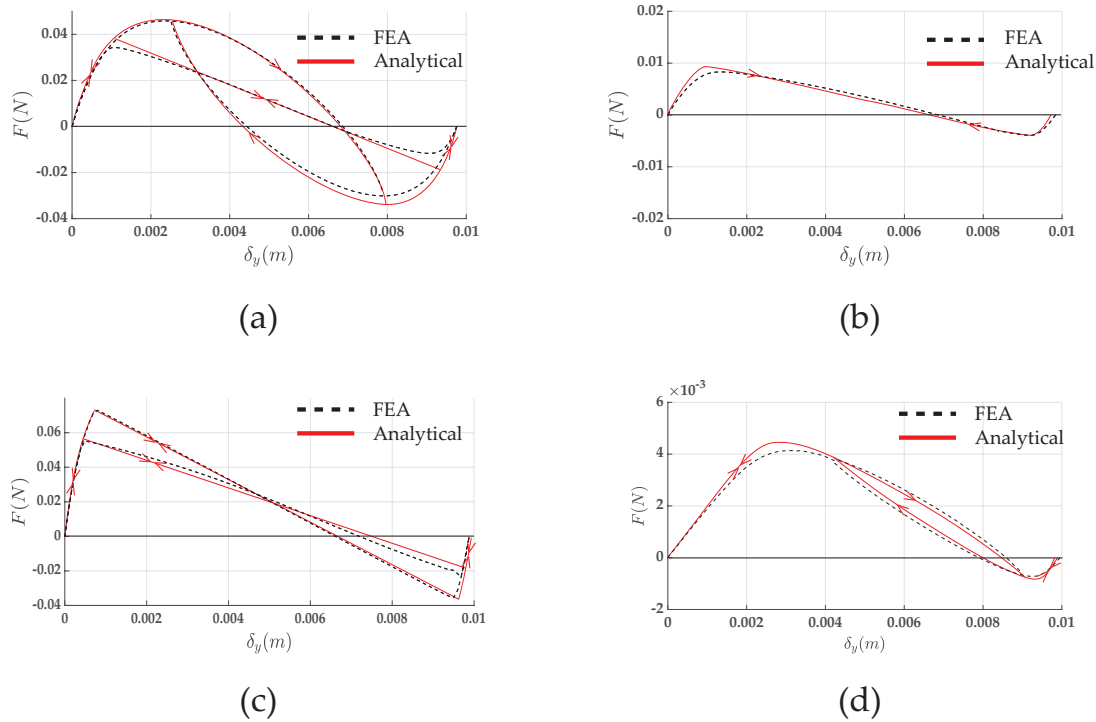


Figure 5.10: Comparison of force-displacement characteristics obtained from analytical modelling with FEA in ABAQUS for (a) pinned-pinned spatial (b) fixed-fixed spatial arch (c) fixed-fixed planar arch with spatial deformation, and (d) pinned-pinned arch with an eccentric load.

shapes for approximating the deformed profiles, this error can be minimised as shown in Fig. 5.11. With five mode shapes, the force-curve shows closer agreement compared to the one with four mode shapes.

The cases of the fixed-fixed spatial arch (Fig. 5.6), fixed-fixed planar arch with spatial deformations (Fig. 5.8), and the pinned-pinned spatial arch with eccentric loading (Fig. 5.9a) are shown in Figs. 11b-11d, respectively. The geometric and material parameters considered are the same as the ones in their respective examples considered in Sections 3 and 4.

5.6 A note

The result from the optimisation problem that led us to study spatial deformation pathways suggested that, for a given volume, a spatial distribution of material reduces the switching forces more than in the optimal in-plane solutions. Figure 5.12 shows a comparison between the pinned spatial arch considered in Section 3a and a planar pinned-pinned arch of the same volume.

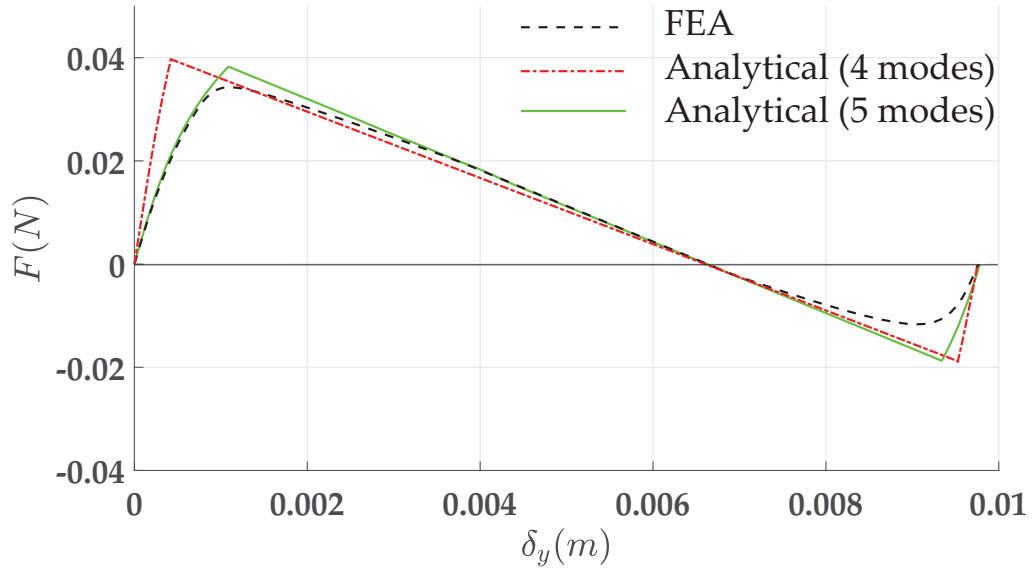


Figure 5.11: Comparison of force-displacement characteristics obtained from analytical modelling with FEA in Abaqus for a varying number of mode shapes.

The reduction in forces can be accounted for by reduced axial compression in the spatial arch and the reduced travel is due to the residual torsional energy in the spatial arch. The results from the model validate that the spatial deformation pathways reduce the switching forces in a bistable arch. This is relevant in two scenarios: while designing arches of reduced switching forces and while designing planar arches that should not deform out of plane.

5.7 Closure

We discussed the analysis of doubly curved spatial arches that are bistable. The analytical model captures the coupling between in-plane and out-of-plane bending, and the torsion with an extension of the St. Venant and Michell relationship that was given for arches with spatial deformation pathways. We observed that the spatial deformation pathways reduce the switching forces in certain bistable arches. In particular, it was shown that this reduction in the switching forces in planar arches can also sometimes cause the arch to lose its bistability.

The desirable features of bistable structures such as two force-free stable states, negative structural stiffness, change in shape in the two stable states, snap-through action, and nonlinear force-displacement characteristics, find a wide range of applications. Furthermore, spatial bistable arches will enrich the list of applications when the force

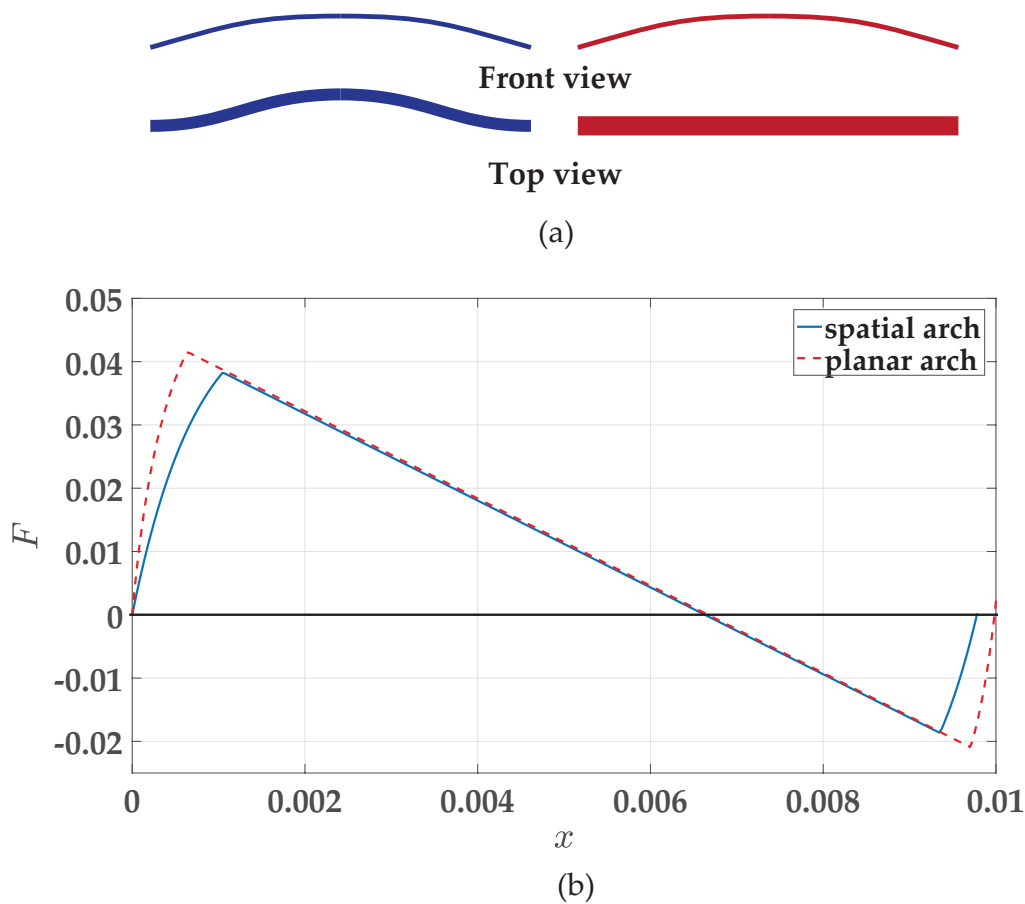


Figure 5.12: (a) Spatial and planar arches with the same volume and pinned-pinned boundary conditions, and (b) comparison of their force-displacement characteristics.

needed to switch between the stable states ought to be minimal.

With this chapter we conclude our development of the theory of bistable arches. An alternative method of designing bistable arches using kinetoelastostatic maps is described in Appendix B. In the next chapter, with help of the theory developed on bistable arches, we look at the design of two applications using them.

Chapter 6

Applications

Synopsis

In this chapter, we present the design of two applications using bistable arches: an electrothermally actuated microswitch and a mechanical OR gate. The electrothermally actuated two-terminal bistable microswitch has bimodal bistability which is obtained by using a pair of arches, a V-beam electrothermal actuator, and a novel initially retracting actuator. We use the analytical model of bistable arches to decide the geometric parameters of these components.

The OR gate is designed using pinned-pinned bistable arches. The compliant OR gate consists of five bistable arches arranged in such a way that the central arch acts as the output with 0 and 1 stable states while two pairs of arches, with their own 0 and 1 states, act as inputs. The arch-profiles of all the arches are designed so that the forces of switching and switching back between the two stable states and the travel between the two stable configurations are as desired.

6.1 Application 1 - A two-terminal bistable electrothermally actuated microswitch¹

MEMS-based Radio-frequency (RF) switches play an important role in communication systems (Varadan et al., 2003). These switches are used for routing and selection operations in communication modules. Typical applications include filter selection and antennae selection (Sanayei and Nosratinia, 2004) in reconfigurable RF systems. Another

¹Work done with Dhananjay Yadav

class of applications that relies on switches is redundancy selection, where the switch is used to transfer operations from a main system to a redundant system if the main system malfunctions. Even with relatively a long switching time, RF MEMS switches can be employed in redundancy applications (Daneshmand and Mansour, 2011). Such RF switches can be implemented in various technologies such as sub-miniature relays, microelectromechanical (MEMS) switches, gallium-arsenide (GaAs) or CMOS FET (Complementary Metal Oxide Semiconductor Field Effect Transistor) switches, and even PIN diodes. Mechanical switches tend to handle the highest power, offer the lowest insertion loss and best isolation, due to which the development of MEMS relays has attracted considerable attention in recent years. MEMS switches are typically cantilever type structures that require a continuous voltage supply to maintain the active state. The ON and OFF states are maintained for long durations in some of the aforementioned applications. In such cases, employing bistability will obviate the need for a continuous power supply, thus making the switch efficient in terms of power consumption.

We present a two-terminal bistable switch with a distributed compliant design that limits the maximum stress, thus increasing the potential for high reliability. A double cosine arch is used as the bistable element. There are two actuators that share a single pair of terminals to pull and push the bistable arch. Thus, the actuation is two-terminal, which is mechanically decoupled but electrically coupled. For push-on and push-off capability, the design requires that the secondary actuator have an atypical transient behavior, which is realized by a novel initially-retracting microactuator (Yadav and Ananthasuresh, 2018), which initially retracts and then moves forward while continuing the application of a constant voltage. Electrothermal actuation is used because in comparison with other actuators such as electrostatic, piezoelectric, etc., it has a larger force and stroke at a lower driving voltage (Moulton and Ananthasuresh, 2001). The disadvantage of using electrothermal actuation is its high power usage, which is less of a concern because the bistable switch requires power for a few milliseconds, just to switch in between states.

6.1.1 Design

Figure 6.1a shows the schematic of the proposed device. The design comprises three elements: a pair of cosine arches, a V-beam thermal actuator and an initially-retracting actuator (Yadav and Ananthasuresh, 2018). The top arch acts as a displacement-amplifier of the input given by the primary V-beam thermal actuator and the bottom double-cosine arch serves as the bistable element. The initially-retracting actuator at the left end of the

bistable arch acts as the secondary actuator and pulls it to the left when a voltage pulse is applied.

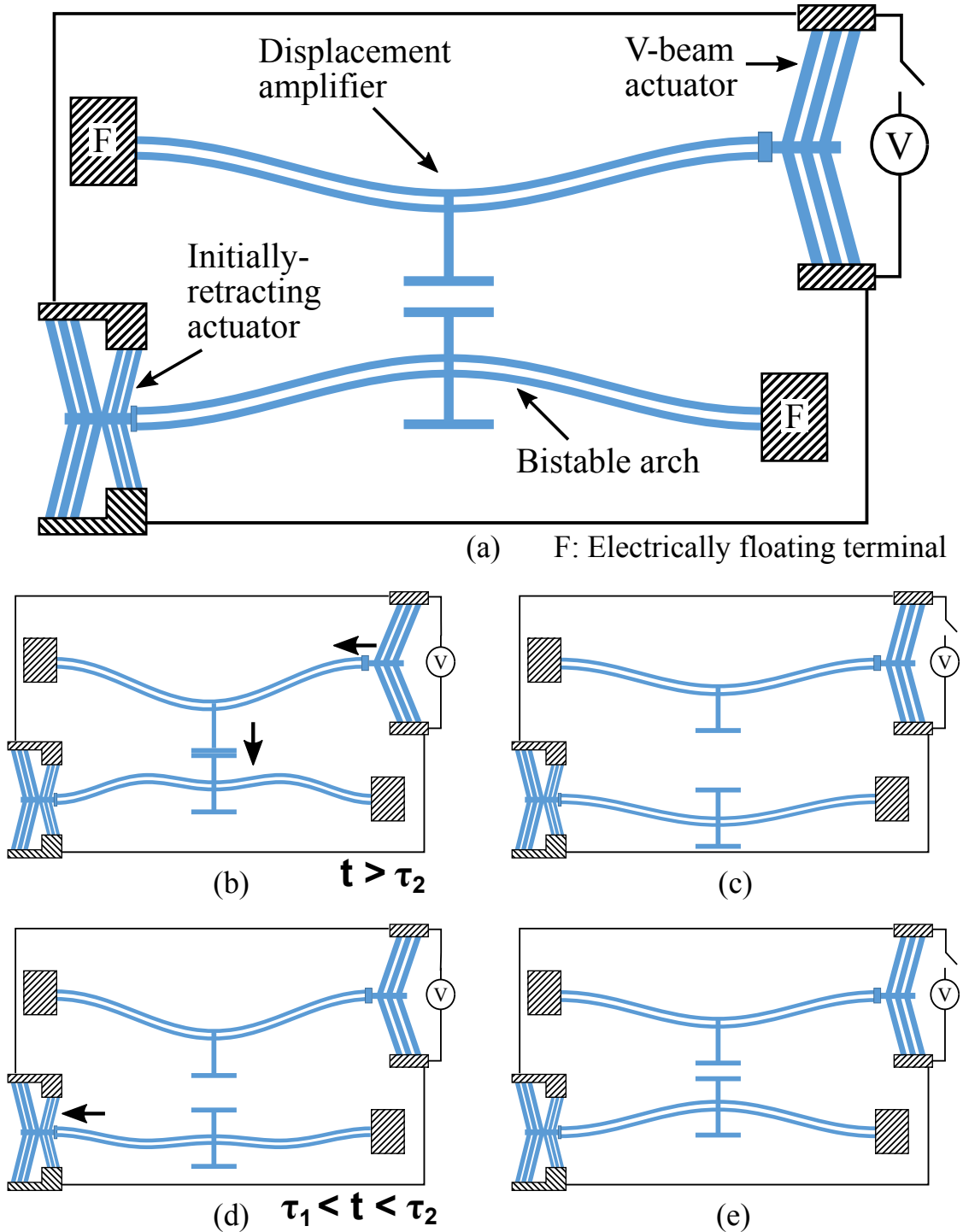


Figure 6.1: Schematic of the proposed device and its working.

Figure 6.1b-e explain the working of the mechanism. The initial state depicted in Fig. 6.1a is the OFF state. This is the as-fabricated or stress-free state of the bistable

arch. In anticipation of its application as an electrical switch, we designate this state as the OFF state and the second stable state as the ON state. A voltage pulse applied between the two terminals, simultaneously actuates the V-beam actuator and the initially-retracting actuator, causing the bistable arch to switch into its second stable ON state as shown in Fig. 6.1b and Fig. 6.1c. To switch back into the OFF state, we use the bimodal switching property of the arch. Bimodality enables the arch to trace different paths to switch between states. Therefore, instead of applying a transverse force, an axial force generated by the initially-retracting actuator is applied to switch the arch back into the OFF state. This can be observed in Fig. 6.1d-e. In doing so, we ensure that two transverse electrothermal actuators, which occupy more space and power, are not necessary for the working of the device. The voltage is applied between the same two terminals to produce the required axial force. Thus, this design retains two-terminal actuation while avoiding a highly stressed flexural hinge joint.

In the proposed design, the secondary actuator has to pull the arch beyond a certain threshold displacement (U_{th}) for the arch to lose bistability when switching from the ON to the OFF state as shown in Fig. 6.1d. The magnitude of U_{th} depends on the geometric parameters of the arch, whose closed-form analytical expression is derived in a later section. Since both the actuators share the same terminals, the primary actuator also gets activated during the switch-OFF process. This implies that the response time of the secondary actuator should be less than that of the primary actuator to prevent the displacement-amplifier from obstructing the switch-back of the bistable arch. Contrary to this, while switching from the OFF to the ON state, the axial displacement of the arch should be less than U_{th} for the arch to attain the second stable state. But since the response time of the secondary actuator has to be less than that of the primary actuator, a traditional electrothermal secondary actuator will pull the arch beyond threshold displacement by the time the primary actuator responds. So, there is a need for a new kind of actuator that can actuate beyond U_{th} for small durations of time and then attain a steady state lower than U_{th} for a constant voltage supply. In order to satisfy this requirement, an initially-retracting actuator was conceptualized.

An initially-retracting actuator consists of an integrated pair of V-beam electrothermal actuators of different lengths, each of which actuates in opposite directions operating as an antagonistic pair as shown in Fig. 6.2a. Shorter beams heat up faster than longer beams, which results in the initial retraction of the actuator. Fig. 6.2b depicts the transient behavior of the initially-retracting actuator. The steady-state displacement can be configured to be positive, zero, or negative by varying the geometric parameters

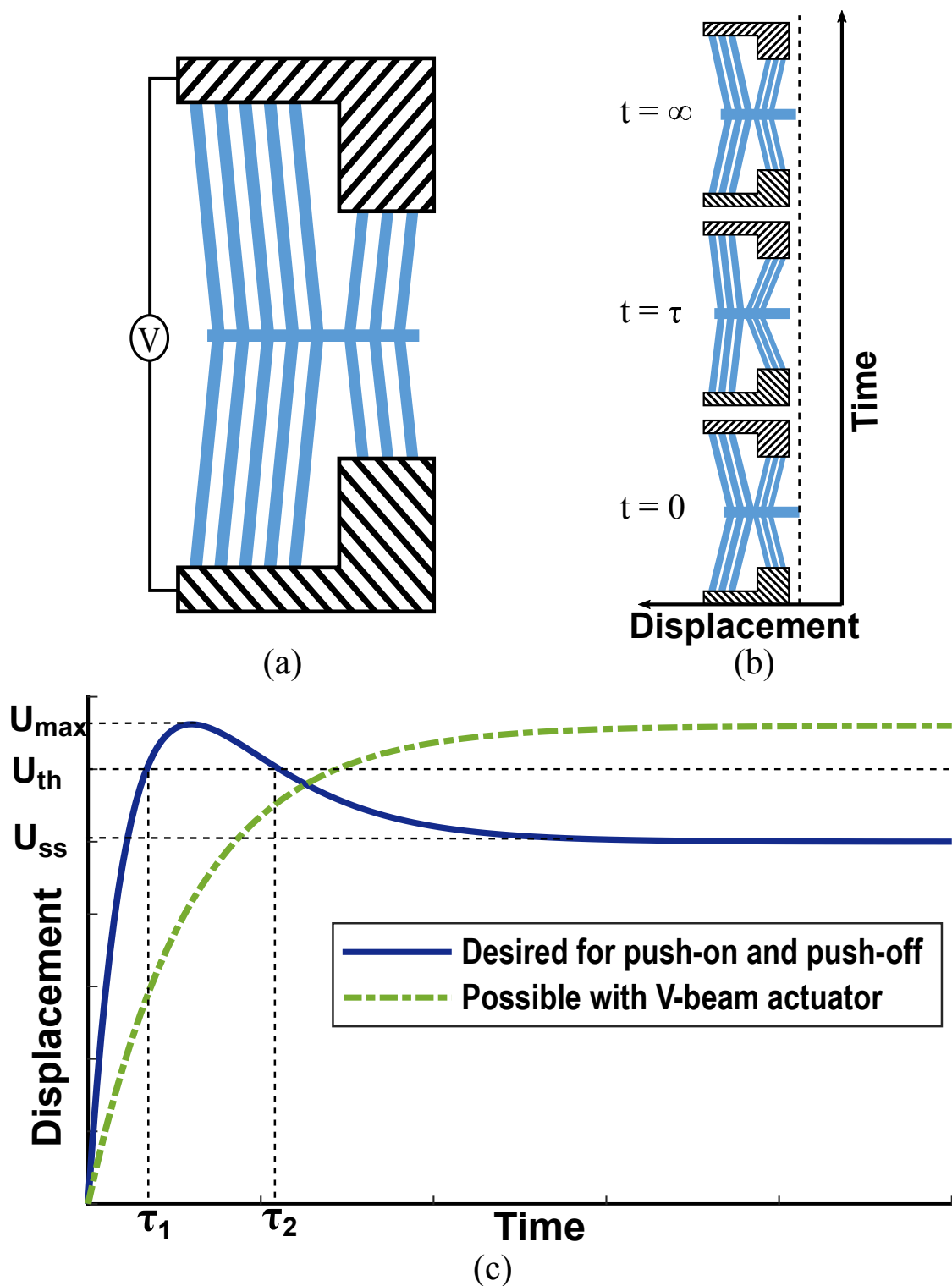


Figure 6.2: Initially-retracting actuator: (a) schematic, (b) transient behavior, and (c) plot depicting desired transient profile vs. possible with V-beam actuator.

of the integrated pair of short and long beams. The solid line in Fig. 6.2c, represents the desired transient behavior for bistable switch applications. In this case, the actuator

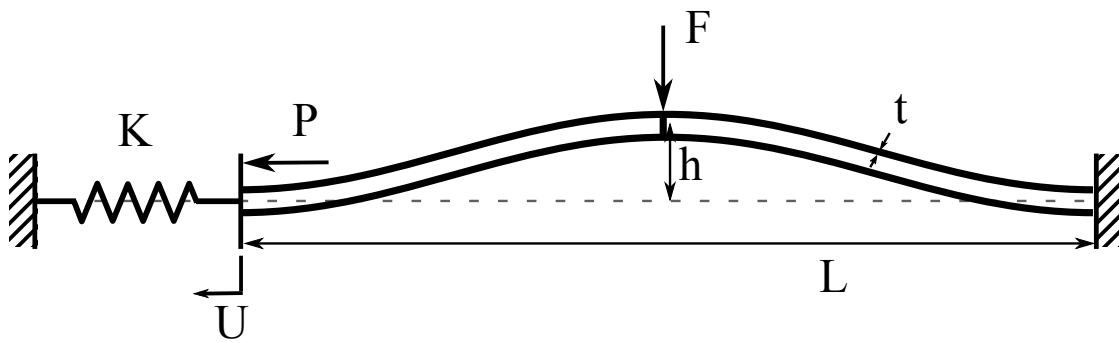


Figure 6.3: Lumped model of a spring restrained arch.

crosses U_{th} at time $t = \tau_1$ and falls below U_{th} at time $t = \tau_2$. This implies that, for switching from the ON to the OFF state, a voltage pulse of duration greater than τ_1 but less than τ_2 should be applied and for switching from the OFF to the ON state, the pulse duration should be greater than τ_2 . The exact duration of the pulse in the latter case depends on the geometry of the primary actuator.

6.1.2 Analytical Model

In this section, we analytically model the integrated components of the switch to find the critical design parameters. First, the mathematical expressions for threshold axial displacement (U_{th}) to be applied at the end of the arch to lose bistability and the threshold axial stiffness (K_{th}) for the arch to be bistable are derived. Following this, two optimization problems are posed to calculate the optimum dimensions of each actuator for minimizing the power consumption during switching.

6.1.2.1 Modeling the bistable arch

Figure 6.3 shows the lumped model of a spring-restrained arch, where P is the axial force exerted by the secondary actuator and K its inherent axial stiffness. F is the force due to the displacement-amplifier. While switching from the ON to the OFF state, the only actuating force on the arch is the axial pull by the initially-retracting actuator. In this case, the displacement amplifier does not come in contact with the arch i.e., $F = 0$. The dimensions of the bistable arch are listed in Table 6.1. Following the same notations and normalizing factors in Table 3.1, we represent the as-fabricated and deformed shape

Parameter	Value
Bistable arch length (L)	2000 μm
Width of bistable arch (t)	8 μm
Gap between curved beams	8 μm
Central offset (h)	30 μm
Depth	25 μm

Table 6.1: Arch Parameters

of the arch, respectively as follows:

$$H(X) = \frac{1}{2} (1 - \cos(2\pi X)) \quad (6.1)$$

$$W(X) = \frac{A_1}{2} (1 - \cos(2\pi X)) + \frac{A_3}{2} (1 - \cos(4\pi X)) + \frac{A_5}{2} (1 - \cos(6\pi X)) \quad (6.2)$$

We analyze the double cosine bistable arch with external forces from the primary and the secondary thermal actuators denoted by F and P , as shown in Fig. 6.3. The stiffness, K , of the secondary thermal actuator, is modeled as a linear spring. The potential energy of the system is derived by a summation of the strain energy in the arch, compression energy in the spring and the work potential due to the actuator forces. The normalized strain energy due to bending in the arch is given by

$$SE_b = \frac{1}{2} \int_0^1 \left(\frac{d^2 H}{dX^2} - \frac{d^2 W}{dX^2} \right)^2 dX \quad (6.3)$$

$$= \pi^4 \left((1 - A_1)^2 + 16A_3^2 + 81A_5^2 \right)$$

where $H(X)$ and $W(X)$ are given by Eqs. (6.1) and (6.2), respectively. The normalized compression energy due to the change in length of the beam is

$$SE_c = 6Q^2 (S_{initial} - S - U)^2 \quad (6.4)$$

where Q is the geometric constant equal to the height to depth ratio of the beam (h_{mid}/t), $S_{initial}$ the total arc length of the stress-free beam, S the total arc length of the deformed beam, and U the axial displacement at the end. By using the shallow beam assumptions,

the arch-length can be written as

$$S_{initial} = \int_0^1 \left[\frac{L^2}{h^2} + \frac{1}{2} \left(\frac{dH}{dX} \right)^2 \right] dX = \frac{L^2}{h^2} + \frac{\pi^2}{4} \quad (6.5)$$

$$\begin{aligned} S &= \int_0^1 \left[\frac{L^2}{h^2} + \frac{1}{2} \left(\frac{dW}{dX} \right)^2 \right] dX \\ &= \frac{L^2}{h^2} + \frac{\pi^2}{4} (A_1^2 + 4A_3^2 + 9A_5^2) \end{aligned} \quad (6.6)$$

By using these expressions, the strain energy term simplifies to

$$SE_c = 6Q^2 \left(U + \frac{\pi^2}{4} (A_1^2 + 4A_3^2 + 9A_5^2 - 1) \right)^2 \quad (6.7)$$

The strain energy in the axial spring is

$$SE_s = \frac{1}{2} KU^2 \quad (6.8)$$

where K is the normalized spring stiffness. The work potential due to F and P is

$$WP = -F(1 - A_1 - A_5) - PU \quad (6.9)$$

where $(1 - A_1 - A_5)$ is the transverse displacement of the arch at the mid-span.

By using the preceding equations, the potential energy, PE , of the system can be written with all its constituent terms as follows

$$PE = 2SE_b + 2SE_c + SE_s + WP \quad (6.10)$$

where SE_b and SE_c are taken twice since two arches are used in a double cosine configuration. By differentiating the potential energy with respect to the unknown weights, A_1 , A_3 , and A_5 , and the unknown displacement, U , we get the following governing

equations:

$$\frac{\partial PE}{\partial A_1} = 4\pi^4 (A_1 - 1) + 12\pi^2 Q^2 A_1 \Psi = 0 \quad (6.11)$$

$$\frac{\partial PE}{\partial A_3} = 64\pi^4 A_3 + 48\pi^2 Q^2 A_3 \Psi = 0 \quad (6.12)$$

$$\frac{\partial PE}{\partial A_5} = 324\pi^4 A_5 + 108\pi^2 Q^2 A_5 \Psi = 0 \quad (6.13)$$

$$\frac{\partial PE}{\partial U} = 24Q^2 \Psi - P + KU = 0 \quad (6.14)$$

$$\text{where, } \Psi = \left(U + \frac{\pi^2}{4} (A_1^2 + 4A_3^2 + 9A_5^2 - 1) \right)$$

Equations (6.12) and (6.13) imply that A_3 and A_5 are equal to zero. This is true for all the higher mode shapes too, if considered. From this we can conclude that under pure axial load, the arch remains in the as-fabricated mode shape. By nullifying A_3 and A_5 in Eq. (6.11), we get a cubic equation in A_1 .

$$A_1^3 + \left(\frac{4}{\pi^2} U + \frac{4}{3Q^2} - 1 \right) A_1 - \frac{4}{3Q^2} = 0 \quad (6.15)$$

Equation (6.15) should have more than one real root for the arch to be bistable. For a cubic to have all real roots, the discriminant should be greater than zero. By applying this, we get the value of U_{th} as follows:

$$U_{th} = \frac{\pi^2}{4} \left(1 - \frac{4}{3Q^2} - \left(\frac{12}{Q^4} \right)^{\frac{1}{3}} \right) \quad (6.16)$$

Equation (6.16) is in a normalized form. For U less than U_{th} , Eq. (6.15) will have three real roots for A_1 ; two for stable equilibrium states and one for unstable equilibrium. By rearranging and simplifying Eq. (6.14), we get the axial force P as follows:

$$P = KU + 24Q^2 U + 6Q^2 \pi^2 (A_1^2 - 1) \quad (6.17)$$

We replace A_1^2 in the right hand side of Eq. (6.17) implicitly in terms of U using Eq. (6.15) with the help of a symbolic manipulation program. Fig. 6.4 shows the plot of axial force (P) vs. axial displacement (U) for different values of K . In this figure, we can see that snap-through occurs at $0.57 \mu\text{m}$, the threshold axial displacement (U_{th}) for the arch with dimensions listed in Table 6.1. In Fig. 6.4, we also observe that the

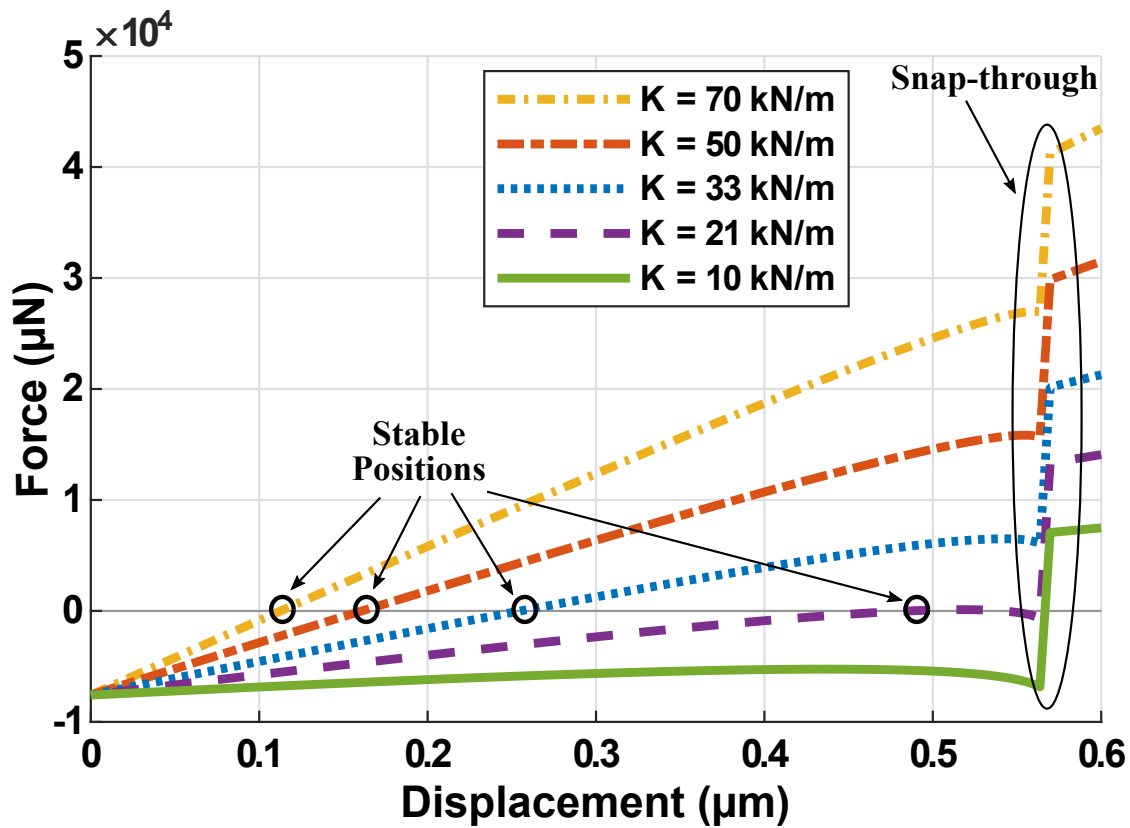


Figure 6.4: Analytically obtained axial force (P) vs. axial displacement (U) of the bistable arch.

green curve corresponding to $K = 10 \text{ kN/m}$, undergoes snap-through without crossing the zero ordinate before, denoting the absence of a second stable state. For increasing values of stiffness, the arch becomes bistable and the corresponding curves cross the zero ordinate before the snap-through region. So, for the arch to be bistable, P should be greater than zero for $U = U_{th}$ in Eq. (6.17). By satisfying this condition, we get the normalized threshold stiffness as follows:

$$K_{th} = \frac{\left(32 + \frac{552}{27}(12Q^2)^{\frac{1}{3}}\right)}{\left(1 - \frac{4}{3Q^2} - \left(\frac{12}{Q^4}\right)^{\frac{1}{3}}\right)} \quad (6.18)$$

The initially-retracting actuator is designed such that its lumped stiffness K is greater than K_{th} in the preceding equation.

6.1.2.2 Optimization of the initially-retracting actuator

Electrothermal actuators use low actuation voltage but consume more power as compared to other microactuators. So, it is important to find optimum actuator parameters to minimize the power requirement. We mentioned that the stroke of the initially-retracting actuator has to exceed U_{th} momentarily and drop down at a steady state. In Fig. 6.4, we observe that all the curves are predominantly straight lines and change curvature slightly upon nearing the snap-through region. The slopes of these curves are less than the corresponding stiffness K in each case. This difference is due to the inherent axial stiffness of an arch in its stressed state. That stiffness is calculated by fitting a straight line for P in Eq. (6.17) with $K = 0$, which turns out to be -5105 N/m. Hence, we model the arch as a spring with this negative stiffness attached to the actuator. The stiffness of the initially-retracting actuator should be 33 kN/m to get a minimum contact force of 100 μ N in the ON state. We get this specific stiffness by plotting the transverse force vs. the transverse displacement curve of the arch for a range of stiffness and ensuring that the switch-back force is 100 μ N. Based on these criteria, we pose an optimization problem for an initially-retracting actuator to get the transient behavior depicted in Fig. 6.2c.

Minimize Power
 $l_1, l_2, N_1, N_2, d_1, d_2$

Subject to:

- a. $\tau \leq 1$ ms
- b. $-U_{max} \leq -0.6$ μ m
- c. $U_{ss} \leq 0.5$ μ m
- d. Stiffness (K) = 33 kN/m
- e. Temperature ≤ 750 K
- f. Axial load in beam $\leq 0.8 \times$ Critical buckling load
- g. Maximum stress $\leq 0.5 \times$ Yield strength

The first condition ensures that U_{max} occurs by the specified time of 1 ms. If no upper bound on time is specified, the optimization algorithm keeps increasing the length of the beams to minimize power such that the displacement constraints are satisfied but the actuator becomes slow. The expressions for τ , displacement, stiffness, temperature,

maximum stress and axial load in the beams are derived in [Yadav and Ananthasuresh \(2018\)](#) and summarized in Appendix A. The results of this optimization study are listed in Table 6.2.

	Initial guess		Optimized values		Units
	Longer beams	Shorter beams	Longer beams	Shorter beams	
Offset	10	10	12	15	μm
Width	10	10	10	10	μm
Length	500	200	620	443	μm
Number	12	12	10	11	-
Power	0.84		0.44		W

Table 6.2: Optimized values of an initially-retracting actuator

6.1.2.3 Optimization of the V-beam actuator

As discussed previously, the time response of the primary V-beam actuator should be slower than the initially-retracting actuator. The primary actuator has to push the displacement-amplifier that in turn pushes the bistable arch until it toggles to the second stable state. After the displacement-amplifier makes contact with the arch, the whole switch acts as a single degree of freedom system. The displacement-amplifier is made of four parallel cosine arches. So, its deformed shape can also be taken as a linear combination of higher cosine mode shapes. Similar to [Palathingal and Ananthasuresh \(2017a\)](#), the stable equilibrium state of the system can be found by the principle of minimum potential energy, accounting for the energies of both the bistable arch and the displacement-amplifier.

$$PE = PE_{arch} + PE_{amp} + \lambda (d_{arch} - d_{amp} + g) \quad (6.19)$$

Equation (6.19) represents the total potential energy of the system, where the last term on the right hand side is added to satisfy the unilateral constraint of the contact between the arch and displacement-amplifier in accordance with the method of Lagrange multipliers. The contact force between them is captured by the Lagrange multiplier λ . Fig. 6.5 shows the plot of axial force by the V-beam actuator vs. the axial displacement of its tip. At point A in Fig. 6.5, there is a sudden change in the slope of the curve because the displacement-amplifier comes in contact with the arch at this point, after covering the initial gap g between them. At point C, the contact between them breaks as the bistable

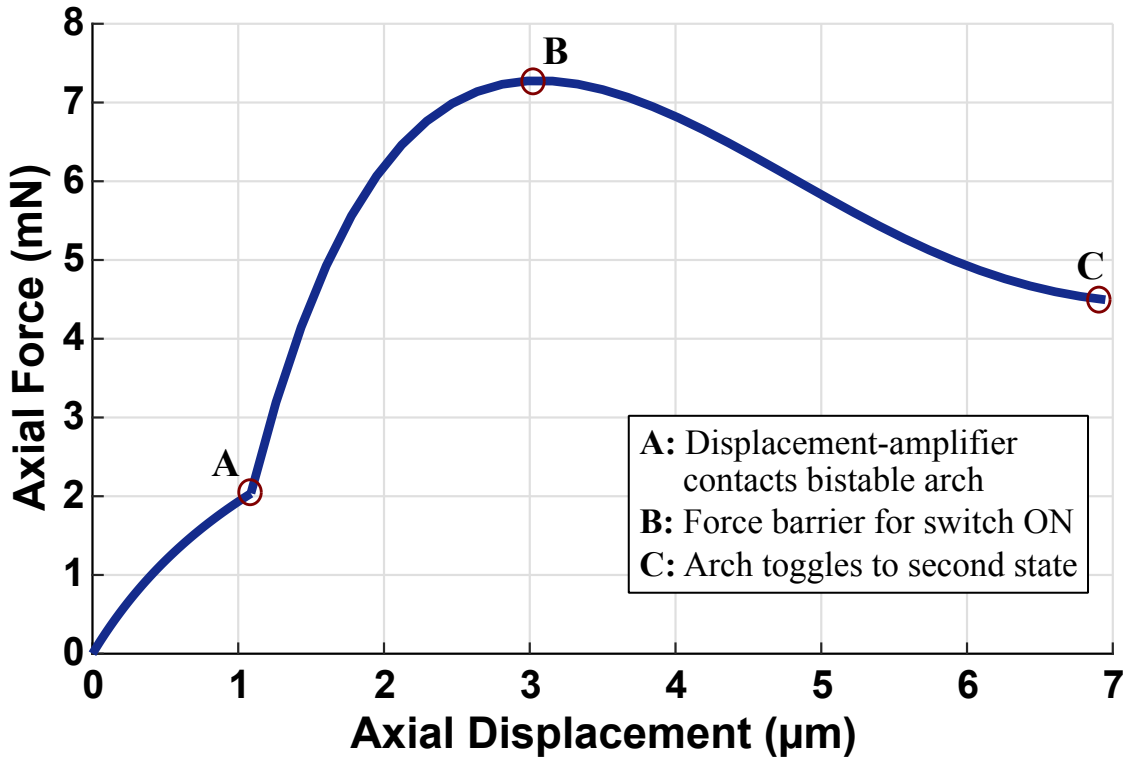


Figure 6.5: Axial force vs. axial displacement of displacement-amplifier for switch ON.

arch snaps-through to the second stable state. Point B just indicates the maximum force point that occurs in between this transition. Points B and C denote the force and displacement constraints that the V-beam actuator has to meet in order to switch the arch. Similar to the case of the V-beam actuator design, we pose an optimization problem for the V-beam actuator as follows:

Minimize Power
 l, N, d

Subject to:

- a. $\theta \leq 5$ ms
- b. $-(F_{t=\tau} - k_v u_B) \leq -7.3$ mN
- c. $-(F_{t=3\tau} - k_v u_C) \leq -4.5$ mN
- d. Temperature ≤ 750 K
- e. Axial load in beam $\leq 0.8 \times$ Critical buckling load
- f. Maximum stress $\leq 0.5 \times$ Yield strength

θ denotes the time constant of the V-beam actuator. The upper limit on θ is kept five

times more than τ to ensure that the V-beam actuator starts pushing the bistable arch after the initially-retracting actuator has attained a steady state. F denotes the force generated by the V-beam actuator at that instant, whereas k_v symbolizes its stiffness. The expressions for these quantities are summarized in Appendix A. Table 6.3 lists the result of this optimization study.

	Initial guess	Optimized values	Units
Offset	15	14.5	μm
Width	10	10	μm
Length	2000	1410	μm
Number	100	50	-
Power	0.50	0.35	W

Table 6.3: Optimized values of V-beam actuator

6.1.3 Testing and Discussion

The design of the switch based on the optimized values of the parameters, was verified in finite element analysis software, ABAQUS. Subsequently, the switches were fabricated using SOIMUMP's bulk micromachining process (www.memscap.com). A Silicon-on-Insulator (SOI) wafer of a $25 \mu\text{m}$ thick device layer, a $2 \mu\text{m}$ buried oxide layer and a $400 \mu\text{m}$ substrate layer was used in the process. Fig. 6.6 shows the SEM images of the fabricated switches. The minimum feature size is $8 \mu\text{m}$, the width of the bistable arch,

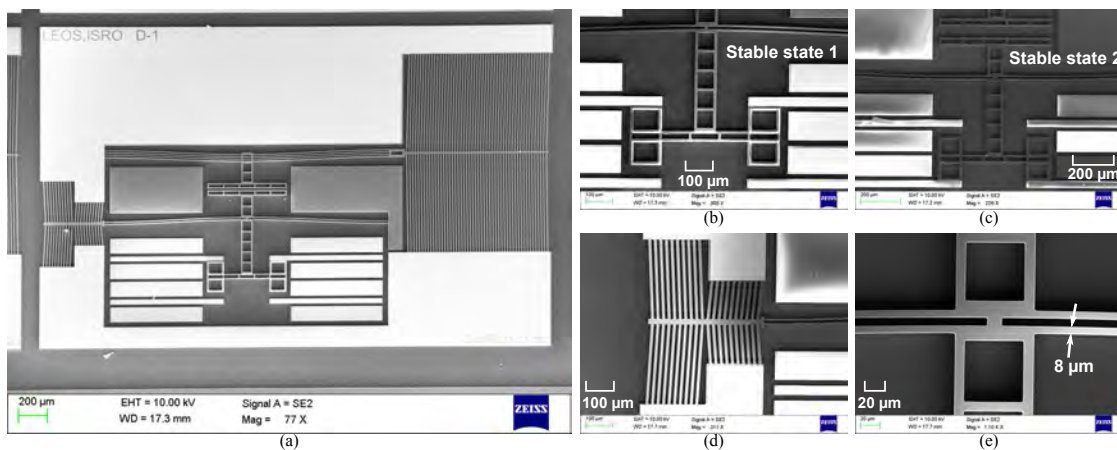


Figure 6.6: SEM images of the fabricated switch showing critical dimensions: (a) full view, (b)-(c) two stable states of the switch, (d) initially-retracting actuator, and (e) bistable arch.

as shown in Fig. 6.6d. Coplanar waveguide (CPW) lines are present at the bottom end for conducting RF signals. The extended ladder structure of the arch bridges the gap between the CPW lines on the left and right hand side by forming a lateral contact. In this layout, the switch has a Single Pole Double Throw (SPDT) configuration. Various tests were performed on the switches to verify their working and operating conditions. It was observed that a 100 ms pulse of 11.8 V, switches the arch from the OFF to the ON state and a 25 ms pulse of 11.8 V switches it back from the ON to the OFF state. Fig. 6.7a and Fig. 6.7b show the fabricated switch in the OFF and the ON states, respectively.

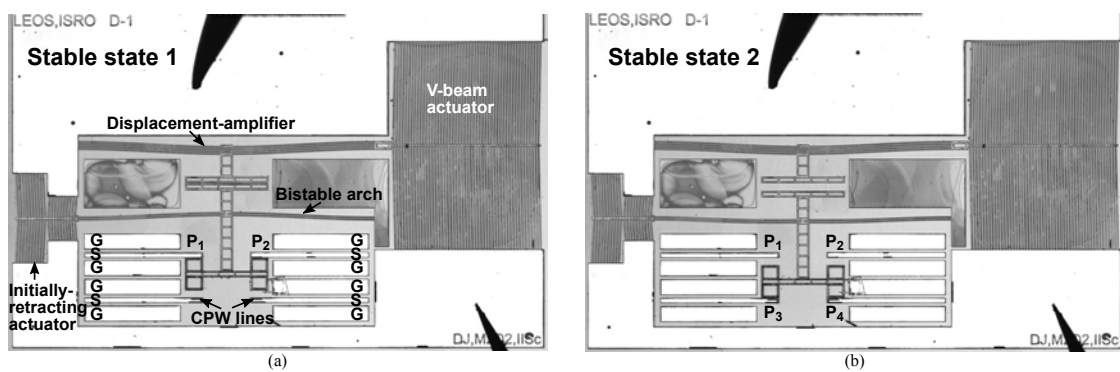


Figure 6.7: Image of fabricated switch in (a) stable state 1 (OFF), and (b) stable state 2 (ON). In stable state 1, connection between ports P_1 and P_2 is closed while P_3 and P_4 are open and in stable state 2, vice versa.

Fig. 6.8a and Fig. 6.8b show the thermal imaging results for the V-beam and initially-retracting actuator, respectively. Thermal imaging was carried out using an FLIR SC5200 thermal camera, to check whether the temperature of the thermal actuators was under the limit. The maximum temperature of the V-beam actuator was recorded as 77.8 °C, whereas that of the initially-retracting actuator reached 148.3 °C. The dynamic response

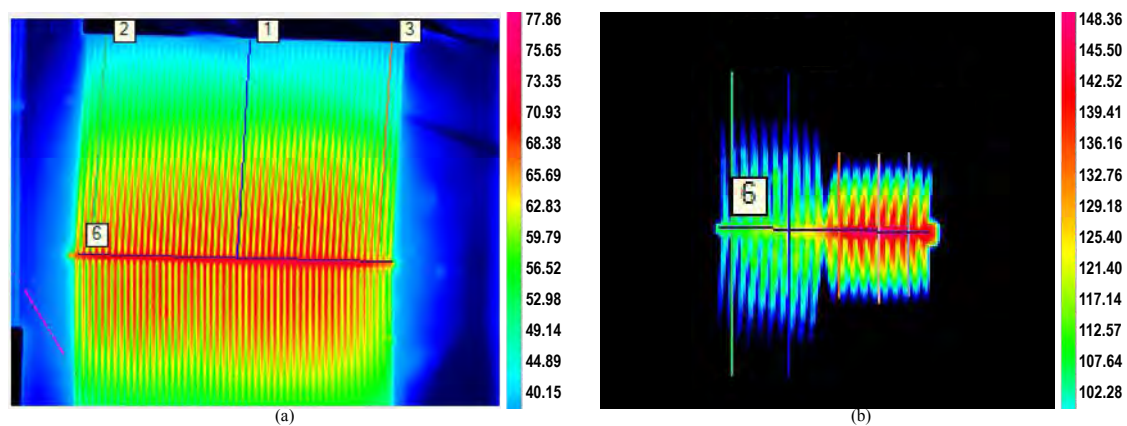


Figure 6.8: Thermal imaging of (a) V-beam actuator and, (b) initially-retracting actuator. (Temperature scale in °C)

of both the actuators was recorded using Polytec MSA-500, a Laser Doppler Vibrometer (LDV). The stroboscopic video microscopy feature of MSA-500 was utilized for the in-plane motion detection of the planar device. Fig. 6.9a and Fig. 6.9b show the comparison between analytical, FEA and experimentally obtained transient displacements for the V-beam and the initially-retracting actuator respectively. The differences between the analytical, FEA and experimental results arise owing to the following factors: (1) to simplify analytical modeling the natural convection coefficient is assumed to be constant, which in reality is dependent on temperature distribution; (2) material properties such as specific heat, elastic modulus, thermal conductivity, density, thermal expansion coefficient, resistivity, vary locally after doping, however in FEA and analytical analysis uniform material properties of single-crystal silicon is assumed; (3) the analytical heat transfer problem is modeled as a one-dimensional whereas in reality is two-dimensional.

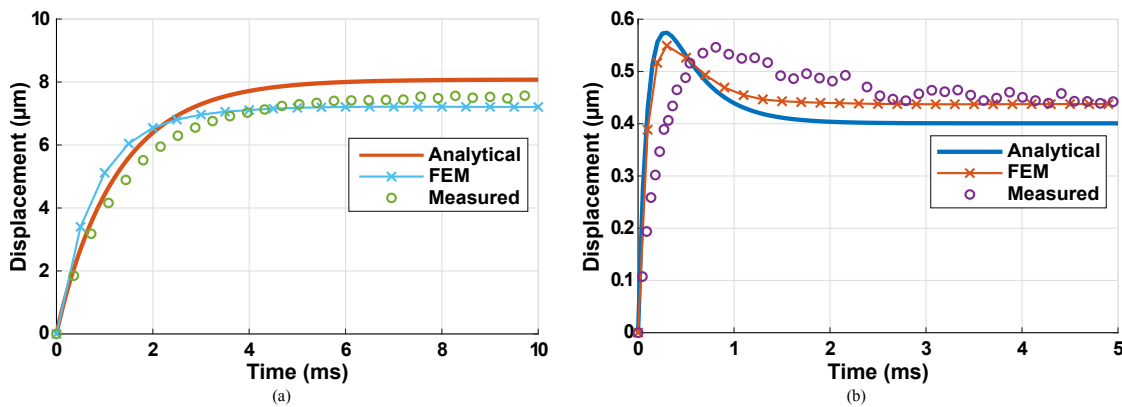


Figure 6.9: Comparison of analytical, FEM and experimentally measured transient displacement of (a) V-beam actuator, and (b) initially-retracting actuator.

6.2 Application 2 - A mechanical OR gate using pinned-pinned bistable arches²

The earliest logic gates were mechanical. Nonetheless, they remained reasonably large in size, comprising revolute joints. To be used in logical circuits, they should be sufficiently small so as to accommodate several of them in a small area. Since manufacturing at small scales essentially requires structures to be monolithic, all kinematic joints should be avoided using a compliant design. We present a design of logic gates using

²Work done with Deepayan Banik

compliant bistable arches. From the point of view of designing at micro or nano scales, one needs to be able to do the same at larger scales first, because manufacturing micro-mechanisms is not only expensive but also time-consuming. Here, we have tried to achieve the design of an OR gate in the macro scale first using pinned-pinned arches. At the micro scale, we ought to use fixed-fixed arches that can be easily realized using photolithography.

6.2.1 The OR logic

According to the OR logic, when either of the two inputs is 1, the output must also be 1. The shape of the bistable arch corresponding to its as-fabricated shape represents the binary digit 0, while the toggled state corresponds to binary digit 1. We identify two positions on the bistable arch to give input displacements, namely, Location 1 and Location 2. A threshold displacement given at either of these locations should switch the arch to its second state (binary 1) from its as-fabricated state (binary 0). Also, when both the input displacements are given at both the locations, the arch should still be in the second state, exhibiting the OR logic.

6.2.2 The design for the mechanical OR gate

With the aid of the analytical techniques described in the earlier chapters, we check the bistability of a few standard combinations of modes and their mode weights. The shape of arch that shows the OR gate logic is taken as a combination of the first and the fifth buckling modes as it provides for two valleys (Locations 1 and 2) to accept inputs as shown in Fig. 6.10. The length of the arch is 100 mm, the thickness is 1 mm, the weight of the first and the fifth modes are 10 and 2.5 respectively while the in-plane depth is 5 mm. Locations 1 and 2 are at 25 mm along the length of the arch from either ends. Thus, the shape of the arch is given by the following expression

$$h(x) = 10 \sin\left(\frac{\pi x}{100}\right) + 2.5 \sin\left(\frac{5\pi x}{100}\right) \quad (6.20)$$

From the bilateral relationship for analysis, Eq. (4.19), we obtain the toggled shape of the arch as given in Fig. 6.10 and the corresponding expression is

$$h(x) = -8.25885 \sin\left(\frac{\pi x}{100}\right) + 2.74253 \sin\left(\frac{5\pi x}{100}\right) \quad (6.21)$$

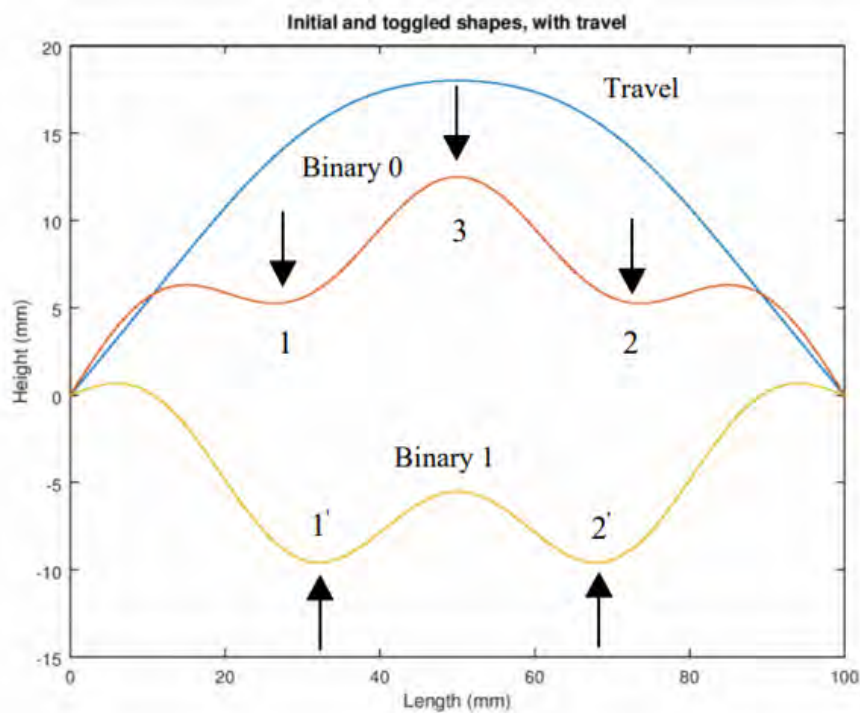


Figure 6.10: The as-fabricated (middle) and toggled (bottom-most) shapes with travel (top-most). The arrows represent the direction of actuation.

6.2.2.1 Switching of the arch from binary 0 to binary 1

We use smaller bistable arches for providing the input to the arches as depicted in Fig. 6.11. In order to decide the parameters of arches corresponding to inputs 1 and 2, we need to obtain the displacement required at Locations 1 and 2 for the output arch to toggle to its other state.

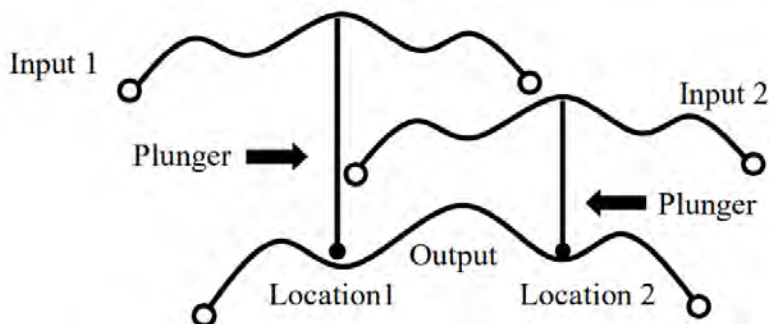


Figure 6.11: Schematic arrangement of the input and output arches

Figure 6.12 shows the force-displacement characteristic obtained from FEA for actuation along Location 1 which is positioned eccentrically for receiving inputs. Note that the displacement is assumed to be positive in the downward direction while the force is

assumed to be negative in the same direction. In Fig. 6.12, we note that the abscissa at the point where the curve cuts the x-axis for the second time (position for unstable equilibrium) gives us the travel (T1) required for switching from binary 0 to binary 1, which is 13.25 mm.

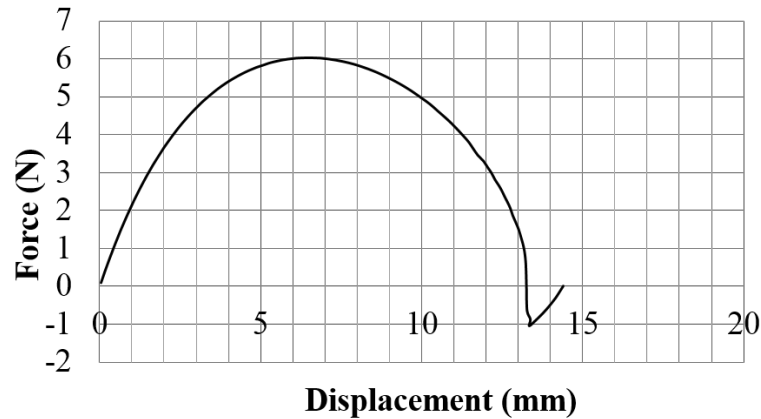


Figure 6.12: Force-displacement curve for eccentric actuation (location 1 or 2).

When both locations 1 and 2 are actuated simultaneously, the switching is perfectly symmetric. The force-displacement curve corresponding to this mode of actuation is given in Fig. 6.13. Thus, when both the inputs are acting together, a displacement of 10

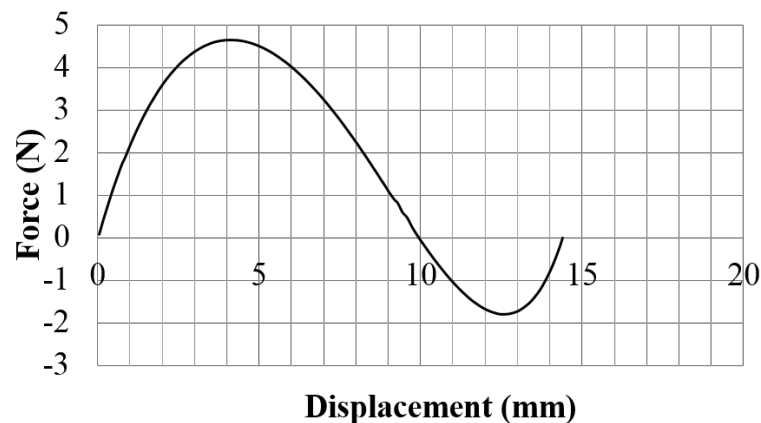


Figure 6.13: Force-displacement curve for symmetric eccentric actuation (location 1 and 2).

mm is required to toggle the arch. However, T1 (13.25 mm) is greater than 10 mm. So, inputs 1 and 2 should have a travel of at least T1 at their mid-points. By taking arches of span 70 mm, thickness 0.7 mm, out-of-plane width 5 mm, and weights of the first and the fifth modes as 8 and 2, this can be achieved. These parameters are arrived at using

Eq. (4.19) and a verification of the design using FEA is given in Fig. 6.14. The travel at the mid-point of the arch is 14.25 mm, which satisfies our design requirement.



Figure 6.14: Force-displacement curve for actuation at the mid-point of the input arches 1 and 2

6.2.2.2 Switching of the arch from Binary 1 to Binary 0

According to the OR gate logic, we need to apply a displacement (T_2) at locations 1' and 2' shown in Fig. 6.10 to switch it back to 0. That is to say, the output arch should return to State 1 (binary 0) when both the inputs are reverted to their as-fabricated shapes (binary 0). This is necessary for an OR gate. We do this by using input arches 3 and 4 positioned below the toggled configuration of the arch as shown in Fig. 6.15. Locations 1' and 2' receive actuation given by inputs 3 and 4, respectively. Note that, according to OR logic, both inputs 3 and 4 must be made 0 for the output arch to return to 0.

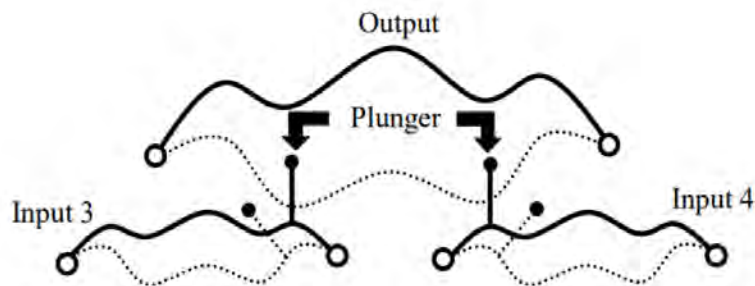


Figure 6.15: Schematic arrangement of the input and output arches for reverse actuation.

From Fig. 6.13 we note that the value of T_2 is 4.4 mm. If we try to design an arch with such a small travel at the mid-point, then the entire size of the arch has to

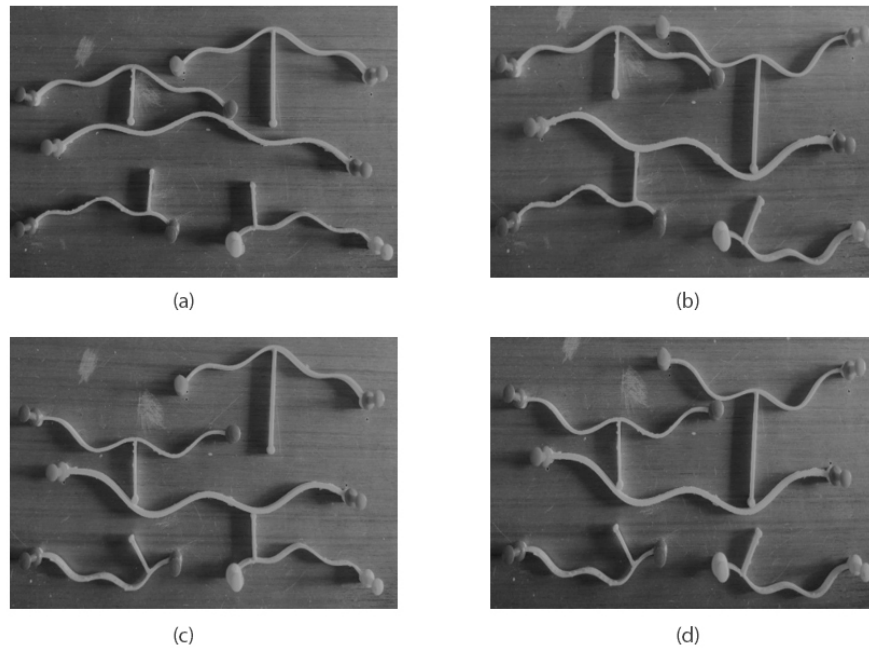


Figure 6.16: 3D-printed prototype of the OR gate design

be reduced to such an extent that it would result in a loss of bistability and structural strength. Hence, the plungers in these arches are located eccentrically (8.6 mm from the corresponding end), which allows for a smaller travel. These arches are of span 50 mm, thickness 0.5 mm, out-of-plane width 5 mm, with weight of the first and the fifth modes, 5 and 1.25 respectively. By using equation Eq. (4.19), we find the travel at this location to be 4.65 mm, which is slightly greater than T_2 (4.44 mm).

In Fig. 6.16, the different configurations of the entire assembly have been displayed. The models for all the arches are 3D-printed using ABS (Acrylonitrile Butadiene Styrene). It must be noted here that inputs 1 and 3 have to be actuated simultaneously and the same is true for inputs 2 and 4. Figure 6.16a shows the initial undeformed state of the assembly corresponding to binary 0. In Fig. 6.16b, one of the inputs has been actuated to 1 causing the output to switch to 1 as well. When both the inputs are actuated, as in Fig. 6.16d, the output remains in the toggled state. Finally, in Fig. 6.16c, we see that, as one of the inputs is reverted to 0, the output arch does not switch back to 0, just as it should, to maintain the OR logic. Figure 6.16a also represents the state when both the inputs have been switched back to 0 causing the output to return to 0 as well.

6.3 Closure

An improved design of a push-on, push-off bistable micromachined switch is presented here. The design has three features: (i) avoiding a flexural joint and thus eliminating the possibility of high stress; (ii) mechanical decoupling of the push-on and push-off actuations that facilitates design of the two actuators independently to a large extent; and (iii) incorporating a novel initially-retracting actuator to achieve consistent switching back. The design also illustrates the importance of analytical modeling for the bistable arches to determine the design parameters. The efficacy of the design is demonstrated using a micromachined prototype that is successfully tested.

The OR gate design presented here is preliminary and a lot of work lies further in this direction. The way logic has been demonstrated in this work paves way for the designing of AND, NAND and NOR gates which could result from modifications of the current design itself. This mechanism has to be designed at micro-scales because that is where the real utility of the system lies.

In the next chapter, building on our understanding of bistable arches, we study bistable shells and an application based on them.

Chapter 7

Bistable shells

Synopsis

First, we discuss bistability in shells and present their shape optimization for maximum travel. The optimization is done numerically and semi-analytically. We compare the shell with maximum travel with the arch with maximum travel, discussed in Chapter 3. Second, we present a passive monolithic compliant grasping mechanism that works based on an everting bistable shell. It comprises grasping arms made of beam segments that work in conjunction with the bistable shell. The grasper is capable of picking up a stiff object of any shape up to a maximum size and weight.

7.1 Introduction

Bistable shells can maintain two force-free equilibrium states as shown in Fig. 7.1. Many of the existing bistable shells in engineered devices and the natural world rely on pre-stress for their bistable behaviour. However, the bistable shells considered here are stress-free in their as-fabricated state and stressed in their everted state. In this work, we consider shallow, thin shells that can be bistable without pre-stress.

A cross section of a bistable shell is shown in Fig. 7.2. The shell of as-fabricated profile, $h(r)$, deforms to $w(r)$ on the application of a point force, F , at $r = 0$. The height of the shell is H , the radius of the planform R and the thickness t . A shallow shell is one whose height is much smaller than its planform, i.e., $H \ll R$. A thin shell is one whose thickness is much smaller than its height, i.e., $t \ll H$. There is scope for the shape optimization of shallow-thin shells in view of the switching and switch-back forces as well as the distance travelled by points of interest between the two stable

states. In the next section, we present our preliminary results on the shape optimization of bistable shells for maximum travel. Our aim is to understand bistability in shells before designing a gripper based on bistable shells.

In the subsequent section, we use the ability of bistable shells to maintain two structural orientations without consuming power and thereby conceptualize a passive gripper. We use a bistable shell attached with grasping arms as the critical element to design a gripper that is passive and yet is capable of picking up objects of a variety of shapes. The gripper is a monolithic design that combines a compliant mechanism, a bistable shell, and grasping arms. The bistable shell everts by pushing on the object to enable the grasping arms to envelop the object. The compliant mechanism releases the grasped objects by transmitting the input force to the bistable shell.

7.2 Shape optimization for shell travel

Similar to arches, bistability in shells arises from the interplay between compression and bending energies. Our aim is to analytically model bistability in shells for a range of as-fabricated shapes with pinned-pinned boundary conditions, to obtain the optimal shapes for a specified bistable characteristic. To simplify the problem, the travel of the mid-point, W_{tr} shown in Fig. 7.3, of an axisymmetric shell is taken as the objective function for a chosen thickness t . Two approaches are followed to pose and solve the

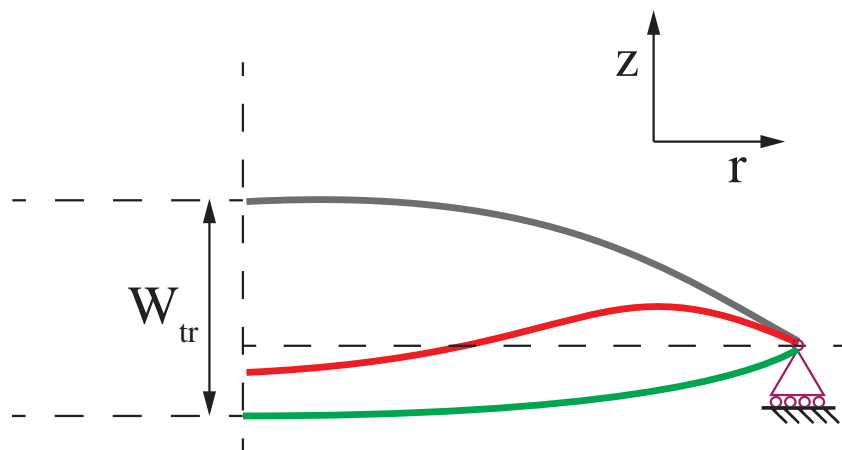


Figure 7.3: Travel of the mid-point of the shell between two stable states of a bistable shell

optimization problem for maximizing the travel with constraints on the switching and switch-back forces. The first approach that entails numerical optimization is given next.

7.2.1 Numerical approach

The shape of the shell is taken as a linear combination of basis functions that are chosen based on pinned-pinned boundary conditions. Thus, the as-fabricated shape is expressed as

$$h(r) = \sum_{n=1,3,5} a_n \sin\left(\frac{n\pi}{2} \left(1 + \frac{r}{R}\right)\right) \quad (7.1)$$

where a_n denotes the mode weight corresponding to the n^{th} sine mode shape, similar to the case of pinned-pinned bistable arches. Thus, the optimization variables are the weights in the linear combination. We only consider odd mode shapes because of the axisymmetric assumption and take the first three mode weights, a_1 , a_3 , and a_5 , as design variables.

The optimization problem can be stated as:

$$\text{Maximize } W_{tr}$$

$$a_1, a_3, a_5$$

$$\Lambda_1 : a_1 - a_3 + a_5 = H$$

$$\Lambda_2 : |a_3| < \frac{H}{2}$$

$$\Lambda_3 : |a_5| < \frac{H}{2}$$

$$\text{Data} : E, \nu, t, H, R$$

where the constraint $a_1 - a_3 + a_5 = H$ is to ensure that the height remains constant and the bounds on a_3 and a_5 limits the area of interest. In this approach, a sensitivity analysis is challenging because the analytical expressions for gradients are not easily tractable. Hence, we use an optimization toolbox in Matlab 2016b in conjunction with a Comsol Matlab livelink to carry out computations without gradients. The function written in Matlab calculates the travel from FEA carried out in Comsol. The $fmincon()$ routine in Matlab calls Comsol FEA engine iteratively to improve the travel. For a radius of 30 mm, a thickness of 0.8 mm, a height of 5 mm, a Young's modulus of 2.1 GPa and a Poisson's ratio of 0.3, the optimal profiles obtained are given in Fig. 7.4.

The values of the design variables in the three cases are: (a) $a_1 = 4.5$, $a_3 = -2$, $a_5 = -1.5$, (b) $a_1 = 3.6$, $a_3 = -1.2$, $a_5 = 0.2$, and (c) $a_1 = 1$, $a_3 = -2$, $a_5 = 2$. These multiple solutions are due to different initial guesses. This indicates the existence of multiple local minima. Certain initial guesses could not converge confirming that the shell is not bistable for all combinations of a_1 , a_3 , and a_5 , as to be expected. Next, we present our second approach, which is semi-analytical wherein the deformation of the

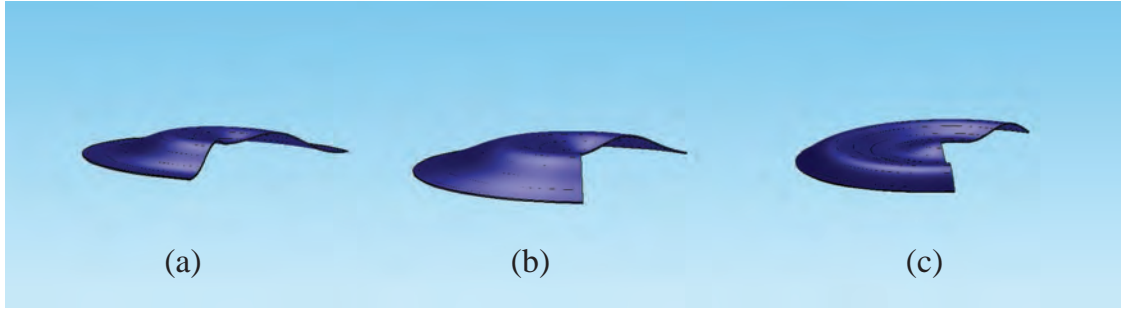


Figure 7.4: Optimal bistable shells that maximize travel at the mid-point between the two stable states.

shell is also expressed as a linear combination of the basis functions used for defining the shape of the shell.

7.2.2 Semi-analytical approach

This approach follows the methods developed for shallow arches, and we take the deformed shape of the shell as:

$$w(r) = \sum_{n=1,3,5} A_n \sin\left(\frac{n\pi}{2} \left(1 + \frac{r}{R}\right)\right) \quad (7.2)$$

where A_n is the mode weight corresponding to the n^{th} sine mode shape. The axial deformation in the arch is taken as

$$w(r) = \sum_{n=1,3,5} C_n \sin\left(\frac{n\pi r}{2R}\right) \quad (7.3)$$

where C_n is the mode weight corresponding to the n^{th} sine mode shape. Thus, we can write the compression energy as

$$SE_c = \int_0^R \pi t (\sigma_r \epsilon_r \sigma_\theta \epsilon_\theta) r dr \quad (7.4)$$

where the radial strain ϵ_r , circumferential strain ϵ_θ , radial stress σ_r and circumferential stress σ_θ are given by

$$\epsilon_r = \frac{du(r)}{dr} + \frac{1}{2} \left[\left(\frac{dw(r)}{dr} \right)^2 - \left(\frac{dh(r)}{dr} \right)^2 \right] \quad (7.5)$$

$$\epsilon_\theta = \frac{u(r)}{r} \quad (7.6)$$

$$\sigma_r = \frac{E}{1-\nu^2} (\epsilon_r + \nu\epsilon_\theta) \quad (7.7)$$

$$\sigma_\theta = \frac{E}{1-\nu^2} (\epsilon_\theta + \nu\epsilon_r) \quad (7.8)$$

Thus, the bending energy can be written as

$$SE_b = \int_0^R \frac{\pi E t^3}{6(1-\nu^2)} [(\chi_r + \chi_\theta)^2 - 2(1-\nu)\chi_r\chi_\theta] r dr \quad (7.9)$$

where χ_r and χ_θ are the change in curvatures given by $\frac{d^2w(r)}{dr^2} - \frac{d^2h(r)}{dr^2}$ and $\frac{1}{r} \left(\frac{dw(r)}{dr} - \frac{dh(r)}{dr} \right)$, respectively. Since we are interested in the travel of the shell corresponding to the second stable state where $F = 0$, the work potential is zero. So, the potential energy, PE , comprises only bending and compression energies. By minimizing PE with A_i and C_j we get the second stable state of the shell.

Thus, we can write the optimization problem as:

$$\begin{aligned} & \underset{a_1, a_3, a_5}{\text{Maximize}} W_{tr} \\ & \lambda_i : \frac{dPE}{dA_i} \\ & \lambda_j : \frac{dPE}{dC_j} \\ & \Lambda_1 : a_1 - a_3 + a_5 = H \\ & \Lambda_2 : |a_3| < \frac{H}{2} \\ & \Lambda_3 : |a_5| < \frac{H}{2} \\ & \text{Data} : E, \nu, t, H, R \end{aligned} \quad (7.10)$$

By solving numerically, we obtain two solutions where $a_1 = 5, a_3 = -2.5, a_5 = -1.5$ and $a_1 = 1.5, a_3 = -2.5, a_5 = 2$ as depicted in Fig. 7.5a and Fig. 7.5b, respectively.

To understand the problem better, the design space is generated as shown in Fig. 7.6. A point in this space corresponds to a shape of the shell. In the white region the shell

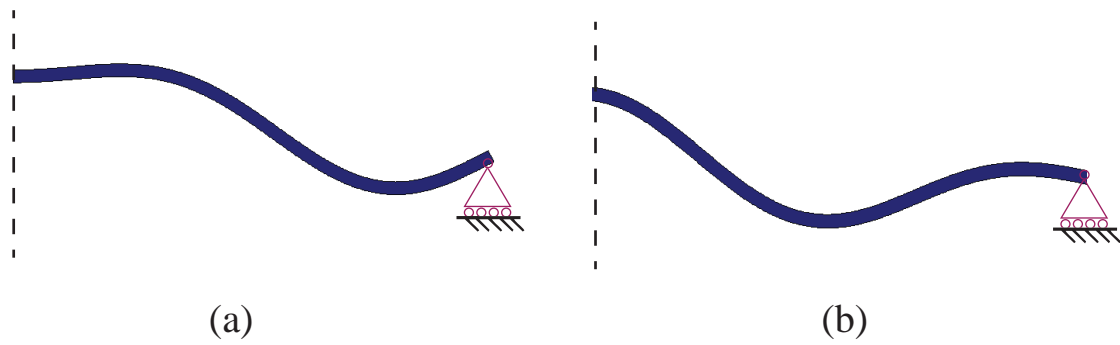


Figure 7.5: Optimal bistable shells that maximize travel at the mid-point between the two stable states obtained using a semi-analytical approach.

is not bistable, or in other words it is monostable. Note that the design space of the arches

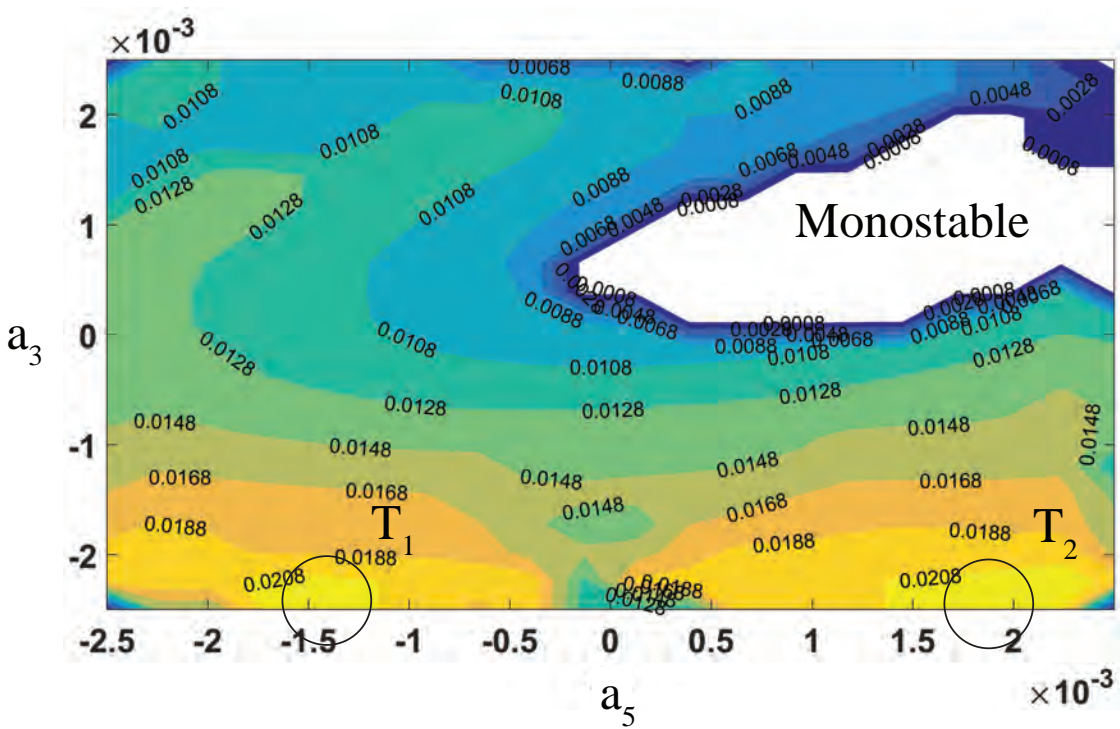


Figure 7.6: Design space of arches with contours indicating the travel of shells

shells is much larger than that of the arches discussed in Chapter 3. Points T_1 and T_2 are the optimal solutions corresponding to $a_1 = 5, a_3 = -2.5, a_5 = -1.5$ and $a_1 = 1.5, a_3 = -2.5, a_5 = 2$, with a travel of 20.1 mm. Note that this is almost double the travel of the shell with $a_1 = 1, a_3 = 0, a_5 = 0$.

Interestingly, the optimal travel values in shells are much larger than those in arches of similar geometric parameters. If we imagine a shell revolved from an arch shown in

Fig. 7.7 and obtain the optimal shell by revolving the optimal arch, the travel is only 11.2 mm.

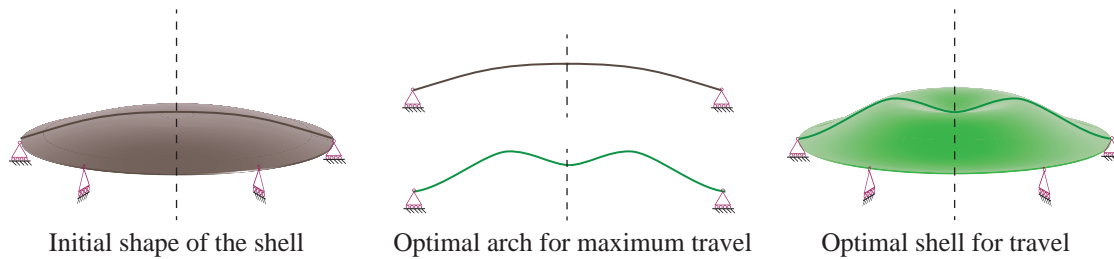


Figure 7.7: Optimal shell obtained from revolving an arch with optimal travel

Our model gives reasonable accuracy in computing the travel. As mentioned before, the travel is obtained based on the equilibrium configuration of the arch at the second stable state, where the strain energy of the shell is minimal. However, our energy expressions fail to accurately capture the strain energy values in the in-between configurations of the shell. Thus, our model needs improvements to find the switching and switch-back points. Hence, we have relied on FEA for designing a gripper using the bistable shell described in the next section. The gripper illustrates the utility of bistable shells as passive universal grippers.

7.3 A passive universal gripper using a bistable shell ¹

In this section, we first explain the working principle of the gripper. And then, an analysis of the bistable shell, switching mechanism, and grasping arms is presented. We use FEA in ABAQUS software to obtain force-displacement characteristics for the selected shape of the shell. The switching mechanism is designed by incorporating the force needed to switch the shell and the maximum actuation force available. The results from the preliminary grasping trials using a 3D-printed prototype are given subsequently.

7.3.1 Working principle

The bistable compliant gripper consists of a switching compliant mechanism, a bistable shell, and grasping arms as shown in Fig. 7.8. The switching mechanism is the connecting element between the actuator and the bistable shell. It switches the bistable shell from its stress-free configuration to the second stable everted configuration of the shell

¹Work done with Mytra V. S. Balakuntala

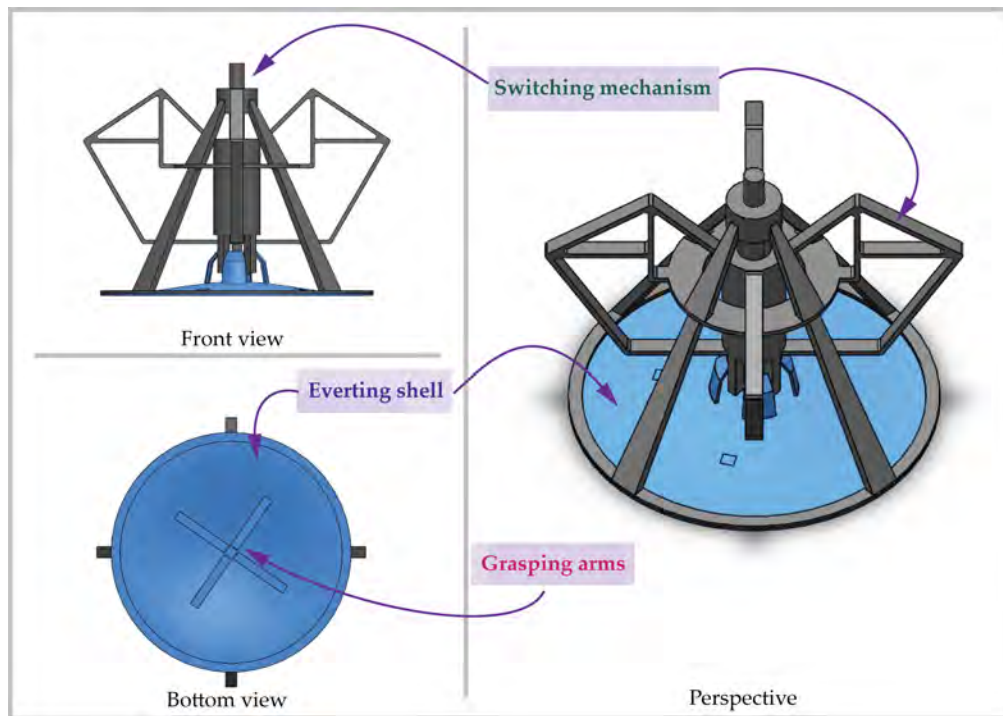


Figure 7.8: A compliant monolithic grasping mechanism based on a bistable shell. The mechanism consists of three parts, (1) switching mechanism, (2) bistable shell, and (3) grasping arms.

resulting in the opening of the grasping arms. Figure 7.9 shows the grasping arms opening and closing in conjunction with the bistable shell. As illustrated in Fig. 7.10, these three parts work in the following three steps to grasp and release objects: (1) the input force applied on the switching mechanism switches the bistable shell and opens the grasping arms to grasp the object of interest (see Fig. 7.10(a)-(c)); (2) the everted shell upon contact with the object returns to the stress-free configuration causing the grasping arms to close around the object and grasp it (see Fig. 7.10(d)-(f)); (3) the switching mechanism is actuated again to release the object.

The design of the switching mechanism and the grasping arms is dependent on the bistable characteristics of the shell. These characteristics determine the topology and size of the switching mechanism, and the dimensions of the grasping arms as explained



Figure 7.9: Bistable shell with contracting mechanism and grasping arms attached.

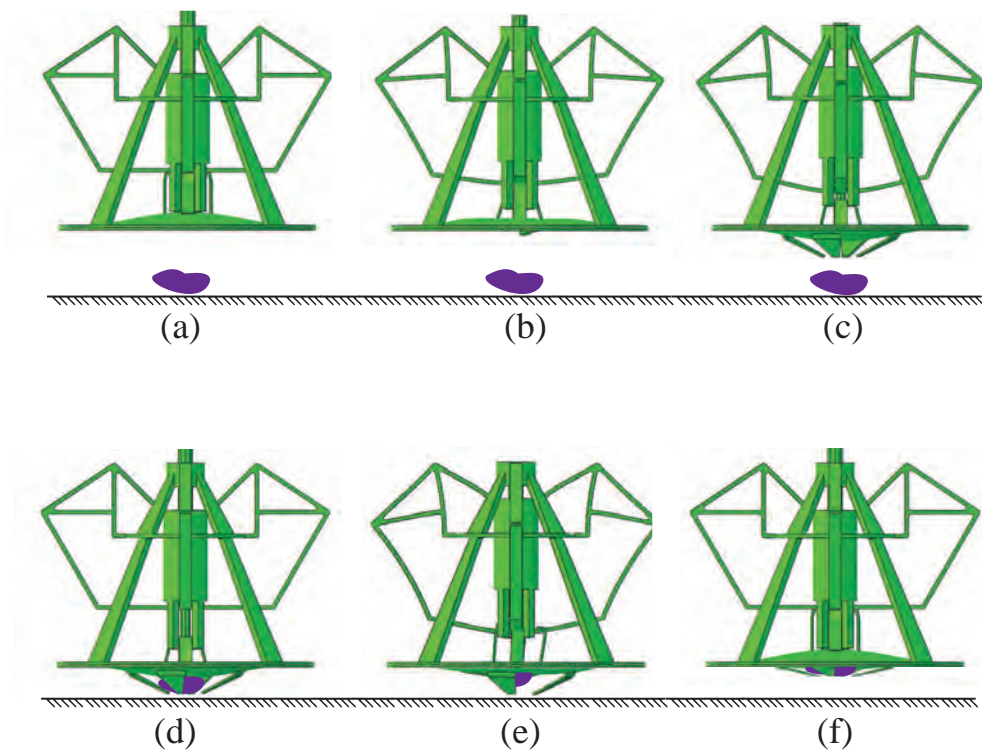


Figure 7.10: Working of the grasping mechanism simulated in Abaqus.

in the next two subsections. We systematically approach the analysis of the gripper considering the design of the bistable shell first, followed by the switching mechanism and the grasping arms.

7.3.2 Bistable shell

The two force-free stable equilibrium configurations of the bistable shell correspond to the open and closed positions of the gripper. The critical static characteristics of the shell are the switching (F_s) and switch-back (F_{sb}) forces, the switching displacement (u_s), and the travel (u_{tr}). These characteristics are labeled in the force-displacement curve given in Fig. 7.1. F_s is the minimum force required by the shell to switch from the stress-free stable configuration to the stressed everted shape. F_{sb} is the maximum force that can be resisted by the shell in the everted state before switching back to its as-fabricated initial shape. u_s is the minimum displacement the shell needs to be actuated to initiate its eversion and u_{tr} is the total displacement of the point of interest between the two stable states. Note that the bistable shell considered here is bistable solely because of its as-fabricated shape, not because of pre-stress. This is preferred as the gripper in its closed configuration, which is its default position, is stress-free.

In the case of planar arches, it is known that a single cosine arch does not show

bistability for fixed-fixed boundary conditions. Here, we show that a shell formed from a revolved cosine profile is bistable for fixed-periphery boundary conditions. The height of the shell at a distance r from the center, $h(r)$, is taken as:

$$h(r) = \frac{H}{2} \left[1 - \cos \left(2\pi - \frac{2\pi r}{R} \right) \right] \quad (7.11)$$

where H is the height at the midpoint of the shell and R the radius of the planform. We analyze the shell for an uniform thickness, $t = 1$ mm, $H = 7$ mm, and $R = 30$ mm using a quasi-static FEA in Abaqus. The dimensions were selected for realizing a prototype design that can be actuated by hand. Young's modulus and Poisson's ratio of Verowhite and TangloPlus mixture, a 3D printing material used in Objet Conex 260 for prototyping, were taken as $E = 1.2$ GPa and $\nu = 0.3$ respectively. For a point load applied at the center of the shell with edge fixed, the force displacement characteristics obtained are shown in Fig. 7.11. Note that u_{mid} is the deformation at the point of application of the load, F . The curve intersects the u_{mid} axis, $F = 0$, at three points corresponding to two stable and one in-between unstable states, indicating bistability. Two important design

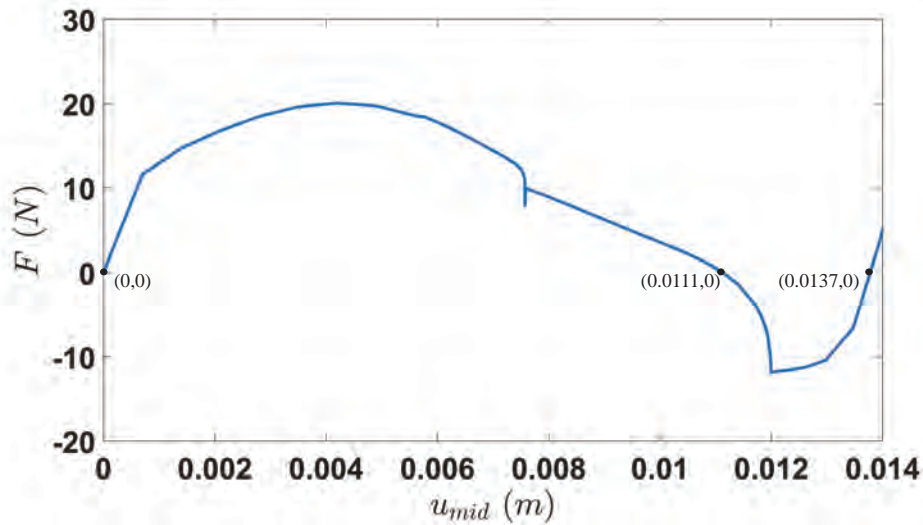


Figure 7.11: Bistable shell with contracting mechanism and grasping arms attached.

considerations for the prototype gripper, and has a sufficiently high $\frac{F_{sb}}{F_s}$ ratio and a low F_s . An ideal $\frac{F_{sb}}{F_s}$ of one implies that the forces required to switch from one state to the other are identical. F_s is kept low so that the gripper can be actuated by hand. The dimensions of the shell were arrived at iteratively for $\frac{F_{sb}}{F_s} > 0.5$ and $F_s < 35$ N.

7.3.3 Switching mechanism and grasping arms

The switching mechanism transmits the force from the actuator to the center of the bistable shell. Hence, the parameters that affect the switching mechanism design are the force and output displacement from the actuator, and the switching force and displacement of the shell. For the bistable shell considered here, $F_s = 20N$ and $u_s = 11.12$ mm. The switching mechanism selected here attaches to the edge of the shell as shown in Fig. 7.8. The force is applied at the protruding part at the top of the central axis of the mechanism. This initiates a contact at the top of the shell. When the deformation at this point of contact exceeds u_s , the shell everts to the second stable state. For other cases where force or displacement amplification is required, the switching mechanism could be designed to be a force or displacement amplifying compliant mechanism without affecting the aforementioned grasping functionality.

Four symmetrically arranged rectangular beams that are attached to the bottom surface of the bistable shell act as the grasping arms that hold objects. In the as-fabricated state of the arch, the grasping arms assume a horizontal configuration. When the shell is in the second stable state, the grasping arms protrude outwards as shown in Fig. 7.9. The grasping arms should be wide apart when the shell is in the second stable state. This is important to hold objects of larger size. This determines the length of the arms and the position at which they are attached to the bottom surface of the shell. For the prototype considered here, beams of length 12 mm attached at a distance of 15 mm from the shell edge satisfy these constraints. When the everted shell comes in contact with stiff objects, it switches back to its initial state. In the process, the grasping arms come together and hold the object firmly. By taking the width of the beam as 5 mm and the depth as 1 mm the grasping arms are compliant enough to wrap around the object, while at the same time, stiff enough to support the weight of the object.

7.3.4 Results and performance

The 3D-printed prototype of the bistable shell and grasping arms in Object Conex 260 is given in Fig. 7.12(a)-(e). The figure illustrates the grasping of a wide range of objects such as: (a) ring (b) paper clip (c) aluminum cylinder (d) mini motor (e) plastic spoon. A complete 3D-printed prototype of the grasping mechanism is given in Fig. 7.12(f)-(h). In Fig. 7.12(f), the gripper with an everted shell comes in contact with a screwdriver, which acts as the object here. The grasping mechanism holds the screwdriver by the bistable shell in Fig. 7.12(g). In Fig. 7.12(h), the gripper releases the screwdriver by

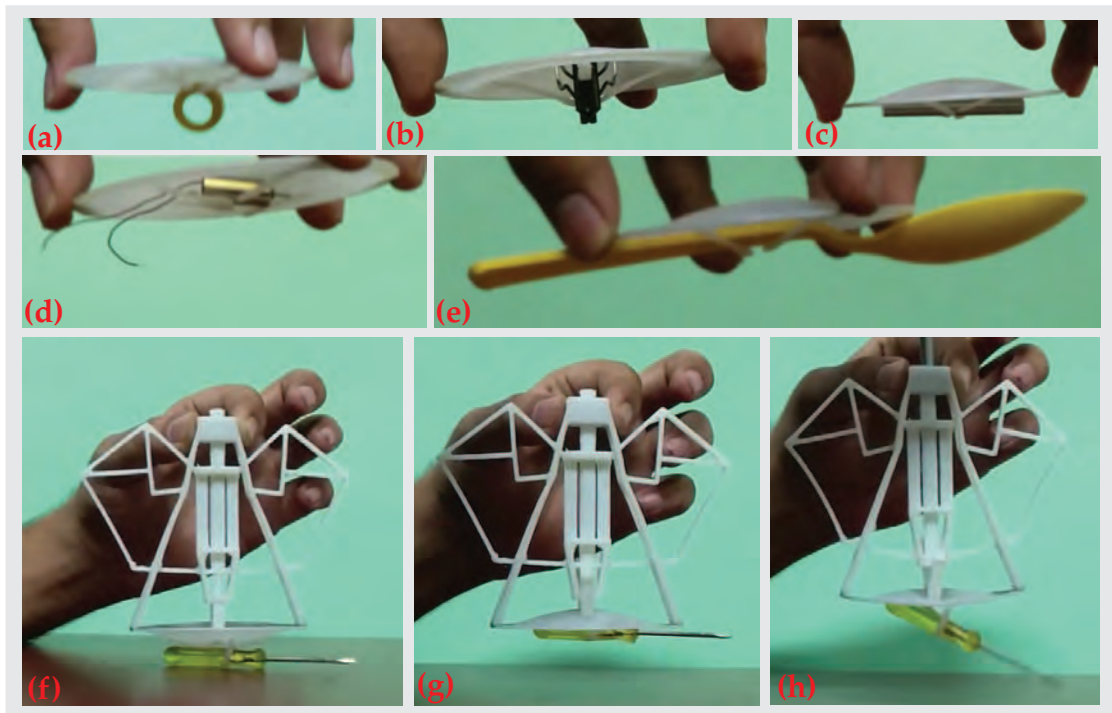


Figure 7.12: Grasping arms can capture objects of varying sizes, shapes, and weights: (a) ring (b) paper clip (c) aluminum cylinder (d) mini motor (e) plastic spoon. 3D-printed prototype made in Object Connex 260. The grasping mechanism (f) grasps a screwdriver, (g) holds, and (h) releases it using the switching mechanism.

actuating at the actuating point of the switching mechanism.

One can note here that the gripper is able to grasp objects with a length larger than the span of the planform of the shell; for example, the plastic spoon in Fig. 7.12(e). This is possible due to the free space left in between the grasping arms by limiting their number to four. If one increases the number of grasping arms, the gripping performance improves but limits the size of the objects that can be grasped due to the reduction in the free space between the grasping arms.

7.4 Closure

Bistable shells are explored with a shape optimization problem to maximize the travel. Optimal bistable shell profiles are obtained with numerical and semi-analytical approaches. Furthermore, a monolithic compliant grasping mechanism based on the bistability of a bistable shell is proposed and illustrated with the aid of a 3D-printed prototype. The salient features of the grasping mechanism include: lower power consumption, ability to grasp objects of a variety of shapes, grasping of stiff objects initiated from contact,

and a completely monolithic design. Both the optimization on shells and the gripper design have scope for improvement. In the next chapter, we summarize the contributions of this thesis and briefly discuss the scope for future work.

Chapter 8

Closure and future work

8.1 Summary

In the preceding chapters, we discussed the analysis, design, and optimization of bistable arches. The statics of the arch such as the force-displacement relationship, arch-profile relationship, and deformation pathways were studied. The key step in the analytical methods developed is to express both the as-fabricated and deformed profiles of the arch with buckling mode shapes of a straight column with the corresponding boundary conditions of the arch. This helped us derive the potential energy and equilibrium equations of the arch for multiple design and analysis cases.

For bistable arches with general boundary conditions, where analytical solutions are intractable, we proposed a semi-analytical strategy to find the critical points on the force-displacement curve. We illustrated with examples that by using critical points, we could design and analyze arches for any given boundary conditions. Furthermore, we obtained optimal profiles of arches for a minimal switching force, a maximum switch-back force and a maximum travel between two configurations.

The closed-form analytical expression is derived for designing arch-profiles. It makes the design extremely easy because just by substituting the mode-weights of the required toggled arch-profile, the as-fabricated shape can be obtained. By checking the positive definiteness of the Hessian matrix, the stability of the obtained design can also be ensured. The bilateral form of the relationship is used for analysis. Here, unlike the critical-point method, the analysis is done without considering the switching and switch-back forces.

A generalized framework of analysis has been developed for spatial arches. Since planar arches are a subset of spatial arches, this model can reproduce the results of planar

analysis and at the same time capture spatial deformation pathways in planar arches as well. We illustrated the importance of spatial analysis in planar arches without which the analysis would lead to incorrect results.

We used the planar analytical model to design a bistable arch that can be used in a bistable RF-MEMS switch. The arch is designed so that it switches with a specified point load at the mid-span and switches back with a specified displacement at one of its ends. Thus, we realize a two-terminal electrically coupled but mechanically decoupled switch.

Furthermore, we also presented our studies on bistable shells. Profiles of bistable shells that maximize travel were obtained using numerical and approaches. By attaching flexible beams, which act as grasping arms, to a bistable shell we designed a passive gripper. The gripper is also universal as it can grasp objects of varying shape and size. In the next section, we list the contributions of this thesis.

8.2 Contributions of the thesis

- A general model of a bistable arch with revolute flexures at the ends, which can be used to design bistable arches of multiple boundary conditions.

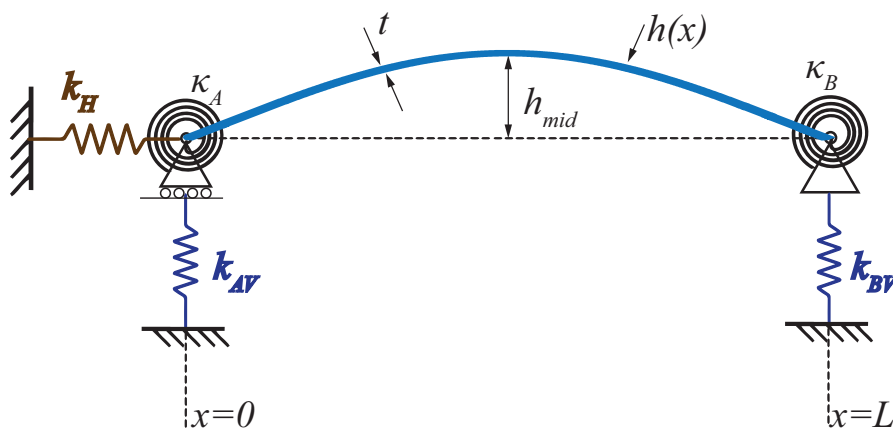


Figure 8.1: Model of a bistable arch with flexures at the ends

- A computationally effective design method for planar bistable arches using three critical points on the force-displacement curve.

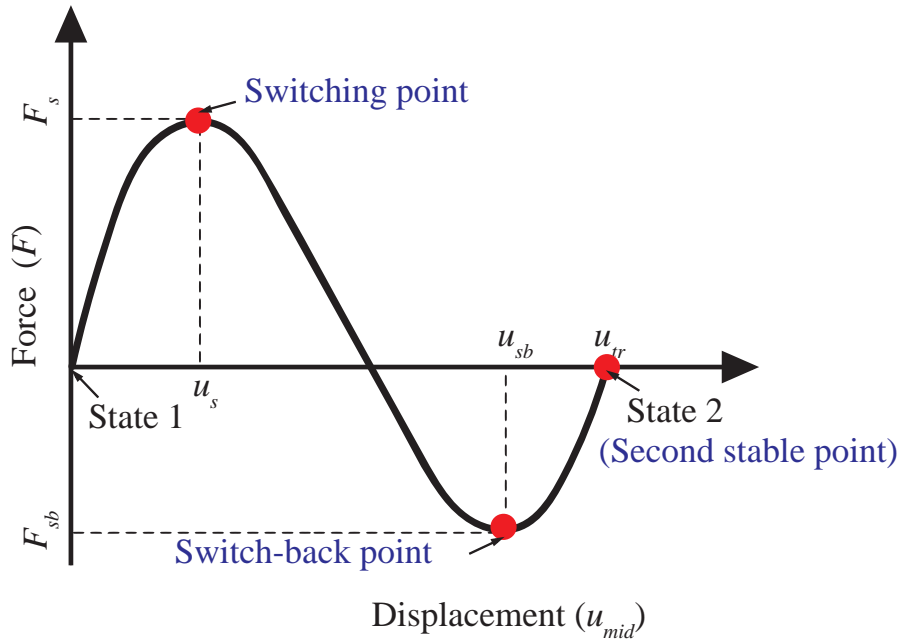


Figure 8.2: Critical points on the force-displacement curve.

- Shape optimization for improving the travel and the switch-back force of the arch using the critical-point method.

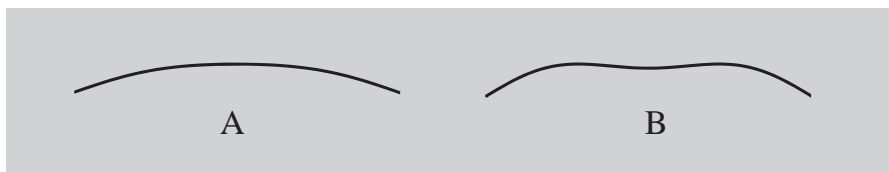


Figure 8.3: Optimal profiles of a bistable arch with split-tube flexure at the ends

- A design method for a new class of asymmetric bistable arches with potential applications owing to their bimodal nature.

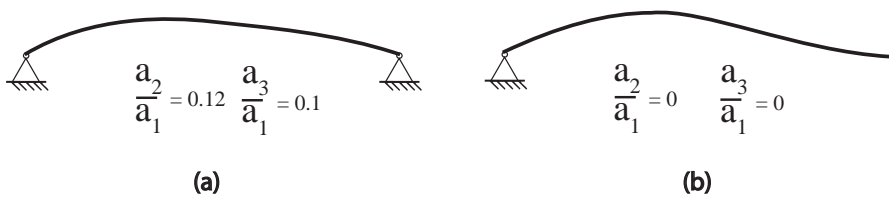


Figure 8.4: Asymmetric bistable arches with (a) asymmetric initial shape and (b) asymmetric boundary conditions designed using the critical-point method.

- An upper bound on the axial compression energy in arches for them to be bistable.

$$\text{For pinned-pinned arches,} \quad 3Q^2C \leq 4\pi^2$$

$$\text{For fixed-fixed arches,} \quad 3Q^2C \leq 8.17\pi^2$$

- Conditions on fundamental mode weights in the arch-profiles of bistable arches.
 1. *If the fundamental mode weight a_1 is zero in the initial profile of an arch, it cannot be bistable.*
 2. *The fundamental mode weight A_1 cannot be zero in the toggled profile of an arch.*
- A bilateral relation between the stable states of bistable arches for design and analysis for pinned-pinned and fixed-fixed boundary conditions.

$$3Q^2 \sum_{i=1}^{\infty} \left\{ \frac{\frac{M_1^2}{M_i^2} \left(1 - \frac{a_1}{A_1}\right) - 2}{\left[1 - \frac{M_1^2}{M_i^2} \left(1 - \frac{a_1}{A_1}\right)\right]^2} \right\} a_i^2 = 1 \quad (8.1)$$

$$a_1 = A_1 \frac{\sum_{i=1}^{\infty} \frac{M_1^2 A_i^2}{M_i^2} - 2 \sum_{i=1}^{\infty} A_i^2 - \frac{1}{3Q^2}}{\sum_{i=1}^{\infty} \frac{M_1^2 A_i^2}{M_i^2}} \quad (8.2)$$

$$A_i = \frac{a_i}{1 - \frac{M_1^2}{M_i^2} \left(1 - \frac{a_1}{A_1}\right)} \quad (8.3)$$

- Results on the symmetries of shapes in the two stable states of arches.
 - 1a. *For $i > 1$, $A_i = 0$ implies $a_i = 0$ and vice versa.*
 - 1b. *The toggled-profile of a bistable arch with a symmetric initial profile will also be symmetric and vice versa.*
 - 1c. *For $i > 1$, $A_i \neq 0$ implies $a_i \neq 0$ and vice versa.*
 - 1d. *The toggled-profile of a bistable arch with an asymmetric initial profile will also be asymmetric and vice versa.*
 - 2a. $(a_1 A_1) < 0$
 - 2b. $(a_{i>1} A_{i>1}) > 0$
 - 3a (inexact). *A_i is approximately equal to a_i for higher values of i .*

3b (inexact). For arch-profiles composed of only a_i s with higher values of i ($i \geq m$) along with a_1 , $a_1^2 - 8 \sum_{i=m}^{\infty} a_i^2 - \frac{4}{3Q^2} > 0$ is necessary and sufficient for bistability.

- A new class of bistable arches, namely, spatial bistable arches.

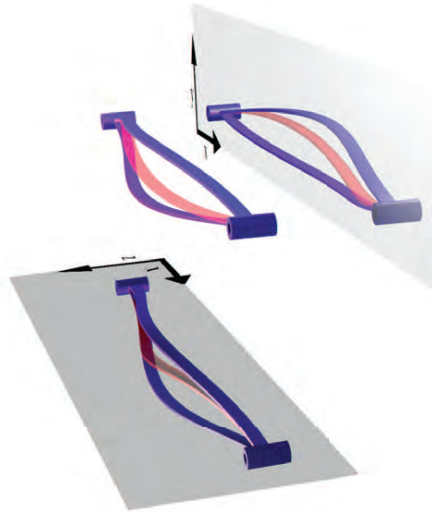


Figure 8.5: A pinned-pinned spatial arch in its as-fabricated stress-free, in-between stressed, and second stressed stable states.

- An analytical model that captures the coupling between in-plane and out-of-plane bending, and the torsion with an extension of the St. Venant and Michell relationship that was given for arches with spatial deformation pathways.

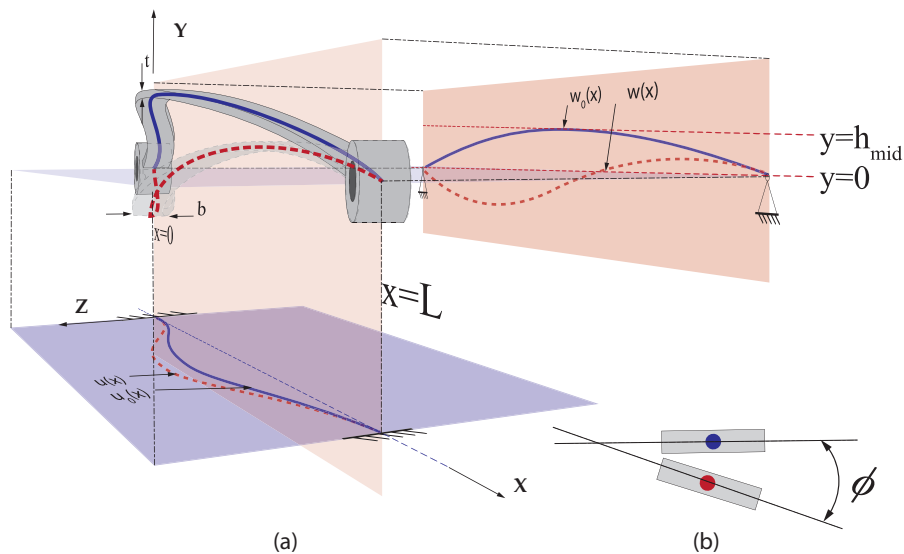


Figure 8.6: A spatial arch with breadth, b , depth, t , span, L , and mid-span height in the xy plane, h_{mid} .

- Analysis on spatial arches with varying as-fabricated shapes and boundary conditions for mid-point and eccentric loading.
- Analysis on spatial deformation pathways in planar arches, which is a special case of the initial profile of spatial arches.

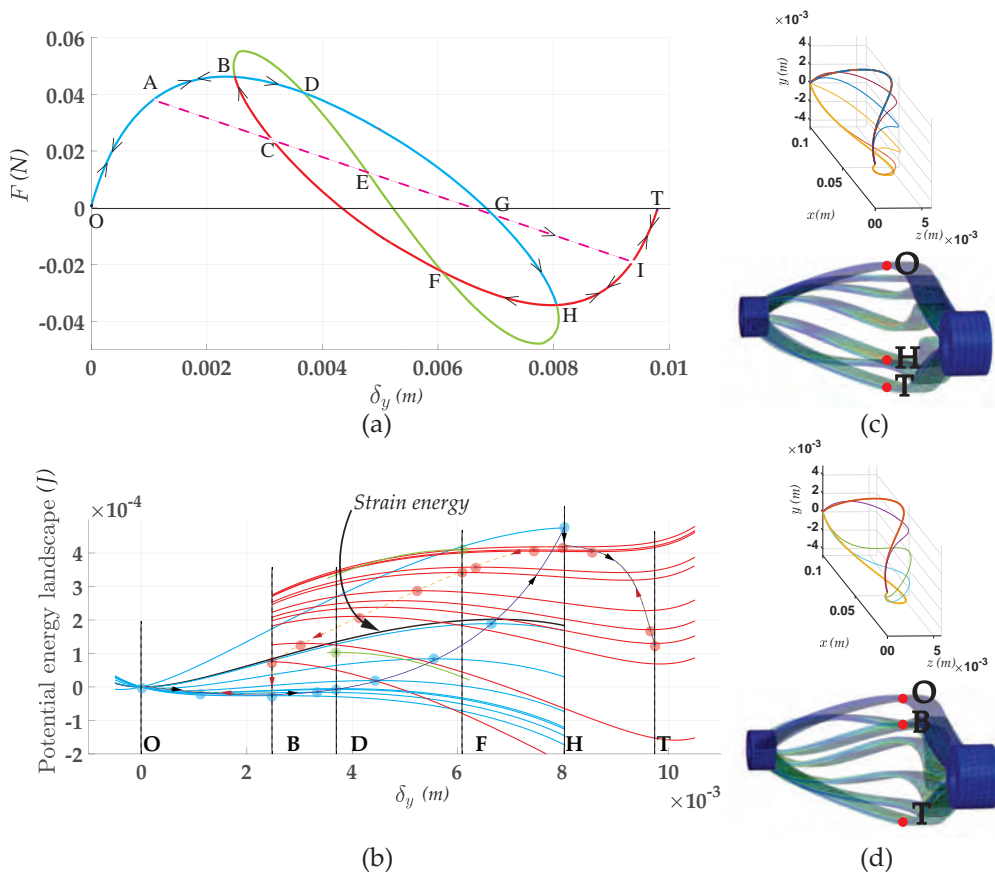


Figure 8.7: Symmetric deformation pathways of a pinned-pinned spatial bistable arch.

8.3 Future work

In this thesis, we discussed the statics of bistable arches. However, in certain applications where the high-speed switching of bistable arches is desirable, dynamic studies are required. Considering dynamics would predict smaller switching and switch-back forces compared to a quasi-static analysis. Even though the dynamics of the snap-through buckling of arches have been well studied, dynamic bistability is not well explored, especially for arches with varying shapes and general boundary conditions.

Interconnected bistable arches are an unexplored area of study. Imagine two arches with pinned-pinned boundary conditions, which are connected at one of their pin joints.

If these two arches are bistable unattached, would they be bistable when connected? Conversely, can two arches that are not bistable be connected to make interconnected bistable arches? Answers to these questions would help in designing intricate interconnected bistable systems.

Our work on bistable shells is preliminary and there is scope for further investigation. An analytical model that can accurately capture compression and bending energies would be one, which is very challenging due to the involved nonlinearity. The presented design of the universal passive gripper can also be improved. The cosine profile is not the only shape that shows bistability with fixed-fixed boundary conditions. For example, selecting the fundamental buckling mode of a circular plate with fixed-fixed boundary conditions as the as-fabricated shape also shows bistability. Furthermore, optimizing the arch-profile that fits into design constraints can improve the function of the grasper.

The gripper presented here holds objects that are stiff. However, the grasping of delicate objects cannot be initiated from contact as it would apply excessive force on them. One possibility in holding such soft objects is to initiate the contraction of grasping arms actively, i.e., not from contact with the object. This functionality could be achieved by redesigning the switching mechanism and the bistable shell. The profile, orientation, cross-section parameters and the number of grasping arms can significantly improve the gripping performance. An optimal design that considers the compliance, strength, and volume of the grasping arms could be an addition to the present design.

Appendix A

An analytical model of electrothermal actuator

The analysis of a generic electrothermal actuator involves three energy domains: electrical, thermal and elastic. In the electrical domain, the current distribution is determined for an applied voltage, which causes Joule heating. By accounting for Joule heating as internal heat generation and considering heat transfer through convection and conduction (Mankame and Ananthasuresh, 2001), the temperature distribution is calculated in the thermal domain. Non-uniform temperature distribution will give rise to a thermally-induced strain to cause deformation, which is used in the elastic domain. Table A.1 lists the constants involved in the modeling of a V-beam electrothermal actuator and the design parameters are denoted by:

- V : Voltage
- b : Out of plane thickness of beams
- w : In-plane thickness of beams
- d : Central offset of beams
- l : Length of beams
- N : Number of beams

The transient temperature distribution (Maloney et al., 2003) along the beams of the V-beam actuator is given by

$$T = T_{\infty} + \sum_{n=1}^{\infty} \frac{\xi_n}{\gamma_n + \beta} [1 - e^{-(\gamma_n + \beta)t}] \sin\left(\frac{n\pi x}{l}\right) \quad (\text{A.1})$$

$$\text{where, } \xi_n = \frac{2}{cpn\pi} \frac{V^2}{\rho l^2} [1 - \cos(n\pi)], \quad \gamma_n = \frac{n^2 \pi^2 k_s}{l^2 cp}, \quad \beta = \frac{h}{bcp}$$

	Parameter	Value	Unit
c	Specific heat, silicon	700	J/kg-K
E	Elastic modulus, silicon	170	GPa
k_s	Thermal conductivity, silicon	130	W/m-K
p	Density, silicon	2330	kg/m ³
T_∞	Ambient temperature	298	K
α	Thermal expansion coefficient	2.6×10^{-6}	K ⁻¹
ρ	Resistivity, silicon	2.5×10^{-4}	$\Omega\text{-m}$

Table A.1: Parameters Involved In Actuator Modeling

The axial stiffness, k_v , and the transient force, F_v , generated by the V-beam actuator are given by

$$k_v = \frac{16wbE(d^2 + w^2)}{l^3} N \quad (\text{A.2})$$

$$F_v = \frac{4\alpha wbEdN}{\pi l} \sum_{n=1}^{\infty} \frac{1}{n} \frac{\xi_n}{\gamma_n + \beta} [1 - \cos(n\pi)] (1 - e^{-(\gamma_n + \beta)t}) \quad (\text{A.3})$$

The transient force is obtained by using Maizel's theorem (Kovalenko, 1969). For the converging series, Eq. (A.3), the first term gives the time constant, θ , of the V-beam actuator as

$$\theta = \frac{1}{\gamma_1 + \beta} \quad (\text{A.4})$$

The axial load and the maximum stress in the actuator are represented respectively as

$$F_{axial} = F_v \frac{dl}{4N(d^2 + w^2)} \quad (\text{A.5})$$

$$\sigma_{\max} = F_v \frac{l}{Nb(d^2 + w^2)} \left(3 + \frac{d}{4w} \right) \quad (\text{A.6})$$

The power consumption of the V-beam actuator is obtained as

$$Power = \frac{VbwN}{\rho l} \quad (\text{A.7})$$

The initially-retracting actuator is composed of an integrated pair of V-beam actuators with different lengths opposing each other's motion. So, the resultant force of the initially-retracting actuator is the difference of the forces due to the two embedded actuators, individually given by Eq. (A.3). Similarly, the total axial stiffness and power

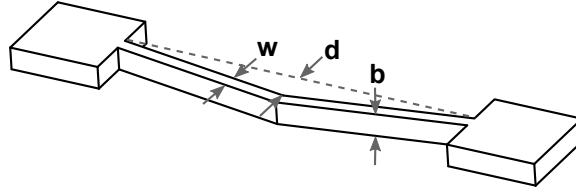


Figure A.1: Geometric parameters of an actuator beam.

consumption of the initially-retracting actuator will be a summation of the respective quantities of the two embedded actuators. Hence, the displacement of the initially-retracting actuator is given by

$$u = \frac{F_{v1} - F_{v2}}{k_{v1} + k_{v2} + k_{ext}} \quad (\text{A.8})$$

where the subscripts 1 and 2 denote the values for the two embedded actuators and k_{ext} is the stiffness of the object being actuated i.e., the arch in this case. The time of inflection, τ , for the initially-retracting actuator is obtained by solving for the time instant, where the derivative of Eq. (A.8) with respect to time is zero. The expression for τ is given by

$$\tau = \frac{cpl_1^2 l_2^2}{\pi^2 k_s (l_2^2 - l_1^2)} \log \left(\frac{w_1 d_1 N_1 l_2^3}{w_2 d_2 N_2 l_1^3} \right) \quad (\text{A.9})$$

The maximum temperature and stress occur in the set of smaller beams in the initially-retracting actuator.

Appendix B

Design of bistable arches using a non-dimensional kinetoelastostatic map

A kinetoelastostatic (KES) map is an excellent tool to design the size of the compliant mechanism once its shape and topology are fixed (Bhargav et al., 2013). The map is called kinetoelastostatic because it considers elastic deformation kinematics under static conditions. The map uses non-dimensional quantities so that the intrinsic behaviour of the mechanism is captured without being affected by its size and material as well as by the forces acting on it. Thus, a few force and stress curves plotted against displacement on the KES map can be used to obtain similar design curves for a large number of mechanisms with different sizes and material properties.

We demonstrate the construction and utility of a KES map for bistable arches using a design example of a fixed-fixed arch. Consider a double-cosine arch with span L , height h , thickness t , out of plane width b , Young's modulus E , and slenderness ratio $s = \frac{L}{t}$. A KES map for displacement at the mid-point, u_{mid} , can be generated by plotting $\frac{u}{L}$ against $\eta = \frac{Fs^2}{Etb}$ for different $\frac{L}{h}$ ratios as shown by the solid curves in Fig. B.1. Similarly, the dashed curves in Fig. B.1 are the KES map for stress, where $\frac{\sigma s}{E}$ is plotted against $\eta = \frac{Fs^2}{Etw}$. To generate each curve on the map, an analysis for the corresponding $\frac{L}{h}$ is required. In this case, the analysis is done in finite element software Comsol. However, as mentioned before, these few analyses give us the benefit of numerous FEA analyses for arches with various sizes and material properties.

Consider the design of a fixed-fixed arch with the following design requirements:

- $L \leq 30$ mm
- Travel of the mid-point of the arch (u_{tr}) ≥ 13 mm

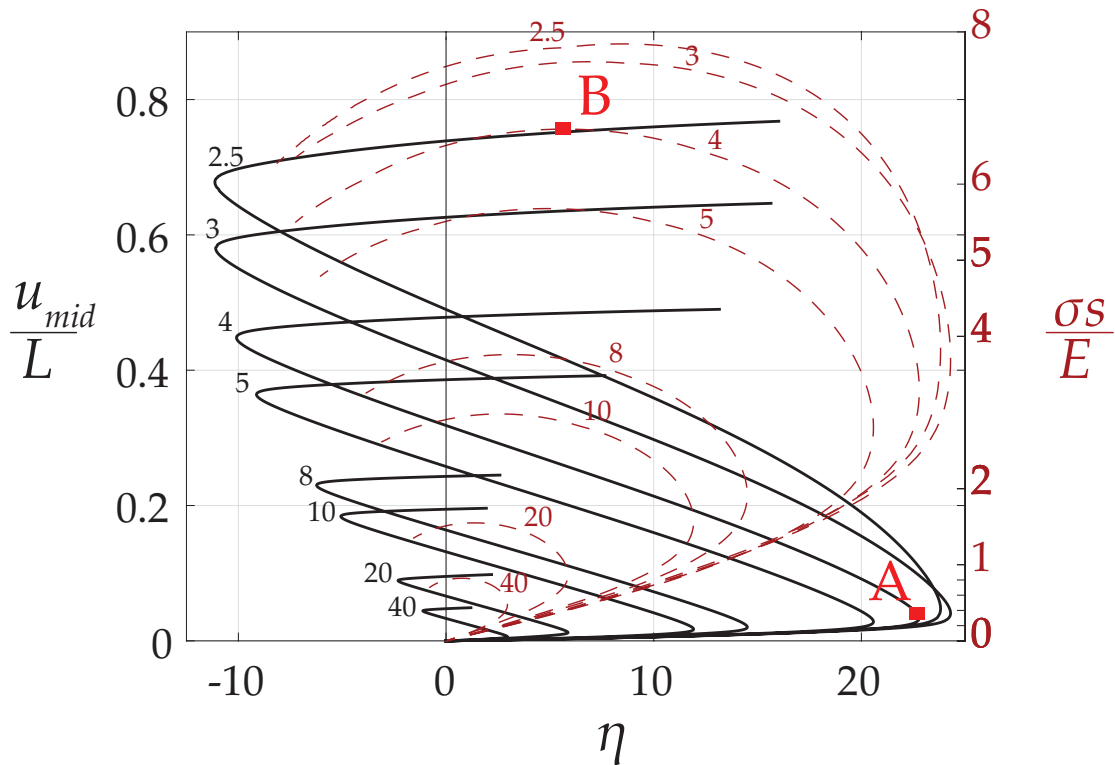


Figure B.1: Kinetoelastostatic map for fixed-fixed bistable arches.

- Switching force = 50 N
- Material of the arch - spring steel

Let us take the span of the beam to be $L = 30$ mm. The travel of the midpoint of the arch is the distance traveled by the midpoint between the two stable states of the arch. On the KES map, this corresponds to the third point of intersection of the solid curves on the vertical axis at $\eta = 0$. Usually this measure is a little less than twice the height of an arch. To get a travel greater than 13 mm, let us take the height, $h = 7.5$ mm. Thus, the L/h ratio can be obtained as:

$$\frac{L}{h} = \frac{30}{7.5} = 4 \quad (\text{B.1})$$

We select the values of L and h such that a curve of that $\frac{L}{h}$ exists on the map. If that is not possible, we can obtain the curve of the required $\frac{L}{h}$ ratio by interpolating between the existing $\frac{L}{h}$ curves.

Thickness t , and width b , can be calculated once we obtain the η value. For $\frac{L}{h} = 4$, the η value corresponding to the switching force, F_s , is marked by the point A in

Fig. B.1. At point A, we note that $\eta = 22.79$. Now to obtain t and b we have:

$$\eta = \frac{F_s s^2}{Ebt} = \frac{F_s L^2}{Ebt^3} \quad (\text{B.2})$$

$$\implies 22.786 = \frac{50 \times (30e - 3)^2}{210e9 \times bt^3} \quad (\text{B.3})$$

$$\implies bt^3 = 9.4e - 15 \text{ mm}^4 \quad (\text{B.4})$$

Thus, for $b = 1 \text{ mm}$, t should be 0.21 mm , which completes our design.

The maximum stress in the mechanism can be obtained from the stress-curve corresponding to $\frac{L}{h} = 4$. The maximum $\frac{\sigma s}{E}$ value for $\frac{L}{h} = 4$, denoted by point B on the dashed curve in Fig. B.1, is 6.62 , i.e.,

$$\frac{\sigma s}{E} = 6.62 \quad (\text{B.5})$$

$$\implies \sigma = 9268 \text{ MPa} \quad (\text{B.6})$$

The verification of this design in Comsol Multiphysics is given in Fig B.2. It is evident that the travel is greater than 13 mm and the switching force is 50 N . The maximum stress obtained from Comsol is 9824 MPa .

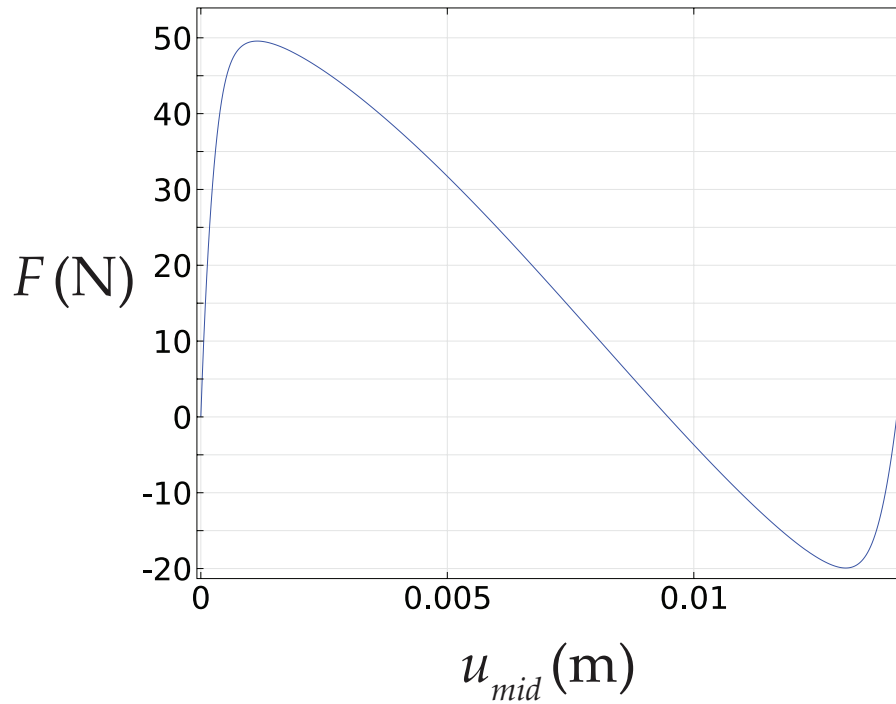


Figure B.2: Force-displacement curve for a bistable arch designed using a KES map simulated in Comsol Multiphysics 5.0

Bibliography

- ABAQUS, C. (2015). Analysis user manual, version 2016.
- Akkas, N. and Odeh, G. (2001). A novel snap-through buckling behaviour of axisymmetric shallow shells with possible application in transducer design. *Computers & Structures*, 79(29):2579–2585.
- Amend, J. R., Brown, E., Rodenberg, N., Jaeger, H. M., and Lipson, H. (2012). A positive pressure universal gripper based on the jamming of granular material. *IEEE Transactions on Robotics*, 28(2):341–350.
- Baker, M. S. and Howell, L. L. (2002). On-chip actuation of an in-plane compliant bistable micromechanism. *Journal of microelectromechanical systems*, 11(5):566–573.
- Balakuntala, M. V. S., Palathingal, S., and Ananthasuresh, G. K. (2018). A passive universal grasping mechanism based on an everting shell. to be presented at the 5th Asian Mechanism and Machine Science Conference, Dec 2018.
- Bhargav, S. D., Varma, H. I., and Ananthasuresh, G. (2013). Non-dimensional kinetoelastostatic maps for compliant mechanisms. In *ASME 2013 International Design Engineering Technical Conferences and Computers and Information in Engineering Conference*, pages V06AT07A018–V06AT07A018. American Society of Mechanical Engineers.
- Bicchi, A. and Kumar, V. (2000). Robotic grasping and contact: A review. In *ICRA*, volume 348, page 353. Citeseer.
- Biezeno, C. (1938). Throwing a weakly twisted rod. *ZAMM-Journal of Applied Mathematics and Mechanics / Applied Mathematics and Mechanics*, 18(1):21–30.
- Brown, E., Rodenberg, N., Amend, J., Mozeika, A., Steltz, E., Zakin, M. R., Lipson, H., and Jaeger, H. M. (2010). Universal robotic gripper based on the jamming of granular material. *Proceedings of the National Academy of Sciences*, 107(44):18809–18814.
- Budiansky, B. and Roth, R. S. (1962). Axisymmetric dynamic buckling of clamped shallow spherical shells. *1962.*, pages 597–606.

- Cazottes, P., Fernandes, A., Pouget, J., and Hafez, M. (2009). Bistable buckled beam: modeling of actuating force and experimental validations. *Journal of Mechanical Design*, 131(10):101001.
- Chen, J.-S. and Chang, Y.-Y. (2007). On the unsymmetrical deformation and reverse snapping of a spinning non-flat disk. *International Journal of Non-Linear Mechanics*, 42(8):1000–1009.
- Chen, J.-S. and Huang, T.-M. (2006). Deformation and reverse snapping of a circular shallow shell under uniform edge tension. *International journal of solids and structures*, 43(25):7776–7792.
- Chen, J.-S. and Hung, S.-Y. (2012). Exact snapping loads of a buckled beam under a midpoint force. *Applied Mathematical Modelling*, 36(4):1776–1782.
- Chen, J.-S. and Lin, C.-C. (2005a). Axisymmetrical snapping of a spinning nonflat disk. *Journal of applied mechanics*, 72(6):879–886.
- Chen, J.-S. and Lin, J.-S. (2005b). Exact critical loads for a pinned half-sine arch under end couples. *ASME Journal of Applied Mechanics* 72:, pages 147–148.
- Chen, J.-S., Ro, W.-C., and Lin, J.-S. (2009). Exact static and dynamic critical loads of a sinusoidal arch under a point force at the midpoint. *International Journal of Non-Linear Mechanics*, 44(1):66–70.
- Chen Jen-San and Lin Jian-San (2004). Effects of Prescribed End Motion on the Dynamic Stability of a Shallow Arch on an Elastic Foundation. *Journal of Engineering Mechanics*, 130(3):359–362.
- Choi, H. and Koc, M. (2006). Design and feasibility tests of a flexible gripper based on inflatable rubber pockets. *International Journal of Machine Tools and Manufacture*, 46(12-13):1350–1361.
- Chwalla, E. (1927). Die Stabilität eines elastisch gebetteten Druckstabes. *ZAMM - Zeitschrift für Angewandte Mathematik und Mechanik*, 7(4):276–284.
- Daneshmand, M. and Mansour, R. R. (2011). Rf mems satellite switch matrices. *IEEE Microwave magazine*, 12(5):92–109.
- Dellaert, D. and Doutreligne, J. (2014). Compact thermally actuated latching mems switch with large contact force. *Electronics Letters*, 51(1):80–81.
- Euler, L. (1744). *Methodus inveniendi lineas curvas maximi minimive proprietate gaudentes*. apud Marcum-Michaelem Bousquet.
- Fitch, J. R. (1968). The buckling and post-buckling behavior of spherical caps under concentrated load. *International Journal of Solids and Structures*, 4(4):421–446.
- Friedrichs, K. O. (1945). *Lectures on Non-linear Elasticity*.

- Fulton, R. E. and Barton, F. W. (1971). Dynamic buckling of shallow arches. *Journal of the Engineering Mechanics Division*, 97(3):865–877.
- Fung, Y.-C. and Kaplan, A. (1952). Buckling of low arches or curved beams of small curvature. *National Advisory Committee for Aeronautics; Washington, DC, United States, Technical Note 2840*, page 78.
- Gjelsvik, A. and Bodner, S. (1962). The energy criterion and snap buckling of arches. *J. Eng. Mech. Div*, 88(5):87–134.
- Goldfarb, M. and Speich, J. E. (1999). A well-behaved revolute flexure joint for compliant mechanism design. *Journal of Mechanical Design*, 121(3):424–429.
- Gomez, M., Moulton, D. E., and Vella, D. (2017). Critical slowing down in purely elastic snap-through instabilities. *Nature Physics*, 13(2):142.
- Gregory, W. E. and Plaut, R. H. (1982). Dynamic stability boundaries for shallow arches. *Journal of the Engineering Mechanics Division*, 108(6):1036–1050.
- Guest, S. and Pellegrino, S. (2006). Analytical models for bistable cylindrical shells. In *Proceedings of the Royal Society of London A: Mathematical, Physical and Engineering Sciences*, volume 462, pages 839–854. The Royal Society.
- Hoff, N. J. and Bruce, V. G. (1953). Dynamic analysis of the buckling of laterally loaded flat arches. *Studies in Applied Mathematics*, 32(1-4):276–288.
- Holmes, D. P. (2019). Elasticity and stability of shape-shifting structures. *Current Opinion in Colloid & Interface Science*, 40:118–137.
- Hsu, C. S. (1966). On dynamic stability of elastic bodies with prescribed initial conditions. *International Journal of Engineering Science*, 4(1):1–21.
- Hsu, C. S. (1967). The Effects of Various Parameters on the Dynamic Stability of a Shallow Arch. *Journal of Applied Mechanics*, 34(2):349–358.
- Hsu, C. S. (1968a). Equilibrium configurations of a shallow arch of arbitrary shape and their dynamic stability character. *International Journal of Non-Linear Mechanics*, 3(2):113–136.
- Hsu, C. S. (1968b). Equilibrium configurations of a shallow arch of arbitrary shape and their dynamic stability character. *International Journal of Non-Linear Mechanics*, 3(2):113–136.
- Hsu, C. S. (1968c). Stability of Shallow Arches Against Snap-Through Under Timewise Step Loads. *Journal of Applied Mechanics*, 35(1):31–39.
- Hu, N. and Burgueño, R. (2015). Buckling-induced smart applications: recent advances and trends. *Smart Materials and Structures*, 24(6):063001.
- Hu, T., Zhao, Y., Li, X., Zhao, Y., and Bai, Y. (2016). Design and characterization of

- a microelectromechanical system electro-thermal linear motor with interlock mechanism for micro manipulators. *Review of Scientific Instruments*, 87(3):035001.
- Huang, H.-W., Lee, F.-W., and Yang, Y.-J. J. (2016). Design criteria for a push-on push-off mems bistable device. *Journal of Microelectromechanical Systems*, 25(5):900–908.
- Huang, H.-W. and Yang, Y.-J. (2013). A mems bistable device with push-on–push-off capability. *Journal of Microelectromechanical Systems*, 22(1):7–9.
- Huang, N.-C. (1964). Unsymmetrical buckling of thin shallow spherical shells. *Journal of Applied Mechanics*, 31(3):447–457.
- Huang, N. C. and Nachbar, W. (1968). Dynamic Snap-Through of Imperfect Viscoelastic Shallow Arches. *Journal of Applied Mechanics*, 35(2):289–296.
- Huddleston, J. V. (1970). Behavior of a steep prestressed arch made from a buckled strut. ASME.
- Humphreys, J. S. (1966). On dynamic snap buckling of shallow arches. *AIAA J*, 4(5):878–886.
- Hurlbrink, E. (1907). Festigkeits-Berechnung von rohrenartigen Korpern, die unter ausserem Drucke stehen. *Schiffbau*, 1908:517–523.
- Iqbal, K. and Pellegrino, S. (2000). Bi-stable composite shells. In *41st Structures, Structural Dynamics, and Materials Conference and Exhibit*, page 1385.
- Iqbal, K., Pellegrino, S., and Daton-Lovett, A. (2000). Bi-stable composite slit tubes. In *IUTAM-IASS Symposium on deployable structures: Theory and Applications*, pages 153–162. Springer.
- Johnson, E. (1980). The effect of damping on dynamic snap-through. *Journal of Applied Mechanics*, 47(3):601–606.
- Johnson, E. R. and McIvor, I. K. (1978). The Effect of Spatial Distribution on Dynamic Snap-Through. *Journal of Applied Mechanics*, 45(3):612–618.
- Kaplan, A. and Fung, Y. (1954). A nonlinear theory of bending and buckling of thin elastic shallow spherical shells.
- Karman, T. V. (1939). The buckling of spherical shells by external pressure. *Journal of the Aeronautical Sciences*, 7(2):43–50.
- Kebadze, E., Guest, S., and Pellegrino, S. (2004). Bistable prestressed shell structures. *International Journal of Solids and Structures*, 41(11):2801–2820.
- Koiter, W. T. (1970). The stability of elastic equilibrium. Technical report, Stanford Univ Ca Dept of Aeronautics and Astronautics.
- Kovalenko, A. (1969). *Thermoelasticity-Basic theory and Applications*. Walters-

- Noordhoff Publishing.
- Laliberté, T., Birglen, L., and Gosselin, C. (2002). Underactuation in robotic grasping hands. *Machine Intelligence & Robotic Control*, 4(3):1–11.
- Lee, C. and Wu, C.-Y. (2004). Study of electrothermal v-beam actuators and latched mechanism for optical switch. *Journal of Micromechanics and Microengineering*, 15(1):11.
- Lee, J.-H., Lee, M.-H., Jang, W.-I., Choi, C.-A., and Joo, J. W. (1999). Bistable planar polysilicon microactuator with shallow arch-shaped leaf springs. pages 274–279, Santa Clara, CA.
- Lin, J.-S. and Chen, J.-S. (2003). Dynamic snap-through of a laterally loaded arch under prescribed end motion. *International Journal of Solids and Structures*, 40(18):4769–4787.
- Lo, D. L. and Masur, E. F. (1976). Dynamic buckling of shallow arches. *Journal of the Engineering Mechanics Division*, 102(5):901–917.
- Lock, M. H. (1966). Snapping of a shallow sinusoidal arch under a step pressure load. *AIAA Journal*, 4(7):1249–1256.
- Love, A. E. H. (2013). *A treatise on the mathematical theory of elasticity*. Cambridge university press.
- Maloney, J. M., Schreiber, D. S., and DeVoe, D. L. (2003). Large-force electrothermal linear micromotors. *Journal of Micromechanics and Microengineering*, 14(2):226.
- Mankame, N. D. and Ananthasuresh, G. (2001). Comprehensive thermal modelling and characterization of an electro-thermal-compliant microactuator. *Journal of Micromechanics and Microengineering*, 11(5):452.
- Manti, M., Cacucciolo, V., and Cianchetti, M. (2016). Stiffening in soft robotics: a review of the state of the art. *IEEE Robotics & Automation Magazine*, 23(3):93–106.
- Marguerre, K. (1938). The force of a weakly curved bar. *seat. Berlin Math. Ges.*, 37(92):92–108.
- Maruyama, R., Watanabe, T., and Uchida, M. (2013). Delicate grasping by robotic gripper with incompressible fluid-based deformable fingertips. In *Intelligent Robots and Systems (IROS), 2013 IEEE/RSJ International Conference on*, pages 5469–5474. IEEE.
- Masters, N. D. and Howell, L. L. (2003). A self-retracting fully compliant bistable micromechanism. *Journal of Microelectromechanical Systems*, 12(3):273–280.
- Masur, E. F. and Lo, D. L. C. (1972). The shallow arch general buckling, postbuckling, and imperfection analysis. *Journal of Structural Mechanics*, 1(1):91–112.

- Medina, L., Gilat, R., and Krylov, S. (2016). Bistable behavior of electrostatically actuated initially curved micro plate. *Sensors and Actuators A: Physical*, 248:193–198.
- Mohri, F., Azrar, L., and Potier-Ferry, M. (2002). Lateral post-buckling analysis of thin-walled open section beams. *Thin-Walled Structures*, 40(12):1013–1036.
- Moulton, T. and Ananthasuresh, G. K. (2001). Micromechanical devices with embedded electro-thermal-compliant actuation. *Sensors and Actuators A: Physical*, 90(1-2):38–48.
- Murray, R. M. (2017). *A mathematical introduction to robotic manipulation*. CRC press.
- Navier, C. L. M. H. (1864). *Rsum des Leons sur l'Application de la Mcanique*, volume 2. Dunod.
- Nguyen, T.-A. and Wang, D.-A. (2016). A gripper based on a compliant bistable mechanism for gripping and active release of objects. In *Manipulation, Automation and Robotics at Small Scales (MARSS), International Conference on*, pages 1–4. IEEE.
- Ojalvo, M., Demuts, E., and Tokarz, F. (1969). Out-of-plane buckling of curved members. *Journal of the Structural Division*, 95(10):2305–2318.
- Palathingal, S. and Ananthasuresh, G. (2017a). Design of bistable pinned-pinned arches with torsion springs by determining critical points. In *Mechanism and Machine Science: Proceedings of ASIAN MMS 2016 & CCMMS 2016, December, Guangzhou, China*, pages 677–688. Springer.
- Palathingal, S. and Ananthasuresh, G. (2018). A bilateral relationship between stable profiles of pinned-pinned bistable shallow arches. *International Journal of Solids and Structures*, 143:183 – 193.
- Palathingal, S. and Ananthasuresh, G. K. (2017b). Design of bistable arches by determining critical points in the force-displacement characteristic. *Mechanism and Machine Theory*, 117:175–188.
- Palathingal, S. and Ananthasuresh, G. K. (2019a). Analysis and Design of FixedFixed Bistable Arch-Profiles Using a Bilateral Relationship. *Journal of Mechanisms and Robotics*, 11(3):031002.
- Palathingal, S. and Ananthasuresh, G. K. (2019b). Analytical modelling of spatial deformation pathways in planar and spatial shallow bistable arches. *Proceedings of the Royal Society A: Mathematical, Physical and Engineering Sciences*.
- Palathingal, S., Sarojini, D., Katti, A. N., and Ananthasuresh, G. K. (2015). A generalized method to investigate the bistability of curved beams using buckling analysis. In *2nd International and 17th National Conference on Machines and Mechanisms, December, Kanpur, India*, page 73. iNaCoMM.

- Papangelis, J. P. and Trahair, N. S. (1987). *Flexural-torsional buckling of arches*. University of Sydney.
- Patricio, P., Adda-Bedia, M., and Amar, M. B. (1998). An elastica problem: instabilities of an elastic arch. *Physica D: Nonlinear Phenomena*, 124(1-3):285–295.
- Patricio, P., Adda-Bedia, M., and Ben Amar, M. (1998). An elastica problem: instabilities of an elastic arch. *Physica D: Nonlinear Phenomena*, 124(1):285–295.
- Pellegrini, S. P., Tolou, N., Schenk, M., and Herder, J. L. (2013). Bistable vibration energy harvesters: a review. *Journal of Intelligent Material Systems and Structures*, 24(11):1303–1312.
- Pi, Y.-L., Bradford, M., and Tong, G.-S. (2010). Elastic lateral–torsional buckling of circular arches subjected to a central concentrated load. *International Journal of Mechanical Sciences*, 52(6):847–862.
- Pippard, A. (1990). The elastic arch and its modes of instability. *European Journal of Physics*, 11(6):359.
- Pirmoradi, E., Mirzajani, H., and Ghavifekr, H. B. (2015). Design and simulation of a novel electro-thermally actuated lateral rf mems latching switch for low power applications. *Microsystem technologies*, 21(2):465–475.
- Plaut, R. and Virgin, L. (2009). Vibration and snap-through of bent elastica strips subjected to end rotations. *Journal of Applied Mechanics*, 76(4):041011.
- Plaut, R. H. (1979). Influence of load position on the stability of shallow arches. *Zeitschrift für angewandte Mathematik und Physik ZAMP*, 30(3):548–552.
- Pontecorvo, M. E., Barbarino, S., Murray, G. J., and Gandhi, F. S. (2013). Bistable arches for morphing applications. *Journal of Intelligent Material Systems and Structures*, 24(3):274–286.
- Qiu, J., Lang, J. H., and Slocum, A. H. (2004). A curved-beam bistable mechanism. *Journal of microelectromechanical systems*, 13(2):137–146.
- Qiu, J., Lang, J. H., Slocum, A. H., and Weber, A. C. (2005). A bulk-micromachined bistable relay with u-shaped thermal actuators. *Microelectromechanical Systems, Journal of*, 14(5):1099–1109.
- Que, L., Udeshi, K., Park, J., and Gianchandani, Y. B. (2004). A bi-stable electro-thermal rf switch for high power applications. In *Micro Electro Mechanical Systems, 2004. 17th IEEE International Conference on.(MEMS)*, pages 797–800. IEEE.
- Reis, P. M. (2015). A perspective on the revival of structural (in) stability with novel opportunities for function: from buckliphobia to buckliphilia. *Journal of Applied Mechanics*, 82(11):111001.

- Sanayei, S. and Nosratinia, A. (2004). Antenna selection in mimo systems. *IEEE Communications Magazine*, 42(10):68–73.
- Sano, T. G. and Wada, H. (2019). Twist-induced snapping in a bent elastic rod and ribbon. *Physical Review Letters*, 122(11):114301.
- Sarojini, D., Lassche, T., Herder, J., and Ananthasuresh, G. (2016). Statically balanced compliant two-port bistable mechanism. *Mechanism and Machine Theory*, 102:1–13.
- Schreyer, H. L. and Masur, E. F. (1966). Buckling of shallow arches. *Journal of the Engineering Mechanics Division*, 92(4):1–20.
- Seffen, K. A. and Guest, S. D. (2011). Prestressed morphing bistable and neutrally stable shells. *Journal of Applied Mechanics*, 78(1):011002.
- Simitses, G. J. (1973). Snapping of Low Pinned Arches on an Elastic Foundation. *Journal of Applied Mechanics*, 40(3):741–744.
- Simitses, G. J. and Hodges, D. H. (2006). *Fundamentals of structural stability*. Butterworth-Heinemann.
- Sobota, P. M. and Seffen, K. A. (2017). Effects of boundary conditions on bistable behaviour in axisymmetrical shallow shells. *Proceedings of the Royal Society A: Mathematical, Physical and Engineering Science*, 473(2203):20170230.
- Stavenuiter, R. A., Birglen, L., and Herder, J. L. (2017). A planar underactuated grasper with adjustable compliance. *Mechanism and Machine Theory*, 112:295–306.
- Steiner, H., Hortschitz, W., Stifter, M., and Keplinger, F. (2014). Thermal actuated passive bistable mems switch. In *Microelectronic Systems Symposium (MESS), 2014*, pages 1–5. IEEE.
- Sterner, M., Roxhed, N., Stemme, G., and Oberhammer, J. (2007). Coplanar-waveguide embedded mechanically-bistable dc-to-rf mems switches. In *Microwave Symposium, 2007. IEEE/MTT-S International*, pages 359–362. IEEE.
- Sundararajan, V. and Kumani, D. (1972). Dynamic snap-buckling of shallow arches under inclined loads. *AIAA Journal*, 10(8):1090–1091.
- Taffetani, M., Jiang, X., Holmes, D. P., and Vella, D. (2018). Static bistability of spherical caps. *Proceedings of the Royal Society A: Mathematical, Physical and Engineering Sciences*, 474(2213):20170910.
- Timoshenko, S. P. (1936). *Theory of Elastic Stability*, by S. Timoshenko... McGraw-Hill Book Company, Incorporated.
- Vangbo, M. (1998). An analytical analysis of a compressed bistable buckled beam. *Sensors and Actuators A: Physical*, 69(3):212–216.
- Varadan, V. K., Vinoy, K. J., and Jose, K. A. (2003). *RF MEMS and their applications*.

John Wiley & Sons.

Vlasov, V. Z. (1959). Thin-walled elastic beams. *PST Catalogue*, 428.

Weight, B. L., Howell, L. L., Lyon, S. M., and Wait, S. M. (2002). Two-position micro latching mechanism requiring a single actuator. In *ASME 2002 International Design Engineering Technical Conferences and Computers and Information in Engineering Conference*, pages 797–803. American Society of Mechanical Engineers.

Yadav, D. and Ananthasuresh, G. K. (2018). A novel initially-retracting electrothermal microactuator. to be presented at the 5th Asian Mechanism and Machine Science Conference, Dec 2018.

Yadav, D., Murthy, N. S., Palathingal, S., Shekhar, S., Giridhar, M., and Ananthasuresh, G. (2019). A two-terminal bistable electrothermally actuated microswitch. *Journal of Microelectromechanical Systems*.

Yang, Y.-J., Liao, B.-T., and Kuo, W.-C. (2007). A novel 2×2 mems optical switch using the split cross-bar design. *Journal of Micromechanics and Microengineering*, 17(5):875.

Yin, L. and Ananthasuresh, G. K. (2003). Design of distributed compliant mechanisms. *Mechanics based design of structures and machines*, 31(2):151–179.

Zhang, Y.-h., Ding, G., Shun, X., Gu, D., Cai, B., and Lai, Z. (2007). Preparing of a high speed bistable electromagnetic rf mems switch. *Sensors and Actuators A: Physical*, 134(2):532–537.